

Measurement of Single and Double Spin Asymmetries in  $\vec{p}(e, e' \pi^{\pm,0})X$   
Semi-Inclusive Deep-Inelastic Scattering

Sucheta Shrikant Jawalkar

Williamsburg, Virginia

Master of Science, College of William and Mary, 2007  
Bachelor of Science, Truman State University, 2006

A Dissertation presented to the Graduate Faculty  
of the College of William and Mary in Candidacy for the Degree of  
Doctor of Philosophy

Department of Physics

The College of William and Mary  
January 2012

## **APPROVAL PAGE**

This Dissertation is submitted in partial fulfillment of  
the requirements for the degree of

Doctor of Philosophy

---

Sucheta Shrikant Jawalkar

Approved by the Committee, October 2011

---

Committee Chair  
Professor Keith Griffioen, Physics  
The College of William & Mary

---

Professor Todd Averett, Physics  
The College of William & Mary

---

Associate Professor Jeffrey Nelson, Physics  
The College of William & Mary

---

Associate Professor Konstantinos Orginos, Physics  
The College of William & Mary

---

Dr. Harut Avakian, Physics  
Thomas Jefferson National Accelerator Facility

**COPYRIGHT PAGE**

©2011, Sucheta Shrikant Jawalkar  
All Right Reserved

## ABSTRACT PAGE

Measurements in the late 1980s at CERN revealed that quark spins account for a small fraction of the proton's spin. This so-called spin crisis spurred a number of new experiments to identify the proton's silent spin contributors, namely, the spin of the gluons, which hold the quarks together, and the orbital angular momentum of both quarks and gluons. One such experiment was eg1-dvcs at the Thomas Jefferson National Accelerator Facility in Newport News, Va., which ran in 2009 and collected approximately 19 billion electron triggers for hydrogen. I will present new measurements of the single and double-spin asymmetries  $A_{LU}$ ,  $A_{UL}$  and  $A_{LL}$  for  $\pi^+$ ,  $\pi^-$  and  $\pi^0$ , measured as a function of Bjorken  $x_B$ , squared momentum transfer  $Q^2$ , hadron energy fraction  $z$ , and hadron transverse momentum  $P_{h\perp}$ . These asymmetries, which are convolutions of transverse-momentum-dependent parton distributions and fragmentation functions, correlate with the transverse momentum, and therefore with the orbital motion, of the struck quark.

## TABLE OF CONTENTS

	Page
<b>Acknowledgments</b> . . . . .	<b>v</b>
<b>List of Tables</b> . . . . .	<b>vi</b>
<b>List of Figures</b> . . . . .	<b>viii</b>
<b>CHAPTER</b>	
<b>1 Introduction</b> . . . . .	<b>1</b>
<b>2 Interpretation and Theory</b> . . . . .	<b>5</b>
2.1 Semi Inclusive Asymmetries . . . . .	5
2.2 Semi Inclusive Cross sections . . . . .	7
2.3 Transverse Momentum Dependent distributions . . . . .	11
2.3.1 Longitudinally polarized TMDs . . . . .	11
2.3.2 Twist . . . . .	13
2.3.3 Connection to Asymmetries . . . . .	15
2.4 Previous Measurements . . . . .	17
2.5 Models used within the TMD Phenomenology . . . . .	21
2.5.1 Leading Order Parton Model . . . . .	21
2.5.2 Quark and Diquark Spectator Models . . . . .	22
2.5.3 Other Models . . . . .	23

<b>3</b>	<b>Experiment</b>	<b>25</b>
3.1	The CEBAF Electron Accelerator	25
3.2	Hall B Beamline devices	28
3.3	Polarized Target	31
3.3.1	Theory Overview	31
3.3.2	Polarized Target Components	33
3.3.3	NMR Calibration	37
3.4	Inner Calorimeter	40
3.5	CEBAF Large Acceptance Spectrometer	42
3.5.1	Torus Magnet	44
3.5.2	Scintillator Counters	45
3.5.3	Drift Chambers	47
3.5.4	Cherenkov Counters	51
3.5.5	Electromagnetic Calorimeters	53
3.5.6	Trigger and Data Acquisition	54
3.6	Run Summary	59
<b>4</b>	<b>Data Analysis I</b>	<b>62</b>
4.1	Corrections before Event Selection	62
4.1.1	Raster Correction	62
4.1.2	Tracking Correction	67
4.1.3	Fiducial cuts for the Inner Calorimeter	68
4.2	Event Selection	69
4.2.1	Electron	70
4.2.2	Charged Pions	71

4.2.3	Neutral Pions . . . . .	73
4.2.4	Quality Checks . . . . .	74
4.3	Corrections after Event Selection . . . . .	95
4.3.1	Beam and target polarization . . . . .	95
4.3.2	Pair Symmetric Background . . . . .	97
<b>5</b>	<b>Data Analysis II . . . . .</b>	<b>99</b>
5.1	Dilution Factor . . . . .	99
5.1.1	Areal Densities . . . . .	101
5.1.2	SIDIS nucleon cross sections . . . . .	107
5.2	Systematic Errors . . . . .	119
<b>6</b>	<b>Asymmetry Results and Discussion . . . . .</b>	<b>123</b>
6.1	Asymmetry and Error Formulae . . . . .	123
6.1.1	$A_{LU}$ . . . . .	123
6.1.2	$A_{LL}$ . . . . .	125
6.1.3	$A_{UL}$ . . . . .	126
6.2	Kinematic Coverage . . . . .	127
6.3	Results . . . . .	133
6.3.1	$A_{LU}$ . . . . .	133
6.3.2	$g_1/F_1$ . . . . .	134
6.3.3	$A_{UL}$ . . . . .	134
6.4	Comparison to Model and Existing Data . . . . .	154
6.5	Future Studies . . . . .	160
<b>7</b>	<b>Conclusion . . . . .</b>	<b>161</b>
<b>APPENDIX A</b>		
	<b>Angles in SIDIS . . . . .</b>	<b>165</b>

<b>APPENDIX B</b>	
<b>Light Cone Coordinates</b> . . . . .	<b>167</b>
<b>Bibliography</b> . . . . .	<b>169</b>

## ACKNOWLEDGMENTS

A special word of gratitude for my advisor, Keith Griffioen. Thanks to him, I had the opportunity to work in a diverse and creative environment, receptive to new ideas and open to people from all over the world. In addition to his expertise, Keith's reserve of patience, and ability to successfully explain new subject matter to me is unparalleled.

It has been a pleasure learning from members of the "eg1-dvcs" run-group at Jefferson Lab. Harut Avakian and Peter Bosted, in particular, have been instrumental in shaping my research. Their enthusiasm for physics is contagious and I am thankful for their encouragement.

I am thankful for valuable discussions with Yelena Prok and Mher Aghasyan. A special thank you to the graduate students in the group - Erin Seder, Nicholas 'Stache' Kvaltine, Andrey Kim, Gary Smith and Suman Koirala. I wish them only the best and the brightest and look forward to following their careers.

My first semester at William and Mary would have very well been my last without the constant encouragement and support from Sylvia Stout, Carolyn Hankins and Paula Perry. They have made William and Mary home for the past five years.

Thank you to my house-mates, Mimi Tatum, Kimberley Piro, and Kathryn Holt. I had the best time and my William and Mary experience would just not be the same without our adventures! Thank you to my friends for being a fantastic support system - Cara Campbell Leckey, Jie Xu, Aubrey Evans, Oseyi Ikuenobe, Mehdi Mezziani, Josh Hoskins, Tulika Makharia, Dan Pechkis and Eric Walter.

Thank you to my 'baby' brother Sumit who is a constant source of inspiration. Thank you to my parents Medha and Shrikant Jawalkar. Their love, encouragement, and sacrifices have provided me with opportunities that make everything seem possible.

## LIST OF TABLES

Table		Page
3.1	Run summary of the eg1-dvcs experiment. The experiment ran in three blocks from February to September 2009. The beam energy in the latter part of A was lowered due to mechanical problems with the accelerator. Data with reversed field for the torus magnet were collected for background studies. The center of the target was shifted in reference to CLAS, in B and C which gave higher acceptance for the charged pions. . . . .	59
3.2	Summary of Møller measurements for the eg1-dvcs experiment. The Møller polarimeter measures the beam polarization ( $P_b$ ) for both helicities using elastic scattering on polarized Permendur foil Ref. [1]. Differences in the polarization between the two helicities on the order of a 1-2% are consistent with previous CLAS experiments. However we had some differences as large as 9% for Møller runs that did not run long enough. .	60
4.1	Summary of electron identification criteria. The cuts in the EC and CC remove negative pion contamination in the sample. Electrons with momentum less than 0.8 GeV are removed from sample to minimize events with large radiative corrections. The vertex cut ensures that the electron in the event actually came from the target region. . . . .	70
4.2	Summary of charged pion selection cuts. The cuts in the EC and CC remove electron contamination in the sample. The timing cuts is based on the time of flight of the charge particle through the detector. This cuts removes heavier particles that would take longer than the pion, e.g. proton, kaon, etc. The vertex cut ensures that the data are collected from the target region. . . . .	71
4.3	Summary of photon selection cuts in the Electromagnetic Calorimeter. . .	73
4.4	Summary of photon selection cuts in the Inner Calorimeter. . . . .	73

4.5	Summary of $P_b P_t$ extractions for the $\text{NH}_3$ target using exclusive e-p scattering. The average beam polarization value is obtained from weighting the Møller measurements from Table 3.2 with e-p elastic events. The analysis was done separately for runs with positive target polarization and for negative target polarization. . . . .	97
5.1	Nominal and corrected values for center of the $\text{NH}_3$ target in CLAS coordinates. The raster correction study is described in 4.1.1. . . . .	100
5.2	Summary of volume densities and lengths of materials in the target. . . . .	102
5.3	Average banjo lengths, $L_{banjo}$ and target lengths $L_{\text{NH}_3}$ for parts A and B of the experiment. Values are calculated separately for top and bottom ammonia targets. . . . .	107
5.4	The $\chi^2/dof$ values for fitting the semi-inclusive rate ratio of ammonia to carbon using the ad-hoc SIDIS model. The data were divided by eg1dvcs run periods A (58800 - 59161) and B (59400 - 60200). . . . .	115
5.5	Sources of systematic uncertainties and their estimated values for eg1dvcs run periods A (58800 - 59161) and B (59400 - 60200). . . . .	121
6.1	Lower bin edges for this experiment. The bin size was constant for all variables except $Q^2$ for which we used logarithmic bin sizes. . . . .	128
7.1	Transverse Momentum Distributions and Fragmentation Functions accessed by observables from the eg1-dvcs measurement. . . . .	163

## LIST OF FIGURES

Figure	Page
1.1	World data on $g_1^p$ [2]. . . . . 3
1.2	World data on $\Delta g/g$ [2]. . . . . 4
2.1	Semi-inclusive deep inelastic scattering kinematics. The electron $l = (E, \vec{l})$ exchanges a virtual photon $q$ with the stationary nucleon and recoils with a 4-momentum $l' = (E', \vec{l}')$ . The reaction produces a hadron with 4-momentum $P_h = (E_h, \vec{P}_h)$ . The plane formed by the incoming lepton and virtual photon is called the lepton plane. The plane formed by the virtual photon and the newly formed hadron is called the hadron plane. The angle between these two planes is given by $\phi_h$ . The transverse component of the hadron momentum is denoted by $P_{h\perp}$ . The component of the nucleon spin transverse to the virtual photon is called $S_\perp$ and $\phi_S$ is the angle between $S_\perp$ and the virtual photon. . . . . 6
2.2	Examples of diagrams contributing to tree level SIDIS scattering Ref. [3]. The correlators for the quark distribution and fragmentation functions are $\Phi$ and $\Delta$ respectively. The dotted line is called the final state cut. The 4-momenta for the virtual photon, quark before scattering and quark after scattering are $q$ , $p$ and $k$ respectively. At the node, we have $q + p = k$ . Diagram (b) and (c) include one transversely polarized gluon. . . . . 10
2.3	Probabilistic interpretation of the leading-order transverse momentum distributions for all combinations of quark and nucleon polarization. The green arrows indicate nucleon polarization and the red arrows indicate quark polarization. . . . . 12
2.4	The sine- $\phi_h$ moments of longitudinal single spin target asymmetries for $\pi^+$ as measured in Ref. [4] as a function of $x_B$ (left) and $P_{h\perp}$ (right). The $A_{UL}^{\sin 2\phi_h}$ component was found to be consistent with zero. . . . . 17

2.5	The various azimuthal moments appearing in the measurement of the $\sin \phi_h$ modulations of single-spin asymmetries as measured by Ref. [5] on a longitudinally polarized hydrogen target for charged pions as functions of $x_B$ (left) and $z$ (right). The open symbols are the measured lepton-axis moments. The ones from a transversely polarized target are multiplied by $\sin \phi_\gamma$ according to their appearance in the longitudinal lepton-axis moments. The closed symbol is the subleading-twist contribution to the measured lepton-axis asymmetries on a longitudinally polarized target. The triangles are slightly shifted horizontally for distinction. An overall systematic error of 0.003 is not included here. . . . .	18
2.6	The sine- $2\phi_h$ moment of the target spin asymmetry measured by CLAS in 2010 Ref. [6] on the proton. The systematic errors for CLAS are the empty blocks on the bottom of each figure and the yellow regions indicate the systematic error from the HERMES measurements. . . . .	19
2.7	Comparison of double spin asymmetry measured by COMPASS Ref. [7] in comparison to HERMES data from 2005 for inclusive electron (left), charged pions (middle) and charged kaons (right). . . . .	20
2.8	Predictions for azimuthal asymmetries $A_{UL}$ vs. $x_B$ for different beam energies and the corresponding kinematical cuts at CLAS. The thick lines correspond to $W(\phi) = \sin \phi$ , the thin lines correspond to $W(\phi) = \sin 2\phi$ . Here the solid lines refer to $\pi^+$ range, long-dashed lines to $\pi^0$ range, and short-dashed lines to $\pi^-$ range [8]. . . . .	22
2.9	The single spin asymmetry $A_{UL}^{\sin 2\phi}$ as a function of $x_B$ at different kinematics with $Q^2 = 3.0 \text{ GeV}^2$ for the proton target. Dashed curves correspond to approach 1, while solid curves correspond to approach 2 in Ref. [9]. . .	24
3.1	A cryomodule consisting of several resonant superconducting RF cavities. These modules are used in the injector assembly and in the linear accelerators (linacs) Ref. [10]. . . . .	26
3.2	Schematic diagram of the CEBAF accelerator. Polarized electrons produced in the injector are transferred to the north linear accelerator (linac). They circle through the recirculation arcs via bending magnets and enter the south linear accelerator, and then go through another set a bending magnets. This loop can be repeated up to five times. The electrons can be extracted for use after each pass and are transferred to each of the three end stations through a beam separator Ref. [10]. . . . .	28

3.3	Hall B schematic showing beamline devices in relation to CLAS Ref. [11]. The beamline shown in red, enters Hall B and can pass through the Møller Polarimeter (blue), Beam Position Monitors (BPM) (red), Harp Scanner (green), the experimental target, and Faraday cup (yellow), before passing out of Hall B and on into the beam dump. . . . .	29
3.4	Beam position read back during the Spring 2009 run for the eg1-dvcs experiment. The plot shows $x$ component of the beam position as a function of time from the three BPMs coded 2C21A (red), 2C24B (blue) and 2H01(yellow). The nominal value required is $x = 1.00$ mm. . . . .	30
3.5	Harp scan for run number 59097 taken during the Spring 2009 run for the eg1-dvcs experiment. The scattered particles (PMT counts) in the detector are shown as a function of the $x$ and $y$ plane projections. The beam diameter here is about 0.5 mm. . . . .	31
3.6	Energy levels for the proton and electron using the simple solid state approach. The green line represents the transition excited by the microwaves and the yellow line represents the relaxation of electron spins Ref. [12]. The sample is placed in a magnetic field $\vec{B}$ . . . . .	33
3.7	Schematic diagram of the polarized target and associated apparatus Ref. [13]. Seen on the left are Helmholtz magnet coils and the space to insert the target stick. The refrigerator, connected at an angle, is also shown along with the liquid helium reservoir and pump assembly. . . . .	34
3.8	The target stick used during the experiment. The first two cups contained ammonia and the third had a carbon disk. The last one was left empty for background studies. The cross-hairs at the bottom were used to align the beam on the target. . . . .	35
3.9	Photograph of the target stick in the banjo enclosure. The photo was taken with a mirror held on the bottom of the target stick. The mirror shows an empty Kapton cup higher up on the target stick. The banjo is the metal enclosure surrounding the target stick. . . . .	36
3.10	Signal from the NMR setup as function of scanning frequency $\omega$ (Hz) Ref. [13]. The left plot shows the baseline voltage scan at thermal equilibrium. The middle plot shows the baseline subtracted data. The right plot shows the background subtracted value of the Thermal Equilibrium (TE) voltage. . . . .	38

3.11	Target polarization values after NMR calibration as a function of run number. The polarization of each target falls with beam dose as is seen for both target cups. The red points denote runs with a wide variation in target polarization within a small time period. . . . .	39
3.12	A photograph of the Inner Calorimeter (IC) on a laboratory table top with surrounding electronics. The IC has an octagonal geometry and fits in between the polarized target and CLAS. The black opening in the center is to let the beam pass through. . . . .	40
3.13	Schematic of the IC in reference to CLAS and the polarized target. The red line simulates the path of a charged particle originating in the target, passing through the IC and into the first region of the drift chambers in CLAS. . . . .	41
3.14	The neutral pion mass as measured in the IC (black) and EC (green) after they were calibrated for gain (ADC) and timing (TDC). The stability of the neutral pion mass peak over the run period indicates an acceptable calibration quality. The resolution for the $\pi^0$ is significantly better in the IC (red) than the EC (blue) as seen in the $3\sigma$ boundary . . . . .	42
3.15	CLAS schematic showing the main detector components. Green marks the electromagnetic calorimeter. The next layers in are the scintillator counters in red and Cherenkov counter (CC) in pink which distinguishes electrons from hadrons. The torus magnet (yellow) creates a field that allows for momentum determination using the drift chambers (blue). . . .	43
3.16	Schematic (left) and actual view (right) of the CLAS torus magnet Ref. [1]. The photograph shows the initial installation of the CLAS Torus magnet. The six fold symmetry of the magnet forms the skeleton of CLAS and the dashed arrow on the schematic indicates beam direction. Each sector contains a set of drift chambers (DC), a Cherenkov counter (CC), time of flight scintillators (TOF) and an electromagnetic calorimeter (EC).	44
3.17	The orientation of scintillator strips for one sector with respect to the beam direction. Each strip is 5 cm thick and connected to two PMTs. . . .	45
3.18	The dependance of $\beta$ on particle momenta after the paddles in the SC have been calibrated. The process starts with obtaining $\beta = 1$ for electrons (and photons) and then correcting the timing for heavier particles Ref. [14]. The broad band under $\beta = 1$ shows the pions and the smaller band under that one identifies the proton. . . . .	46
3.19	Drift chamber cell configuration with a typical track indicated (left) and photograph of a completed drift chamber sector (right)Ref. [1]. . . . .	47

3.20	Residual distribution (cm) as a function of wire layers after DC alignment for each CLAS sector Ref. [15]. The white area is a dead wire layer. . . .	49
3.21	Calibration quality for the drift chamber vs run number. DC sigma is a measure of the spatial resolution of the chamber. The gap between runs comes from the Summer 2009 accelerator down time between parts A and B of this experiment. Each run number is approximately three hours of data taking. The stability of the DC signal indicates an acceptable calibration quality. . . . .	50
3.22	Optical module of the CLAS Cherenkov detector showing light reflected off the set of mirrors, as collected by a PMT. The Cherenkov light is reflected off the hyperbolic and cylindrical mirrors placed in a configuration to direct light to the collection cone. The PMTs are placed in the acceptance dark regions of the coils of the torus magnet Ref. [1]. . . . .	52
3.23	Cherenkov timing differences $\Delta t = t_{CC} - t_{SC}$ and widths $\sigma$ as a function of PMT number after calibration using one run. PMT 22 (Sector 1) was dead throughout the experiment. This is reflected in the point with biggest error bars in mean and standard deviation. The data for large PMT numbers fluctuate wildly because of poor statistics near the edge of CLAS acceptance Ref. [16]. . . . .	56
3.24	Cherenkov counter light intensity spectrum for a single photoelectron. The gain calibration is done by fitting the single photoelectron peak. The fit in red is shown for one channel in Sector 2 in the CC. An ADC channel value of $\approx 200$ corresponds to the single photoelectron peak Ref. [17]. . .	57
3.25	One sector in the CLAS electromagnetic calorimeter Ref. [18]. The three layers of scintillator are placed in three different orientations rotated from the one above by $120^\circ$ . This is done to allow triangulation of the shower position in the detector Ref. [1]. . . . .	57
3.26	The time difference between the EC and SC versus run number fit using a Gaussian. Data for the means (blue) and standard deviations (red) are shown for the duration of the experiment. The stability of the values indicates an acceptable calibration quality. . . . .	58

4.1	Side view of raster correction geometry. The vertex position in the CLAS $z$ direction is corrected for tracking which assumes the electron traveled along the center of the beam line. The black ray is the uncorrected particle path which forms an angle $\theta$ with the beam direction. The red ray is the traced-back ray, and the blue path is the final, raster corrected path through the true vertex Ref. [11]. The vertex position given by CLAS tracking software is $v_{z0}$ and the corrected vertex is $v_{zc}$ . . . . .	63
4.2	Cross-section view of the raster correction geometry Ref. [11].The black dotted line represents the (uncorrected) particle trajectory; while the solid black line ( $s$ ) is the reference line of the triggered sector. The projection of the raster coordinates (green) on the trajectory is defined as $x'$ (blue). . . . .	65
4.3	Raster pattern for Run 59000 with a selected section on the target area (top row). The second row shows the vertex position $v_z$ before applying the raster correction for the selected target area above it. The third shows the vertex position $v_z$ after applying the raster correction. . . . .	66
4.4	Beam energy calculated from $ep$ elastic scattering for each sector using an $\text{NH}_3$ run. The dashed lines use the momenta and angles from the reconstruction algorithm from RECSIS and the solid lines are the spectra after applying the track reconstruction corrections. . . . .	67
4.5	Distribution of $x$ (cm), $y$ (cm) at the IC front face for electrons, positrons, positive pions, and photons, for part A run 59000 Ref. [19]. The inner red lines define the standard fiducial cut, while the outer red lines define the stricter cut. To save space, points beyond a radius of 24 cm are not plotted. . . . .	69
4.6	Histogram of the number of photoelectrons detected in the CC for candidate electrons (lower plot) and the track/CC phototube matching $\chi^2$ (upper plot). The blue shows the data before cuts and the black shows data eliminated by the electron cuts. . . . .	77
4.7	$E/p$ versus $p$ (upper plot) and vertex $z$ position (lower plot) for electron candidates. The black points (upper) and lines (lower) indicate events that are eliminated by the full electron cuts. . . . .	78

4.8	Electron candidates as a function of momentum after applying the selection criteria from Table 4.1. We start with all negatively charged particles detected in CLAS. We then cut out negative pions in the EC using the momentum-dependent cut. This is followed by cuts on the Cherenkov counter for both the signal and mirror matching. These cuts reduce the initial sample by $\approx 15\%$ . The last two cuts remove low momentum electrons and electrons coming from regions other than the target area leaving us with $\approx 67\%$ of the initial sample. . . . .	79
4.9	$E/p$ vs. $p$ for positive (upper plot) and negative (lower plot) pions. The colored region is selected as a good pion candidate and the black region is removed prior to physics analysis. . . . .	80
4.10	$p$ vs. $\Delta\beta$ for positive (upper) and negative (lower) pions. The colored region is selected as a good pion candidate and the black region is removed prior to physics analysis. The $\Delta t$ cut removes signals from the kaon and proton as seen in the top plot. . . . .	81
4.11	Vertex $z$ distributions for $\pi^+$ (upper plot) and $\pi^-$ (lower plot). The colored region is selected as a good pion candidate and the black region is removed prior to physics analysis. The vertex selection ensures the data are coming from the target region. . . . .	82
4.12	Charged pion candidates as a function of their momentum. The effect of applying the selection criteria from Table 4.2 seen here for run 60100. The upper plot shows the progression of cuts for the positive pion and the lower plot is for the negative pion. The cut on timing removes the most number of positive pion candidates. . . . .	83
4.13	Invariant two-photon mass distributions for three different photon topologies. The three possible topologies to calculate the invariant $\pi^0$ mass are two $\gamma$ s in the IC, two $\gamma$ s in the EC and, one $\gamma$ in the EC and one $\gamma$ in the IC. The yellow region is selected as a good neutral pion candidate and the black region is eliminated from physics analysis. . . . .	84
4.14	Candidates for the neutral pion as a function of photon momentum. The progression of cuts to select a photon in the IC (top) and EC (bottom) seen for run 60100. Low momentum photons for each case are removed. A cut on $\beta$ implemented for the neutral pion in the EC. This cut is designed to remove any signal from neutrons. The $\Delta t$ cut in the IC is a cut on the time difference between the event start time and the photon hit in the IC. This is designed to remove signal uncorrelated with with event start time. The events are shown on a logarithmic scale. . . . .	85

4.15	Electron rate on the ammonia target as a function of run number for the data files used in the analysis for Sector 1 (top) and Sector 2 (bottom). Each run number has approximately eighty data files. Plotted in color is the distribution of rates in each of the files in the experiment. Data files with low rates in each sector are removed. The jump in the rate around Run 59150 comes from a change in the beam energy to 4.7 GeV and the slight jump around Run 60000 comes from reversing the polarity of the torus magnet current. The white space between Runs 59250 and 59400 is the accelerator summer down. . . . .	86
4.16	Same as Figure 4.15 except showing Sector 3 (upper) and Sector 4 (lower).	87
4.17	Same as Figure 4.15 except showing Sector 5 (upper) and Sector 6 (lower).	88
4.18	Photoelectrons measured in the CC as a function of run number for the data files used in the analysis for Sector 1 (top) and Sector 2 (bottom). Each run number has approximately eighty data files. Data files with low rates in each sector are removed. The jump in the rate around Run 59150 comes from a change in the beam energy to 4.7 GeV and the slight jump around Run 60000 comes from reversing the polarity of the torus magnet current. The white space between Runs 59250 and 59400 is the accelerator summer down between parts A and B. . . . .	89
4.19	Same as Figure 4.18 except showing Sector 3 (upper) and Sector 4 (lower).	90
4.20	Same as Figure 4.18 except showing Sector 5 (upper) and Sector 6 (lower).	91
4.21	The beam charge asymmetry as a function of run number. The color scale denotes the file number. . . . .	92
4.22	Energy deposited in the EC scaled by a function of electron momentum as a function of run number. Each sector is mostly stable except for the drop about every 50 runs. This plot shows the version we got by fine tuning the EC gain calibration. We deemed this acceptable for the purposes of calculating asymmetries. . . . .	93
4.23	Raster distribution for ADC $y$ vs ADC $x$ . The red crescent shows the beam hitting the Kapton cell on the top left corner. The bottom of the plot corresponds to the top of the target. . . . .	94
4.24	Average $P_b P_t$ deduced from e-p elastic scattering. The progression of polarization product as a function of $Q^2$ (GeV) <sup>2</sup> . “Part A2” refers to the inbending data from part B of the experiment. . . . .	96

5.1	Schematic side view of the target material in CLAS. Shown here are ammonia, empty and carbon (top to bottom) targets used in 58799 - 59250 with a central nominal value of $z_{nom} = 58.3$ cm. The beam passes through the grey Aluminum windows, liquid Helium in the target and a Kapton target cell window before interacting with actual polarized target material.	101
5.2	The calculated $\chi^2$ for multiple values of $L_{test}$ used to deduce $L_{banjo}$ by comparing rate ratios to inclusive models Ref. [20] Ref. [21]. The minimum $\chi^2$ in this case gives the length between the banjo windows to be $L_{banjo} = 2.01 \pm 0.01$ cm. This value is smaller in than the room temperature value which suggests that the Aluminum windows bow inward.	103
5.3	Determinations of $L_{banjo}$ by $\chi^2$ minimization for several combinations of runs over the course of the experiment. The extreme outliers in the experiment come from using the combination of an empty target run in combination with an empty target run with no helium.	105
5.4	Distribution of vertex $z$ for Run 60023 for electrons with momentum greater then 2 GeV for the empty target. The two peaks correspond to the banjo windows with a nominal separation of 2.18 cm.	106
5.5	The extracted ammonia length for each target (TOP and BOT) for the Run range 58800 - 59300 (A) and 59400 - 60200 (B).	108
5.6	Inclusive event rate as a function of run number for the NH <sub>3</sub> TOP (blue), NH <sub>3</sub> TOP (red) and carbon target (black). The horizontal lines indicate a change in run configuration. Around Run 59160 is a change in beam energy and around Run 59995 is a change in torus polarity.	113
5.7	SIDIS rate ratio of ammonia to carbon for the positive pion (top) and the corresponding model prediction for dilution (bottom). The run range in this case is 59400 - 60200 and each data point on the horizontal axis corresponds to one kinematic bin in $(Q^2, x_B, z, P_{h\perp})$ .	114
5.8	Same as Figure 5.7 for the negative pion.	114
5.9	Same as Figure 5.7 for the neutral pion.	115
5.10	The dependence of ratio of (NH <sub>3</sub> /C) on $P_{h\perp}$ in different $x_B$ bins for positive (top row), negative (middle row) and neutral (bottom row) pions. The data are integrated over all other kinematics and are shown here for Runs 59400 - 60250. The open circles show the SIDIS model result.	116
5.11	Same as Figure 5.10 except as a function of $Q^2$ .	117
5.12	Same as Figure 5.10 except as a function of $z$ .	118

5.13	The ratio ( $R = \sigma_L/\sigma_T$ ) in SIDIS as a function of $z$ as measured at Cornell Ref. [22]. The red symbols reflect the data on a hydrogen target for $\pi^+$ (filled circle), and $\pi^-$ (filled triangle). The blue symbols reflect the data on a deuterium target for $\pi^+$ (open circle), and $\pi^-$ (open triangle). The solid curves reflect the parameterization of $R$ for DIS. Projected data for the E12-06-104 experiment have been added as black solid circles Ref. [23]. . . . .	122
6.1	The kinematic coverage in $x_B$ and $Q^2$ (GeV <sup>2</sup> ) in CLAS for semi-inclusive $\pi^+$ (top), $\pi^-$ (middle) and $\pi^0$ (bottom) events. The independent variables $x_B$ and $Q^2$ are correlated here because of CLAS acceptance. . . . .	130
6.2	The kinematic coverage in $x_B$ and $P_{h\perp}$ (GeV) in CLAS for semi-inclusive $\pi^+$ (top), $\pi^-$ (middle) and $\pi^0$ (bottom) events. The majority of $\pi^\pm$ are dominated by $P_{h\perp}$ values around 0.45 GeV. The $\pi^0$ events are concentrated at slightly lower $P_{h\perp}$ values. . . . .	131
6.3	The kinematic coverage in $P_{h\perp}$ (GeV) and $\phi_h$ (degrees) in CLAS for semi-inclusive $\pi^+$ (top), $\pi^-$ (middle) and $\pi^0$ (bottom) events. About two thirds of the neutral pions are detected fully or partially in the IC. This is reflected in the higher event rate on the edges of the bottom plot as compared to the charged pions which are detected only in CLAS. . . . .	132
6.4	The integrated beam spin asymmetry for $\pi^+$ (top, red points), $\pi^-$ (middle, blue points), and $\pi^0$ (bottom, green points). The data were fit to $f(\phi_h) = A_{LU}^C + A_{LU}^{\sin\phi_h} \sin\phi_h + A_{LU}^{\sin 2\phi_h} \sin 2\phi_h$ and were integrated over all bins of $(Q^2, x_B, z, P_{h\perp})$ . . . . .	136
6.5	The beam spin asymmetry vs $\phi_h$ for $\pi^+$ in bins of $x_B$ and $P_{h\perp}$ . Each $x_B$ and $P_{h\perp}$ bin is fit to $f(\phi_h) = A_{LU}^C + A_{LU}^{\sin\phi_h} \sin\phi_h + A_{LU}^{\sin 2\phi_h} \sin 2\phi_h$ . The $A_{LU}$ distribution for the $\langle x_B \rangle = 0.33$ and $\langle P_{h\perp} \rangle = 0.44$ is highlighted. . . . .	137
6.6	Same as Figure 6.5 except for $\pi^-$ . . . . .	138
6.7	Same as Figure 6.5 except for $\pi^0$ . . . . .	139
6.8	The $\sin\phi_h$ moments of $A_{LU}$ as a function of $P_{h\perp}$ for different bins in $x_B$ . The average value of $x_B$ is displayed in the title of each plot for $\pi^+$ (red), $\pi^-$ (blue), and $\pi^0$ (green). . . . .	140
6.9	The $\sin 2\phi_h$ moments of $A_{LU}$ as a function of $P_{h\perp}$ for different bins in $x_B$ . The average value of $x_B$ is displayed in the title of each plot for $\pi^+$ (red), $\pi^-$ (blue), and $\pi^0$ (green). . . . .	141

6.10	The ratio of polarized to unpolarized structure functions integrated over $(Q^2, x_B, z, P_{h\perp})$ for $\pi^+$ (red, top), $\pi^-$ (blue, middle) and, $\pi^0$ (green, bottom). The data are fit to $f(\phi_h) = A_{LL}^C + A_{LL}^{\cos\phi_h} \cos\phi_h$ . . . . .	142
6.11	The ratio of polarized to unpolarized structure functions, $g_1/F_1$ versus $P_{h\perp}$ for different bins in $x_B$ . The average value of $x_B$ is displayed in the title of each plot for $\pi^+$ (red), $\pi^-$ (blue), and $\pi^0$ (green). . . . .	143
6.12	The ratio of polarized to unpolarized structure functions integrated over $(Q^2, z)$ for $\pi^+$ . The data are fit to $f(\phi_h) = A_{LL}^C + A_{LL}^{\cos\phi_h} \cos\phi_h$ . . . . .	144
6.13	Same as Figure 6.12 except for $\pi^-$ . . . . .	145
6.14	Same as Figure 6.12 except for $\pi^0$ . . . . .	146
6.15	The cosine $\phi_h$ moment of the ratio of polarized to unpolarized structure functions, $g_1/F_1$ versus $P_{h\perp}$ for different bins in $x_B$ . The average value of $x_B$ is displayed in the title of each plot for $\pi^+$ (red), $\pi^-$ (blue), and $\pi^0$ (green). . . . .	147
6.16	The integrated target spin asymmetry for $\pi^+$ (top, red points), $\pi^-$ (middle, blue points), and $\pi^0$ (bottom, green points). The data were fit to $f(\phi_h) = A_{UL}^C + A_{UL}^{\sin\phi_h} \sin\phi_h + A_{UL}^{\sin 2\phi_h} \sin 2\phi_h$ and were integrated over all bins of $(Q^2, x_B, z, P_{h\perp})$ . . . . .	148
6.17	The target spin asymmetry vs $\phi_h$ for $\pi^+$ in bins of $x_B$ and $P_{h\perp}$ . Each $x_B$ and $P_{h\perp}$ bin is fit to $f(\phi_h) = A_{UL}^C + A_{UL}^{\sin\phi_h} \sin\phi_h + A_{UL}^{\sin 2\phi_h} \sin 2\phi_h$ . . . . .	149
6.18	Same as Figure 6.17 except for $\pi^-$ . . . . .	150
6.19	Same as Figure 6.17 except for $\pi^0$ . . . . .	151
6.20	The target spin asymmetry vs $\phi_h$ for $\pi^0$ in bins of $x_B$ and $P_{h\perp}$ . Each $x_B$ and $P_{h\perp}$ bin is fit to $f(\phi_h) = A_{UL}^C + A_{UL}^{\sin\phi_h} \sin\phi_h + A_{UL}^{\sin 2\phi_h} \sin 2\phi_h$ . . . . .	151
6.21	The $\sin\phi_h$ moments of $A_{UL}$ as a function of $P_{h\perp}$ for different bins in $x_B$ . The average value of $x_B$ is displayed in the title of each plot for $\pi^+$ (red), $\pi^-$ (blue), and $\pi^0$ (green). . . . .	152
6.22	The $\sin 2\phi_h$ moments of $A_{UL}$ as a function of $P_{h\perp}$ for different bins in $x_B$ . The average value of $x_B$ is displayed in the title of each plot for $\pi^+$ (red), $\pi^-$ (blue), and $\pi^0$ (green). . . . .	153
6.23	The ratio of polarized to unpolarized structure functions integrated over $(Q^2, x_B, z, P_{h\perp})$ for $\pi^+$ (red). The gray bar at the bottom denotes systematic errors from Table 5.5. The dashed line represents the Anselmino model prediction Ref. [24]. . . . .	156
6.24	Same as Figure 6.23 except for $\pi^-$ . . . . .	157
6.25	Same as Figure 6.23 except for $\pi^0$ . . . . .	158

6.26 The  $\sin \phi_h$  moments of  $A_{LU}$  as a function of  $P_{h\perp}$  for different bins in  $x_B$ .  
The average value of  $x_B$  is displayed in the title of each plot for  $\pi^0$  from  
eg1-dvcs data (green) and  $\pi^0$  from Ref. [25]. . . . . 159

A.1 The lepton plane in the target rest frame. The  $y$  and  $y'$  axes coincide and  
point out of the plane of the paper [26]. . . . . 166

# CHAPTER 1

## Introduction

Deep Inelastic scattering (DIS) has been used as a tool over the past thirty years to study the origins of nucleon spin. DIS occurs when a lepton scatters from an individual quark inside a nucleon. Studying the spin observables of the reaction provide access to nucleon spin.

The leading theory that explained the internal structure of the nucleon in the 1960s was the Quark Parton model (QPM). It predicted that the nucleon was made of point-like particles called “partons” Ref. [27]. This was confirmed by experiments at the Stanford Linear Accelerator facility that measured Bjorken scaling. The proton in particular was thought to be made up of two up ( $u$ ) and one down ( $d$ ) quark. The gluon was the mediating particle for the strong force that held the quarks together in the proton. The spins of the up and down quarks are  $+\frac{1}{2}$  and  $-\frac{1}{2}$  respectively. If the origin of the proton spin is the spin contribution of its constituents, then summing the spins of the individual partons (quarks and gluons) should theoretically results in the then widely known fact that the proton spin is  $\frac{1}{2}$ . Angular momentum conservation requires that the spin of the nucleon

be written as

$$\frac{1}{2} = \frac{\Delta\Sigma}{2} + \Delta G + L_z \quad (1.1)$$

in which  $\Delta\Sigma$  denotes the net quark helicity,  $\Delta G$  denotes the net gluon helicity and  $L_z$  is the orbital angular momentum of the quarks and gluons.

In the late 1980s the EMC Collaboration at CERN measured  $\Delta\Sigma$  and concluded that it contributes to only a small fraction of the spin of the proton Ref. [28]. This spurred a ‘‘spin crisis’’ in search of the other contributors of proton spin. Experiments measured both the spin structure function  $g_1^p$  as defined in the QPM as well as,  $\Delta G$ . The spin contribution from a third, strange quark ( $s$ ) was also included in  $g_1^p$ .

$$g_1^p = \frac{1}{2} \left( \frac{4}{9}(\Delta u + \Delta\bar{u}) + \frac{1}{9}(\Delta d + \Delta\bar{d}) + \frac{1}{9}(\Delta s + \Delta\bar{s}) \right) \quad (1.2)$$

where  $\Delta u(\Delta\bar{u})$ ,  $\Delta d(\Delta\bar{d})$  and  $\Delta s(\Delta\bar{s})$  are the polarized  $u(\bar{u})$ ,  $d(\bar{d})$ , and  $s(\bar{s})$  quark (anti-quark) distributions (number of quarks with their helicity aligned minus those with their helicity anti-aligned with the nucleon spin), respectively Ref. [2]. More accurate measurements of  $g_1^p$  and  $\Delta G$  as recent as 2011 still do not add to the total proton spin.

In the naive QPM, the spin observables arising from the transverse motion of the quark are zero. To completely, understand nucleon spin structure via  $L_z$ , the transverse dimension can no longer be ignored. Semi-Inclusive DIS (SIDIS) holds the promise for being sensitive to the third possible contributor of proton spin, namely, the orbital motion of quarks.

Consider the reaction,

$$e + p \rightarrow e' + \pi + X \quad (1.3)$$

The electron scatters off a quark in the proton. The scattering products, undergo a

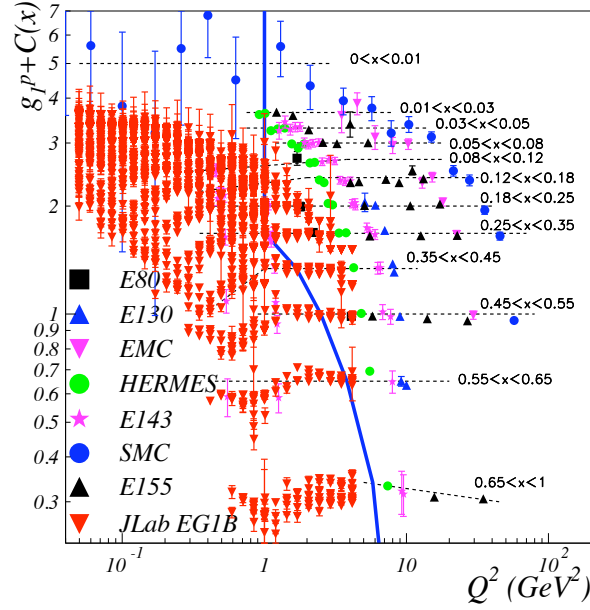


FIG. 1.1: World data on  $g_1^p$  [2].

hadronization process to form a new hadron or meson that carries the struck quark. The transverse motion of the quark is transferred to the transverse momentum,  $P_{h\perp}$  of the  $\pi$  meson. We study three flavors of the  $\pi$  meson (or pion) - positive ( $u\bar{d}$ ), negative ( $d\bar{u}$ ) and neutral  $(u\bar{u} - d\bar{d})/\sqrt{2}$ .

An analogy can be drawn with the spin structure function  $g_1^p(x_B, Q^2)$  where  $Q^2$  is the virtuality of the photon in the inclusive reaction,  $x_B = \frac{Q^2}{2M\nu}$  is the momentum fraction,  $M$  is the proton mass and  $\nu$  is the lepton energy transfer. Similarly, SIDIS equivalent structure functions are extracted in terms of  $(x_B, Q^2, z, P_{h\perp}, \phi_h)$  Ref. [26]. The fractional energy of the outgoing pion is  $z = \frac{E_\pi}{\nu}$ ,  $\phi_h$  is the angle between the lepton and hadron planes as discussed in Chapter 2. The missing mass in the reaction is denoted by  $X$ .

The SIDIS unintegrated structure functions are multi-dimensional and take into account the transverse motion of quarks thus providing more information than the standard collinear polarized structure functions like  $g_1^p$ . These new structure functions can be fur-

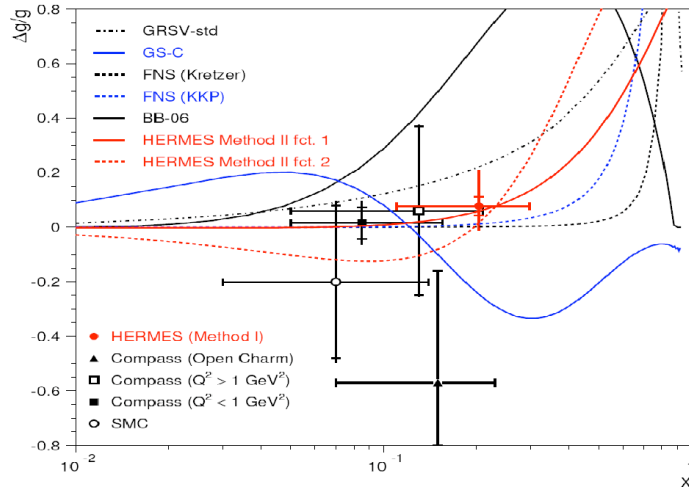


FIG. 1.2: World data on  $\Delta g/g$  [2].

ther factorized into fragmentation functions (FFs) and transverse momentum distributions (TMDs). TMDs describe the orbital motion of quarks before scattering and FFs describe the quark fragmenting into a hadron or meson. We measure single and double spin asymmetries in SIDIS which access TMDs.

The description of TMD theory and phenomenology are detailed in Chapter 2. The details of the eg1-dvcs experiment to measure asymmetries  $A_{LU}$ ,  $A_{UL}$  and  $A_{LL}$  are explained in Chapter 3. The analysis procedure is described in Chapters 4 and 5. I present the final results and conclusions in Chapter 6.

# CHAPTER 2

## Interpretation and Theory

### 2.1 Semi Inclusive Asymmetries

We measure the electron-proton scattering process of the form,

$$e(l) + N(P) \rightarrow e(l') + \pi(P_h) + X(P') \quad (2.1)$$

with the 4-momenta for each particle given in parentheses. The kinematic diagram for the reaction is shown in Figure 2.1. The conventional kinematic variables, as defined in the introduction, are used throughout this section. The electron  $l = (E, \vec{l})$  exchanges a virtual photon  $q = (\nu = E - E', \vec{q})$  with the stationary nucleon and recoils with a 4-momentum  $l' = (E', \vec{l}')$ . The reaction produces a hadron with 4-momentum  $P_h = (E_h, \vec{P}_h)$ . The plane formed by the incoming lepton and virtual photon is called the lepton plane. The lepton plane also contains the scattered lepton. The plane formed by the virtual photon and the newly formed hadron is called the hadron plane. The angle between these two planes is given by  $\phi_h$ . The component of the hadron momentum transverse to  $\vec{q}$  is denoted by

$P_{h\perp}$ . The component of the nucleon spin transverse to  $\vec{q}$  is called  $\vec{S}_\perp$  and  $\phi_S$  is the angle between  $\vec{S}_\perp$  and the lepton plane. The remainder of the reaction products are given by  $X$ .

It is often useful to express the spin dependence of the process using asymmetries, which are constructed by looking at differences in polarized cross sections normalized by their sums. In this thesis, we specifically look at three single and double spin asymmetries obtained with a longitudinally polarized nucleon and a longitudinally polarized lepton.

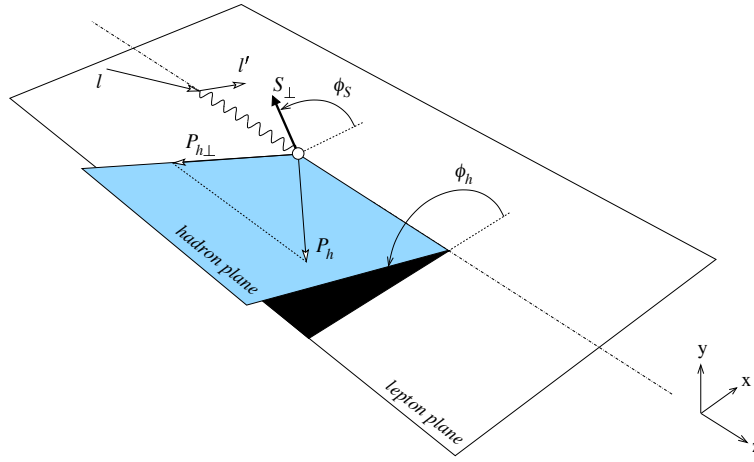


FIG. 2.1: Semi-inclusive deep inelastic scattering kinematics. The electron  $l = (E, \vec{l})$  exchanges a virtual photon  $q$  with the stationary nucleon and recoils with a 4-momentum  $l' = (E', \vec{l}')$ . The reaction produces a hadron with 4-momentum  $P_h = (E_h, \vec{P}_h)$ . The plane formed by the incoming lepton and virtual photon is called the lepton plane. The plane formed by the virtual photon and the newly formed hadron is called the hadron plane. The angle between these two planes is given by  $\phi_h$ . The transverse component of the hadron momentum is denoted by  $P_{h\perp}$ . The component of the nucleon spin transverse to the virtual photon is called  $S_\perp$  and  $\phi_S$  is the angle between  $S_\perp$  and the virtual photon.

The target single spin asymmetry (SSA) is obtained when an unpolarized lepton is incident on a longitudinally polarized target. It is written in terms of cross sections as follows,

$$A_{UL} = \frac{d\sigma^{0\rightarrow} - d\sigma^{0\leftarrow}}{d\sigma^{0\rightarrow} + d\sigma^{0\leftarrow}} \quad (2.2)$$

Similarly, the beam single spin asymmetry is obtained when a longitudinally polarized lepton is incident on an unpolarized target nucleon. It is written as,

$$A_{LU} = \frac{d\sigma^{\rightarrow 0} - d\sigma^{\leftarrow 0}}{d\sigma^{\rightarrow 0} + d\sigma^{\leftarrow 0}} \quad (2.3)$$

The double spin asymmetry (DSA) explores the case where both the lepton and target nucleon are longitudinally polarized. It is given by,

$$A_{LL} = \frac{d\sigma^{\rightarrow\rightarrow} - d\sigma^{\leftarrow\rightarrow} - d\sigma^{\rightarrow\leftarrow} + d\sigma^{\leftarrow\leftarrow}}{d\sigma^{\rightarrow\rightarrow} + d\sigma^{\leftarrow\rightarrow} + d\sigma^{\rightarrow\leftarrow} + d\sigma^{\leftarrow\leftarrow}} \quad (2.4)$$

The first subscript represents beam polarization and the second denotes target polarization. The letter  $U$  (or 0) indicates an unpolarized lepton or nucleon and  $L$  denotes a longitudinally polarized lepton or nucleon. The arrows  $\rightarrow$  and  $\leftarrow$  denote cross sections with right-handed and left-handed helicity, respectively, for the lepton, or spin along or opposite the beam direction for the nucleon. To understand the physics hidden in these asymmetries we look at their theoretical foundations in the following sections.

## 2.2 Semi Inclusive Cross sections

The expression for the semi-inclusive cross section in terms of structure functions  $F_{UL}$ ,  $F_{LL}$ , etc. is derived in Ref. [26]. The differential cross section written in terms of

seven dimensions is given by,

$$\begin{aligned}
\frac{d^7\sigma}{dK^7} &= \frac{\alpha^2}{x_{By}Q^2} \frac{y^2}{2(1-\varepsilon)} \left(1 + \frac{\gamma}{2x}\right) F_{UU,T} + \varepsilon F_{UU,L} + \sqrt{2\varepsilon(1+\varepsilon)} \cos\phi_h F_{UU}^{\cos\phi_h} \\
&+ \varepsilon \cos(2\phi_h) F_{UU}^{\cos 2\phi_h} + \lambda_e \sqrt{2\varepsilon(1-\varepsilon)} \sin\phi_h F_{LU}^{\sin\phi_h} \\
&+ S_{\parallel} \left[ \sqrt{2\varepsilon(1+\varepsilon)} \sin\phi_h F_{UL}^{\sin\phi_h} + \varepsilon \sin(2\phi_h) F_{UL}^{\sin 2\phi_h} \right] \\
&+ S_{\parallel} \lambda_e \left[ \sqrt{1-\varepsilon^2} F_{LL} + \sqrt{2\varepsilon(1-\varepsilon)} \cos\phi_h F_{LL}^{\cos\phi_h} \right] \\
&+ |S_{\perp}| \left[ \sin(\phi_h - \phi_S) \left( F_{UT,T}^{\sin(\phi_h + \phi_S)} + \varepsilon F_{UT,L}^{\sin(\phi_h - \phi_S)} \right) \right] \\
&+ \varepsilon \sin(\phi_h + \phi_S) F_{UT}^{\sin\phi_S} + \varepsilon \sin(3\phi_h - \phi_S) F_{UT}^{\sin(3\phi_h - \phi_S)} \\
&+ \sqrt{2\varepsilon(1+\varepsilon)} \sin\phi_S F_{UT}^{\sin\phi_S} + \sqrt{2\varepsilon(1+\varepsilon)} \sin(2\phi_h - \phi_S) F_{UT}^{\sin(2\phi_h - \phi_S)} \\
&+ |S_{\perp}| \lambda_e \left[ \sqrt{1-\varepsilon^2} \cos(\phi_h - \phi_S) F_{LT}^{\cos(\phi_h - \phi_S)} + \sqrt{2\varepsilon(1-\varepsilon)} \cos\phi_S F_{LT}^{\cos\phi_S} \right] \\
&+ \sqrt{2\varepsilon(1-\varepsilon)} \cos(2\phi_h - \phi_S) F_{LT}^{\cos(2\phi_h - \phi_S)} \tag{2.5}
\end{aligned}$$

in which,

$$\frac{d^7\sigma}{dK^7} \equiv \frac{d^7\sigma}{dx_B dy d\psi dz d\phi_h dP_{h\perp}^2}, \tag{2.6}$$

$y = \frac{P_{\cdot q}}{P_{\cdot l}}$ ,  $\alpha$  is the fine structure constant and  $\psi$  is the azimuthal angle of the target spin around the direction of the incoming electron. This expression is valid in the lab reference frame which is the frame in which the direction of the lepton beam is in the direction of the  $z$  axis (which is different from Figure 2.1). The projections of the target polarization vector parallel and perpendicular to the virtual photon direction are given by  $S_{\parallel}$  and  $S_{\perp}$ <sup>1</sup>. The quantity  $\varepsilon$  is the ratio of the longitudinal to transverse photon flux,

$$\varepsilon = \frac{1 - y - \frac{1}{4}\gamma^2 y^2}{1 - y + \frac{1}{2}y^2 + \frac{1}{4}\gamma^2 y^2} \tag{2.7}$$

<sup>1</sup>The target polarization vectors are also often referred to as  $S_L$  and  $S_T$ .

and  $\gamma = 2Mx_B/Q$ . The helicity structure functions have a depolarization associated with them because of the coordinate change from the photon to lepton frame of reference. More details explaining the relationship between  $\psi$ ,  $\phi_S$  and the spin of the target nucleon are explained in Appendix A.

The formulation of the cross section arises from a contraction of the lepton ( $L^{\mu\nu}$ ) and hadron ( $W_{\mu\nu}$ ) tensors Ref. [3] such that,

$$\frac{d\sigma}{dx_B dy d\psi dz d\phi_h dP_{h\perp}^2} = \frac{\alpha^2 y}{8zQ^2} L^{\mu\nu} 2M W_{\mu\nu} \quad (2.8)$$

The lepton tensor is written in terms of the 4-momenta of the incident and recoil electrons as

$$L^{\mu\nu} = l'^\nu l^\mu + l^\nu l'^\mu - (l \cdot l') g^{\nu\mu} + iP_l \varepsilon^{\nu\mu\alpha\beta} q_\alpha l_\beta. \quad (2.9)$$

using the convention  $\varepsilon^{0123} = 1$ . The lepton beam polarization  $P_l = +1$  corresponds to purely right handed and  $P_l = -1$  corresponds to purely left handed beam helicity <sup>2</sup>.

The hadron tensor is written as,

$$2M W_{\mu\nu} = \frac{1}{2\pi^3} \sum_X \int \frac{d^3 \mathbf{P}_X}{2P_X^0} \delta^4(P_X + P_h - P - q) \langle P | J_\mu(0) | hX \rangle \langle hX | J_\nu(0) | P \rangle \quad (2.10)$$

where  $J_\mu$  is the electromagnetic current divided by the elementary charge and a sum is implied over the polarizations of all hadrons in the final state. The sum over all hadron momenta is given by  $\sum_X$ . The discussion is limited to the leading and first sub-leading term in the  $\frac{1}{Q}$  expansion of the hadron tensor at tree level. The corresponding expression is given by,

---

<sup>2</sup> $P_l$  should not be confused with  $P_L$  which is the longitudinal component of the target polarization relative to the lepton beam direction.

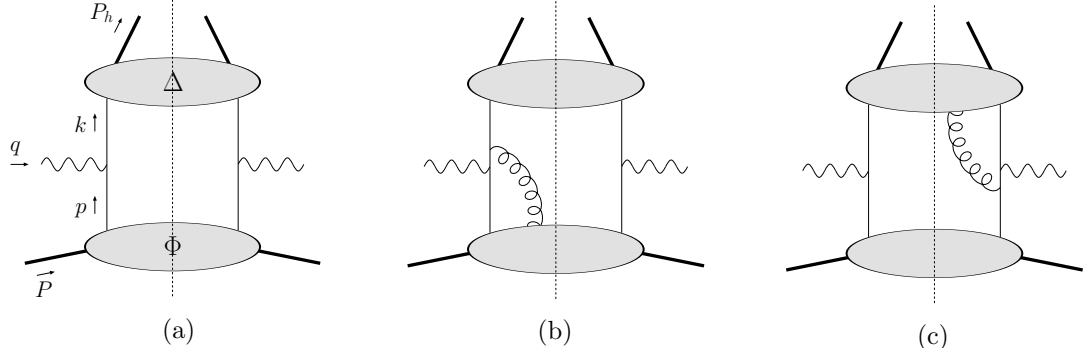


FIG. 2.2: Examples of diagrams contributing to tree level SIDIS scattering Ref. [3]. The correlators for the quark distribution and fragmentation functions are  $\Phi$  and  $\Delta$  respectively. The dotted line is called the final state cut. The 4-momenta for the virtual photon, quark before scattering and quark after scattering are  $q$ ,  $p$  and  $k$  respectively. At the node, we have  $q + p = k$ . Diagram (b) and (c) include one transversely polarized gluon.

$$W_{\mu\nu} = \frac{z}{M} \sum_a e_a^2 \int d^2\mathbf{p}_T d^2\mathbf{k}_T \delta^2(\mathbf{p}_T + \mathbf{q}_T - \mathbf{k}_T) \text{Tr} \Phi^a(x_B, p_T) \gamma^\mu \Delta^a(z, k_T) \gamma^\nu \quad (2.11)$$

$$- \frac{1}{\sqrt{2}Q} [\gamma^\alpha \not{n}_+ \gamma^\nu \tilde{\Phi}_{A\alpha}^a(x_B, p_T) \gamma^\mu \Delta^a(z, k_T) + \gamma^\alpha \not{n}_- \gamma^\mu \tilde{\Delta}_{A\alpha}^a(z, k_T) \gamma^\nu \Phi^a(x_B, p_T) + \text{h. c.}]$$

for which corrections are of order  $\frac{1}{Q^2}$ , the sum runs over the quark and antiquark flavors  $a$  with fractional charge,  $e_a$ . The correlation functions  $\Phi$  and  $\Delta$  represent quark distribution and quark fragmentation, respectively. The addition of one gluon leg to the diagram results in what are called analogs  $\tilde{\Phi}_a$  and  $\tilde{\Delta}$ . Manipulations for these calculations are easier done in terms of light cone coordinates (LCC)  $n_\pm, n_T$ . Details of these are found in Appendix B. The definition of subscript  $T$  for  $q_T$ ,  $p_T$  and  $k_T$  comes from the LCC formalism. The first, second and third term in the trace of the hadron tensor expression correspond to diagrams (a), (b) and (c) in Figure 2.2. The analogs of Figure 2.2 (b) and (c) with the gluon on the other side of the final state cut correspond to the Hermitian

conjugate (h.c.) terms in the hadronic tensor.

The expression for each of the correlators  $\Phi_a$ ,  $\Delta$ ,  $\tilde{\Phi}_a$  and  $\tilde{\Lambda}$  is worked out in detail in Ref. [3]. Inserting the different correlators in the expression of the hadronic tensor, one can calculate the leptoproduction cross section for SIDIS and project out the different structure functions appearing in Equation 2.5. To have a compact notation for the results, we introduce the unit vector  $\hat{h} = \frac{\vec{P}_{h\perp}}{|\vec{P}_{h\perp}|}$  and the condensed expression for the convolution integral  $\mathcal{C}$  is,

$$\mathcal{C}[w f D] = x \sum_a e_a^2 \int d^2 \mathbf{p}_T d^2 \mathbf{k}_T \delta^{(2)}(\mathbf{p}_T - \mathbf{k}_T - \mathbf{P}_{h\perp}/z) w(\mathbf{p}_T, \mathbf{k}_T) f^a(x, \mathbf{p}_T)^2 D^a(x, \mathbf{k}_T)^2. \quad (2.12)$$

The function  $f^a$  comes from the quark distribution correlator  $\Phi$  and is called a Transverse Momentum Distribution (TMD) function. The function  $D^a$  comes from quark fragmentation correlator  $\Delta$  and is called a Fragmentation Function (FF). This holds under the assumption of factorization which means that in semi-inclusive DIS the distribution of the quark in the proton ( $f^a$ ) before scattering is decoupled from the fragmentation structure ( $D^a$ ) of the quark after scattering. The function  $w(\mathbf{p}_T, \mathbf{k}_T)$  gives the expression the appropriate weighting and the summation runs over all quarks and anti-quarks.

## 2.3 Transverse Momentum Dependent distributions

### 2.3.1 Longitudinally polarized TMDs

The structure functions of interest in this thesis are written in terms of TMDs and FFs as follows:

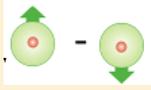
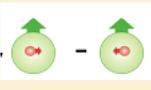
		Quark Polarization			
		N/q	U	L	T
Nucleon Polarization	U	$f_1$			$h_1^\perp$ 
	L			$g_1$ 	$h_{1L}^\perp$ 
	T	$f_{1T}^\perp$		$g_{1T}$ 	$h_1$  $h_{1T}^\perp$ 

FIG. 2.3: Probabilistic interpretation of the leading-order transverse momentum distributions for all combinations of quark and nucleon polarization. The green arrows indicate nucleon polarization and the red arrows indicate quark polarization.

$$F_{LU}^{\sin\phi_h} = \frac{2M}{Q} \mathcal{C} \left[ -\frac{\hat{h} \cdot \mathbf{k}_T}{M_h} \left( x_B e H_1^\perp + \frac{M_h}{M} f_1 \frac{\tilde{G}^\perp}{z} \right) + \frac{\hat{h} \cdot \mathbf{p}_T}{M} \left( x_B g^\perp D_1 + \frac{M_h}{M} h_1^\perp \frac{\tilde{E}}{z} \right) \right], \quad (2.13)$$

$$F_{UL}^{\sin\phi_h} = \frac{2M}{Q} \mathcal{C} \left[ -\frac{\hat{h} \cdot \mathbf{k}_T}{M_h} \left( x_B h_L H_1^\perp + \frac{M_h}{M} g_{1L} \frac{\tilde{G}^\perp}{z} \right) + \frac{\hat{h} \cdot \mathbf{p}_T}{M} \left( x_B f_L^\perp D_1 - \frac{M_h}{M} h_{1L}^\perp \frac{\tilde{H}}{z} \right) \right], \quad (2.14)$$

$$F_{UL}^{\sin 2\phi_h} = \mathcal{C} \left[ -2 \frac{(\hat{h} \cdot \mathbf{k}_T)(\hat{h} \cdot \mathbf{p}_T) - \mathbf{k}_T \cdot \mathbf{p}_T}{MM_h} h_{1L}^\perp H_1^\perp \right], \text{ and} \quad (2.15)$$

$$F_{LL} = \mathcal{C}[g_{1L}D_1], \quad (2.16)$$

where  $M$  is the target nucleon mass and  $M_h$  is the mass of the outgoing hadron. Lower-case letters are used for TMDs and upper-case letters are used for FFs.

The unpolarized FF,  $D_1$ , and the Collins FF,  $H_1^\perp$ , appear in the moments for  $F_{UL}$  and  $F_{LU}$ . The other FFs seen are  $\tilde{G}^\perp$ ,  $\tilde{E}$ , and  $\tilde{H}$ . The TMDs associated with  $F_{LU}^{\sin\phi_h}$  are  $e$ ,  $f_1$ ,  $g^\perp$ , and  $h_1^\perp$ . For the case of the helicity structure function relating to the polarised target, the TMDs listed are  $h_L$ ,  $g_{1L}$ ,  $f_L^\perp$ , and  $h_{1L}^\perp$ . The double polarized case of  $F_{LL}$  also provides access to the semi-inclusive TMD -  $g_{1L}$  - which is analogous to polarized structure function, “ $g_1$ ” from inclusive scattering.

The TMD interpretation is shown in Figure 2.3. For example, the TMD  $h_{1L}^\perp$  describes the spin structure of a transversely polarized quark in a longitudinally polarized hadron and appears in the  $\sin 2\phi_h$  modulation of the helicity structure function  $F_{UL}$ , which in turn appears in the numerator of the asymmetry  $A_{UL}$ . The superscripts on the structure functions indicate the terms in Equation 2.5 corresponding to  $\sin\phi_h$  and  $\sin 2\phi_h$  modulations associated with them. Using the asymmetry equations discussed in Section 2.1 we extract structure functions and their  $\phi_h$  modulations for the specified spin configurations.

### 2.3.2 Twist

Equation 2.5 lists all the terms that appear in leading-order perturbative QCD, together with terms that include a non-perturbative extra power of  $1/Q$ . Three of the four structure functions in Equations 2.13 - 2.16 have this extra factor. Naïvely, the power of  $1/Q$  scaling the structure function can be termed as the twist of that structure function. Using this rudimentary definition we can conclude that the terms in Equation 2.5 are

calculated for twist-2 (leading) and twist-3 (sub-leading).

The more rigorous approach to understanding twist is discussed in Ref. [29] and outlined here. The concept of twist arises from the terms in the Operator Product Expansion (OPE). Equation 2.10 is derived beginning from

$$4\pi W_{\mu\nu} = \int d^4\xi e^{iq\cdot\xi} \langle P, S | [J_\mu(\xi), J_\nu(0)] | P, S \rangle. \quad (2.17)$$

Contributions to this integral are dominated by  $\xi^2 \approx 0$  (or  $Q^2 \rightarrow \infty$ ), and it can be expanded in the OPE around  $\xi^2 = 0$ . The Fourier transform variable,  $\xi$  comes from writing the hadron tensor in terms of electromagnetic currents  $J_\mu$  and  $J_\nu$ .

$$[J_\mu(\xi), J_\nu(0)] \propto \sum_{|\theta|} K_{[\theta]}(\xi^2) \xi^{\mu_1} \dots \xi^{\mu_{n_\theta}} \theta_{\mu_1 \dots \mu_{n_\theta}}(0) \quad (2.18)$$

where  $\theta_{\mu_1 \dots \mu_{n_\theta}}$  are local operators and  $K_{[\theta]}(\xi^2)$  are functions ordered in degree of singularity at  $\xi^2 = 0$ . The dimension of each local operator is given by  $d_\theta$  for a total of  $n_\theta$  local operators. The OPE can be rewritten with suppressed indices, in terms of structure functions analogous to the helicity structure functions in Section 2.2 as

$$4\pi W = \int d^4\xi e^{iq\cdot\xi} \sum_{|\theta|} K_{[\theta]}(\xi^2) \xi^{\mu_1} \dots \xi^{\mu_{n_\theta}} \langle P | \theta_{\mu_1 \dots \mu_{n_\theta}}(0) | P \rangle \quad (2.19)$$

where the matrix elements have the form

$$\langle P | \theta_{\mu_1 \dots \mu_{n_\theta}}(0) | P \rangle = P_{\mu_1} \dots P_{\mu_{n_\theta}} M^{d_\theta - n_\theta - 2} f_\theta + \dots \quad (2.20)$$

The power of the mass scale which appears in the equation is determined by dimensional analysis and corresponds to  $Q^2$  in the SIDIS master equation (Equation 2.5). Twist,

therefore is defined as  $t_\theta \equiv d_\theta - n_\theta$ . If we take the Fourier transform over  $\xi$ , we have

$$4\pi W \approx \sum_{\theta} \left( \frac{M}{\sqrt{Q^2}} \right)^{t_\theta-2} \left( \frac{1}{x_B} \right)^{n_\theta} f_\theta. \quad (2.21)$$

The lowest twist operators in Equation 2.20 have  $t_\theta = 2$ , and the importance of an operator as the scale ( $M$  or  $Q^2$ ) goes to  $\infty$  is determined by the twist. In this formalism, the higher twists are suppressed by a power of  $1/Q$  which makes them disappear at large  $Q^2$ .

### 2.3.3 Connection to Asymmetries

Single and double spin asymmetries provide an excellent tool to gain access to individual helicity structure functions in Equation 2.5. The target single spin asymmetry is defined as,

$$A_{UL} = \frac{\sigma_{UL}}{\sigma_{UU}} \quad (2.22)$$

where  $\sigma_{UL}$  is the cross-section portion from Equation 2.5 that relates to the polarized target,

$$d\sigma_{UL} = \frac{\alpha^2}{x_B y Q^2} \frac{y^2}{2(1-\epsilon)} \left( 1 + \frac{\gamma}{2x} \right) S_{\parallel} \left[ \sqrt{2\epsilon(1+\epsilon)} \sin \phi_h F_{UL}^{\sin \phi_h} + \epsilon \sin(2\phi_h) F_{UL}^{\sin 2\phi_h} \right] \quad (2.23)$$

and

$$d\sigma_{UU} = \frac{\alpha^2}{x_B y Q^2} \frac{y^2}{2(1-\epsilon)} \left( 1 + \frac{\gamma}{2x} \right) \left[ F_{UU} + \epsilon \cos(2\phi_h) F_{UU}^{\cos 2\phi_h} \right]. \quad (2.24)$$

The target spin asymmetry is written in the form of moments of sine functions in the above expressions,

$$A_{UL} = A_{UL}^{\sin \phi_h} \sin \phi_h + A_{UL}^{\sin 2\phi_h} \sin 2\phi_h \quad (2.25)$$

The moment,  $A_{UL}^{\sin 2\phi_h}$  contains the twist 2 TMD  $h_{1L}^\perp$  convoluted with the FF  $H_1^\perp$ , also known as the Collins fragmentation function shown in Equation 2.15. The  $\sin \phi_h$  moment,  $A_{UL}^{\sin \phi_h}$  contains the twist 3 TMD,  $h_L$  convoluted with the Collins fragmentation function.

Similarly, the beam spin asymmetry and double spin asymmetry are defined as,

$$A_{LU} = \frac{\sigma_{LU}}{\sigma_{UU}} \quad (2.26)$$

and

$$A_{LL} = \frac{\sigma_{LL}}{\sigma_{UU}} \quad (2.27)$$

where

$$d\sigma_{LU} = \frac{\alpha^2}{x_B y Q^2} \frac{y^2}{2(1-\epsilon)} \left(1 + \frac{\gamma}{2x_B}\right) \sqrt{2\epsilon(1+\epsilon)} \sin \phi_h F_{LU}^{\sin \phi_h} \quad (2.28)$$

and

$$d\sigma_{LL} = \frac{\alpha^2}{x_B y Q^2} \frac{y^2}{2(1-\epsilon)} \left(1 + \frac{\gamma}{2x_B}\right) S_{\parallel} \lambda_e \left[ \sqrt{1+\epsilon^2} F_{LL} + \sqrt{2\epsilon(1+\epsilon)} \cos \phi_h F_{LL}^{\cos \phi_h} \right]. \quad (2.29)$$

The moment of the beam spin asymmetry is written as the coefficient of the sine function,

$$A_{LU} = A_{LU}^{\sin \phi_h} \sin \phi_h \quad (2.30)$$

and moments of the double spin asymmetry are written terms of a constant term  $A_{LL}^C$  and the coefficient of the cosine term  $A_{LL}^{\cos \phi_h}$ ,

$$A_{LL} = A_{LL}^C + A_{LL}^{\cos \phi_h} \cos \phi_h \quad (2.31)$$

For the beam spin asymmetry, the moment  $A_{LU}^{\sin \phi_h}$  contains the twist 3 TMD  $e$  con-

volved with the Collins fragmentation function,  $H_1^\perp$  (Eqn 2.13). The moments of the double spin asymmetry contain the twist 2 TMD  $g_{1L}$  convoluted with the unpolarized FF,  $D_1$  (Eqn 2.16).

All of these moments are dependent on  $Q^2$ ,  $x_B$ ,  $z$  and,  $P_{h\perp}$  and they contain within them the physics of TMDs.

## 2.4 Previous Measurements

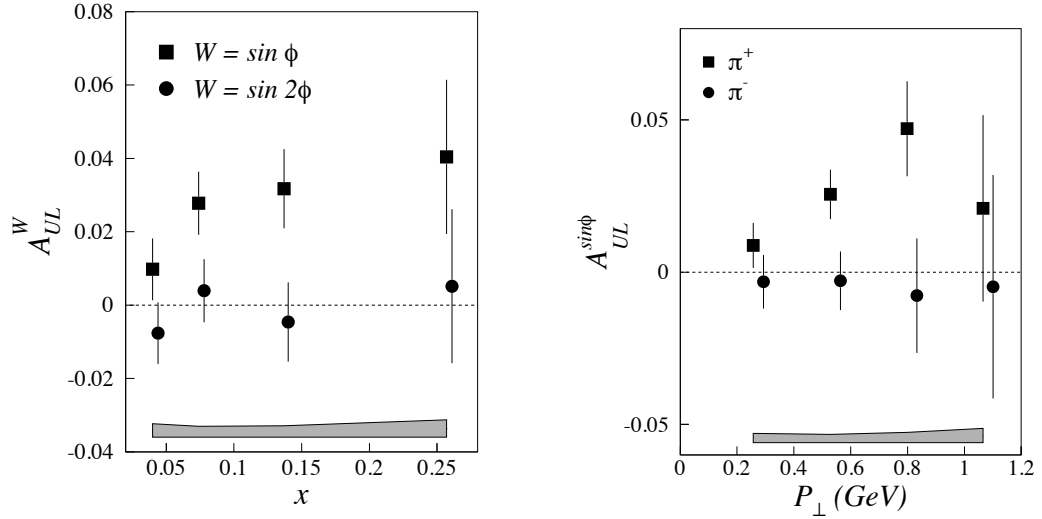


FIG. 2.4: The sine- $\phi_h$  moments of longitudinal single spin target asymmetries for  $\pi^+$  as measured in Ref. [4] as a function of  $x_B$  (left) and  $P_{h\perp}$  (right). The  $A_{UL}^{\sin 2\phi_h}$  component was found to be consistent with zero.

The first observation of a single-spin asymmetry in semi-inclusive DIS pion electroproduction was made by the HERMES Collaboration in 1999 as seen in Figure 2.4 Ref. [4]. This spurred a number of additional measurements by HERMES of single and double spin asymmetries for charged and neutral pions as well as kaons Ref. [30] Ref. [31]. They performed these measurements with polarized hydrogen and deuterium targets Ref. [31].

The newest measurement by HERMES of  $A_{UL}^{\sin\phi_h}$  for longitudinally polarized hydrogen were published in 2005 as seen in Figure 2.5 Ref. [5].

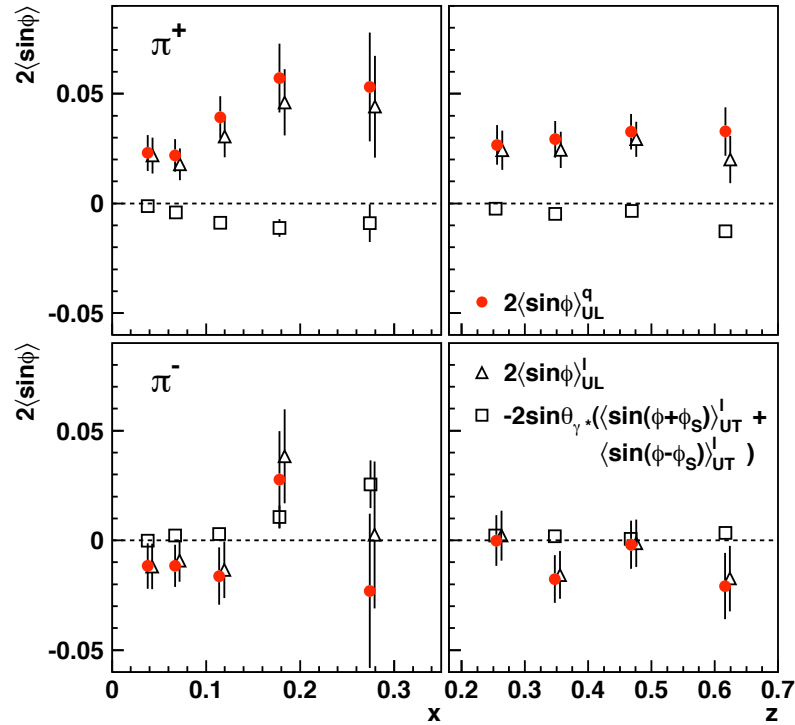


FIG. 2.5: The various azimuthal moments appearing in the measurement of the  $\sin\phi_h$  modulations of single-spin asymmetries as measured by Ref. [5] on a longitudinally polarized hydrogen target for charged pions as functions of  $x_B$  (left) and  $z$  (right). The open symbols are the measured lepton-axis moments. The ones from a transversely polarized target are multiplied by  $\sin\phi_\gamma$  according to their appearance in the longitudinal lepton-axis moments. The closed symbol is the subleading-twist contribution to the measured lepton-axis asymmetries on a longitudinally polarized target. The triangles are slightly shifted horizontally for distinction. An overall systematic error of 0.003 is not included here.

The most recent measurement was performed by the CLAS Collaboration and was published in 2010 Ref. [6]. In addition to refining the HERMES measurements it also showed for the first time a non-zero  $\sin 2\phi_h$  azimuthal moment (Figure 2.6). The improvement also came from extracting azimuthal moments in multi-dimensional kinematic bins. The CLAS Collaboration also recently published data for the beam spin asymmetry for

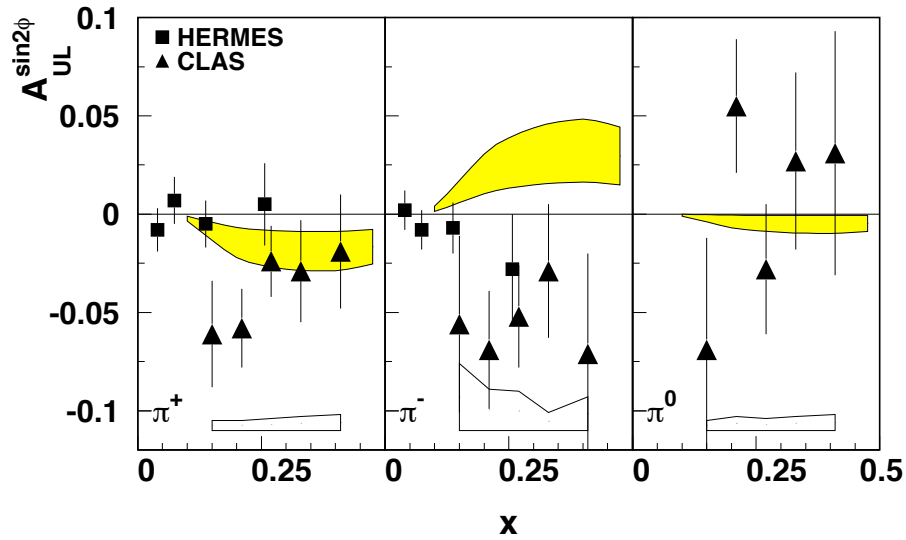


FIG. 2.6: The sine- $2\phi_h$  moment of the target spin asymmetry measured by CLAS in 2010 Ref. [6] on the proton. The systematic errors for CLAS are the empty blocks on the bottom of each figure and the yellow regions indicate the systematic error from the HERMES measurements.

the neutral pion Ref. [25].

The results for the proton double spin asymmetry were released by the COMPASS Collaboration for the low  $x_B$  region Ref. [7]. Their data were obtained on the polarized proton in solid  $\text{NH}_3$  and a positively charged muon beam. The results for the charged pions is shown in Figure 2.7.

The data available for semi-inclusive target asymmetries is dominated by charged pion results. The data for the dependence of the double spin asymmetry on  $P_{h\perp}$  is available in reasonable statistical precision from COMPASS for regions of small  $x_B$  but has low statistics for  $x_B > 0.2$ . The measurement of a  $A_{UL}^{\sin 2\phi_h}$  term for the target spin asymmetry measured for the first time in 2010, has significant room for improvement.

High statistics data are needed to study asymmetries in multiple projections of  $P_{h\perp}$  and  $x_B$  to test factorization. The limited data available thus far do not allow this without

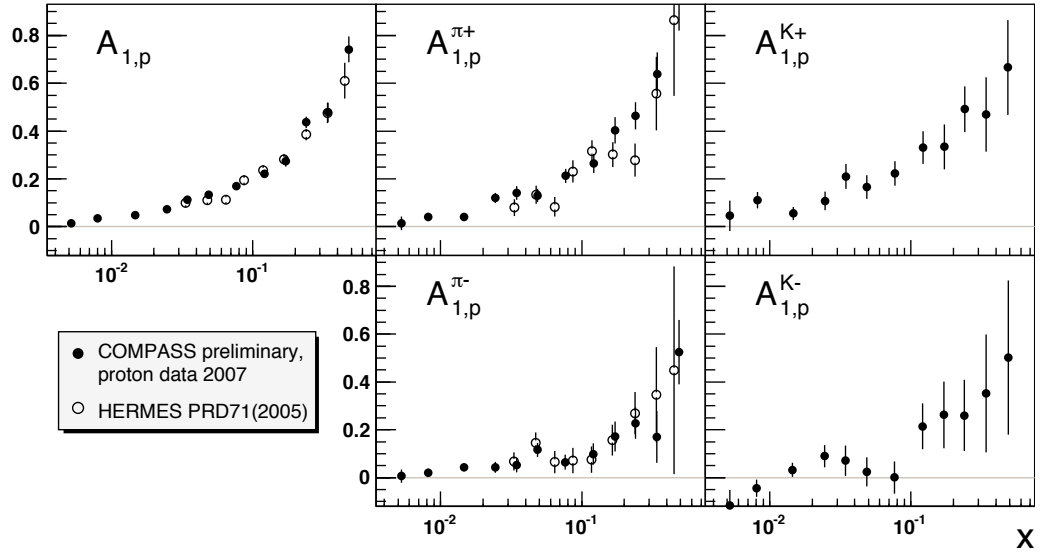


FIG. 2.7: Comparison of double spin asymmetry measured by COMPASS Ref. [7] in comparison to HERMES data from 2005 for inclusive electron (left), charged pions (middle) and charged kaons (right).

running into statistical limits. This is true especially for the case of the neutral pion.

## 2.5 Models used within the TMD Phenomenology

Several phenomenological models have been developed over the last three decades to understand the spin structure of the proton. A selected list of models that predict the single and double spin asymmetries measured in the ‘eg1-dvcs’ measurement are sketched in this section. The quantities measured in the experiment can be divided into two categories, the leading twist observables  $A_{LL}$  and the  $\sin 2\phi_h$  moment of  $A_{UL}$ , and the sub-leading twist observable, the contribution to the  $\sin \phi_h$  moment of  $A_{UL}$ . The  $\sin \phi_h$  moment of  $A_{LU}$  has both leading and sub-leading twist components. The moments of  $A_{UL}$  provide access to the distribution of polarized quarks in the proton and  $A_{LU}$  provide the same for the unpolarized quarks.

A large number of predictions exist for the leading twist observables Ref. [9, 32–37]. However, predictions for the sub-leading twist are scarce Ref. [38, 39].

### 2.5.1 Leading Order Parton Model

The parton model (Ref. [40]) sees the nucleon as fast-moving, non-interacting parts, which we now identify as quarks and gluons. This gives us collinear parton distribution functions (PDF). The TMD formalism extends the collinear simplification to include quark transverse momentum [8]. Predictions for the target single spin asymmetries are made in Ref. [8] for  $\langle z \rangle = 0.61$  using this TMD formalism. The ratio of the Collins fragmentation function to the unpolarized fragmentation function is assumed to be,

$$\frac{\langle H_1^\perp \rangle}{\langle D_1 \rangle} = 20 \pm 4\% \quad (2.32)$$

The model predicts a range for the target single spin asymmetry for all three pions as seen in Figure 2.8.

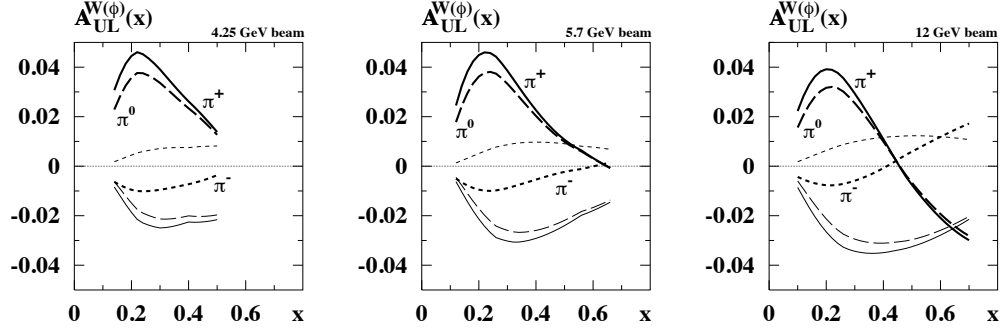


FIG. 2.8: Predictions for azimuthal asymmetries  $A_{UL}$  vs.  $x_B$  for different beam energies and the corresponding kinematical cuts at CLAS. The thick lines correspond to  $W(\phi) = \sin \phi$ , the thin lines correspond to  $W(\phi) = \sin 2\phi$ . Here the solid lines refer to  $\pi^+$  range, long-dashed lines to  $\pi^0$  range, and short-dashed lines to  $\pi^-$  range [8].

## 2.5.2 Quark and Diquark Spectator Models

This model assumes that when the virtual photon interacts with a quark in the target proton the rest of the quarks are only spectators. The spectators are treated as a diquark with spin 0 or 1, as well as isospin 0 or 1. This model is used to make predictions for the double spin asymmetry which written terms of the virtual photon absorption asymmetries ( $A_1$  and  $A_2$ ) is

$$A_{LL} = D(A_1 + \eta A_2) \quad (2.33)$$

where the depolarization factor is given by  $D = \frac{1-E'\epsilon/E}{(1+\epsilon R)}$  and  $\eta = \frac{\epsilon\sqrt{Q^2}}{(E-E'\epsilon)}$ .  $R(x, Q^2) = \sigma_L/\sigma_T$  is the ratio of longitudinal and transverse virtual photon-absorption cross sections

and  $\varepsilon^{-1} = 1 + 2 \tan^2(\theta/2) \left[ 1 + \frac{4M^2 x^2}{Q^2} \right]$ . Conversely,  $A_1$  can also be written as,

$$A_1 = \frac{g_1(x_B, Q^2) - \gamma^2 g_2(x_B, Q^2)}{F_1(x_B, Q^2)} \quad (2.34)$$

Analogous to the case for polarized inclusive structure functions,  $g_1$  and  $g_2$  can be thought of as functions related to the polarized quark helicity distributions for the proton. The unpolarized quark helicity distributions are related to  $F_1$ . For the case when ( $\gamma \ll 1$ ), we assume  $A_1 \approx g_1/F_1$ . Spectator model prediction for semi-inclusive asymmetries are shown in Ref. [32].

### 2.5.3 Other Models

Several other models that are frequently used include bag models [33], the light cone constituent quark model [41] and the chiral quark soliton model [34]. The majority of the bag models follow the prescription of the MIT bag model in which equations for massless Dirac fields are solved for three valence quarks constrained by a “bag” which is the hadron [42]. The TMD formalism is calculated in the bag model, and plots for  $h_{1L}$  and the other distributions can be found in Ref. [33].

Using the light cone constituent quark model, TMDs are studied in the light cone description of the nucleon where the Fock expansion is truncated to only consider the valence quarks Ref. [43]. Predictions for the target single spin asymmetry in the light cone model are presented in Figure 2.9. The predictions in this paper are presented for two different approaches. One (displayed using a dashed line) uses the light cone model in combination with the quark - diquark spectator model. The second approach uses a Gaussian parametrization for the distribution and fragmentation functions. For Jefferson

lab energies, this model predicts a negative value of  $A_{UL}^{\sin 2\phi_h}$  for the positive pion.

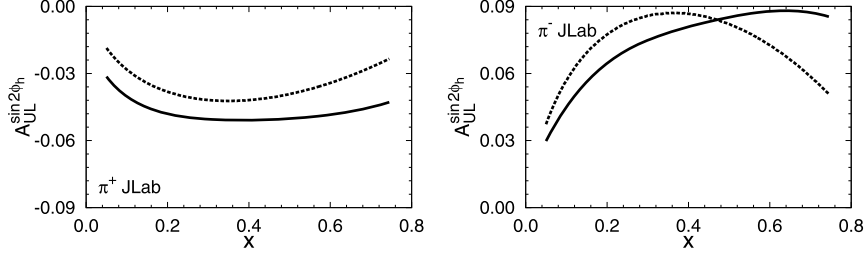


FIG. 2.9: The single spin asymmetry  $A_{UL}^{\sin 2\phi}$  as a function of  $x_B$  at different kinematics with  $Q^2 = 3.0 \text{ GeV}^2$  for the proton target. Dashed curves correspond to approach 1, while solid curves correspond to approach 2 in Ref. [9].

The wealth of model predictions give us a target as to what we might measure. In understanding proton spin structure, the moments of single and double spin asymmetries have proven important. They probe the quark distribution in the proton as well as the fragmentation of the quark into a pion. Previous measurements show non-zero values of these moments. The ‘eg1-dvcs’ measurement will provide new and unique information of SSAs and DSAs. The higher statistics will enable extraction of moments in multiple kinematic dimensions which has been difficult in the past. The measurements will provide new information for the neutral pion especially in the region  $x_B > 0.1 \text{ GeV}$ .

# CHAPTER 3

## Experiment

Our goal is to study single and double spin asymmetries in the semi-inclusive reaction  $p(e, e'\pi)X$ . A stationary polarized proton is struck with a high energy, polarized electron. The Continuous Electron Beam Accelerator Facility (CEBAF) provides the electron, and the polarized proton is obtained from frozen ammonia. The outgoing particles in the reaction are detected using the CEBAF Large Acceptance Spectrometer (CLAS) and the inner calorimeter (IC). This chapter sketches the major components used in data collection.

### 3.1 The CEBAF Electron Accelerator

The CEBAF accelerator provides a continuous electron beam with a maximum energy of 6 GeV and a current of up to 300  $\mu\text{A}$  shared between three user end stations at Jefferson Lab. It uses superconducting radio frequency (RF) technology in a five pass recirculating linear accelerator Ref. [10].

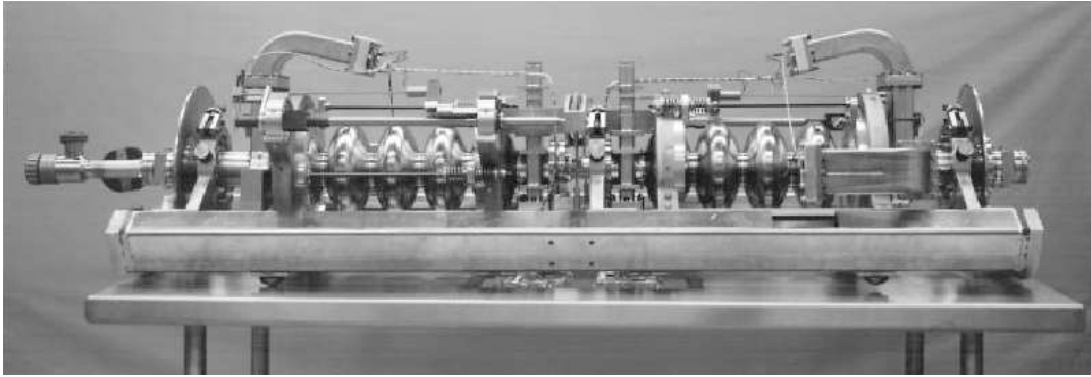


FIG. 3.1: A cryomodule consisting of several resonant superconducting RF cavities. These modules are used in the injector assembly and in the linear accelerators (linacs) Ref. [10].

The source of polarized electrons is the GaAs photocathode at the injector facility at Jefferson Lab Ref. [44]. Under very high vacuum, circularly polarized laser light is used to produce polarized electrons from the photocathode at 100 keV. The helicity of the laser light can be changed by the introduction of a half wave plate (HWP) Ref. [45]. This changes the photon helicity which then changes the electron helicity.

The electron beam produced at the cathode then passes through several superconducting RF cavities and an adjustable three slit aperture system to control its intensity and chopping. To make a short pulse of electrons that can be accelerated, the beam is chopped into pieces and then the electrons are bunched together to form short pulses. Slow electrons are accelerated more than the fast ones. The bunch is squeezed after a distance and the electron bunches are further accelerated to 50 MeV by the time they exit the injector system. This assembly has the capacity to tailor the intensity of the electron beam sent to each of the three end stations. The injector feeds into the north linac. The electron beam then curves around to the south linac via bending magnets Ref. [46]. Each linac contains sets of cryomodules that accelerate the polarized electrons. Each cryomodule has 10 cavity pairs that accelerate the electron beam. One cavity pair is shown in Figure

3.1. Each five cell cavity is 0.5 m long.

The path followed by the electron beam is shown in Figure 3.2. The beam accelerates through the south linac and then is directed back around again to the north linac via more bending magnets. An entire loop through the accelerator is called a pass and one pass increases the beam energy by approximately 1200 MeV. The recirculation arcs at each end of the linac enable up to five passes, producing a maximum beam energy close to 6 GeV. After any number of passes, the beam can be separated at the beam switchyard and sent to the end stations marked A, B and C. The centrally located liquid helium refrigerator is used to cool the cryomodules in the injector and linacs to about 2.08 K Ref. [10].

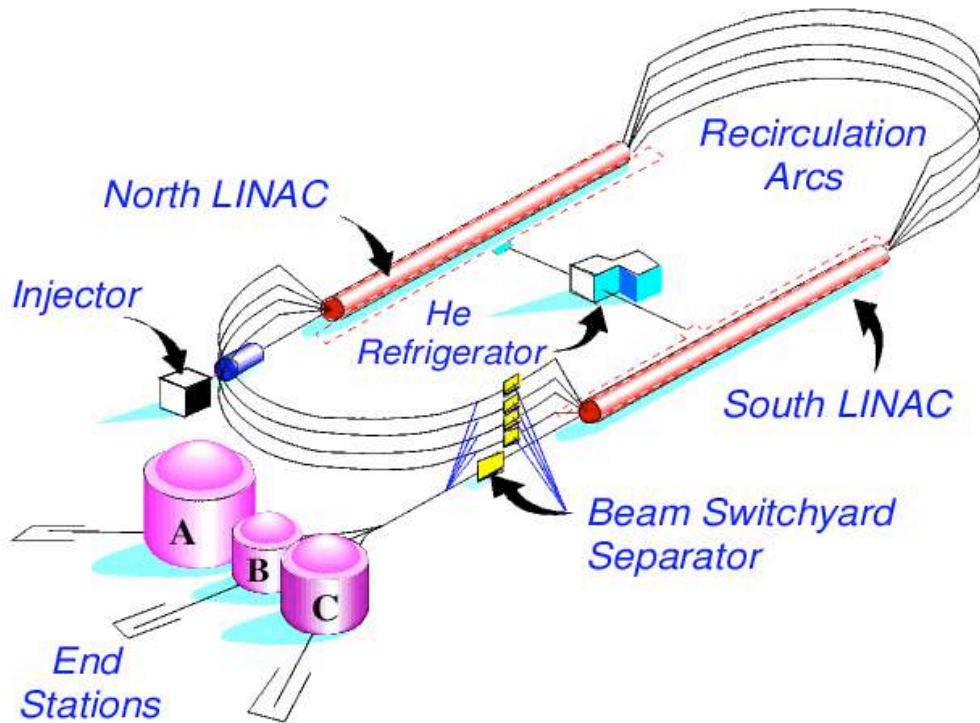


FIG. 3.2: Schematic diagram of the CEBAF accelerator. Polarized electrons produced in the injector are transferred to the north linear accelerator (linac). They circle through the recirculation arcs via bending magnets and enter the south linear accelerator, and then go through another set of bending magnets. This loop can be repeated up to five times. The electrons can be extracted for use after each pass and are transferred to each of the three end stations through a beam separator Ref. [10].

## 3.2 Hall B Beamline devices

The electron upon entering Hall B passes through the Møller Polarimeter, Beam Position Monitors (BPM) and Harp Scanners before entering CLAS. Before passing out of Hall B the beam hits the Faraday Cup and then the beam dump. The beamline schematic is shown in Figure 3.3.

The Møller polarimeter is located upstream from the target as shown in blue in Figure 3.3. It consists of two iron foils which can be polarized parallel or anti-parallel to the spin of the incoming beam. The polarized beam incident on the foils results in electron-

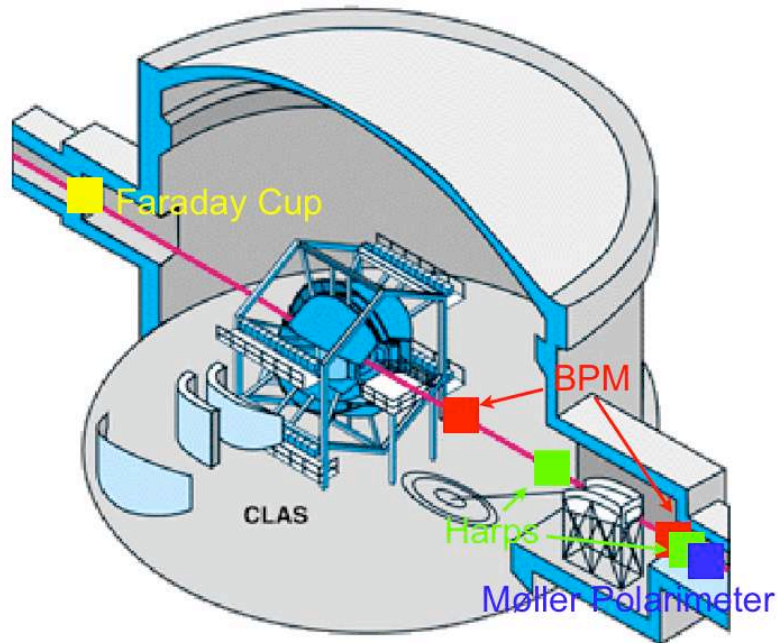


FIG. 3.3: Hall B schematic showing beamline devices in relation to CLAS Ref. [11]. The beamline shown in red, enters Hall B and can pass through the Møller Polarimeter (blue), Beam Position Monitors (BPM) (red), Harp Scanner (green), the experimental target, and Faraday cup (yellow), before passing out of Hall B and on into the beam dump.

electron scattering. The scattered electrons are guided to two scintillator fiber detectors by quadrupole magnets that are located on either side of the beam line Ref. [1]. The quadrupole magnets focus electrons onto the detector. Polarimeter measurements cannot be made in conjunction with experimental data taking.

Beam Position Monitors (BPMs) measure the beam position in the  $x$ - $y$  plane as well as the intensity before it enters CLAS. Three BPMs made of three RF cavities each, are located upstream from the target as marked in red in Figure 3.3. The feedback provided by them helps keep the beam centered on the target Ref. [1].

Harp scans measure the beam profile and diameter Ref. [1]. There are three harp scanners in Hall B upstream of the CLAS target, marked in green in Figure 3.3. The

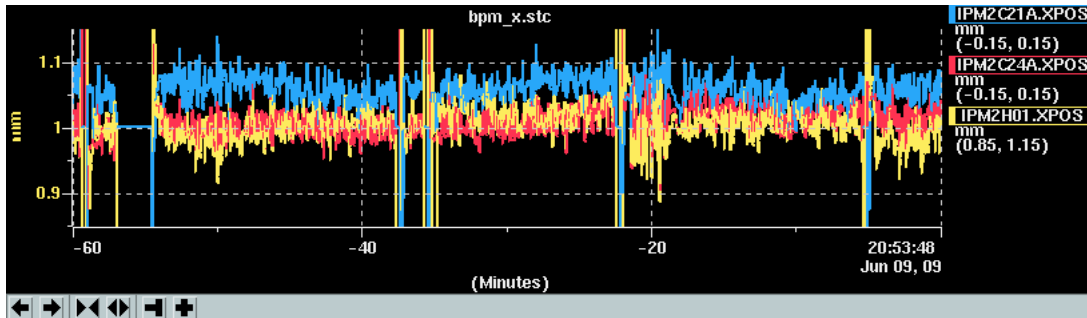


FIG. 3.4: Beam position read back during the Spring 2009 run for the eg1-dvcs experiment. The plot shows  $x$  component of the beam position as a function of time from the three BPMs coded 2C21A (red), 2C24B (blue) and 2H01 (yellow). The nominal value required is  $x = 1.00$  mm.

scanner moves a thin iron wire through the beam to measure its profile. This results in a scattering shower which is detected using Cherenkov detectors (Section 3.5.4). The scattering rate vs wire position is graphed for  $x$  and  $y$ . Fitting this spectrum provides information about the beam intensity, beam position and beam profile. An example of the spectrum and its fit are shown Figure 3.5

Møller measurements and harp scans were performed when there was a change in the beam configuration, as well as, periodically throughout the course of the experiment. This ensured the quality of the beam incident on the target.

The Faraday cup (FC) is located downstream from CLAS as marked in yellow in Figure 3.3. It is a lead cylinder weighing 4000 kg which stops the scattered electron beam. It is connected to a capacitor that is charged by the beam and discharged when approximately  $10^{10}$  C of charge is collected. The total charge collected is recorded in the data acquisition system (DAQ) and is called the ungated FC reading. The Faraday cup also factors in the dead time of the DAQ and records a second value of the integrated charge known as the gated FC value. The latter accurately reflects the charge collected during data taking. The ungated and gated values can be separated by beam helicity as well Ref. [1].

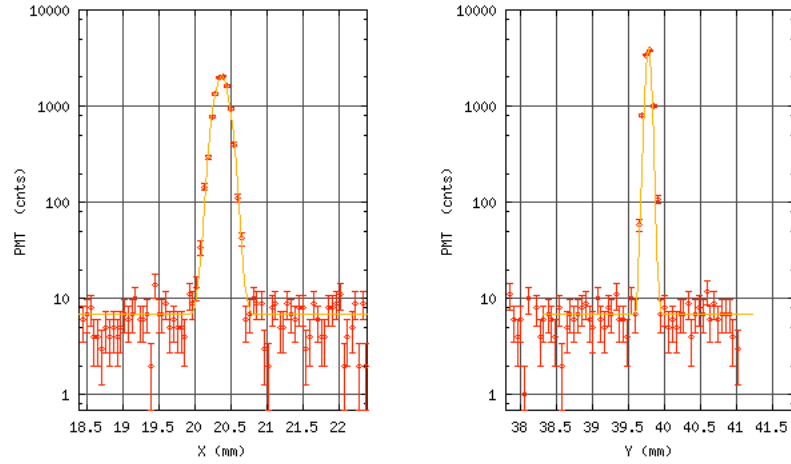


FIG. 3.5: Harp scan for run number 59097 taken during the Spring 2009 run for the eg1-dvcs experiment. The scattered particles (PMT counts) in the detector are shown as a function of the  $x$  and  $y$  plane projections. The beam diameter here is about 0.5 mm.

## 3.3 Polarized Target

### 3.3.1 Theory Overview

The eg1-dvcs target is polarized by way of Dynamic Nuclear Polarization (DNP) as described in [47]. DNP can be explained using equal spin temperature theory or the solid state description (Ref. [12]). Ammonia does not follow either description exactly but has aspects of both. The simpler solid state approach is delineated here and more information about the former description is found in Ref. [12].

The first step is irradiating solid ammonia ( $^{14}\text{NH}_3$ ) using a high-intensity low-energy electron beam to produce localized paramagnetic centers. This results in the material being doped with a low concentration of unpaired electrons. It is then placed in a low temperature and high magnetic field environment.

Under these conditions, the electron spins can be flipped using microwaves that are at the Electron Paramagnetic Resonance (EPR) frequency of the electron in the magnetic

field. The EPR frequency is the frequency that corresponds to the energy required to flip the orientation of the electron spin from anti-parallel to parallel to the magnetic field,  $\vec{B}$ . The EPR frequency does not simultaneously flip the proton spin along with the electron. To achieve this, the electron spins are flipped using a frequency that is lower than the EPR frequency by an amount equal to the Nuclear Magnetic Resonance (NMR) frequency of the proton. The frequency used is given by,

$$\nu_{\mu} = \nu_{EPR} - \nu_{NMR} \quad (3.1)$$

where  $\nu_{\mu}$  is the microwave frequency applied, and  $\nu_{EPR}$  and  $\nu_{NMR}$  are the EPR and NMR frequencies respectively. The green line in Figure 3.6 represents the transition  $e_{\downarrow}p_{\downarrow} \rightarrow e_{\uparrow}p_{\uparrow}$ . The electron relaxes to the lower energy state in about  $10^{-3}$  seconds;  $e_{\uparrow}p_{\uparrow} \rightarrow e_{\downarrow}p_{\uparrow}$ . The yellow line shown in Figure 3.6 represents this relaxation of electron spins.

The electron can now be used to polarize a different proton. Over time, the population of  $p_{\uparrow}$  increases making the sample positively polarized. The same setup is used to get a negatively polarized sample by using microwaves that have a frequency

$$\nu_{\mu} = \nu_{EPR} + \nu_{NMR}. \quad (3.2)$$

This is a simple description of the system. The more involved view takes into account the interactions between free electrons. Typical polarization for an ammonia sample range between 80% to 90%.

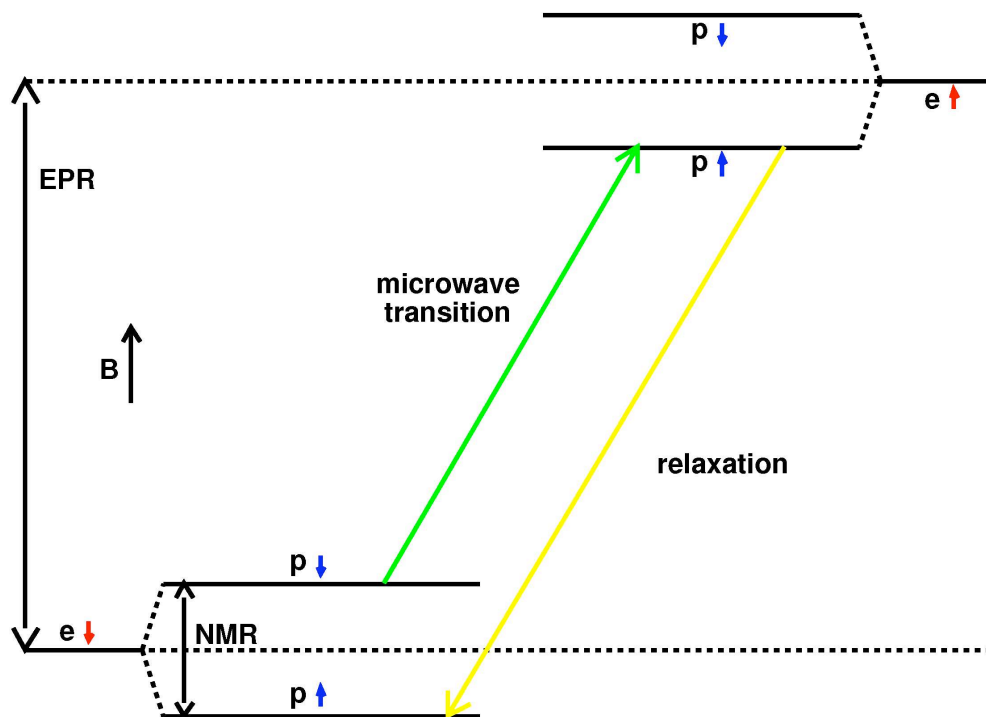


FIG. 3.6: Energy levels for the proton and electron using the simple solid state approach. The green line represents the transition excited by the microwaves and the yellow line represents the relaxation of electron spins Ref. [12]. The sample is placed in a magnetic field  $\vec{B}$ .

### 3.3.2 Polarized Target Components

The eg1-dvcs polarized target consists of five major components - the superconducting magnet, the refrigerator, the target insert, the microwave system to induce polarization and the NMR system to measure polarization in real time. A schematic of the major components are shown in Figure 3.7.

The superconducting magnet produces a 5 T magnetic field using a pair of Helmholtz coils. The coils are made from a niobium-titanium alloy and becomes superconducting below the critical temperature of  $\approx 9 K$ . It produces a uniform field that is coaxial with the

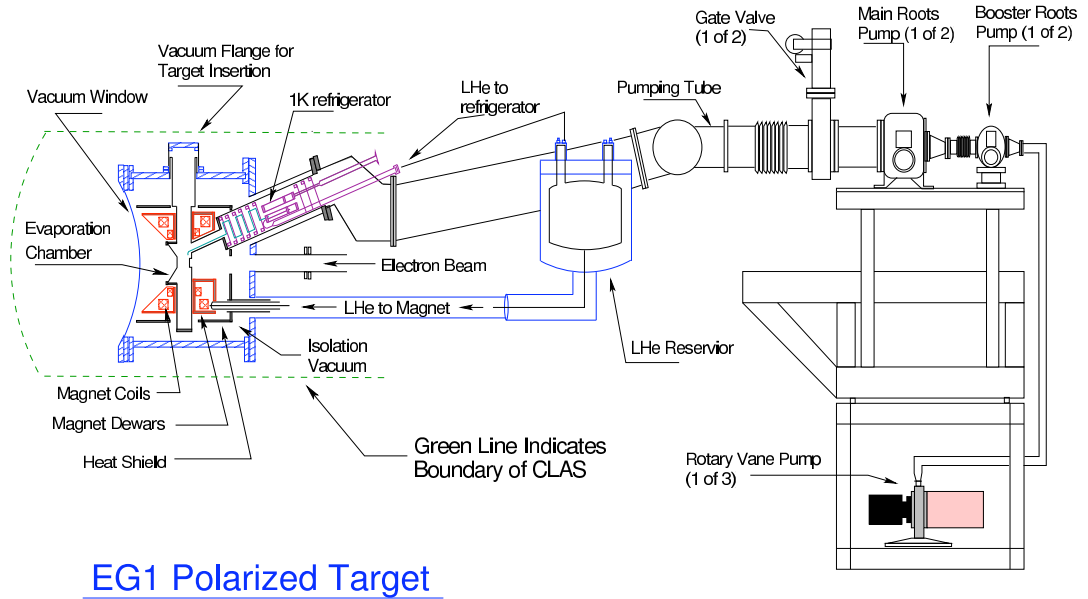


FIG. 3.7: Schematic diagram of the polarized target and associated apparatus Ref. [13]. Seen on the left are Helmholtz magnet coils and the space to insert the target stick. The refrigerator, connected at an angle, is also shown along with the liquid helium reservoir and pump assembly.

beamline and varies less than  $10^{-4}$  T/mm over a cylindrical volume of 20 mm diameter and length Ref. [13]. The field does not interact with the beam and is effective in shielding the drift chambers from low energy Møller electrons.

The helium in the actual target chamber is supplied by the  $^4\text{He}$  refrigerator. It is inserted into CLAS at a  $25^\circ$  angle due to spatial constraints. Helium is pumped into the target chamber via the refrigerator from the helium reservoir which also supplies the magnet. The flow of helium into and out of the refrigerator is monitored constantly by using level probes. This ensures that the target material is kept cold at  $\approx 1$  K.

A schematic of the target stick is shown in Figure 3.8. There were four available target cups made from Kapton and a stepping motor was used to change between them. The two top cups contained crushed beads of irradiated ammonia ( $\text{NH}_3$ ) which was prepared

at University of Virginia and irradiated at the National Institute of Standards and Technology (NIST). The third cup contained a disk of amorphous carbon that was measured to be  $0.398 \pm 0.001$  cm thick. The fourth cup was left empty. At the very bottom of the target stick was the optics or cross hair target that was used to align the beam with the target cup prior to data taking. Data from the carbon and empty target cup were used for background and special studies as described in Chapter 5.



FIG. 3.8: The target stick used during the experiment. The first two cups contained ammonia and the third had a carbon disk. The last one was left empty for background studies. The cross-hairs at the bottom were used to align the beam on the target.

The target stick is inserted into the assembly from the top of the target chamber and immersed in a bath of liquid helium. The enclosure that houses the target stick is shaped like a banjo which has two openings, one for the beam to enter the banjo and the other for the scattered particles to exit. The banjo-like enclosure is sealed using circular

Aluminum windows. A photograph of the target stick in the banjo enclosure is shown in Figure 3.9. The photo was taken with a mirror held at the bottom of the target stick. The mirror shows an empty Kapton cup higher up on the target stick. The banjo is the metal enclosure surrounding the target stick.

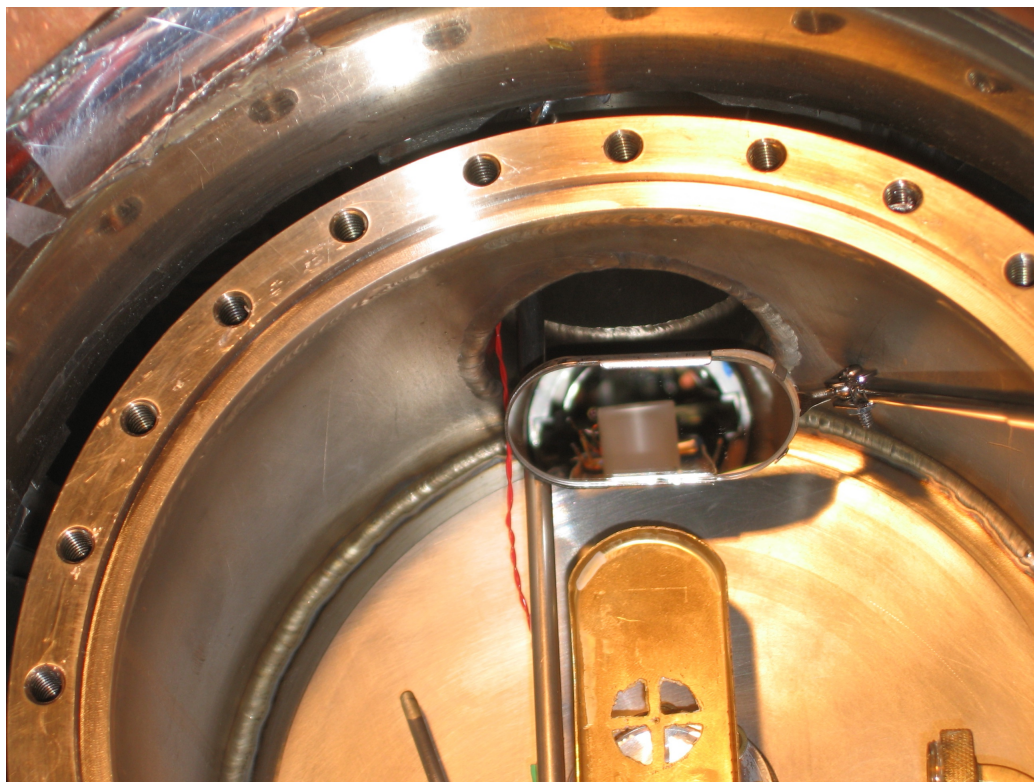


FIG. 3.9: Photograph of the target stick in the banjo enclosure. The photo was taken with a mirror held on the bottom of the target stick. The mirror shows an empty Kapton cup higher up on the target stick. The banjo is the metal enclosure surrounding the target stick.

The irradiated ammonia in the first two cups was polarized using microwaves which were generated by an Extended Interaction Oscillator (EIO), located on top of the refrigerator. The EIO consists of a Klystron in which electrons are emitted from a cathode filament and accelerated through a resonant cavity. As the electrons pass through the resonant cavity, they emit coherent microwave radiation of a fixed frequency which can

be mechanically adjusted by changing the size of the cavity Ref. [48]. The approximate frequency value for the eg1-dvcs experiment was 140 GHz which corresponds to the proton Larmor frequency in the 5 T magnetic field. The positive and negative nuclear spin states are separated by a frequency difference of approximately 500 MHz which enables changing the sign of target polarization without reversing the magnetic field. Microwaves are supplied to the target material by a system of waveguides and incident on the target in the beamline by a gold plated rectangular horn. The combination of the magnetic field, low temperature and microwaves polarizes the proton in the ammonia target.

The target polarization is measured in real-time using continuous-wave nuclear magnetic resonance (NMR). The outer portion of the top two Kapton cups is coated with conducting material and forms a part of a resonant RLC circuit (as seen in top two target cups in Figure 3.8). A varying RF is swept through the circuit. The voltage across the circuit is a function of the frequency and is continuously monitored. The area under the resonance curve is proportional to the polarization of the ammonia beads in that cup.

### 3.3.3 NMR Calibration

The polarization of this target was determined using an NMR set-up which measures the magnetic susceptibility of ammonia. The output of the NMR system is a curve that represents the transmitted or absorbed (depending on positive or negative polarization) power from the target as a function of the NMR frequency. The area under this curve is proportional to the polarization of the target. The constant of proportionality ( $C_P$ ), however, is not well known and, in addition, varies over the course of an experiment Ref. [12]. In order to find the polarization, a method for determining  $C_P$ , known as the calibration constant, is necessary. By allowing the target to come to thermal equilibrium

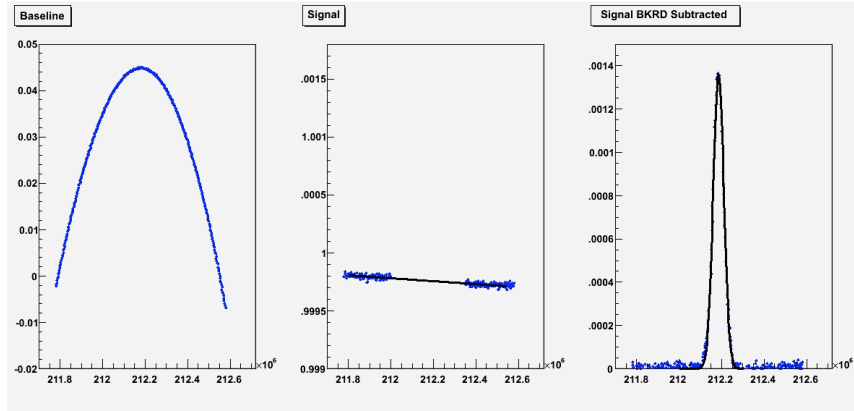


FIG. 3.10: Signal from the NMR setup as function of scanning frequency  $\omega$  (Hz) Ref. [13]. The left plot shows the baseline voltage scan at thermal equilibrium. The middle plot shows the baseline subtracted data. The right plot shows the background subtracted value of the Thermal Equilibrium (TE) voltage.

(TE) in the magnetic field used for polarizing, the target acquires a polarization that is determined by statistical mechanics. The proton polarization at thermal equilibrium is given by,

$$P_{TE} = \tanh\left(\frac{\mu B}{k_B T}\right) \quad (3.3)$$

where  $T$  is the temperature of the material at thermal equilibrium. To improve the signal quality at thermal equilibrium, baseline signals are taken by changing the magnetic field by an amount large enough to remove the polarization signal from the scanning range. This baseline is then subtracted from the actual scans Ref. [49].

$$P_{TE} = C_P A_{TE} \quad (3.4)$$

The constant  $C_P$  is extracted using the known values of area under the thermal equilibrium curve, target temperature and magnetic field. It is then applied to determine target

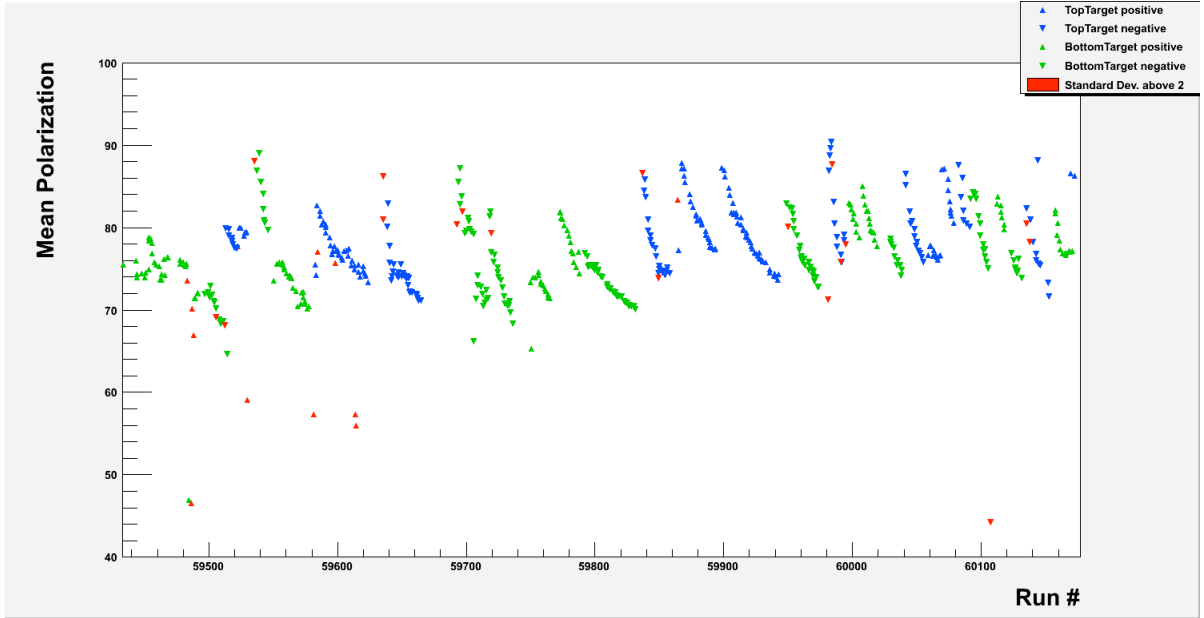


FIG. 3.11: Target polarization values after NMR calibration as a function of run number. The polarization of each target falls with beam dose as is seen for both target cups. The red points denote runs with a wide variation in target polarization within a small time period.

polarization in the scanning frequency range ( $\omega$ ).

$$P_{active} = C_P \int_{\omega_1}^{\omega_2} S_{active} d\omega \quad (3.5)$$

where  $S_{active}$  is the signal for the actively polarized target and  $\omega$  is the frequency of the sweep. The 17 TE measurements from the eg1-dvcs experiment were analyzed and the typical background-subtracted signal for  $^{14}\text{NH}_3$  at thermal equilibrium is shown in Figure 3.10.

The values of target polarization after TE calibration are shown Figure 3.11. The polarization of each target falls with beam dose as is seen for both target cups. The red points denote runs with a wide variation in target polarization within a small time period.

### 3.4 Inner Calorimeter

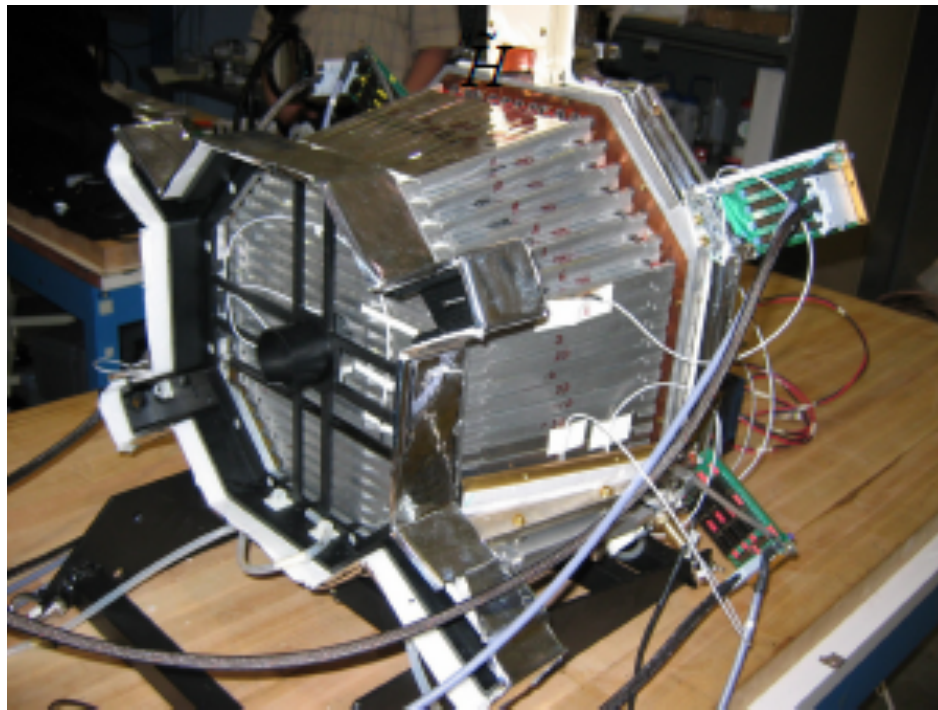


FIG. 3.12: A photograph of the Inner Calorimeter (IC) on a laboratory table top with surrounding electronics. The IC has an octagonal geometry and fits in between the polarized target and CLAS. The black opening in the center is to let the beam pass through.

The standard CLAS configuration allows the detection of photons and hence neutral pions down to  $10^\circ$  in polar angle when the target is placed at the CLAS center Ref. [18]. This acceptance decreases in azimuthal angle due to the presence of the torus coils as explained in Section 3.5. To increase the detection of  $\pi^0$ s in the range of  $5^\circ - 16^\circ$ , the inner calorimeter (IC) is inserted between the polarized target and CLAS as shown in Figure 3.13.

The detector consists of 424 lead tungstate crystals. The tapered crystals are 16 mm in length and are attached to avalanche photodiodes (APDs) on the back end. The APDs are connected to preamplifiers which in turn are connected to analog to digital converters

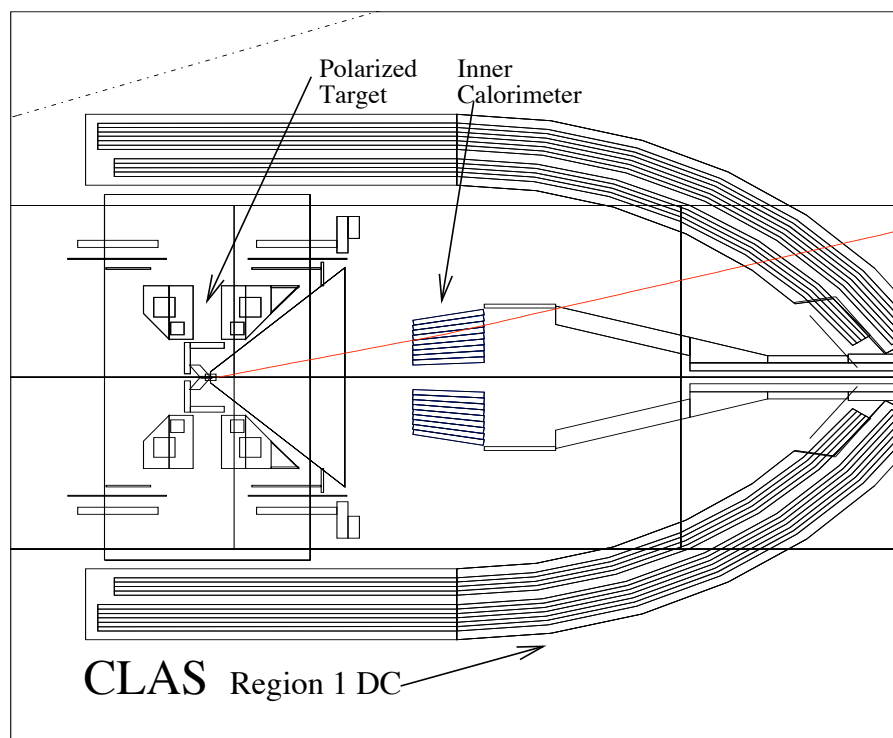


FIG. 3.13: Schematic of the IC in reference to CLAS and the polarized target. The red line simulates the path of a charged particle originating in the target, passing through the IC and into the first region of the drift chambers in CLAS.

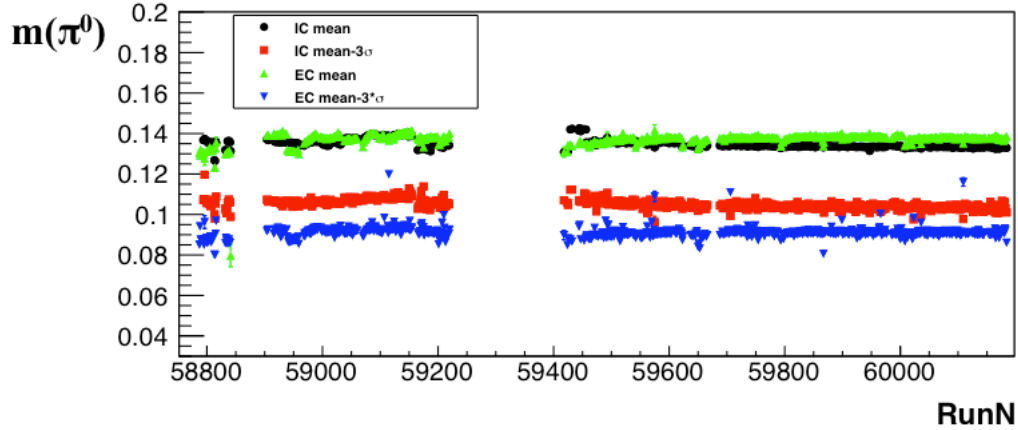


FIG. 3.14: The neutral pion mass as measured in the IC (black) and EC (green) after they were calibrated for gain (ADC) and timing (TDC). The stability of the neutral pion mass peak over the run period indicates an acceptable calibration quality. The resolution for the  $\pi^0$  is significantly better in the IC (red) than the EC (blue) as seen in the  $3\sigma$  boundary

(ADCs) and time to digital converters (TDCs) linked to the data acquisition system Ref. [50].

The IC is calibrated for gain in the ADCs and timing information from TDCs. The event start time is obtained from the scintillator counter as described in Section 3.5.2 and is used for IC time calibration. Calibration of the gain is done using the neutral pion as a reference particle. The stability of the calibration is monitored by looking at the mean of neutral pion pass reconstructed in the IC as shown in Figure 3.14

### 3.5 CEBAF Large Acceptance Spectrometer

The CEBAF Large acceptance spectrometer (CLAS) is designed to detect multiple particles in coincidence, over a wide angular range. For the eg1-dvcs experiment, the presence of the Inner Calorimeter blocks charged particles below  $\approx 15^\circ$  and the target

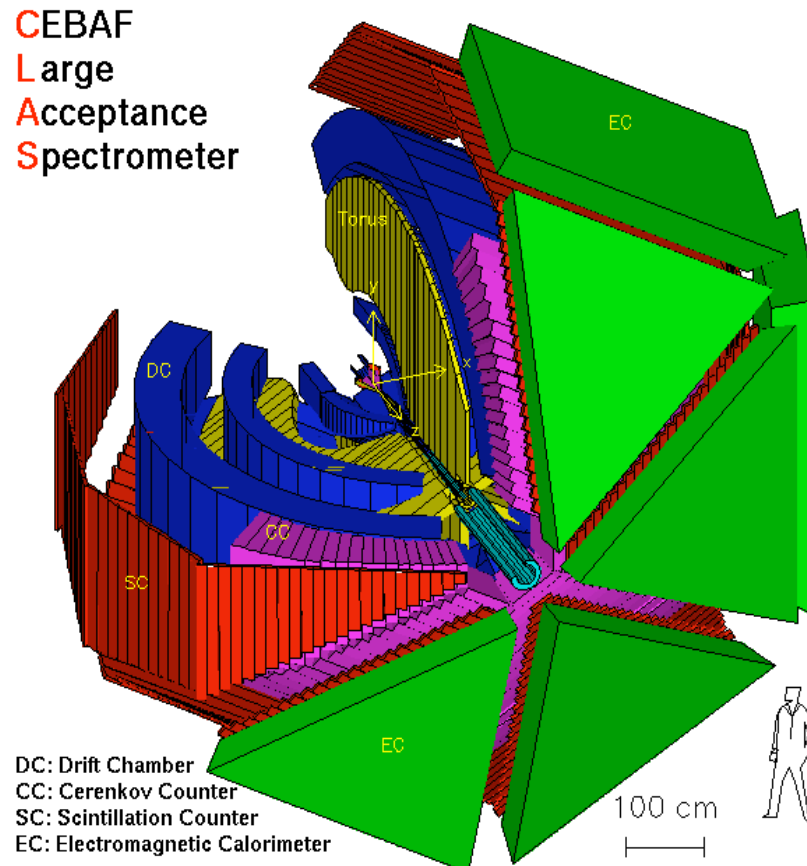


FIG. 3.15: CLAS schematic showing the main detector components. Green marks the electromagnetic calorimeter. The next layers in are the scintillator counters in red and Cherenkov counter (CC) in pink which distinguishes electrons from hadrons. The torus magnet (yellow) creates a field that allows for momentum determination using the drift chambers (blue).

magnet blocks particles with angles greater than  $\approx 50^\circ$ . Our reaction of interest is semi-inclusive DIS which means we need to detect an electron and a pion in the final state. The angular coverage and resolution of CLAS is key to making a high statistics measurement of such an event.

CLAS is divided into six main sectors by the torus magnet. Each sector forms a virtually independent magnetic spectrometer with a common trigger, target and data acquisition system. Each of the sectors have several layers of detection as shown in Figure 3.15. The data acquisition system collected on average 2000 electron-proton collisions per second during the experiment. A brief overview of the detector components is sketched here Ref. [1].

### 3.5.1 Torus Magnet

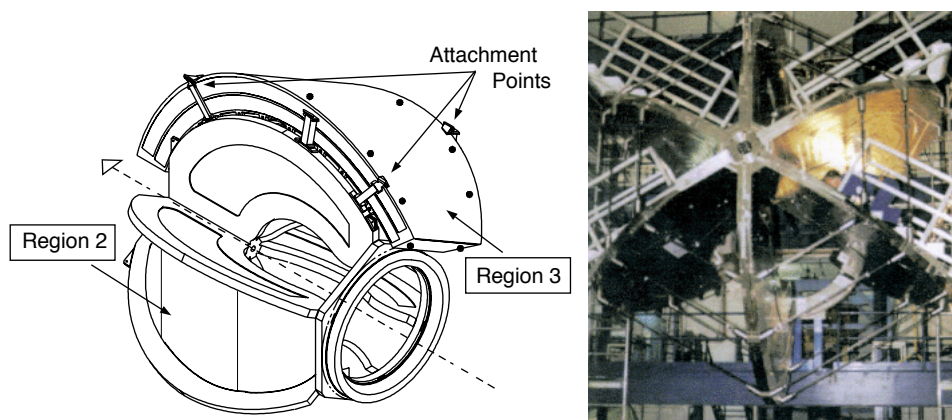


FIG. 3.16: Schematic (left) and actual view (right) of the CLAS torus magnet Ref. [1]. The photograph shows the initial installation of the CLAS Torus magnet. The six fold symmetry of the magnet forms the skeleton of CLAS and the dashed arrow on the schematic indicates beam direction. Each sector contains a set of drift chambers (DC), a Cherenkov counter (CC), time of flight scintillators (TOF) and an electromagnetic calorimeter (EC).

The torus magnet consists of six superconducting coils that provide a magnetic field with a large component transverse to beam direction. The six sectors formed by the

torus, each contain a set of drift chambers (DC), a Cherenkov counter (CC), time of flight scintillators (TOF) and an electromagnetic calorimeter (EC).

The maximum allowed current in the torus magnet is 2250 A which provides a field of up to 2.5 T (Ref. [1]). The torus configuration provides a field free region along the beam line which prevents it from interfering with the field of the polarized target magnet. For this experiment we used a torus current of 2250 A. A positive torus current is known as the “inbending” configuration because scattered electrons are bent into the beam line. We recorded a small fraction of the total data with a reverse toroidal field, also known as the “outbending” configuration, which corresponded to a torus current of -2250 A. This was useful for detection of negative pions which we otherwise lose due to the presence of the IC. It is also essential in order to measure pair-symmetric background as detailed in Chapter 5.

### 3.5.2 Scintillator Counters

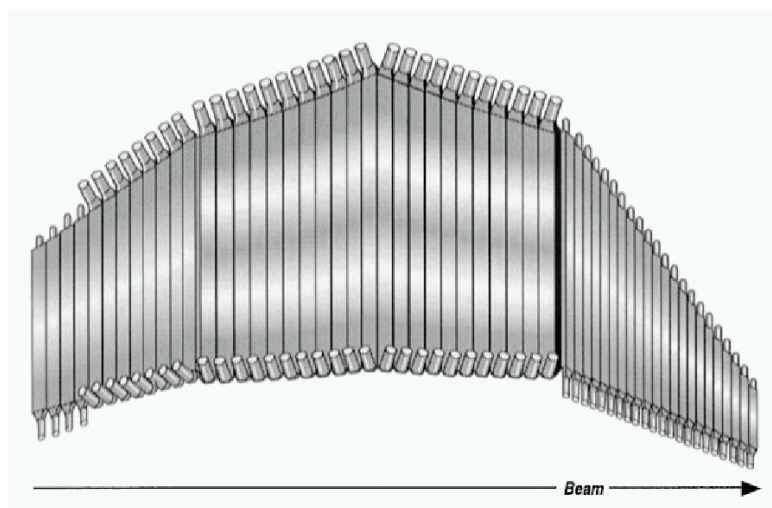


FIG. 3.17: The orientation of scintillator strips for one sector with respect to the beam direction. Each strip is 5 cm thick and connected to two PMTs.

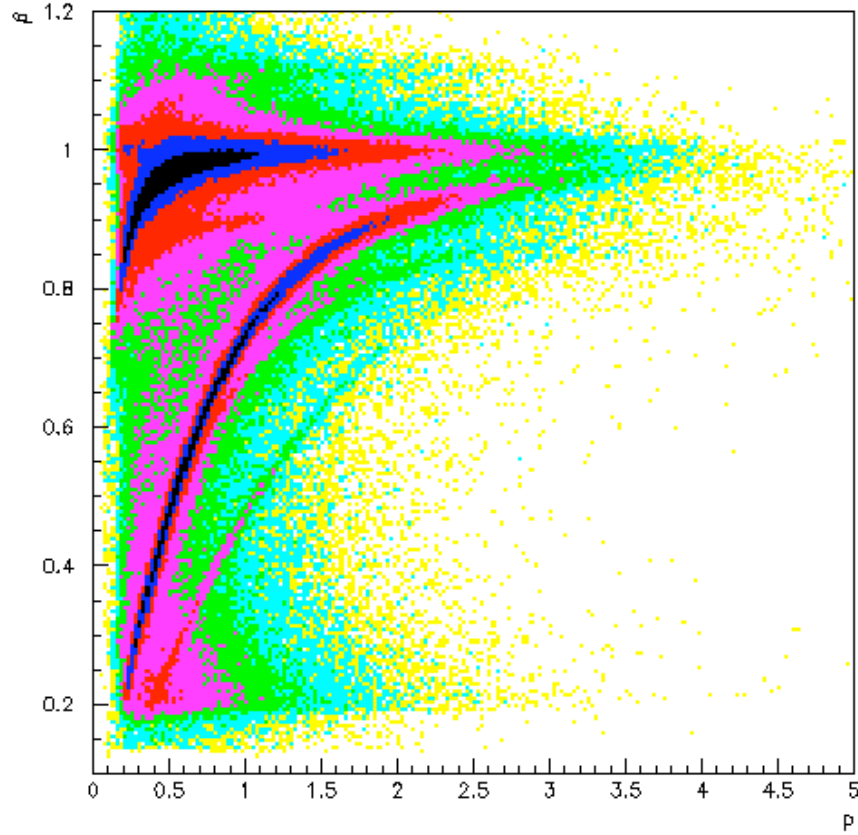


FIG. 3.18: The dependance of  $\beta$  on particle momenta after the paddles in the SC have been calibrated. The process starts with obtaining  $\beta = 1$  for electrons (and photons) and then correcting the timing for heavier particles Ref. [14]. The broad band under  $\beta = 1$  shows the pions and the smaller band under that one identifies the proton.

The scintillator counter (SC) system surrounds the drift chambers in CLAS and is primarily responsible for particle identification. The time of flight of a particle is determined by taking the difference between the event start time from the RF in the accelerator and the time recorded in the SC,  $t_{SC}$ . This  $t_{SC}$  is used to normalize the time for the EC and CC. It is also used for time-based tracking in the DC which measures the flight path. The combination of the flight path and time of flight determines the velocity of the particle. The SC is optimized to separate pions and kaons up to an energy of 2 GeV.

The detector consists of 48 paddles per sector with a photo multiplier tubes (PMT) on either end. This amounts to a total of 288 scintillator strips that provide polar angle coverage up to  $142^\circ$ . The scintillator panel for one sector is shown in Figure 3.17. The timing resolution of the SC is 120 ps at small angles (less than  $90^\circ$ ).

The signal from each PMT is calibrated to account for a pulse-height-dependent timing shift introduced by leading edge discriminators. Signals from the PMT of the SC have a sharply rising leading edge with a long, gently sloping tail. Small pulses trigger the discriminator later in time than larger pulses. A time-walk correction is applied based on the pulse height to correct for this discrepancy. Figure 3.17 shows  $\beta$  vs. momentum after 48 paddles in each of the six sectors were calibrated using the procedure outlined in Ref. [51].

### 3.5.3 Drift Chambers



FIG. 3.19: Drift chamber cell configuration with a typical track indicated (left) and photograph of a completed drift chamber sector (right)Ref. [1].

The CLAS drift chamber system can be divided radially into three regions within each sector. Each region contains a separate physical chamber with two “superlayers”.

Each superlayer has six layers of sense or anode wires, one axial to the torus magnetic field, and the other tilted at a  $6^\circ$  stereo angle. The superlayer for Region 1 has four wire layers because of spatial constraints Ref. [1]. A high voltage system maintains the sense wires at a positive potential. Each sense wire is surrounded by six field (or cathode) wires maintained at a negative potential with a value 50% lower than the positive value. An ionizing gas mixture of Argon and  $\text{CO}_2$  in the ratio of 88% to 12% is used to detect charged particles as they travel through the drift chambers Ref. [1]. The gas mixture is maintained at a constant pressure with Argon providing an ionization gain of  $\approx 10^4$ .

When a charged particle moves through the chamber, it ionizes the gas atoms and releases electrons that drift toward the sense (anode) wires. The sense wires are connected to preamplifiers which are connected in groups to circuit boards on the chamber end plates. The chamber plates are connected to the data acquisition system via a crate-mounted post-amplifier and discriminator board and time-to-digital converter board. The DC system is used for tracking charged particles and determining their momentum. It has to be re-calibrated based on the run conditions for the experiment including but not limited to changes in beam energy, torus current and physical movement of the drift chambers.

The geometry of each chamber is characterized by a set of 6 offsets; 3 translational and 3 rotational. These offsets give the displacement or rotation of a chamber from its ideal position in the engineering drawings. A DC alignment procedure is performed to find these offsets which are responsible for distortions in the particle momenta assuming the ideal position Ref. [15]. The optimal offsets are found through a minimization technique on the spatial residual between the FITDOCA (Distance Of Closet Approach to the wire of the fitted track) and the CALDOCA (Distance Of Closet Approach calculated from the distance vs. time function). These offsets are then applied in the tracking code.

These offsets are applied to the data set and the mean residual for each CLAS sector

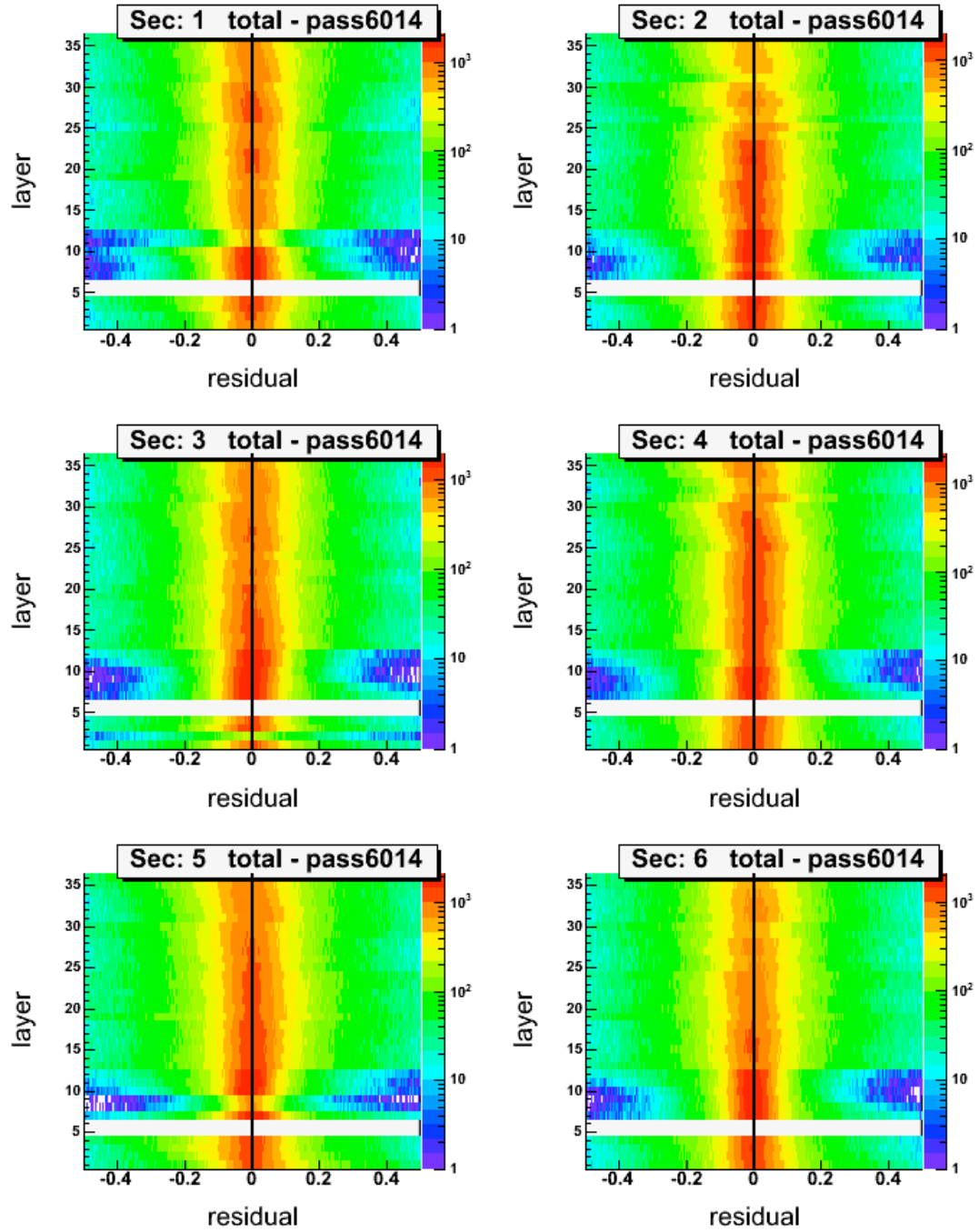


FIG. 3.20: Residual distribution (cm) as a function of wire layers after DC alignment for each CLAS sector Ref. [15]. The white area is a dead wire layer.

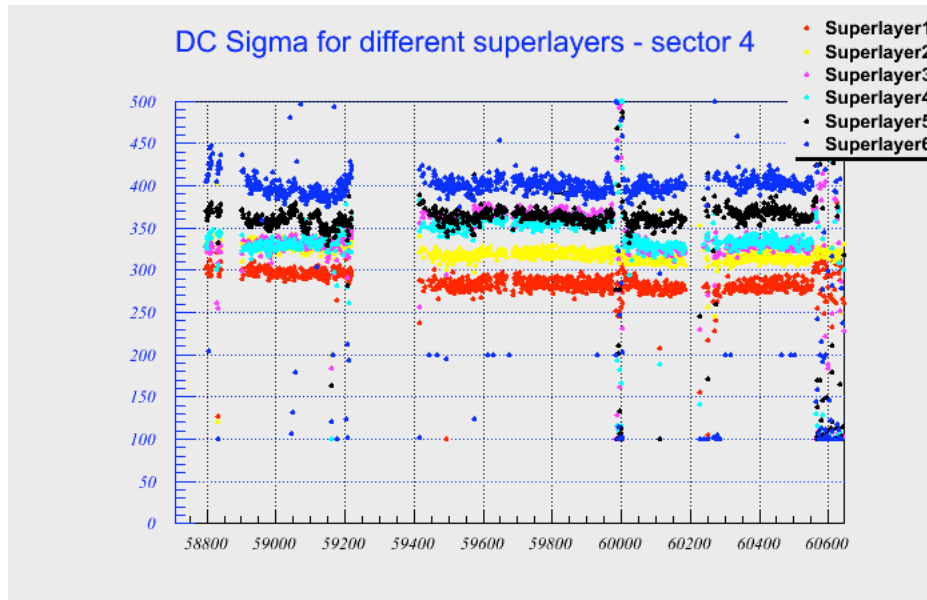


FIG. 3.21: Calibration quality for the drift chamber vs run number. DC sigma is a measure of the spatial resolution of the chamber. The gap between runs comes from the Summer 2009 accelerator down time between parts A and B of this experiment. Each run number is approximately three hours of data taking. The stability of the DC signal indicates an acceptable calibration quality.

is shown in Figure 3.20. The mean of the residual distribution is centered at 0 which indicates an acceptable calibration quality.

The time of flight ( $t_{SC}$ ) for a particle moving through CLAS is determined using the scintillator counters (SC) (Section 3.5.2). This time is used to predict when the charged particle passes through each cell in the DC. The time signal in the hit sense wire is then compared to the reference time from the SC. Both times are converted to a distance measure: the calculated reference distance from the SC (DIST) and the measured value from the DC, the distance of closest approach (DOCA).

Charge induced by an ionizing particle drifts toward the sense wire at a relatively slow velocity of around  $4 \text{ cm}/\mu\text{s}$ . If the relation between drift time and distance to the sense wire is known, the distance of closest approach (DOCA) to the sensor wire in each case can be calculated, thus greatly improving the accuracy of the path through time-based

tracking Ref. [11]. The DOCA function is fit using  $\chi^2$  minimization of a polynomial function to the observed drift times, given by

$$\chi^2 = \frac{|x(t) - x_{path}|^2}{\sigma_{path}^2} \quad (3.6)$$

where the DOCA function is,

$$x(t) = v_0 t + \eta \left( \frac{t}{t_{max}} \right)^p + \kappa \left( \frac{t}{t_{max}} \right)^q. \quad (3.7)$$

The drift velocity at  $t = 0$  is given by  $v_0$  and the maximum drift time is give by  $t_{max}$ . The fit has four coefficients  $\eta$ ,  $\kappa$ ,  $p$  and  $q$ . The DOCA value is obtained separately for each superlayer in each CLAS sector.

This difference gives the residual path difference (cm),

$$RESI = abs(DIST - DOCA) \quad (3.8)$$

The magnitudes of the residuals provide the spatial resolution for the DC. The residuals for all sectors after alignment are shown in Figure 3.20 and the quality of the resolution as a function of the run time of the experiment is shown in Figure 3.21

### 3.5.4 Cherenkov Counters

The Cherenkov Counter (CC) is primarily used to differentiate between electrons and negative pions with momenta below 2.5 GeV after they have passed through the drift chambers.

If a charged particle traversing a medium with refractive index  $n$  exceeds the speed

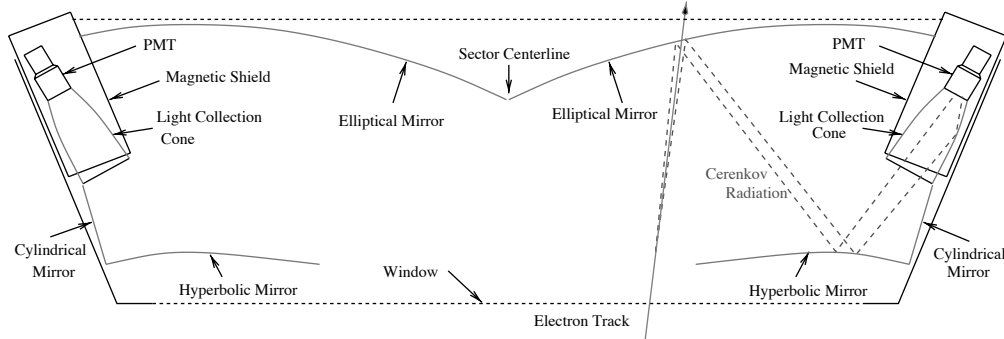


FIG. 3.22: Optical module of the CLAS Cherenkov detector showing light reflected off the set of mirrors, as collected by a PMT. The Cherenkov light is reflected off the hyperbolic and cylindrical mirrors placed in a configuration to direct light to the collection cone. The PMTs are placed in the acceptance dark regions of the coils of the torus magnet Ref. [1].

of light in that medium, it emits electromagnetic radiation known as Cherenkov radiation. The electron has a much lower Cherenkov threshold ( $\approx 0.9$  GeV) compared to pions ( $\approx 2.5$  GeV). The CC is filled with perfluorobutane gas ( $C_4F_{10}$ ) at 1 atm. The gas of this pressure has an index of refraction  $n = 1.00153$  Ref. [1].

The CC has 18 symmetrical mirrors that are used to reflect light into a corresponding photomultiplier tube (PMT) in every CLAS sector. The particle trajectories in CLAS are transverse to the toroidal magnetic field lines in constant  $\phi$  planes. A combination of elliptical and hyperbolic mirrors are used to deflect the emitted Cherenkov radiation in the  $\phi$  direction into the light collecting PMTs. The optical arrangement is shown in Figure 3.22. The polar angle range covered by the CC is up to  $45^\circ$ . The pions start to emit Cherenkov radiation at momenta greater than  $\approx 2.5$  GeV making  $\pi/e$  separation less efficient in this momentum region.

The CC was calibrated for the eg1-dvcs experiment for timing and gain. The time from the SC (See Section 3.5.2) can be used to get a predicted time for a charged particle moving through the Cherenkov Counter. The time recorded by the CC itself is then

compared to the predicted time to determine the timing resolution of the CC. Figure 3.23 shows the mean and standard deviation of  $t_{CC} - t_{SC}$ .

The gain calibration was performed by fitting the single photoelectron peak in the analog to digital converters (ADC) for all sectors. The stable gain calibration was then applied to the run period. A fit for the one photoelectron peak is shown in Figure 3.24

### 3.5.5 Electromagnetic Calorimeters

The electromagnetic calorimeter is capable of detecting charged and neutral particles and is designed to distinguish between hadrons and electrons.

It forms the outermost layer of the CLAS detector for each of the six sectors and is made of alternating sheets of lead and plastic scintillator material. The scintillator layer, in the form of thin strips is spatially placed in three different orientations separated from its closest layer by  $120^\circ$  as shown in Figure 3.25. Each scintillator layer is made of 36 strips that are 10 mm thick. The lead sheet is cut in a triangular shape and is 2 mm thick.

An electron loses its energy in the EC by an electromagnetic shower in which electrons radiate photons, photons produce  $e^+e^-$  pairs in the field of the heavy lead nuclei, and the scintillators produce light for each of the multiplying for each of the electrons in the shower. The total light collected is proportional to the initial electron energy.

Other hadrons such as pions, lose energy in the EC via ionization which produces much less output in the scintillators. The difference in the mechanism of energy deposited helps distinguish between electrons and pions. Neutral pions are detected in the EC by reconstructing the invariant mass of two photons. The lead encourages the electromagnetic shower and the scintillator samples the energy loss.

The energy deposited in the EC by an electron or photon is a product of the parti-

cles total energy and the sampling fraction of the EC ( $\approx 0.27$ ) Ref. [1]. The ADC and TDC boards for the EC are calibrated for energy and timing, respectively. The timing information here is relative to the SC and the difference ( $t_{EC} - t_{SC}$ ) over the course of the run period is shown in Figure 3.26. Some of the outliers in the standard deviations come from low-statistics runs. The stability of the gain calibration is seen in Figure 4.22 for each CLAS sector. Each sector is mostly stable except for the drop about every 50 runs. The version we got by fine tuning the EC gain calibration is deemed acceptable for the purposes of calculating asymmetries.

### 3.5.6 Trigger and Data Acquisition

To record events of interest, a two-level hierarchical system was designed for CLAS which minimizes its dead time. The Level 1 trigger processes all designated raw signals chosen by an experiment to define an event. The processing period of the Level 1 trigger is 90.5 ns. All detector information for the passed event candidate is digitized and read out and passed to the Level 2 trigger.

The Level 2 trigger finds ‘likely’ tracks in each sector, correlates them with the Level 1 trigger, and rejects hits without a likely track in the DC. If a ‘likely’ track is found then the event is recorded. If no track candidates are found, the Level 2 trigger issues a ‘fast-clear’ signal and more triggers are accepted. The detector cannot accept triggers until the events passing the Level 2 trigger are digitized and read out or it receives a ‘fast-clear’ signal. The processing of the Level 2 trigger contributes to the dead time of the detection system. The ‘fast-clear’ signal step was not used in the case of the eg1-dvcs experiment.

The CLAS data acquisition system can collect approximately 2000  $ep$  collisions per second. The signals for an event from all detectors are digitized and transferred to

the CLAS online acquisition computer. Various data blocks from the subcomponents of CLAS are put together using the Event Builder (EB) in the form of tables (or banks). The Event Recorder (ER) picks up the reconstructed event for permanent storage which is a two-step process. The event is first written to a local RAID disk. A fiber link from the raid disk transfers the event for permanent storage to magnetic tape Ref. [1].

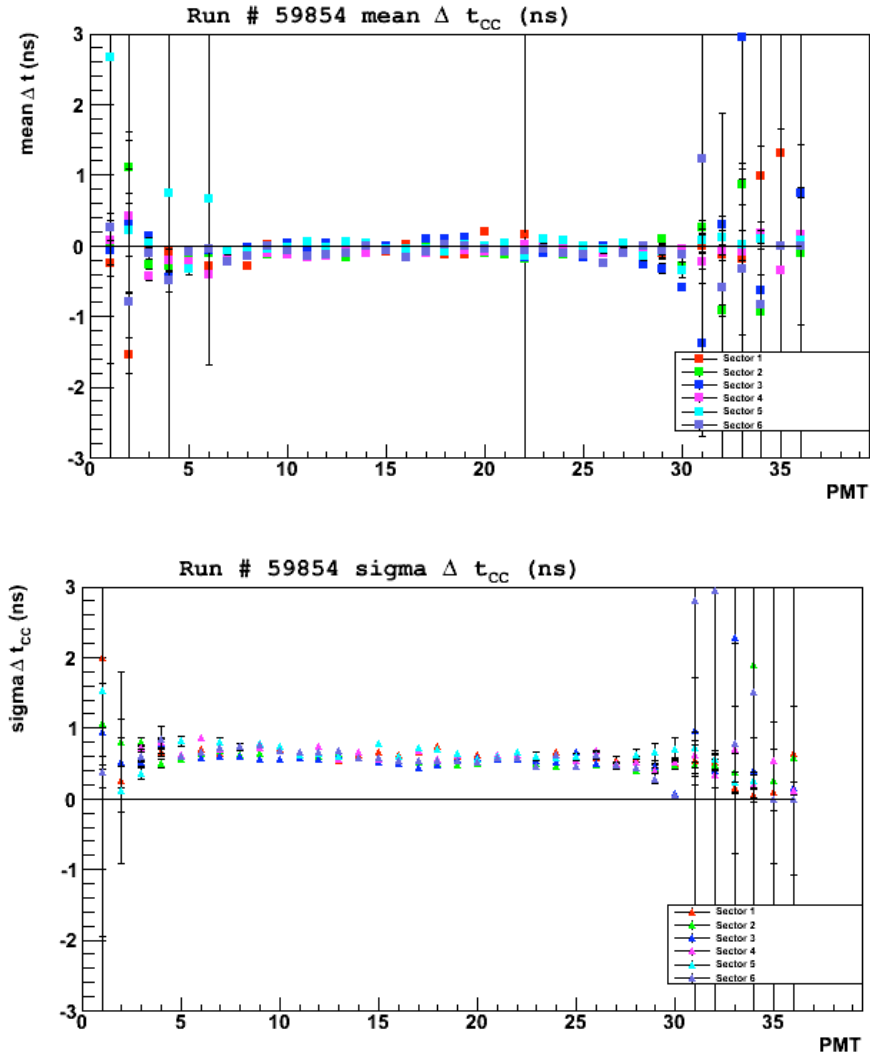


FIG. 3.23: Cherenkov timing differences  $\Delta t = t_{CC} - t_{SC}$  and widths  $\sigma$  as a function of PMT number after calibration using one run. PMT 22 (Sector 1) was dead throughout the experiment. This is reflected in the point with biggest error bars in mean and standard deviation. The data for large PMT numbers fluctuate wildly because of poor statistics near the edge of CLAS acceptance Ref. [16].

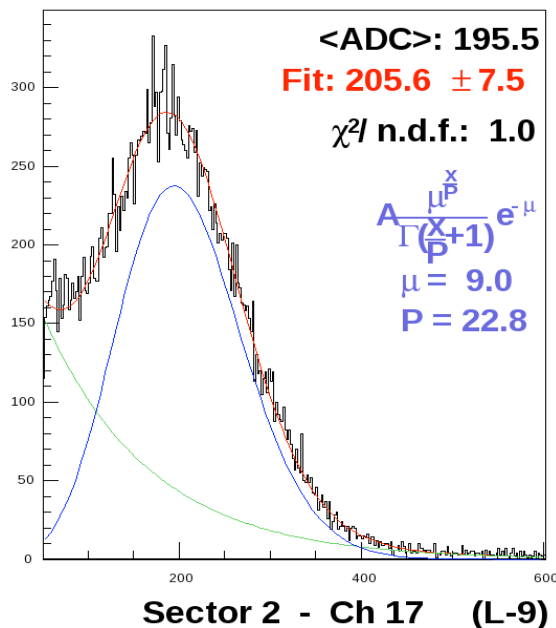


FIG. 3.24: Cherenkov counter light intensity spectrum for a single photoelectron. The gain calibration is done by fitting the single photoelectron peak. The fit in red is shown for one channel in Sector 2 in the CC. An ADC channel value of  $\approx 200$  corresponds to the single photoelectron peak Ref. [17].

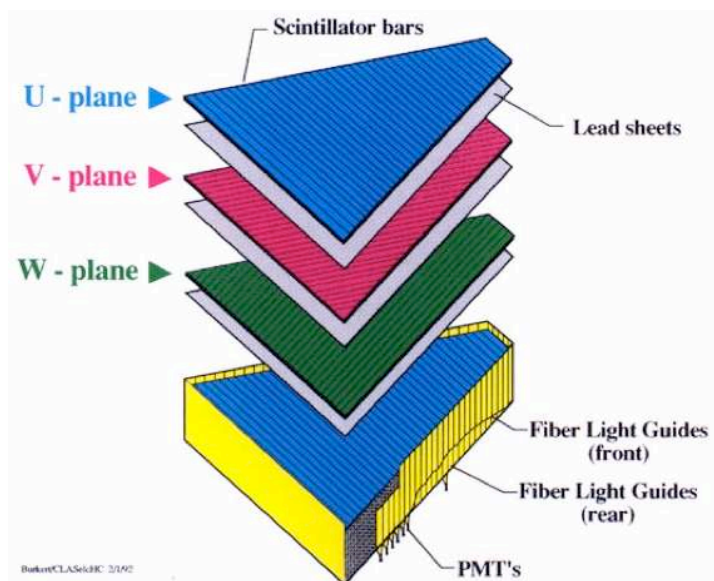


FIG. 3.25: One sector in the CLAS electromagnetic calorimeter Ref. [18]. The three layers of scintillator are placed in three different orientations rotated from the one above by  $120^\circ$ . This is done to allow triangulation of the shower position in the detector Ref. [1].

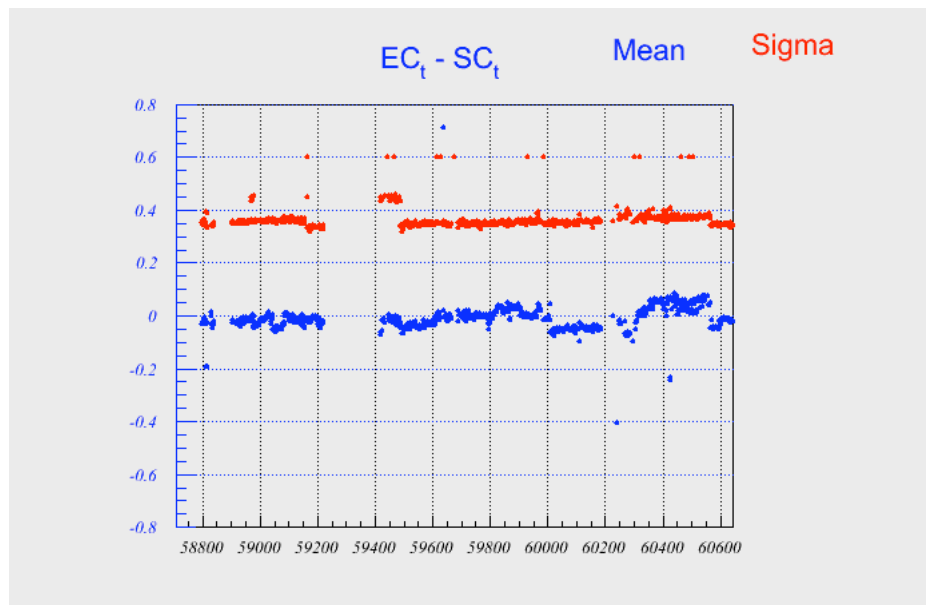


FIG. 3.26: The time difference between the EC and SC versus run number fit using a Gaussian. Data for the means (blue) and standard deviations (red) are shown for the duration of the experiment. The stability of the values indicates an acceptable calibration quality.

### 3.6 Run Summary

Run Range	Name	Dates	Target	$v_z$ (cm)	$I_{TORUS}$ (A)	$E_{BEAM}$ (GeV)
58799 - 59161	A	Feb - Mar 09	NH <sub>3</sub>	-58.3	2250	5.887
59162 - 59300	A	Feb - Mar 09	NH <sub>3</sub>	-58.3	2250	4.730
59400 - 59995	B	Apr - Jun 09	NH <sub>3</sub>	-67.3	2250	5.954
59996 - 60005	B	Apr - Jun 09	NH <sub>3</sub>	-67.3	-2250	5.954
60005 - 60200	B	Apr - Jun 09	NH <sub>3</sub>	-67.3	2250	5.954
60250 - 60564	C	Aug - Sep 09	ND <sub>3</sub>	-67.3	2250	5.752
60565 - 60650	C	Aug - Sep 09	ND <sub>3</sub>	-67.3	-2250	5.752

TABLE 3.1: Run summary of the eg1-dvcs experiment. The experiment ran in three blocks from February to September 2009. The beam energy in the latter part of A was lowered due to mechanical problems with the accelerator. Data with reversed field for the torus magnet were collected for background studies. The center of the target was shifted in reference to CLAS, in B and C which gave higher acceptance for the charged pions.

A summary of the eg1-dvcs data set is given in Table 3.1. The experiment ran in three blocks from February to September 2009. The beam energy in the latter part of A was lowered due so that all three halls could be given maximum polarization given possible Wien angle settings. For the rest of the run period the beam energy was close to 6 GeV. The distance between the target center and the front face of the IC was increased by about 10 cm for parts B and C. This gave a larger acceptance for the charged pions. The nominal value for each beam energy is obtained from the MCC based on the number of passes in the accelerator. To better determine the delivered electron energy, accurate energy measurements made during the same time period by Hall-A were scaled by the relative number of passes of the beam through the accelerator to get the Hall-B energy. These are tabulated in Table 3.1. More details of the Hall-A extrapolation are found in Ref. [52].

A total charge of 30 mC ( $A = 6.9$  mC,  $B = 15.4$  mC,  $C = 7.7$  mC) was collected during the course of the run. Approximately 15% of these data were collected on the carbon target and approximately 3% on the empty target. A small fraction of data were also collected with reversed torus field for background studies. The beam polarization was measured periodically throughout the course of the run. Table 3.2 details the run numbers and measurements made.

Run	Date	Time	$P_b+$	$P_b^{Err+}$	$P_b-$	$P_b^{Err-}$
58739	02/08/09	17:00	88.70	1.48	-80.49	2.26
58825	02/11/09	18:00	90.41	1.48	-82.76	1.48
58977	02/18/09	15:00	90.82	1.48	-87.04	1.48
59036	02/23/09	19:00	89.64	1.00	-84.14	1.00
59077	02/27/09	18:00	90.60	1.45	-79.09	1.49
59127	03/06/09	14:00	75.19	1.49	-68.00	1.49
59164	03/12/09	21:00	90.60	1.32	-84.25	1.42
59443	04/30/09	13:00	87.53	1.54	-81.43	1.52
59537	05/06/09	21:00	81.43	1.47	-82.14	1.47
59565	05/08/09	16:00	86.13	1.48	-84.71	1.51
59705	05/15/09	13:00	89.93	1.34	-80.11	1.45
59780	05/20/09	15:00	91.97	1.44	-86.25	1.88
59792	05/21/09	21:00	81.55	1.44	-82.25	1.38
59894	05/28/09	11:00	85.72	1.50	-80.59	1.50
59909	05/29/09	9:00	84.57	1.49	-82.68	1.48
59965	06/01/09	16:00	82.87	1.49	-87.54	1.49
60006	06/04/09	18:00	88.53	1.28	-74.38	1.50
60111	06/11/09	20:00	85.15	1.48	-83.99	1.48
60121	06/12/09	18:00	85.85	1.48	-85.28	1.49

TABLE 3.2: Summary of Møller measurements for the eg1-dvcs experiment. The Møller polarimeter measures the beam polarization ( $P_b$ ) for both helicities using elastic scattering on polarized Permendur foil Ref. [1]. Differences in the polarization between the two helicities on the order of a 1-2% are consistent with previous CLAS experiments. However we had some differences as large as 9% for Møller runs that did not run long enough.

The data were collected in increments of “runs”. Each data run was approximately 40 million electron triggers which took anywhere between two to four hours to collect, depending on beam quality. One run contained, on average, 85 data files. Each file format was identical in structure and was numbered based on the run and file number. The track reconstruction package (user-ana) was used to convert raw data into physics quantities. The physics output files were further compressed using preliminary cuts in event selection. The details of the event selection cuts and the structure of the data file and the physics variables in them are detailed in Ref. [53].

# CHAPTER 4

## Data Analysis I

To extract the physics of semi-inclusive scattering from the data obtained we conducted several studies. These studies are broadly divided into three parts. The first portion deals with analyses performed prior to selecting the physics events, the second with the actual mechanics of event selection, and the last with corrections applied to physics quantities.

### 4.1 Corrections before Event Selection

#### 4.1.1 Raster Correction

To minimize the effects of target depolarization because of electron beam dose, the beam is scanned, or rastered, over the target area in a circular pattern. The beam spirals inward and outward alternately due to magnetic fields produced by two sets of perpendicular Helmholtz coils. Failure to raster the beam will result in loss of target polarization. Hence, the raster system is an important part of the experiment but does create the prob-

lem of varying the entry point of the beam on the target. The raster correction is used to account for this variation. The geometry of the correction, procedure and code are available in Ref. [54]. A brief description is given below.

The raster magnet current is measured and digitized using ADCs. The signals are synchronized with each event and recorded in the event stream. When calibrated with a gain factor and an offset they yield  $x$  and  $y$  beam positions at the target for each event  $i$  given by

$$x_i = (x_{ADC} - x_{off})x_{gain} \quad (4.1)$$

and

$$y_i = (y_{ADC} - y_{off})y_{gain}. \quad (4.2)$$

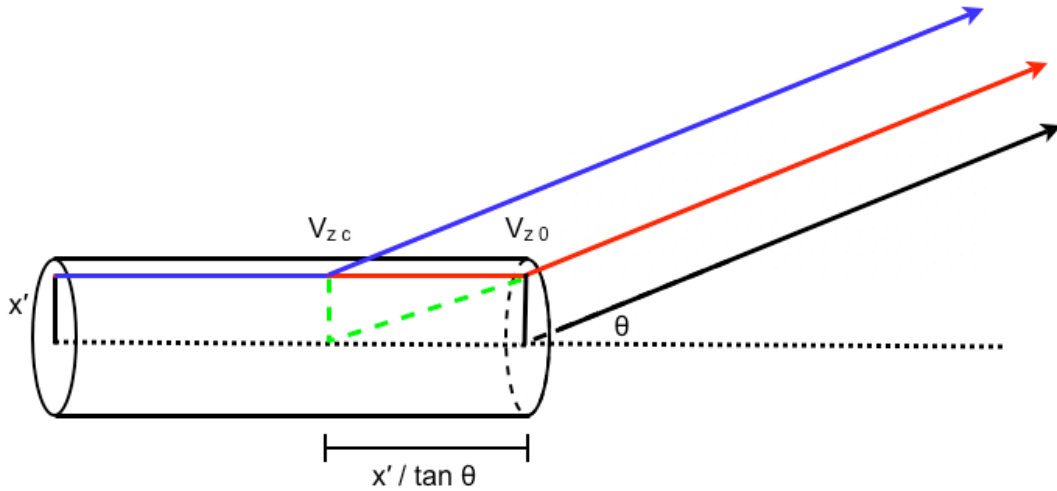


FIG. 4.1: Side view of raster correction geometry. The vertex position in the CLAS  $z$  direction is corrected for tracking which assumes the electron traveled along the center of the beam line. The black ray is the uncorrected particle path which forms an angle  $\theta$  with the beam direction. The red ray is the traced-back ray, and the blue path is the final, raster corrected path through the true vertex Ref. [11]. The vertex position given by CLAS tracking software is  $v_{z0}$  and the corrected vertex is  $v_{zc}$ .

The standard tracking package in CLAS reconstructs particles back to a plane paral-

lel to the torus field lines and perpendicular to the sector containing the track and passing through the beam line. If the actual beam is displaced from the center by a distance  $x'$ , then the average vertex position  $z$  will be displaced as seen in Figure 4.1. The displacement is incorrect by an amount that varies as the cosine of the azimuthal angle  $\phi$ . To correct the vertex, we first define the sector angle,

$$\phi^S = (S - 1) \times \pi/3 \quad (4.3)$$

where  $S$  is the CLAS sector number (1 - 6). The azimuthal scattering angle for each event  $i$  is

$$\phi_i = \arctan(p_y/p_x) \quad (4.4)$$

where  $p_x$  and  $p_y$  are the momenta of the particle in the event  $i$ . The projection of the raster coordinates on to the sector ray  $s$  is given by,

$$s = x_i \cos \phi_i^S + y_i \sin \phi_i^S \quad (4.5)$$

The displacement,  $x'$  is obtained by scaling the sector ray direction along the  $x_i$  direction of the track. The cross-section view of the target is shown in Figure 4.2. Applying trigonometry to the angle  $\phi - \phi^S$ , we get

$$x'_i = [x_i \cos \phi_i^S + y_i \sin \phi_i^S] / \cos(\phi_i - \phi^S). \quad (4.6)$$

The corrected vertex position is thus given by,

$$z_i = z_i^0 + x'_i / \tan(\theta_i) \quad (4.7)$$

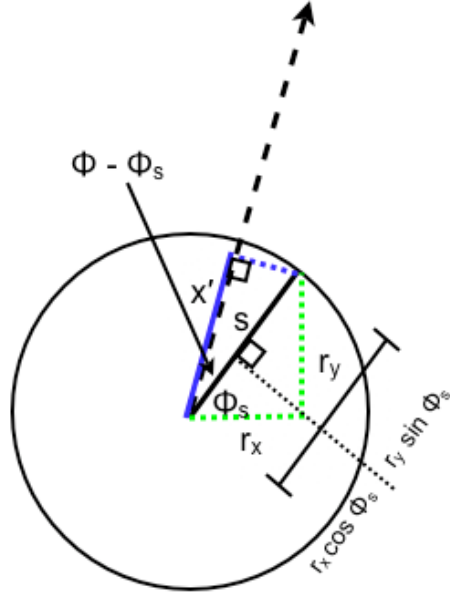


FIG. 4.2: Cross-section view of the raster correction geometry Ref. [11]. The black dotted line represents the (uncorrected) particle trajectory; while the solid black line ( $s$ ) is the reference line of the triggered sector. The projection of the raster coordinates (green) on the trajectory is defined as  $x'$  (blue).

where  $\theta_i$  is the angle made by the track with the beam direction as seen in Figure 4.1.

The correction is applied by minimizing  $z_i$  compared with the nominal target center,  $z_i^{nom}$  for each event  $i$ . The  $\chi^2$  minimization is given by

$$\chi^2 = \sum_{i=1}^N (z_i - z_i^{nom})^2 \quad (4.8)$$

where the uncorrected value  $z_i$  is modified by a track azimuthal angle  $\theta$  dependence on the uncorrected  $x_i$  and  $y_i$  vertex coordinates.

The fit parameters used in the minimization are  $x_{gain}$ ,  $y_{gain}$ ,  $x_{off}$ ,  $y_{off}$  and  $z_i^{nom}$ . The gain factors ( $x_{gain}$ ,  $y_{gain}$ ) are found to be very stable for each beam energy, and scale as  $1/E_{Beam}$ . The offset terms ( $x_{off}$  and  $y_{off}$ ) show considerable variation with time. The

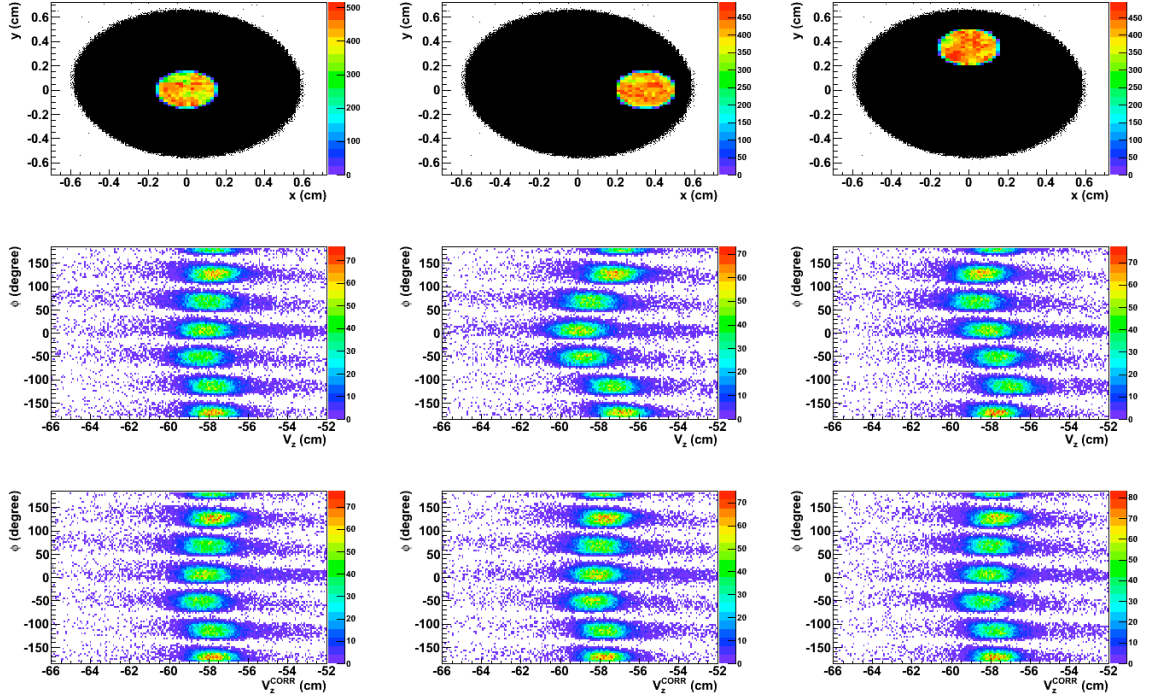


FIG. 4.3: Raster pattern for Run 59000 with a selected section on the target area (top row). The second row shows the vertex position  $v_z$  before applying the raster correction for the selected target area above it. The third shows the vertex position  $v_z$  after applying the raster correction.

range of about 800 ADC counts corresponds to a range of beam positions of about 2 mm. The values for  $z_i^{nom}$  are stable to within 0.3 mm for each part of the experiment, averaging -58.95, -67.97, and -68.18 cm for parts A, B, and C, respectively. The blue line in Figure 4.1 shows final path.

Applying this correction improves the vertex distribution in the 6 CLAS sectors. This is demonstrated in Figure 4.3 which shows the distribution of the vertex position as a function of azimuthal angle, before and after applying the raster correction in different regions of the target cross-section.

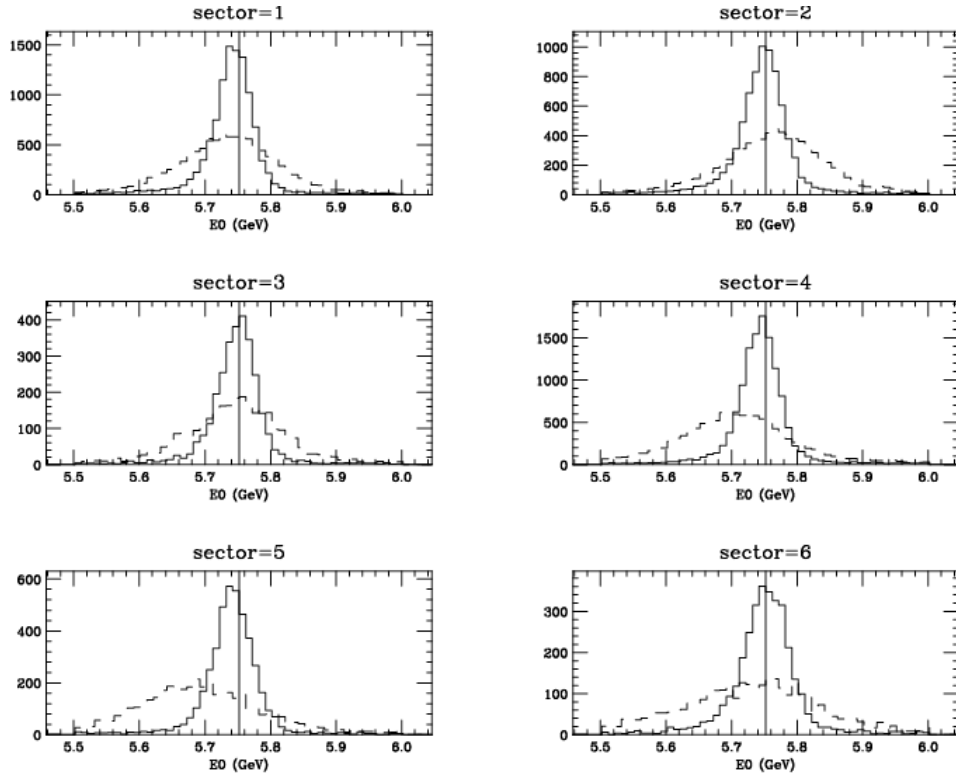


FIG. 4.4: Beam energy calculated from  $ep$  elastic scattering for each sector using an  $\text{NH}_3$  run. The dashed lines use the momenta and angles from the reconstruction algorithm from RECSIS and the solid lines are the spectra after applying the track reconstruction corrections.

### 4.1.2 Tracking Correction

The path of the particles moving through the drift chambers is reconstructed by a tracking reconstruction package (RECSIS). The track in each sector of the drift chamber is reconstructed to Region 1 of the DC taking into account the 5 T target magnet field as well as the CLAS torus magnet. The target magnet field is approximately 5 T up to a radial distance of 24 cm from the magnetic center which is where the polarized target material is located. RECSIS does not take into account any magnetic field between the first layer of the DC and the target. The tracking correction gives a more accurate description of the angles and momentum of a track.

In our case, the track is traced back to the beam  $(x, y)$  coordinates, obtained from the raster correction detailed in the previous section. More accurate track angles also improve the vertex resolution. The track-fitting procedure and code are available in Ref. [55].

The improved angular resolution is apparent especially when looking at the empty target spectrum as shown in the Dilution Factor Study (see Section 5.1). Another test of seeing the effect of the tracking correction is reconstructing the beam energy of the electron using an exclusive reaction. Consider the case for elastic scattering,

$$ep \rightarrow ep. \quad (4.9)$$

Both the scattered electron and proton are detected in CLAS. The energy of the incoming electron is then calculated using

$$E_{beam} = M_p \left( \frac{1}{\tan\left(\frac{\theta_e}{\theta_p}\right)} - 1 \right) \quad (4.10)$$

where the scattering angle of the electron ( $\theta_e$ ) and proton ( $\theta_p$ ) are detected in CLAS (Ref. [55]). The beam energy ( $E_{beam}$ ) resolution for  $ep$  elastic scattering before and after applying the correction is shown in Figure 4.4.

### 4.1.3 Fiducial cuts for the Inner Calorimeter

The Inner Calorimeter (IC) provides high efficiency detection of photons at small angles. It also blocks particles that would typically be detected in CLAS at small angles. Particles hitting the edge of the IC or its shielding can experience significant energy loss and multiple scattering. The edges of the IC apparatus were determined empirically, leading to fiducial cuts that ensure that particles detected in CLAS did not hit the IC on

their way. The methodology and code of the study are found in Ref. [19].

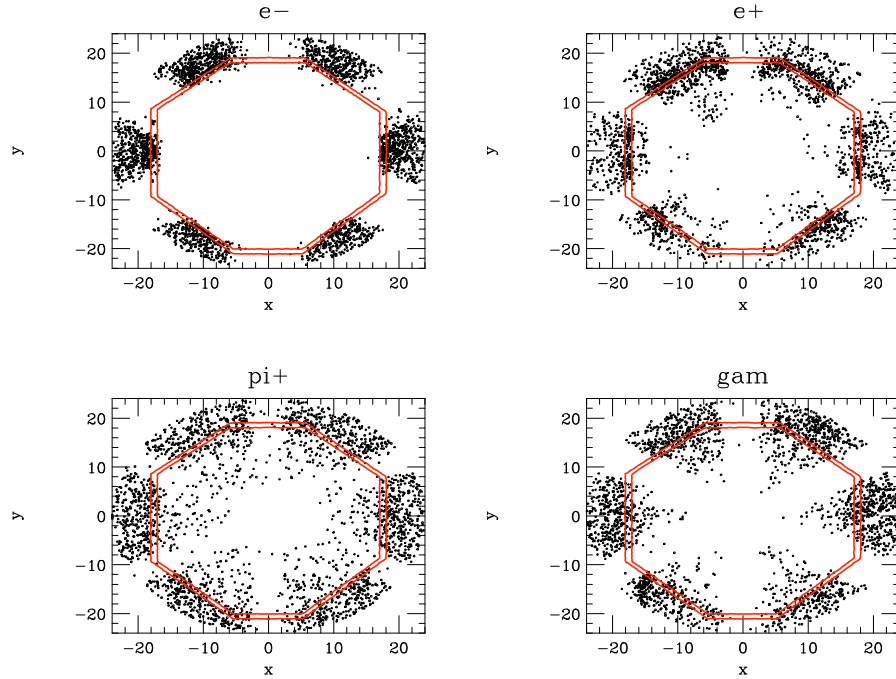


FIG. 4.5: Distribution of  $x$  (cm),  $y$  (cm) at the IC front face for electrons, positrons, positive pions, and photons, for part A run 59000 Ref. [19]. The inner red lines define the standard fiducial cut, while the outer red lines define the stricter cut. To save space, points beyond a radius of 24 cm are not plotted.

The hits in the fiducial region for the electron, positron, positive pion and photon are shown in Figure 4.5. The inner red lines define the standard fiducial cut, while the outer red lines define the stricter cut. I use the stricter cut to remove electrons, charged pions and photons in CLAS that fall in the region potentially blocked by the IC or its shielding.

## 4.2 Event Selection

The corrections from the previous section are applied to the events that produce a trigger in the data acquisition system. These events are then further analyzed to identify

the scattered electron and pion in coincidence. A combination of the electromagnetic calorimeter, drift chambers and Cherenkov counters in CLAS are used to select an electron in CLAS. The scintillators and drift chambers are used in charged pion selection. For the case of the neutral pion, the electromagnetic calorimeter in CLAS and the IC are used.

### 4.2.1 Electron

The primary criteria for electron selection are listed in Table 4.1.

Selection	Limits
Charge	$q = -1$
Visible Energy in EC	$E_{EC} > 0.24 \times (p - 0.12)$
Photoelectron signal in the Cherenkov counter	$nphe > 2.0$
Mirror matching in the Cherenkov counter	$\chi^2 < 0.10$
Electron Momentum	$0.8 < p < p_{Beam}$ GeV
Vertex selection	$ v_z - v_{znom}  < 4.0$ cm

TABLE 4.1: Summary of electron identification criteria. The cuts in the EC and CC remove negative pion contamination in the sample. Electrons with momentum less than 0.8 GeV are removed from sample to minimize events with large radiative corrections. The vertex cut ensures that the electron in the event actually came from the target region.

Low momentum pions lose energy in the EC via ionization and electrons do so by electromagnetic showers. The energy deposited by each in the calorimeter is a function of their momentum. Putting a momentum dependent cut on the visible energy deposited in the EC removes most of the negatively charged pions. To prevent further negative pion contamination for candidates with momenta above 2.5 GeV further cuts on the other detection systems are applied.

The cut on the photoelectron signal in the CC serves this purpose. The ultra-relativistic electron passing through the Cherenkov counter produces a larger signal (number of photoelectrons) than the heavier pions ( $m_\pi \approx 140$  MeV). The variable CC  $\chi^2$  is obtained from

the mirror matching procedure for the CC detailed in Ref. [56] and is standard procedure for improving electron discrimination from background. The particle track in the the DC is matched with the expected phototube that will fire in the CC, which improves electron discrimination. Electrons with momentum less than 0.8 GeV are removed from sample to minimize events with large radiative corrections. The vertex cut ensures that the electron in the event actually came from the target region. Each of these cuts are seen in Figures 4.6 and 4.7. Figure 4.8 shows the effect of adding each successive cut on the electron event sample. We start with all negatively charged particles detected in CLAS. We than cut out negative pions in the EC using the momentum-dependent cut. This is followed by cuts on the Cherenkov counter for both the signal and mirror matching. These cuts reduce the initial sample by  $\approx 15\%$ . The last two cuts remove low momentum electrons and electrons coming from regions other than the target area, leaving us with  $\approx 67\%$  of the initial sample.

### 4.2.2 Charged Pions

Selection	Limits
Charge	$q = \pm 1$
Visible Energy in EC	$E_{EC} < 0.20p$
Photoelectron signal in the Cherenkov counter	$nphe < 2.0$
Timing	$\Delta t = t_{predicted} - t_{expected} < 0.7 \text{ ns}$
Vertex selection	$ v_z - v_{z_{nom}}  < 4.0 \text{ cm}$

TABLE 4.2: Summary of charged pion selection cuts. The cuts in the EC and CC remove electron contamination in the sample. The timing cuts is based on the time of flight of the charge particle through the detector. This cuts removes heavier particles that would take longer than the pion, e.g. proton, kaon, etc. The vertex cut ensures that the data are collected from the target region.

The principal detector used to identify charged pions is the time of flight system. The event start time ( $t_{eventstart}$ ) is obtained from the radio frequency (RF) time of the

accelerator. The time it takes for a charged particle to reach the scintillators is compared to the time a pion, with momentum determined by the drift chambers, would take to traverse the same distance ( $t_{TOF}$ ). This can also be transformed into  $\beta = v/c$  written as,

$$\beta_{measured} = \frac{1}{c} \frac{distance}{t_{TOF} - t_{eventstart}} \quad (4.11)$$

or the measured time for the particle to reach the scintillators,

$$t_{measured} = t_{TOF} - t_{eventstart}. \quad (4.12)$$

The predicted velocity of a pion is given by,

$$\beta_{theory} = \frac{p}{\sqrt{p^2 + M_{\pi}^2}} \quad (4.13)$$

and the predicted time it takes to reach the SC is

$$t_{theory} = \frac{distance}{c\beta_{theory}}. \quad (4.14)$$

The distribution of  $\Delta\beta = \beta_{theory} - \beta_{measured}$ , or  $\Delta t = t_{theory} - t_{measured}$ , as a function of particle momentum provides a clean signal for charged pions as is seen in Figure 4.10. Anti-electron cuts are also applied on the CC and EC to remove electron contamination in the negative pion sample. The photoelectron signal in the CC is required to be less than 2. The momentum-dependent cut on the EC removes electrons as well. The vertex cut is applied to ensure that the pion comes from the target region. The list of cuts is shown in Table 4.2 and the each individual cut is shown in Figures 4.11, 4.10 and 4.9. The effect of each successive cut on the charged pion is shown in Figure 4.12. The the cut on  $\Delta t$

removes the most number of events especially for the positive pion candidates. This is seen in the individual spectrum which shows bands for the kaons and protons. After all cuts we are left with  $\approx 17\%$  of the initial positive candidates sample and  $\approx 36\%$  of initial negative pion candidates. We collect more than twice the number of positive pions as negative pions in our detector.

### 4.2.3 Neutral Pions

Neutral pions are reconstructed from the invariant mass of two detected photons ( $\gamma$ ) detected in the electromagnetic calorimeter or the inner calorimeter. The photon selection for the EC and IC are listed in Tables 4.3 and ?? respectively. Low momentum photons for each case are removed. A cut on  $\beta$  is implemented for the neutral pion detected in the EC. This cut is designed to remove any signal from neutrons. The  $\Delta t$  cut in the IC is a cut on the time difference between the event start time and the photon hit in the IC. This is designed to remove signals uncorrelated with the event start time. The result of applying each successive cut is shown in Figure 4.14.

Selection	Limits
Charge	$q = 0$
Particle velocity	$\beta > 0.80$
Particle momentum	$p > 0.2 \text{ GeV}$

TABLE 4.3: Summary of photon selection cuts in the Electromagnetic Calorimeter.

Selection	Limits
Timing	$\Delta t_\gamma = t_{IC} - t_{eventstart} < 5 \text{ ns}$
Particle momentum	$p > 0.3 \text{ GeV}$

TABLE 4.4: Summary of photon selection cuts in the Inner Calorimeter.

The three possible topologies to calculate the invariant  $\pi^0$  mass are two  $\gamma$ s in the IC, two  $\gamma$ s in the EC and, one  $\gamma$  in the EC and one  $\gamma$  in the IC. A symmetric cut is then made on the invariant mass of two photons  $0.1 < M_{\gamma\gamma}^2 < 0.17 \text{ GeV}^2$  to select the neutral pions found only in the EC or only in the IC. For the third topology, we made an asymmetric cut around the pion mass -  $0.1 < M_{\gamma\gamma}^2 < 0.16 \text{ GeV}^2$  to avoid more of the background on the right. The mass cuts are seen in Figure 4.13. The yellow region is selected as a good neutral pion candidate and the black region is eliminated from physics analysis. The IC is made of lead tungstate bars that have a detector higher resolution than the combination of lead and scintillator sheets in the EC. This is reflected in the resolution of the invariant mass peak in the IC vs the EC. As seen in Figure 3.14 the width of the IC peak is about half the size of the EC peak.

#### 4.2.4 Quality Checks

We have studied the events selected as a function of time to ensure stability of our data sample, and to decide on the good runs to use for analysis. We calculate the rate of inclusive electrons by dividing the number of electrons detected by the gated charge collected in the Faraday cup.

After monitoring inclusive electron rates over the course of the run period, only data files that have rates within 90% of the maximum for that run are included in the data sample. This study is conducted for each CLAS sector. Seen in Figures 4.15, 4.16 and 4.17 are the data files that passed the good file selection criteria. The jump in the rate around Run 59150 comes from a change in the beam energy to 4.7 GeV and the slight jump around Run 60000 comes from reversing the polarity of the torus magnet current. Both of these portions of data are excluded in the final asymmetry analysis. We also

monitor the semi-inclusive rates for three pion cases. No further criteria were used to remove files past this point because of low rates.

The electron helicity flips pseudorandomly at the rate of 30 Hz. To calculate accurate values for asymmetries it is important that we have the same amount of beam charge corresponding to the two helicity states. We monitor this over the course of the run period as well. The beam charge asymmetry is given by,

$$q_{asym}(\%) = \frac{q^+ - q^-}{q^+ + q^-} \times 100\% \quad (4.15)$$

where  $q^{+(-)}$  represents the charge for the positive (negative) helicity electron. As seen in Figure 4.21, the highest beam charge asymmetries we encounter were less than 1.5% and typically less 0.5%, which are deemed reasonable and no data files are removed for this reason.

The average photoelectrons measured by the Cherenkov counter were monitored as well. Between parts A and B the Sector 5 piece of the CC developed a slow gas leak. Consequently, the average photoelectron count for part B seen in Figure 4.20, is lower. This is also reflected in the over all electron rate. Sector 5 was included in generating asymmetries because any acceptance issues cancel.

The energy deposited in the EC for good electrons was monitored file by file to ensure that the cuts made for electrons did not need to be modified because of gain changes in the detector. For an electron energy and momentum can be considered the same (i.e.  $E/p = 1$ ). Figure 4.22 shows the average  $E/p$  for each run in the experiment. Instead of this quantity being unity, it is about 0.27 since the calorimeter is calibrated to yield visible energy rather than the total. The average value of the energy drops as a function of run number in spite of gain calibration. The standard deviation is approximately 0.04.

This is safely away from the pion rejection criterion and so we ignore the variation in the average value.

The other reason data files are removed is because of abnormally high rates. The abnormally high rates were found to be correlated with beam missing the target material and hitting the Kapton cup holding the target. This typically occurred when the beam was over-rastered. An example of the over-rastered beam is shown in Figure 4.23. A list of files where this occurred was compiled and these data were removed from physics analysis. More details of this study are found in Ref. [57].

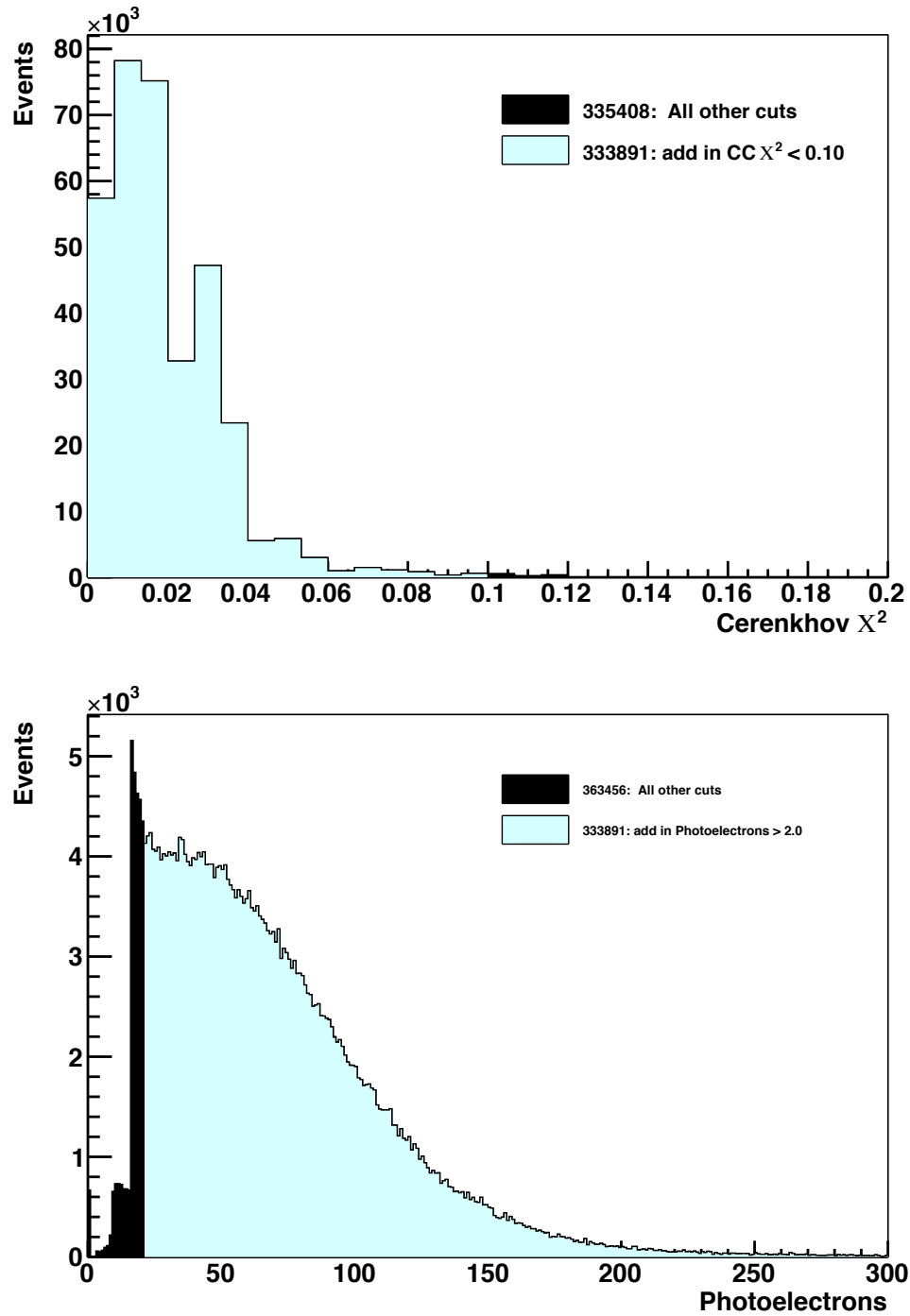


FIG. 4.6: Histogram of the number of photoelectrons detected in the CC for candidate electrons (lower plot) and the track/CC phototube matching  $\chi^2$  (upper plot). The blue shows the data before cuts and the black shows data eliminated by the electron cuts.

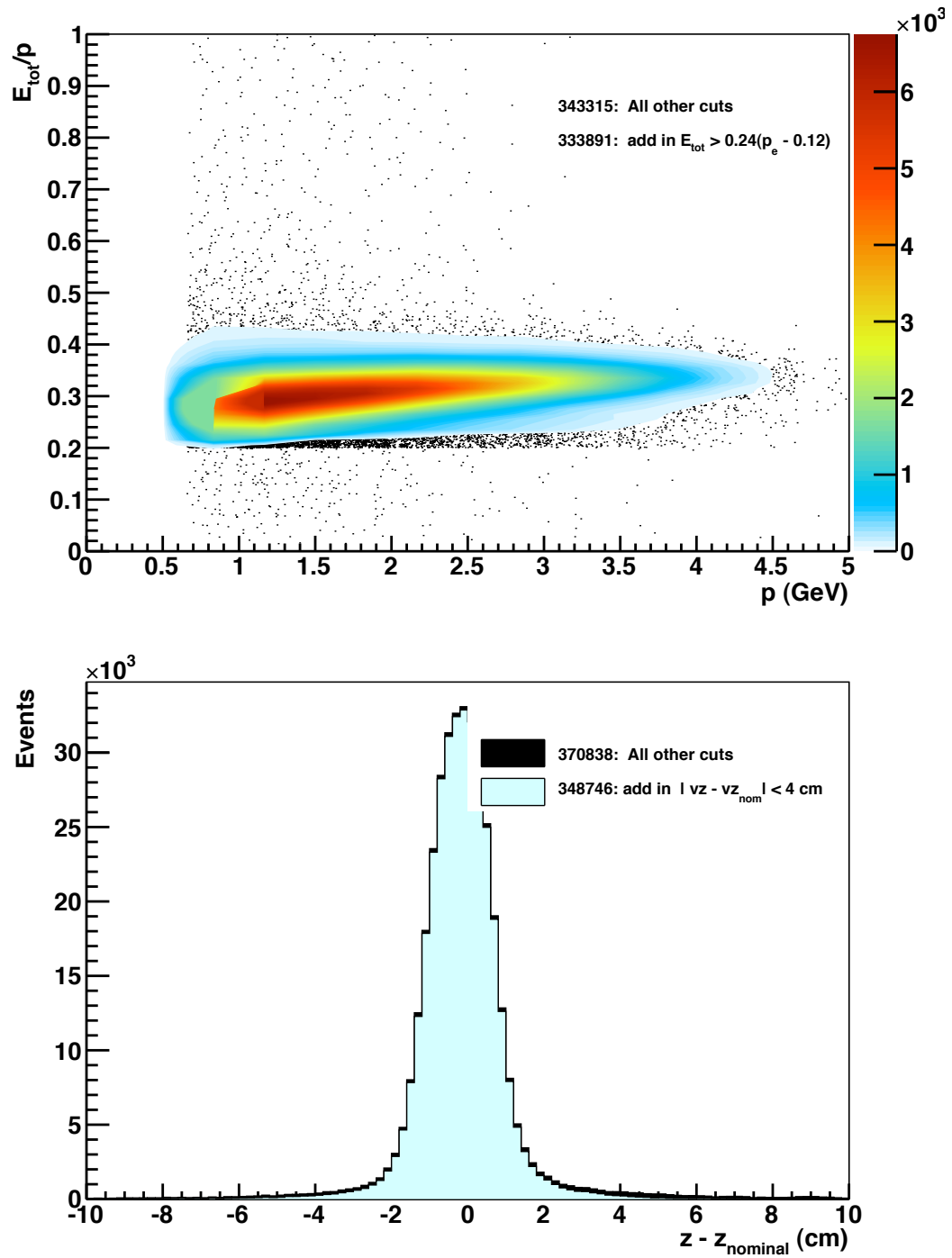


FIG. 4.7:  $E/p$  versus  $p$  (upper plot) and vertex  $z$  position (lower plot) for electron candidates. The black points (upper) and lines (lower) indicate events that are eliminated by the full electron cuts.

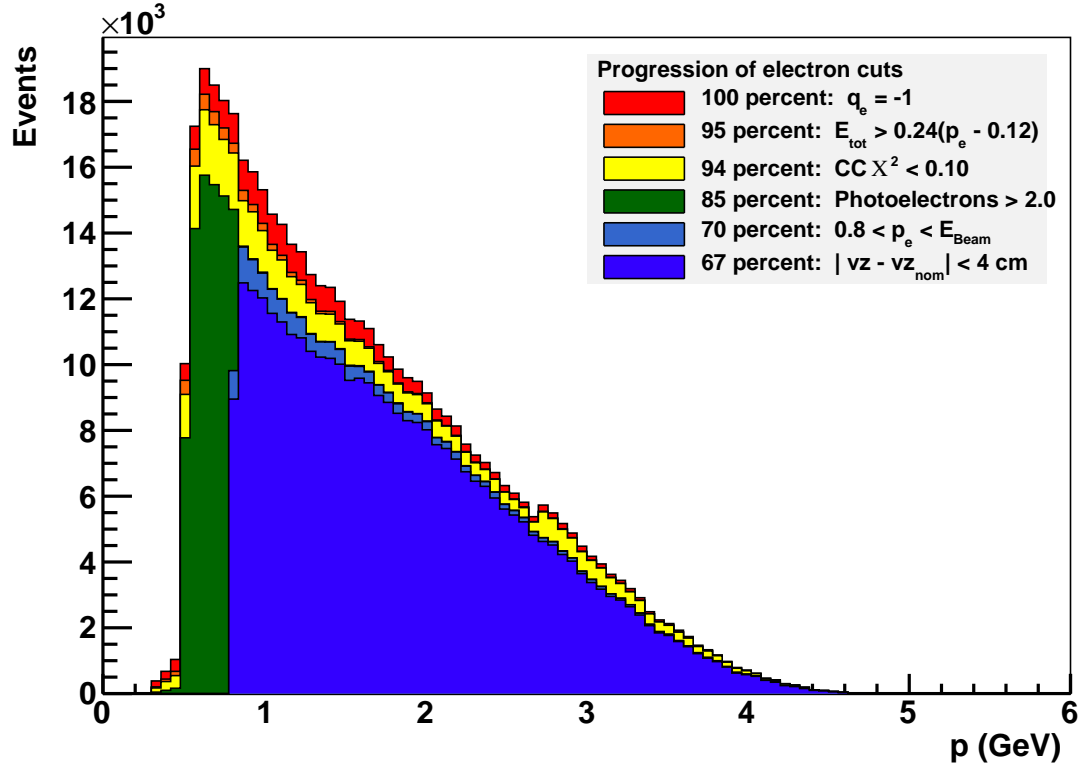


FIG. 4.8: Electron candidates as a function of momentum after applying the selection criteria from Table 4.1. We start with all negatively charged particles detected in CLAS. We then cut out negative pions in the EC using the momentum-dependent cut. This is followed by cuts on the Cherenkov counter for both the signal and mirror matching. These cuts reduce the initial sample by  $\approx 15\%$ . The last two cuts remove low momentum electrons and electrons coming from regions other than the target area leaving us with  $\approx 67\%$  of the initial sample.

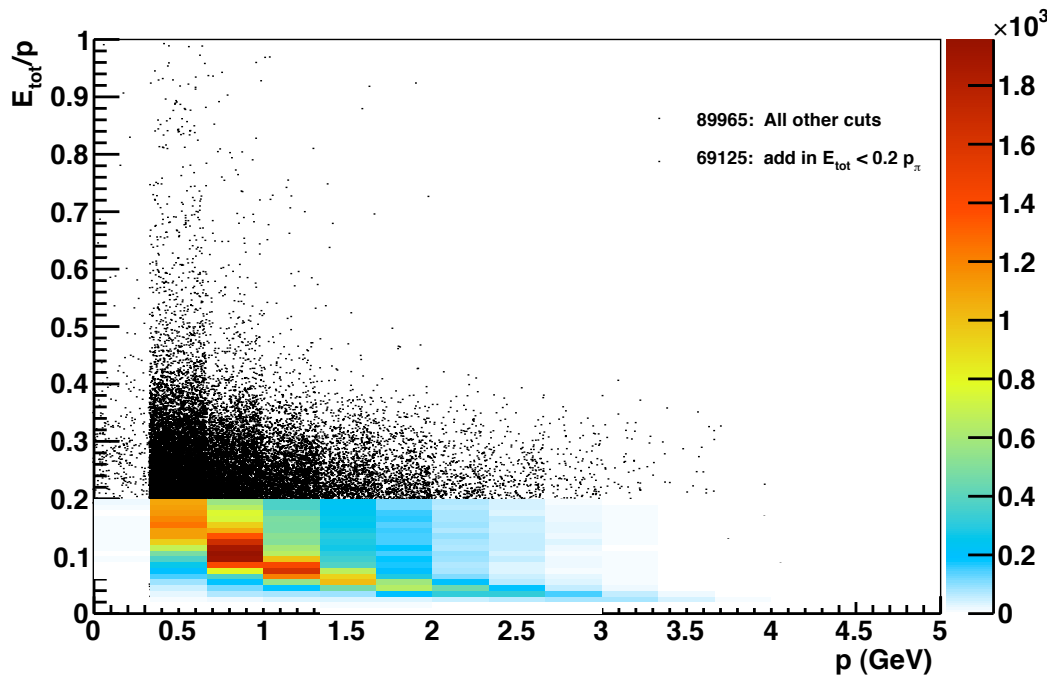
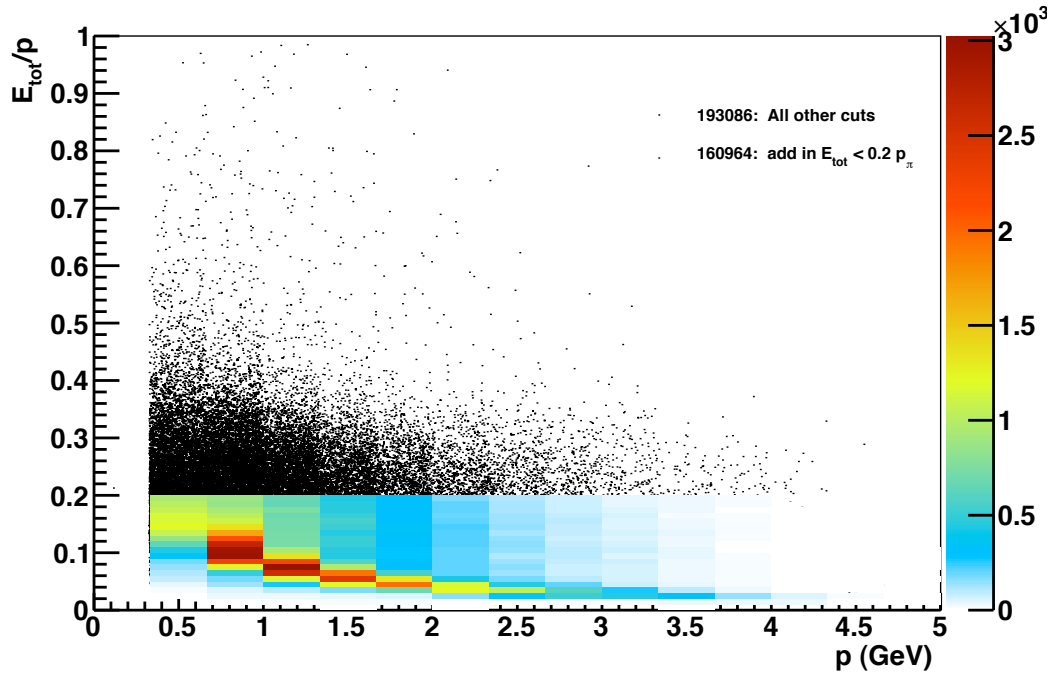


FIG. 4.9:  $E/p$  vs.  $p$  for positive (upper plot) and negative (lower plot) pions. The colored region is selected as a good pion candidate and the black region is removed prior to physics analysis.

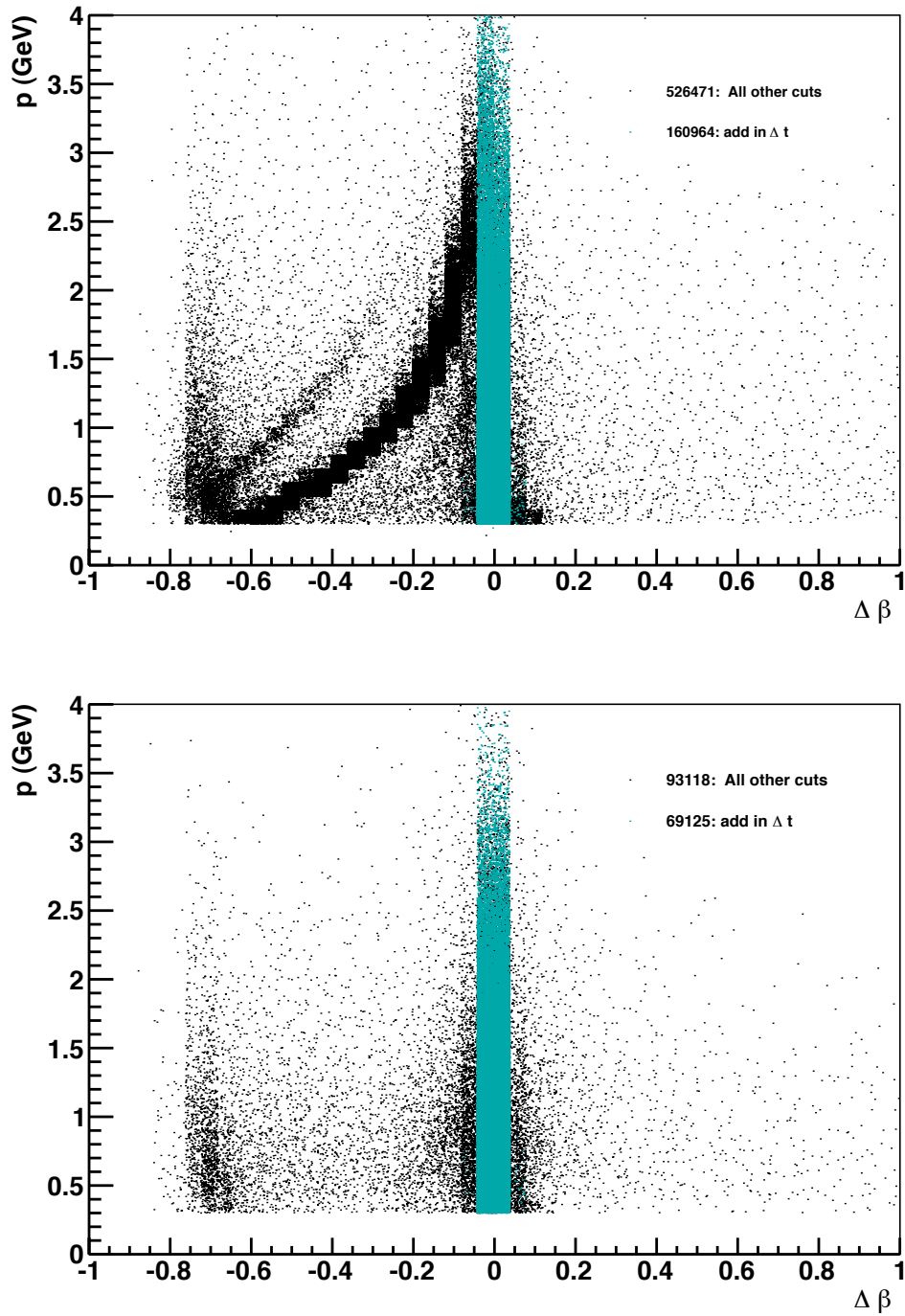


FIG. 4.10:  $p$  vs.  $\Delta\beta$  for positive (upper) and negative (lower) pions. The colored region is selected as a good pion candidate and the black region is removed prior to physics analysis. The  $\Delta t$  cut removes signals from the kaon and proton as seen in the top plot.

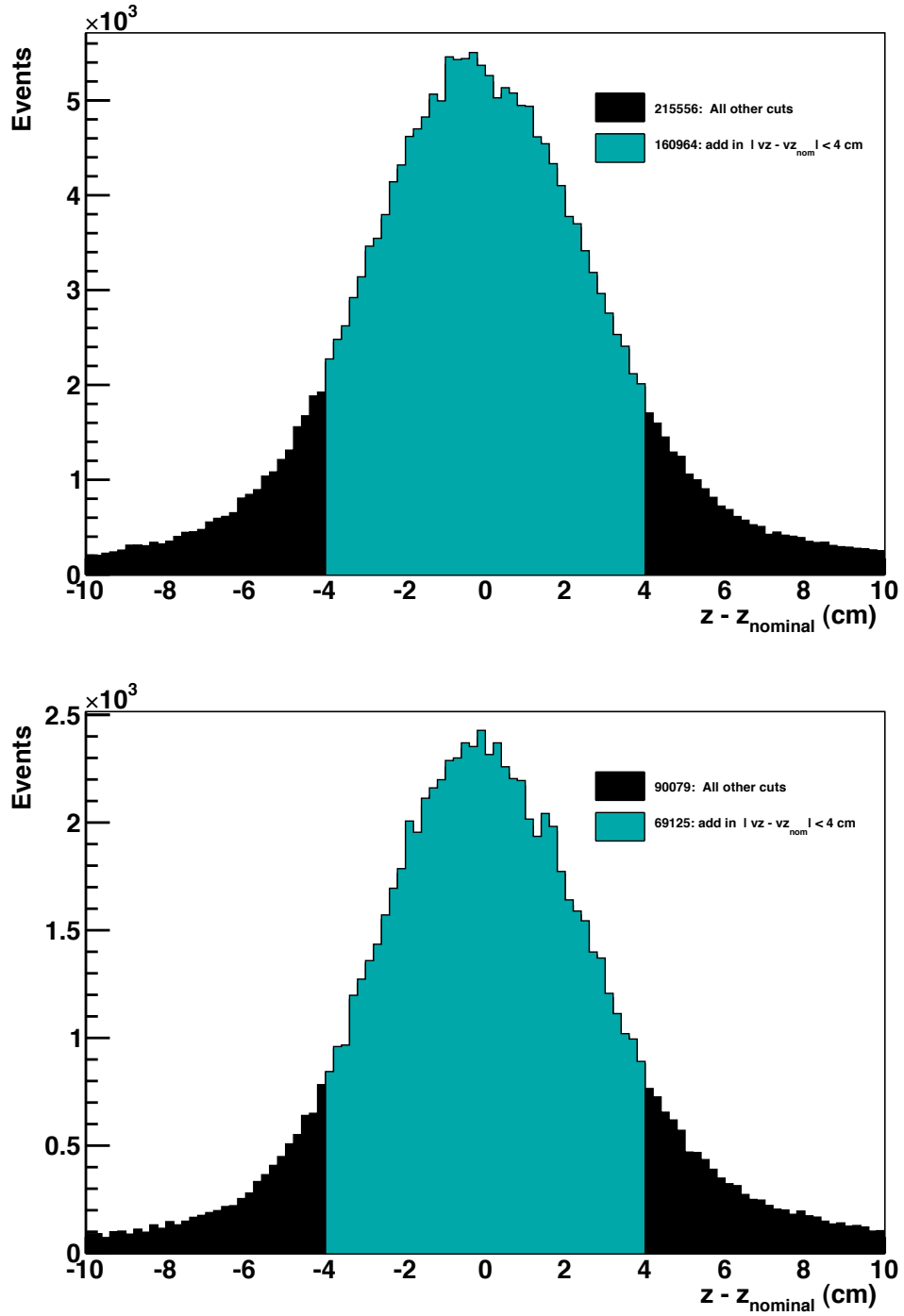


FIG. 4.11: Vertex  $z$  distributions for  $\pi^+$  (upper plot) and  $\pi^-$  (lower plot). The colored region is selected as a good pion candidate and the black region is removed prior to physics analysis. The vertex selection ensures the data are coming from the target region.

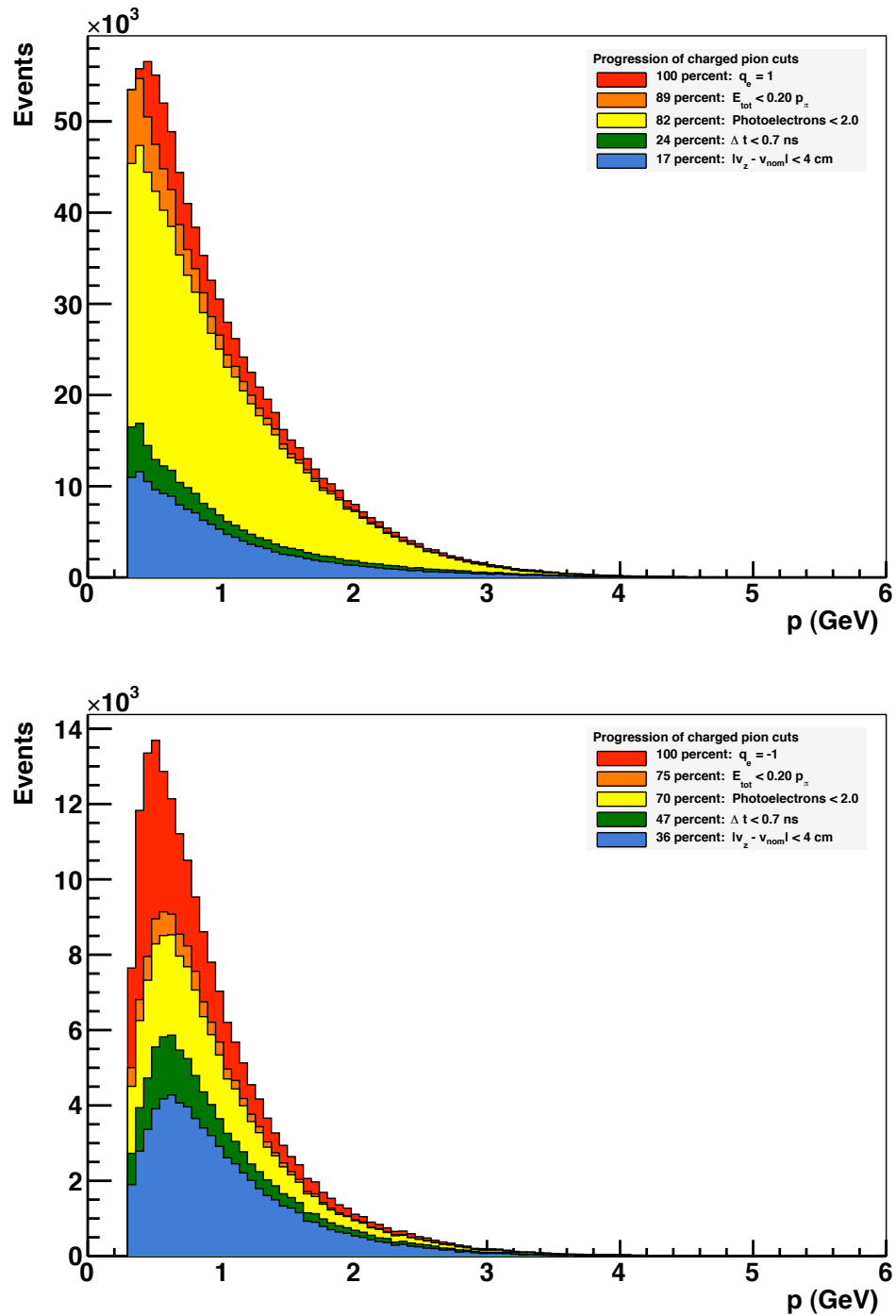


FIG. 4.12: Charged pion candidates as a function of their momentum. The effect of applying the selection criteria from Table 4.2 seen here for run 60100. The upper plot shows the progression of cuts for the positive pion and the lower plot is for the negative pion. The cut on timing removes the most number of positive pion candidates.

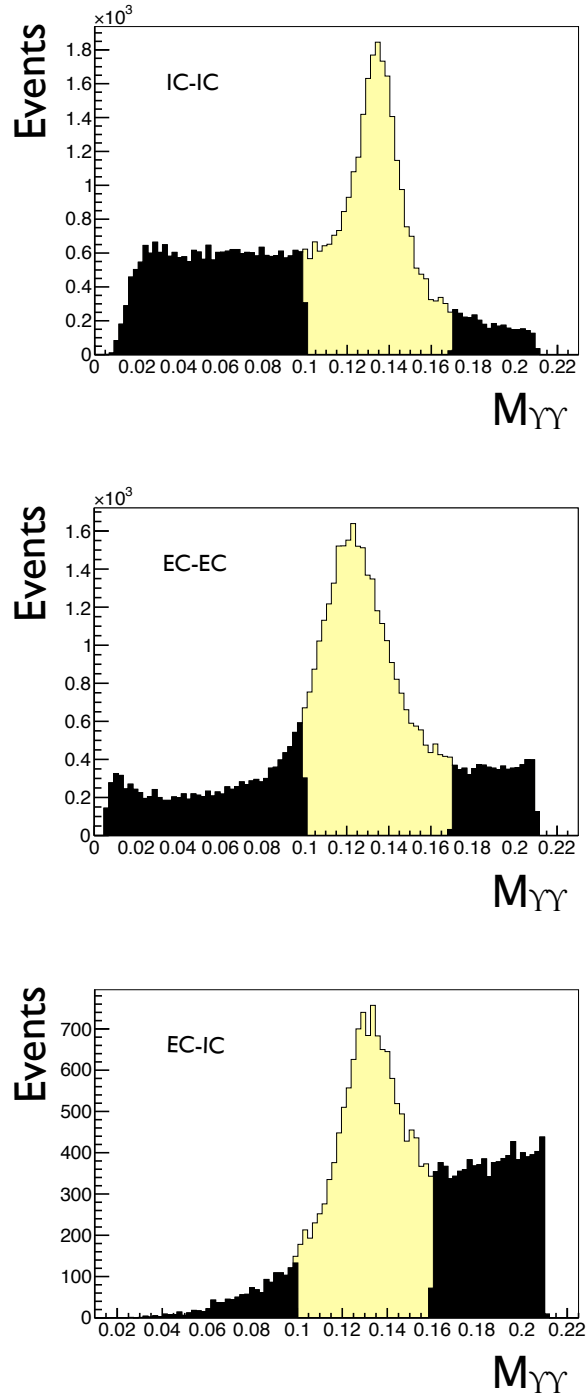


FIG. 4.13: Invariant two-photon mass distributions for three different photon topologies. The three possible topologies to calculate the invariant  $\pi^0$  mass are two  $\gamma$ s in the IC, two  $\gamma$ s in the EC and, one  $\gamma$  in the EC and one  $\gamma$  in the IC. The yellow region is selected as a good neutral pion candidate and the black region is eliminated from physics analysis.

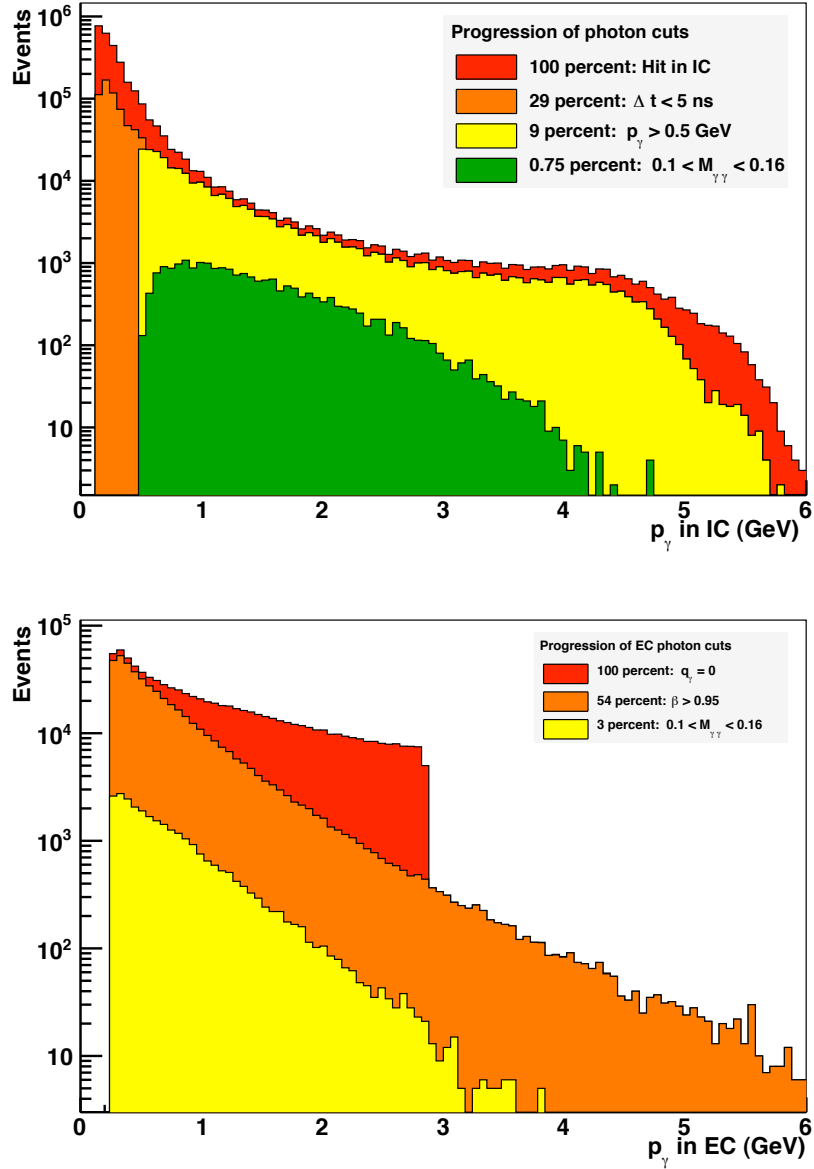


FIG. 4.14: Candidates for the neutral pion as a function of photon momentum. The progression of cuts to select a photon in the IC (top) and EC (bottom) seen for run 60100. Low momentum photons for each case are removed. A cut on  $\beta$  implemented for the neutral pion in the EC. This cut is designed to remove any signal from neutrons. The  $\Delta t$  cut in the IC is a cut on the time difference between the event start time and the photon hit in the IC. This is designed to remove signal uncorrelated with with event start time. The events are shown on a logarithmic scale.

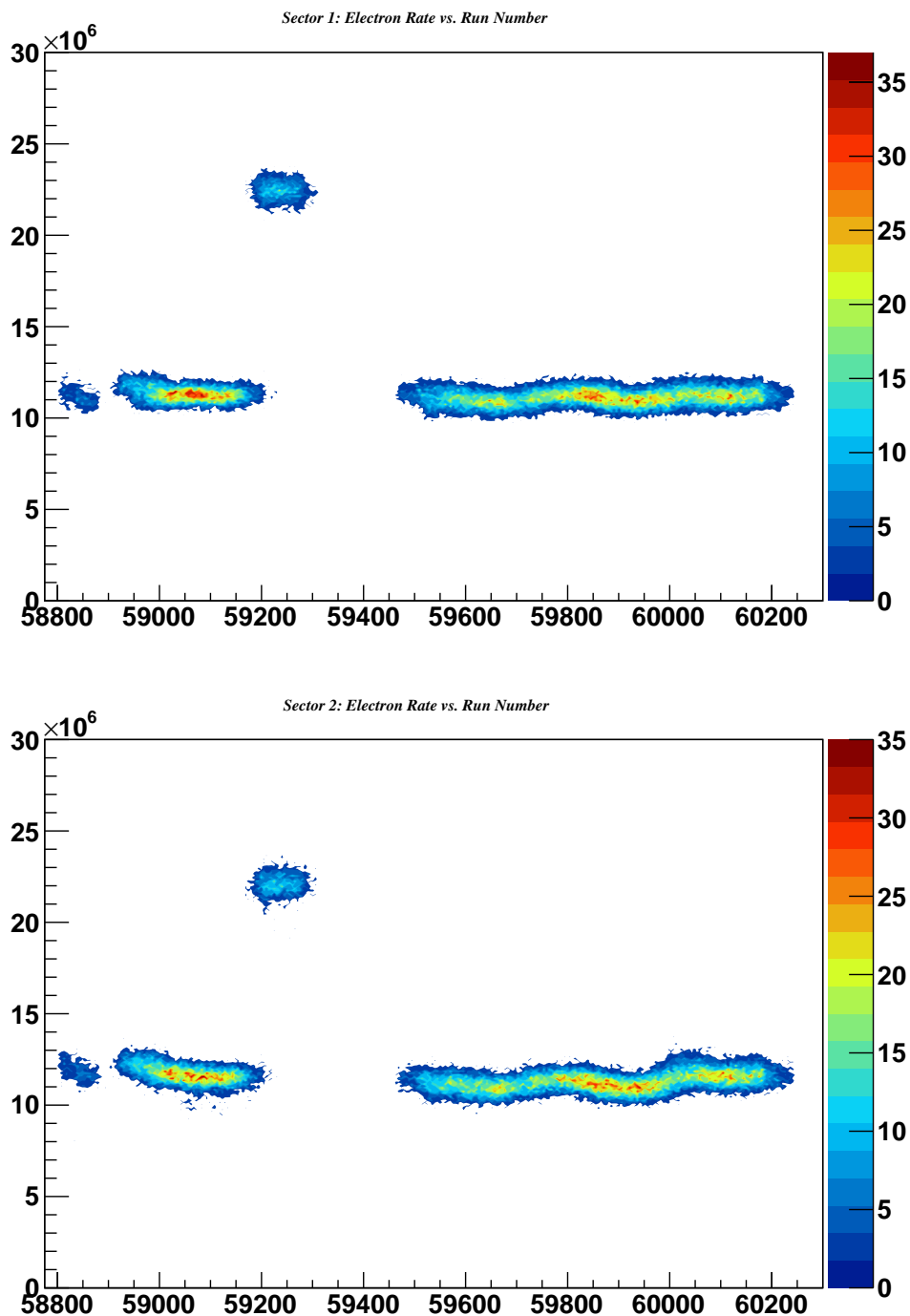


FIG. 4.15: Electron rate on the ammonia target as a function of run number for the data files used in the analysis for Sector 1 (top) and Sector 2 (bottom). Each run number has approximately eighty data files. Plotted in color is the distribution of rates in each of the files in the experiment. Data files with low rates in each sector are removed. The jump in the rate around Run 59150 comes from a change in the beam energy to 4.7 GeV and the slight jump around Run 60000 comes from reversing the polarity of the torus magnet current. The white space between Runs 59250 and 59400 is the accelerator summer down.

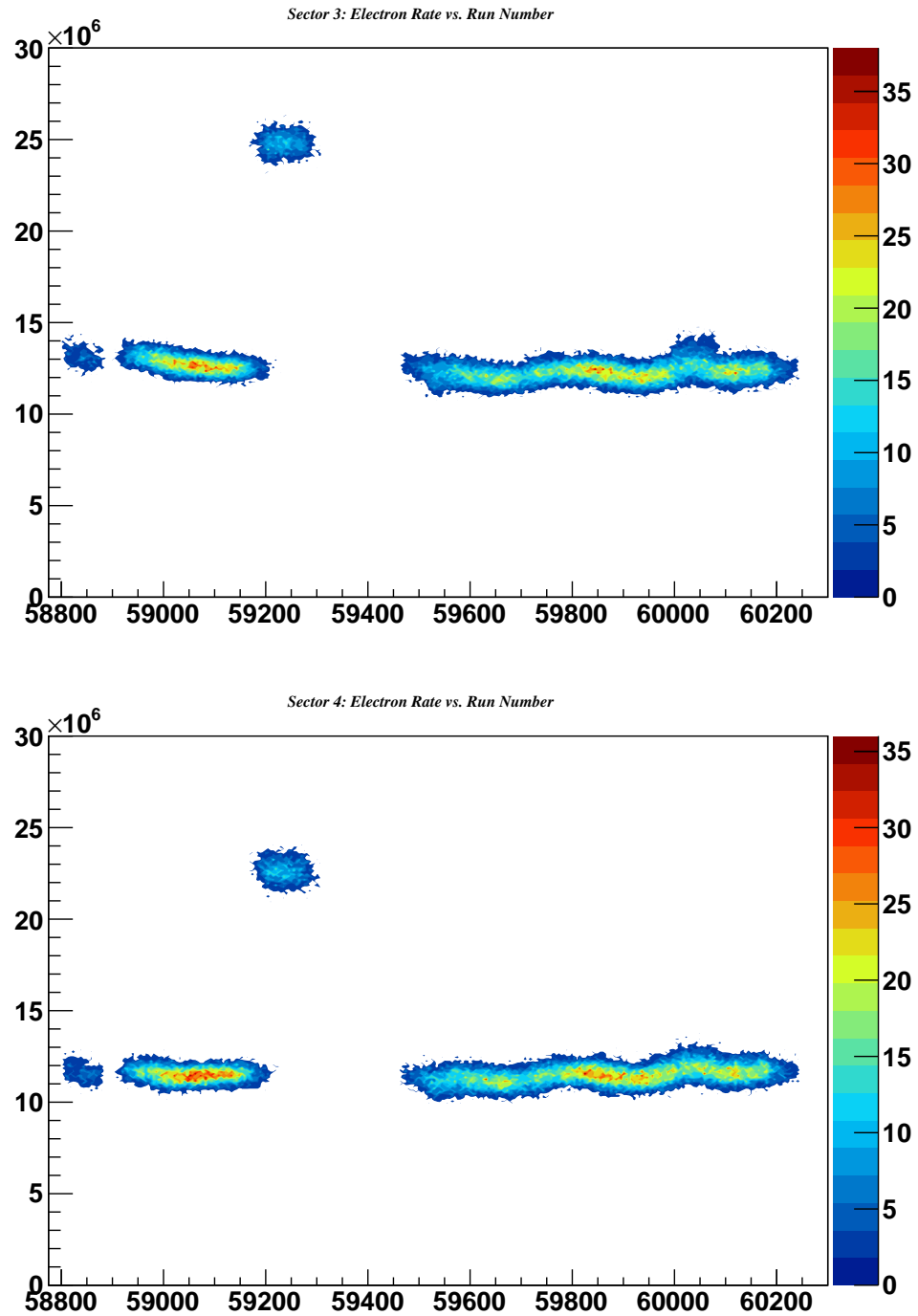


FIG. 4.16: Same as Figure 4.15 except showing Sector 3 (upper) and Sector 4 (lower).

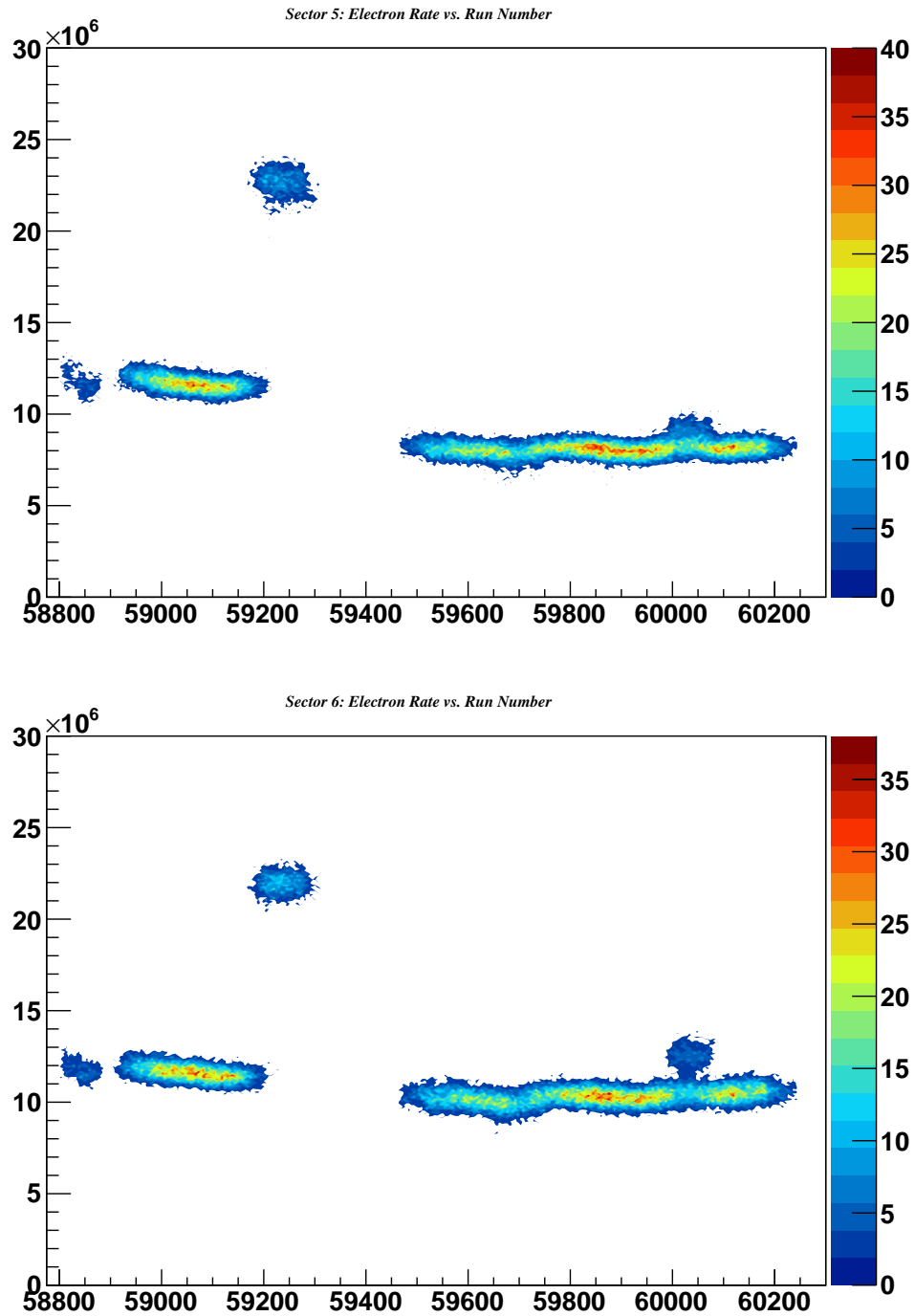


FIG. 4.17: Same as Figure 4.15 except showing Sector 5 (upper) and Sector 6 (lower).

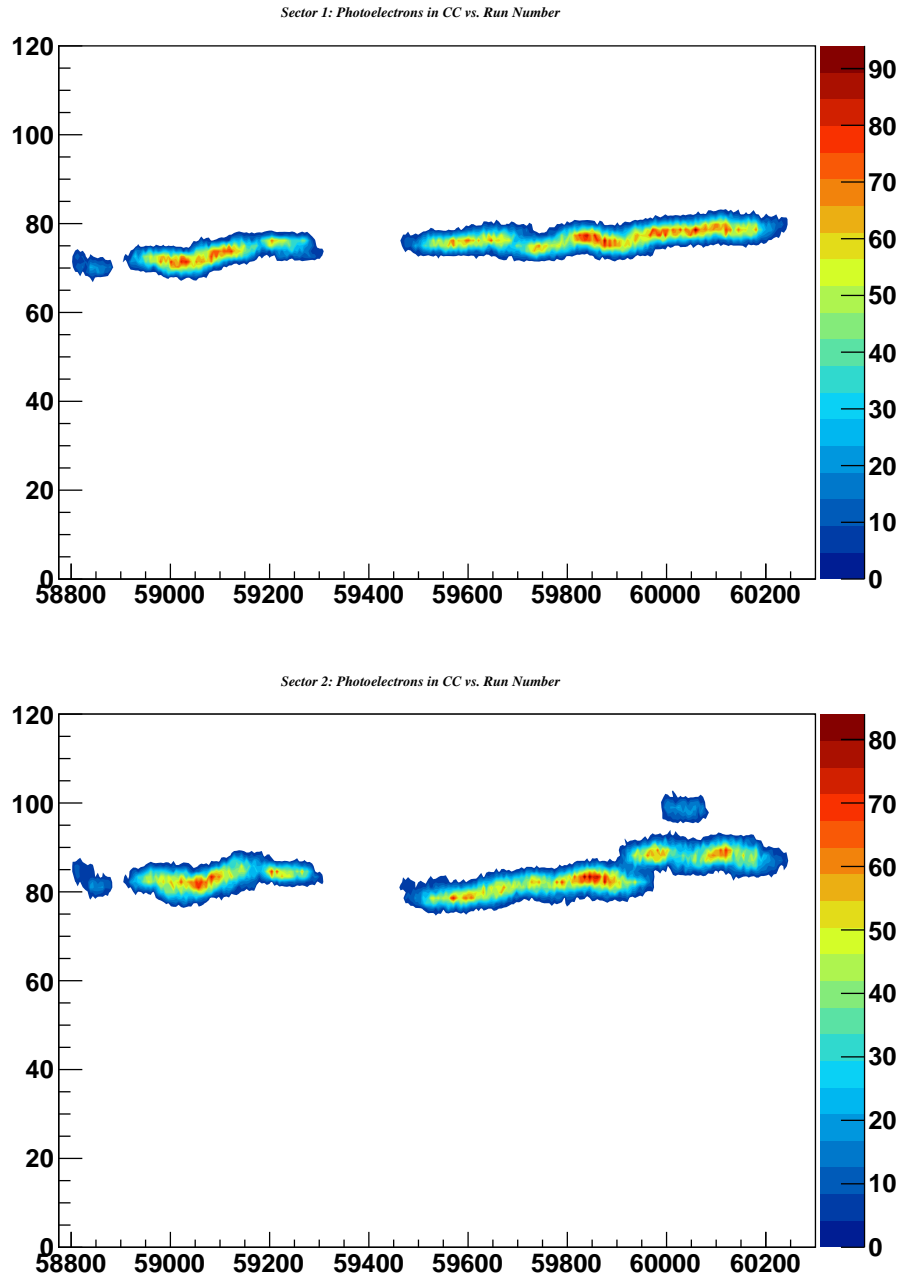


FIG. 4.18: Photoelectrons measured in the CC as a function of run number for the data files used in the analysis for Sector 1 (top) and Sector 2 (bottom). Each run number has approximately eighty data files. Data files with low rates in each sector are removed. The jump in the rate around Run 59150 comes from a change in the beam energy to 4.7 GeV and the slight jump around Run 60000 comes from reversing the polarity of the torus magnet current. The white space between Runs 59250 and 59400 is the accelerator summer down between parts A and B.

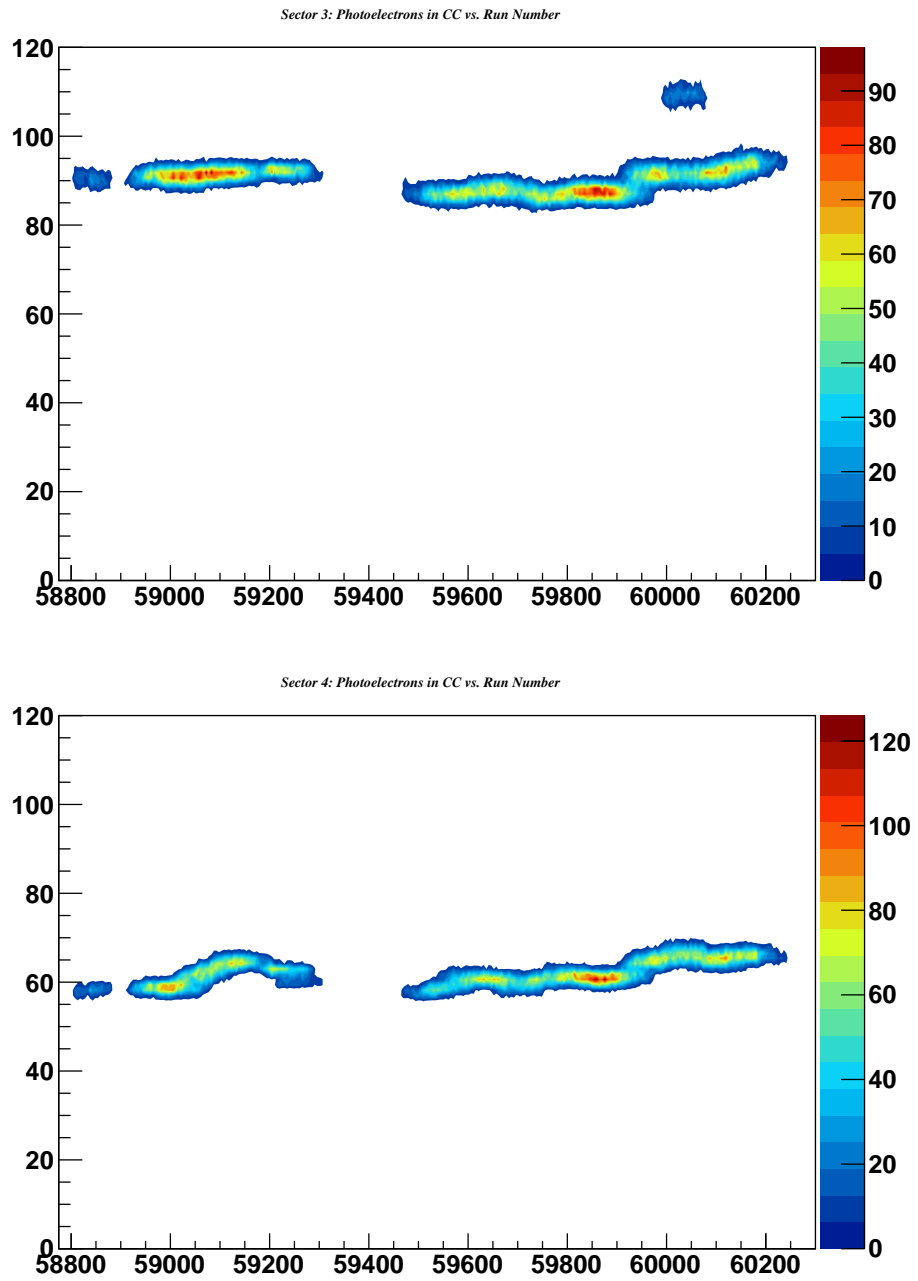


FIG. 4.19: Same as Figure 4.18 except showing Sector 3 (upper) and Sector 4 (lower).

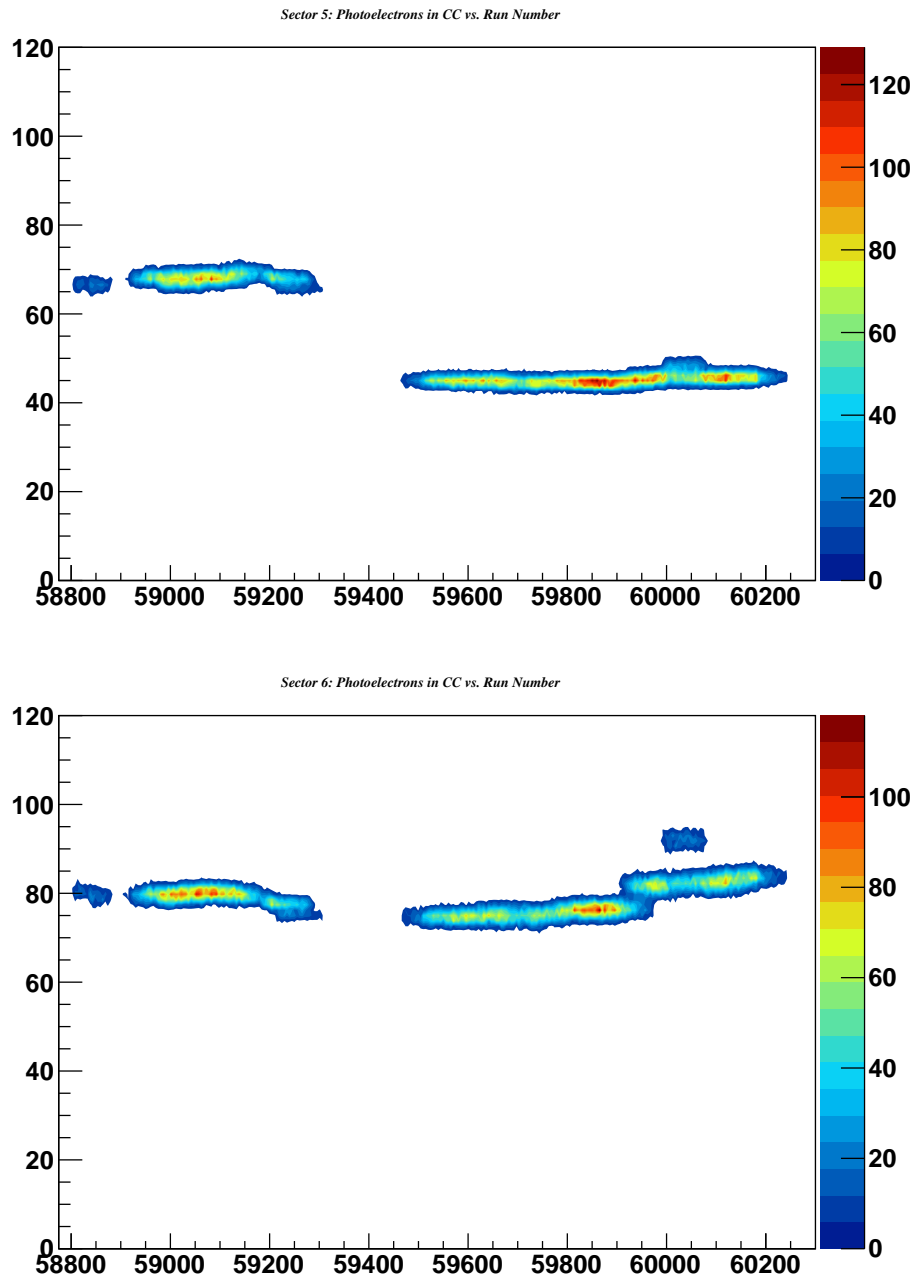


FIG. 4.20: Same as Figure 4.18 except showing Sector 5 (upper) and Sector 6 (lower).

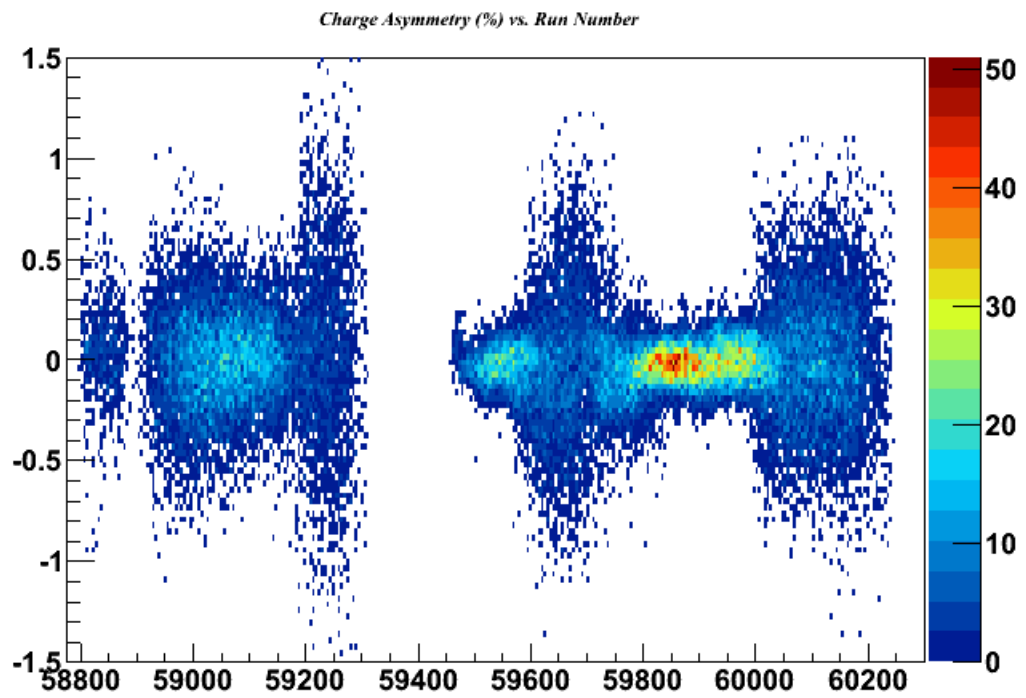


FIG. 4.21: The beam charge asymmetry as a function of run number. The color scale denotes the file number.

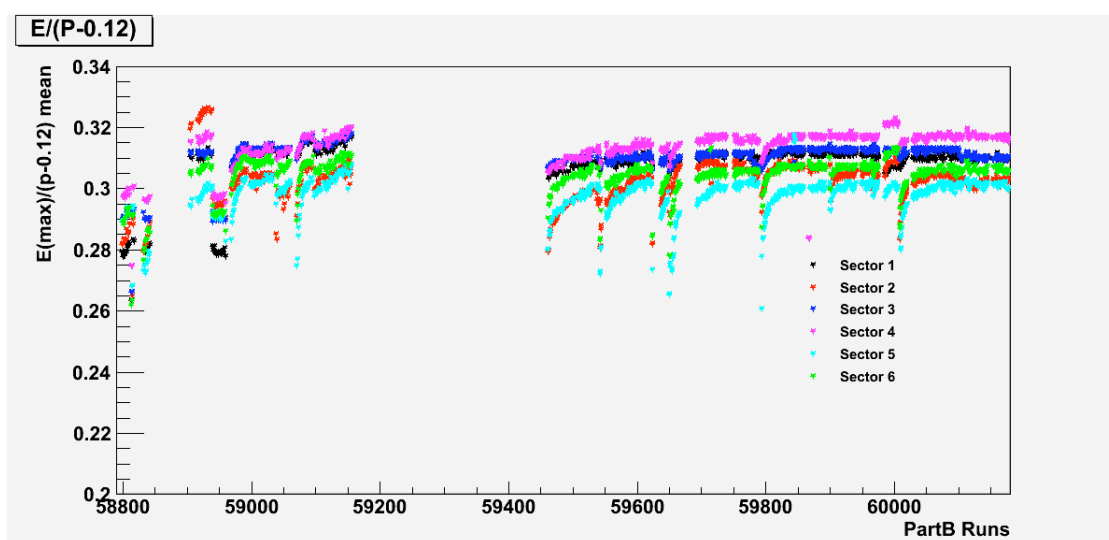


FIG. 4.22: Energy deposited in the EC scaled by a function of electron momentum as a function of run number. Each sector is mostly stable except for the drop about every 50 runs. This plot shows the version we got by fine tuning the EC gain calibration. We deemed this acceptable for the purposes of calculating asymmetries.

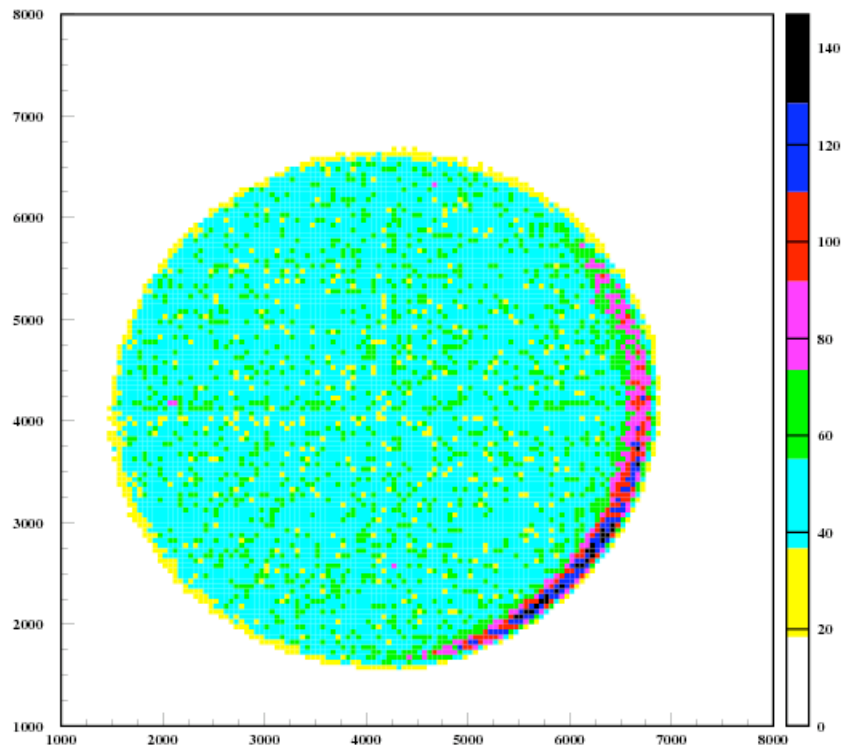


FIG. 4.23: Raster distribution for ADC  $y$  vs ADC  $x$ . The red crescent shows the beam hitting the Kapton cell on the top left corner. The bottom of the plot corresponds to the top of the target.

## 4.3 Corrections after Event Selection

### 4.3.1 Beam and target polarization

The beam ( $P_b$ ) and target ( $P_t$ ) polarization are measured during the course of the experiment using two separate systems<sup>1</sup>. The NMR system detailed in Section 3.3 measures  $P_t$ . The Møller polarimeter described in Section 3.2 measures  $P_b$ . Table 3.2 summarizes measurements over the course of the experiment.

Both the beam and target polarization measurements contain inherent systematic uncertainties. The Møller polarimeter measures the beam polarization for both helicities using elastic scattering on a polarized Permendur foil Ref. [1]. Differences in the polarization between the two helicities on the order of a 1-2% are consistent with previous CLAS experiments, however we had some differences as large as 9% as shown in Table 3.2. The NMR coils are a part of the target cell, hence the target polarization measurement is sensitive to the average of the material in the 1.5 cm diameter cup. The NMR measurements provide no information as to the how the polarization varies through the volume of the target.

Considering these issues, we conduct a separate study from the data to get the product of beam and target polarization. In this case,  $P_b P_t$  is extracted from exclusive elastic e-p scattering by comparing the experimental value of  $A_{\parallel}$  to the theoretical value Ref. [58].

$$A_{\parallel} = \frac{2\tau r \left[ \frac{m_p}{E} + r \left( \tau \frac{m_p}{E} + (1 + \tau) \tan^2(\theta/2) \right) \right]}{1 + \tau \frac{r^2}{\epsilon}}. \quad (4.16)$$

---

<sup>1</sup>The transverse component of the target polarization in the lepton frame is  $P_t$ . In several references cited in this work  $P_{h\perp}$  and  $P_t$  are used interchangeably, neither of which are the target polarization measured in the experiment.

Here  $\tau = \frac{Q^2}{4m_p^2}$ ,  $m_p$  is the proton mass,  $E$  is the beam energy,  $\theta$  is the electron scattering angle,  $\varepsilon = \frac{1}{1+2(1+\tau \tan^2(\theta/2))}$ , and  $r = \frac{G_M}{G_E}$ . The form factors are parametrized using world data Ref. [59]. The product of beam and target polarization is this given by,

$$P_b P_t = \frac{A_{\parallel}^{exp}}{A_{\parallel}}. \quad (4.17)$$

The procedure is repeated for each beam energy and for every relevant bin in  $Q^2$ . The

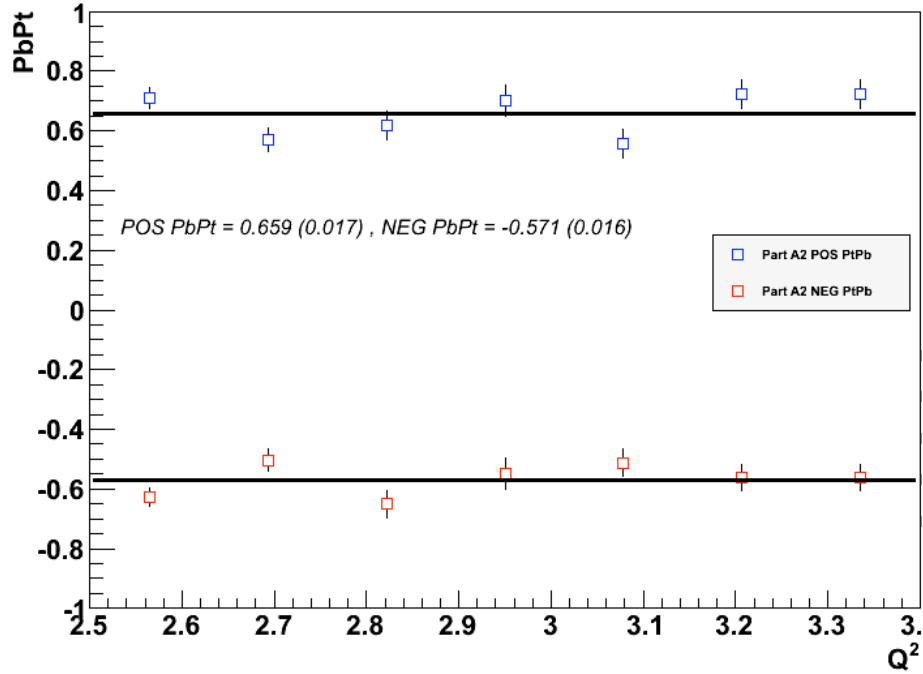


FIG. 4.24: Average  $P_b P_t$  deduced from e-p elastic scattering. The progression of polarization product as a function of  $Q^2$  (GeV)<sup>2</sup>. “Part A2” refers to the inbending data from part B of the experiment.

details of the procedure including event selection are detailed in Ref. [60]. The results are summarized in Table 4.5 which are used to scale the physics asymmetries. The results of  $P_b P_t$  for  $ep$  elastic scattering are very stable as a function of  $Q^2$  are shown in Figure 4.24. The analysis was done separately for runs with positive target polarization and for

negative target polarization.

$E_B$ (GeV)	$P_b P_t^+$	$P_b P_t^-$	$P_b^{ave}$ (%)	$P_t^+$	$P_t^-$
5.887	$0.63 \pm 0.03$	$-0.61 \pm 0.03$	$86.822 \pm 0.006$	$0.72 \pm 0.03$	$-0.69 \pm 0.03$
4.730	$0.64 \pm 0.02$	$-0.61 \pm 0.03$	$87.400 \pm 0.006$	$0.73 \pm 0.03$	$-0.70 \pm 0.04$
5.954	$0.65 \pm 0.02$	$-0.57 \pm 0.02$	$83.600 \pm 0.006$	$0.79 \pm 0.02$	$-0.68 \pm 0.02$

TABLE 4.5: Summary of  $P_b P_t$  extractions for the  $\text{NH}_3$  target using exclusive e-p scattering. The average beam polarization value is obtained from weighting the Møller measurements from Table 3.2 with e-p elastic events. The analysis was done separately for runs with positive target polarization and for negative target polarization.

### 4.3.2 Pair Symmetric Background

The SIDIS event sample contains a certain fraction in which the presumed scattered electron comes from another physics process, most likely neutral pion Dalitz decay Ref. [61]

$$\pi^0 \rightarrow e^- e^+ \gamma. \quad (4.18)$$

The misidentified electron events must be subtracted from our data. The Bethe-Heitler ( $ep \rightarrow e^- e^+ p$ ) process also creates an electron which is a candidate for a misidentified semi-inclusive electron Ref. [61]. The neutral pion decay ( $\pi^0 \rightarrow \gamma\gamma \rightarrow (e^- e^+)(e^- e^+)$ ) into two photons could also lead to an electron at the event vertex. In all the mentioned reactions a positron is produced in addition to the electron with the same kinematical distribution. This is used to estimate the misidentified semi-inclusive electrons in our data sample. Events for the reaction,

$$ep \rightarrow e^+ \pi X \quad (4.19)$$

are recorded using the same selection criteria for the positron as for the electron (except for the charge). We use the run range with opposite torus polarity for this study. To first order, the acceptance for the positrons and electrons is the same. The event rate for the positron should be a good estimate for the event rate of the misidentified electrons coming from reactions other than semi-inclusive scattering. A pair-symmetric dilution is calculated using the ratio of semi-inclusive positron to semi-inclusive electron rate.

$$f_{PS} = 1 - \frac{p(e, e'^+ \pi)X}{p(e, e'^- \pi)X} \quad (4.20)$$

The dilution is calculated in bins of  $x_B$ ,  $Q^2$ ,  $z$ ,  $P_{h\perp}$  and  $\phi_h$  for all three pions as described in Chapter 6 . The value of  $f_{PS}$  ranged between 0.989 to 1.000 with a statistical error on the order of one part in a 1000.

# CHAPTER 5

## Data Analysis II

### 5.1 Dilution Factor

The dilution factor  $f$  is defined as the fraction of semi-inclusive scattering events originating from polarizable nucleons. The target spin azimuthal asymmetries we measure are written as

$$A = \frac{A^{raw}}{f}. \quad (5.1)$$

The value of  $f$  depends on the reaction kinematics ( $Q^2, x_B, z, P_{h\perp}, \phi_h$ ). The polarized ammonia target is detailed in Section 3.3. Here Figure 5.1 shows a schematic representation of the target contents as viewed from a right angle to the beam line. The components of the target shown in the schematic are the elements of the target within the vertex cut imposed for event selection. The nominal values for the target center are listed in Table 5.1. The dilution factor for the ammonia target is,

$$f = \frac{n_{proton}}{n_{NH_3} + n_{He} + n_K + n_{Al}} \quad (5.2)$$

where  $n$  denotes the SIDIS event rate and the subscript indicates the target material ( $He$  = Helium,  $NH_3$  = Ammonia,  $Al$  = Aluminum,  $K$  = Kapton).

Run Range	Target center nominal (cm)	Target center corrected (cm)
58799 - 59250	58.3	58.95
59400 - 60250	68.2	67.97

TABLE 5.1: Nominal and corrected values for center of the  $NH_3$  target in CLAS coordinates. The raster correction study is described in 4.1.1.

The event rate for each material  $i$  is proportional to the product of the areal density  $\rho$  and semi-inclusive DIS cross section  $\sigma$ , i.e.

$$n_i \propto \rho_i \sigma_i. \quad (5.3)$$

Applying Equation 5.3 to 5.2, we get

$$f = \frac{\rho_{proton} \sigma_{proton}}{\rho_{NH_3} \sigma_{NH_3} + \rho_{He} \sigma_{He} + \rho_K \sigma_K + \rho_{Al} \sigma_{Al}} \quad (5.4)$$

where the constant of proportionality in Eqn 5.3 is directly dependent on the acceptance. Since all these materials are in the same target configuration, we can safely assume that the constant of proportionality is the same for both numerator and denominator. We split up the problem of determining the dilution factor into two parts. One involves accurately measuring the areal densities of the materials in the ammonia target. The other involves determining the semi-inclusive DIS cross sections for each pion flavor.

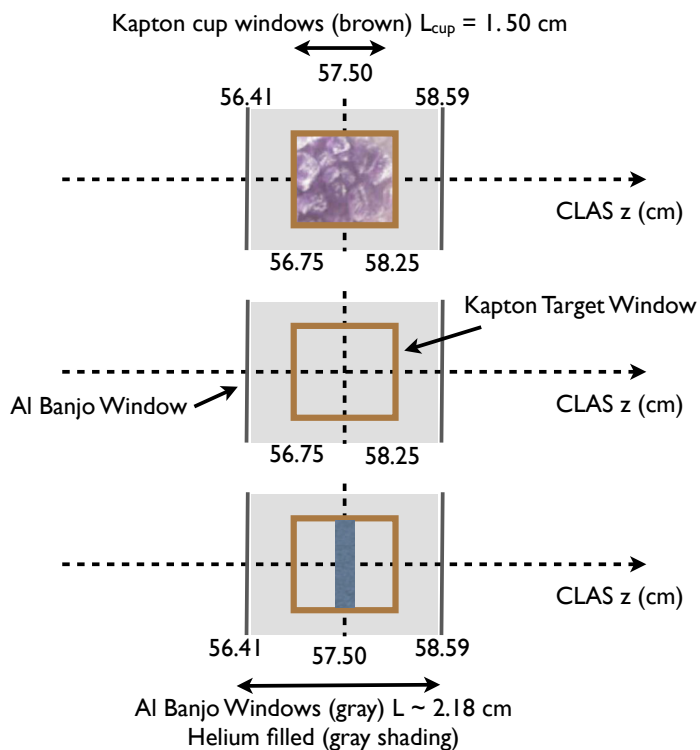


FIG. 5.1: Schematic side view of the target material in CLAS. Shown here are ammonia, empty and carbon (top to bottom) targets used in 58799 - 59250 with a central nominal value of  $z_{nom} = 58.3$  cm. The beam passes through the grey Aluminum windows, liquid Helium in the target and a Kapton target cell window before interacting with actual polarized target material.

### 5.1.1 Areal Densities

The areal density for each material in Equation 5.4 is shown in Table 5.2. The two unknowns in the table are the “length” of the helium and the length of the actual ammonia target. Ammonia is in the form of crushed beads which makes it a challenge to measure its effective length. Electron scattering data were taken with the carbon and empty targets both with and without helium in the target cell. A combination of these data were used to determine the unknown lengths.

Material	Volume Density (g/cm <sup>3</sup> )	Length (cm)
Helium	0.145	$L_{He}$
Carbon	2.193	0.398
Aluminum	2.700	0.0166
Kapton	1.430	0.0066
Ammonia	0.866	$L_{NH_3}$

TABLE 5.2: Summary of volume densities and lengths of materials in the target.

### Determining the Length of Helium

If we know the length of the target between the two aluminum banjo windows,  $L_{banjo}$  then we can infer the length of the helium for each target. The aluminum banjo windows are shown in Figure 5.1 using gray lines. A photograph showing part of the banjo is shown in Figure 3.9.

The nominal value of this length at room temperature is  $L_{banjo} = 2.18$  cm . The target assembly itself is cooled to a temperature below 4 K which clearly can change  $L_{banjo}$ . We deduce  $L_{banjo}$  using a combination of inclusive scattering data from the carbon target and the same carbon target with the helium drained out. The primary reason for using inclusive scattering is the ready availability of models that provide inclusive cross sections using world data. The inclusive electron rate for the carbon target configuration is written as a combination of the areal density times the cross section for each material that the electron encounters. Hence,  $\sigma$  for this section denotes the inclusive cross section. The count rate for the carbon target can be written as,

$$n_C \propto \rho_{Al}\sigma_{Al} + \rho_{He}\sigma_{He} + \rho_K\sigma_K + \rho_C\sigma_C \quad (5.5)$$

or

$$n_C \propto \rho_{Al}^V L_{Al}\sigma_{Al} + \rho_{He}^V L_{He}\sigma_{He} + \rho_K^V L_{Kapton}\sigma_K + \rho_C^V L_C\sigma_C, \quad (5.6)$$

where the subscripts indicate the material in the target and  $\rho^V$  is the volume density such that  $\rho = \rho^V L$ . A similar expression is written for data taken for the carbon target configuration with helium drained out.

$$n_C^{noHe} \propto \rho_{Al} \sigma_{Al} + \rho_K \sigma_K + \rho_C \sigma_C \quad (5.7)$$

$$n_C^{noHe} \propto \rho_{Al}^V L_{Al} \sigma_{Al} + \rho_K^V L_{Kapton} \sigma_K + \rho_C^V L_C \sigma_C$$

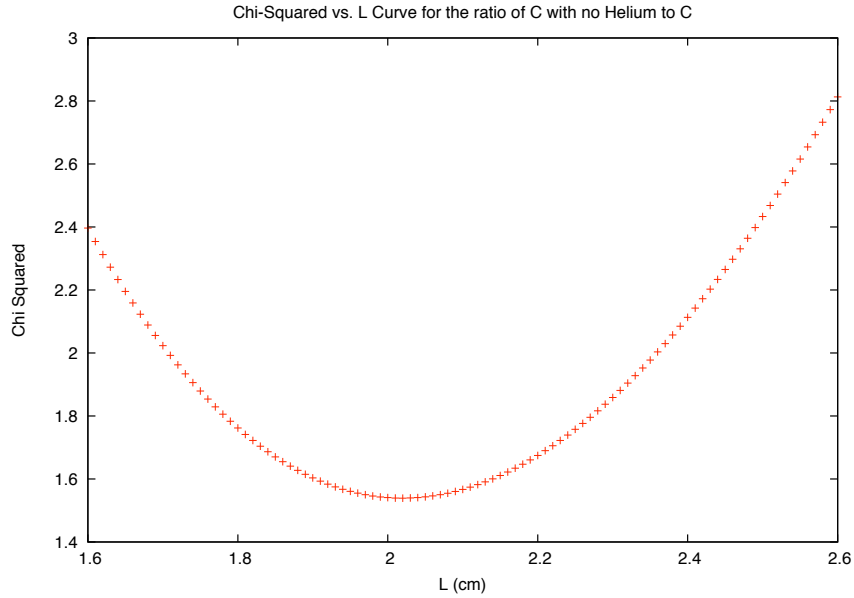


FIG. 5.2: The calculated  $\chi^2$  for multiple values of  $L_{test}$  used to deduce  $L_{banjo}$  by comparing rate ratios to inclusive models Ref. [20] Ref. [21]. The minimum  $\chi^2$  in this case gives the length between the banjo windows to be  $L_{banjo} = 2.01 \pm 0.01$  cm. This value is smaller in than the room temperature value which suggests that the Aluminum windows bow inward.

For the carbon target,  $L_{He} = L_{banjo} - L_{Al} - L_K - L_C$ . The rate ratio

$$r_{data} = n_C^{noHe} / n_C \quad (5.8)$$

from data was determined using a reasonable test value of  $L_{test} = 2.18$  cm. This ratio was compared to the rate ratio

$$r_{model} = n_C^{noHe} / n_C \quad (5.9)$$

predicted by the model for inclusive nucleon cross sections using the same nominal value of  $L_{test}$  Ref. [20] Ref. [21]. The inclusive cross sections for the different nuclei were obtained using the code and table from Ref. [62]. The value of  $L_{test}$  was then varied over a reasonable range to obtain the best  $\chi^2$  value defined as,

$$\chi^2 = \frac{1}{N-1} \sum_i^N \left( \frac{r_{data}^i - r_{model}^i}{\Delta r^i} \right)^2 \quad (5.10)$$

where  $N$  is the number of kinematic bins used and  $\Delta r^i$  is the error on  $r_{data}^i$  for each kinematic bin  $i$ . The model prediction in the same kinematic bin is  $r_{model}^i$ . The effect on  $\chi^2$  for varying values of  $L_{test}$  is seen in Figure 5.2.

Figure 5.3 shows the results for  $L_{banjo}$  for several different combinations of runs over the course of the experiment. The outliers in the study were for the combination of the empty target run compared with the empty target with no helium, run. Ideally this should give the best measurement because we have the least material in the beam line, but its most different from the measured value of 2.18 cm. The best match came from the combination of carbon compared to carbon with no helium runs. The average over the range of runs for parts A and B was  $L_{banjo} = 2.17$  cm with a standard deviation of  $\sigma_L = 0.24$ . A summary of the results is listed in Table 5.3.

We concluded that it was more reliable to use the data from an empty run with no helium and t the two peaks for the Aluminum windows. The difference between the two peaks would give us  $L_{banjo}$ . The procedure described above was then used as a

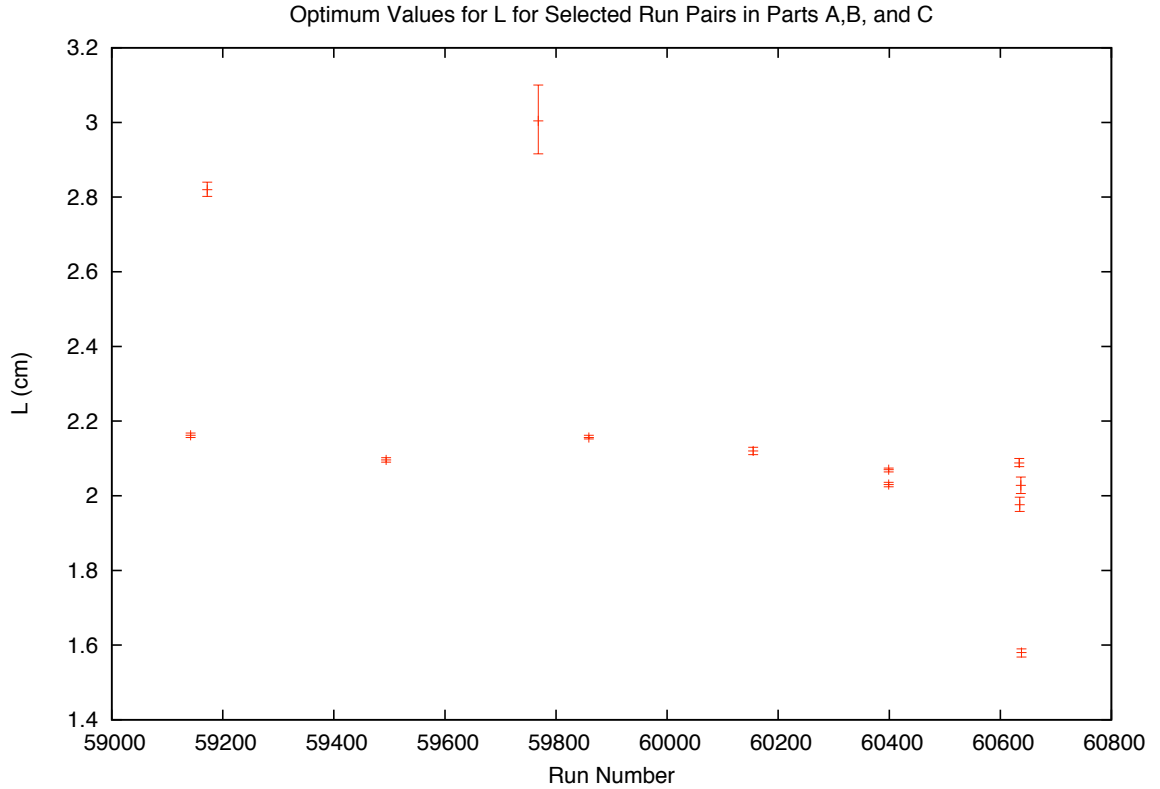


FIG. 5.3: Determinations of  $L_{banjo}$  by  $\chi^2$  minimization for several combinations of runs over the course of the experiment. The extreme outliers in the experiment come from using the combination of an empty target run in combination with an empty target run with no helium.

consistency check for  $L_{banjo}$ . From Figure 5.4 the length was deduced to be  $L_{banjo} = 2.1 \pm 0.1$  cm. This value was then used to determine the length of the helium for the ammonia target configuration.

### Determining the Length of Ammonia

A procedure similar to the one described in the previous section was used to determine the effective length of the ammonia target ( $L_{NH_3}$ ). Rate ratios for inclusive scattering are formed using a combination of one carbon and one ammonia run. The value of  $L_{banjo} = 2.1 \pm 0.1$  cm obtained from the previous discussion was assumed here, and a

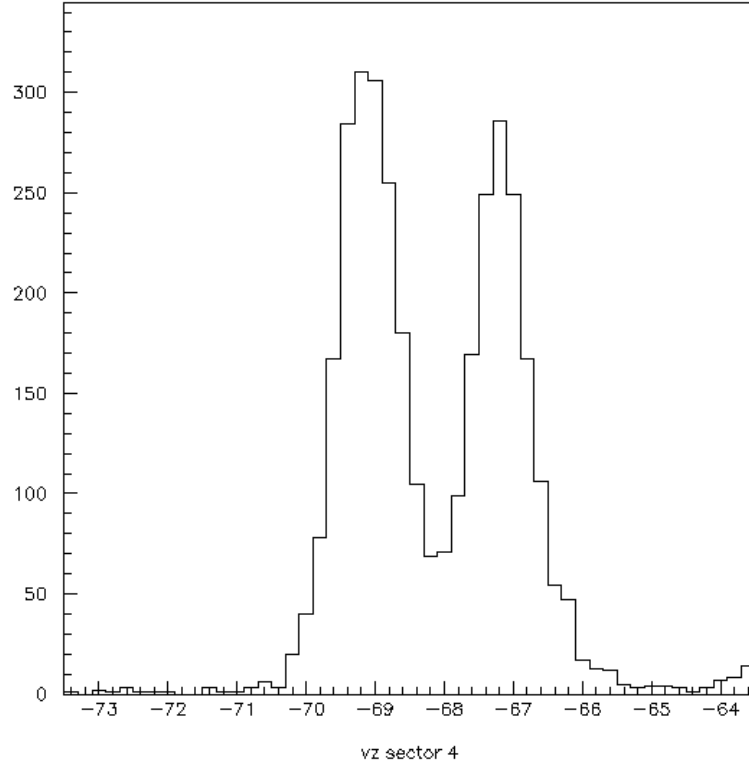


FIG. 5.4: Distribution of vertex  $z$  for Run 60023 for electrons with momentum greater than 2 GeV for the empty target. The two peaks correspond to the banjo windows with a nominal separation of 2.18 cm.

nominal value of  $L_{NH_3}^{test} = 0.9$  cm was used in rate ratio of the carbon and ammonia targets.

The inclusive rate for the carbon target is

$$n_C \propto \rho_{Al}\sigma_{Al}(L_{\bar{C}}) + \rho_{He}\sigma_{He}(L_{\bar{C}}) + \rho_K\sigma_K(L_{\bar{C}}) + \rho_C\sigma_C(L_{\bar{C}}) \quad (5.11)$$

where  $L_{\bar{C}} = L_C + L_{Al} + L_K + L_{He}$  is the total radiation length of all material in the carbon target setting. The inclusive rate for the ammonia target is,

$$n_A \propto \rho_{Al}\sigma_{Al}(L_A) + \rho_{He}\sigma_{He}(L_A) + \rho_K\sigma_K(L_A) + \frac{3}{17}\rho_A\sigma_H(L_A) + \frac{14}{17}\rho_A\sigma_N(L_A). \quad (5.12)$$

	Run Range	Target Cup	$L_{banjo}$ (cm)	$L_{NH_3}$ (cm)	$L_{NH_3}$ Error (cm)
Part A	(58799 - 59300)	Top	$2.17 \pm 0.24$	0.853	$\pm 0.0024$
Part A	(58799 - 59300)	Bottom	$2.17 \pm 0.24$	0.851	$\pm 0.0014$
Part B	(59300 - 60185)	Top	$2.17 \pm 0.24$	0.860	$\pm 0.001$
Part B	(59300 - 60185)	Bottom	$2.17 \pm 0.24$	0.910	$\pm 0.001$

TABLE 5.3: Average banjo lengths,  $L_{banjo}$  and target lengths  $L_{NH_3}$  for parts A and B of the experiment. Values are calculated separately for top and bottom ammonia targets.

where  $L_A = L_{NH_3} + L_{Al} + L_K + L_{He}$  is the total radiation length of all material in the ammonia target setting. For each case the constant of proportionality is directly dependent on the acceptance and cancels in the ratio. The  $\sigma$  in this case denotes the inclusive cross section which is modeled from world data and its radiated value is dependent on the radiation lengths of the material  $L_{\bar{C}}$  and  $L_A$ . The length of the helium in each case is determined as  $L_{He} = L_{banjo} - L_{everything\ else}$ .

We calculate the inclusive rate ratio,

$$r_{data} = n_A/n_{\bar{C}} \quad (5.13)$$

using  $L_{NH_3}^{test} = 0.98$  cm and compare it to  $r_{model}$  using the inclusive cross sections obtained from Ref. [62]. We then vary the value of  $L_{NH_3}^{test}$  to get a minimum  $\chi^2$  value for the comparison. Figure 5.5 shows the optimal values for  $L_{NH_3}$  over the proton run period. The  $\chi^2$  values for each run pair are listed in Ref. [63]. A summary of the error-weighted average values for  $L_{NH_3}$  are seen in Table 5.3.

### 5.1.2 SIDIS nucleon cross sections

Now that we can calculate the areal densities, we need to find a way to estimate the SIDIS cross sections for different materials in Equation 5.4. To address this we construct

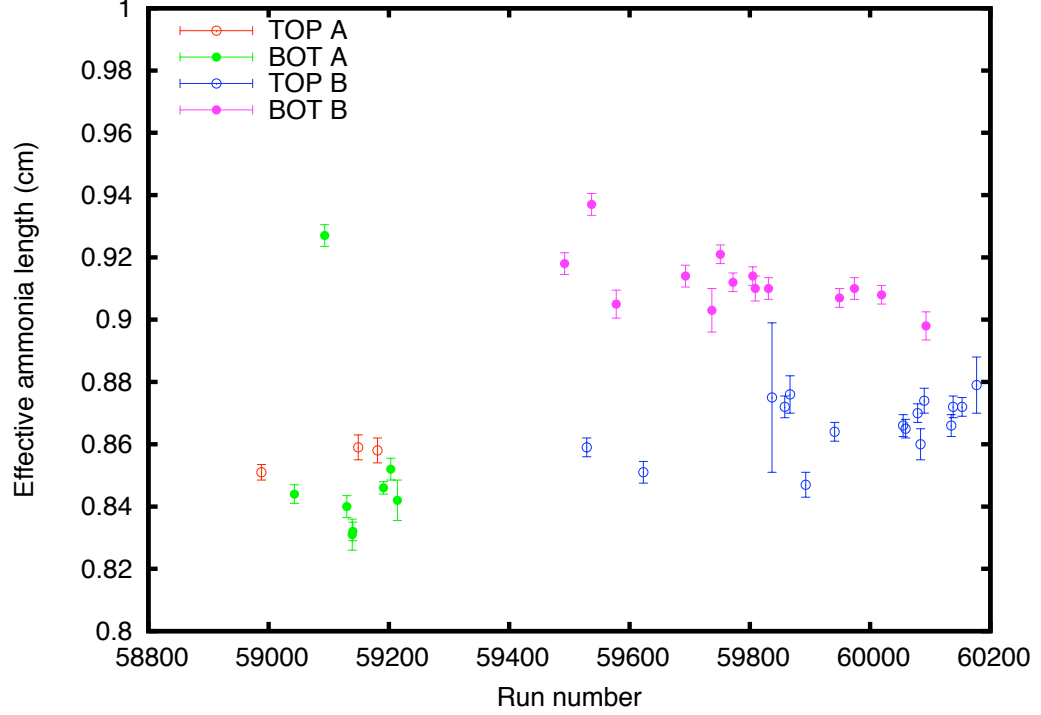


FIG. 5.5: The extracted ammonia length for each target (TOP and BOT) for the Run range 58800 - 59300 (A) and 59400 - 60200 (B).

an ad-hoc model and use our data to constrain its four fit parameters. The symbol  $\sigma$  in this section refers to cross sections in semi-inclusive DIS.

We started with a simple leading order pQCD model to calculate cross section ratios Ref. [64]. The initial assumption is that SIDIS with a pion in the final state can be described as the sum over quark flavors of the product of the quark distribution function  $q(x, Q^2)$  and either a favored or unfavored fragmentation function ( $D^+(z, p_T)$  and  $D^-(z, p_T)$ ). The ratio of fragmentation functions is written as  $r_f = D^-/D^+$ . The semi-

inclusive cross section  $ep \rightarrow e\pi^+X$  is written as

$$\sigma_p^{\pi^+} \propto (4u + d_s) + (4u_s + d)r_f. \quad (5.14)$$

The superscripts on the  $\sigma$  correspond to pion flavor, and  $u = u_v + u_s$  and  $d = d_v + d_s$  are quark distributions. The subscript  $v$  refers to the valence quarks in the nucleon and  $s$  refers to the anti-quark distribution in the proton. No contributions from the strange quark are included in this discussion. We extend this to write a full set of cross sections for all three pion flavor for scattering from a proton or neutron,

$$\begin{aligned} \sigma_p^{\pi^-} &\propto (4u + d_s)r_f + (4u_s + d) \\ \sigma_p^{\pi^0} &\propto (4u + d_s)(1 + r_f) + (4u_s + d)(1 + r_f) \\ \sigma_n^{\pi^+} &\propto (4d + u_s) + (4d_s + u)r_f \\ \sigma_n^{\pi^-} &\propto (4d + u_s)r_f + (4d_s + u) \\ \sigma_n^{\pi^0} &\propto (4d + u_s)(1 + r_f) + (4d_s + u)(1 + r_f) \end{aligned} \quad (5.15)$$

The parton distribution functions from GRV 98 Ref. [65] are used to get  $u$ ,  $d$ ,  $u_s$  and  $d_s$  over our kinematic range of  $x_B$  and  $Q^2$ . We approximate the fragmentation function ratio by  $1/(1+z)^2$  Ref. [66]. This gives us the expressions for scattering from a proton and neutron. Using these, we build the cross sections for each of our target materials. For example, Aluminum has 13 protons and 14 neutrons, we write the cross section as,

$$\sigma_{Al}^{\pi^+} = \frac{13\sigma_p^{\pi^+} + 14\sigma_n^{\pi^+}}{27} \quad (5.16)$$

Following this principle, we write similar expressions for the different materials for each

pion flavor:

$$\begin{aligned}
 \sigma_{He,C,N}^{\pi^+} &= \frac{\sigma_p^{\pi^+} + \sigma_n^{\pi^+}}{2} \\
 \sigma_{He,C,N}^{\pi^-} &= \frac{\sigma_p^{\pi^-} + \sigma_n^{\pi^-}}{2} \\
 \sigma_{Al}^{\pi^-} &= \frac{13\sigma_p^{\pi^-} + 14\sigma_n^{\pi^-}}{27}
 \end{aligned} \tag{5.17}$$

We account for nuclear effects in the different materials by introducing an attenuation factor ( $A_T$ ) depending on  $z$  and  $v = Q^2/2Mx_B$  Ref. [66]. Each attenuation factor is scaled to carbon assuming

$$\begin{aligned}
 A_T^{He}(Q^2, x_B, z) &= \frac{a}{v_F} \sqrt{4/12} \\
 A_T^C(Q^2, x_B, z) &= \frac{a}{v_F} \sqrt{12/12} \\
 A_T^N(Q^2, x_B, z) &= \frac{a}{v_F} \sqrt{14/12} \\
 A_T^{Al}(Q^2, x_B, z) &= \frac{a}{v_F} \sqrt{27/12}.
 \end{aligned} \tag{5.18}$$

The scaling for the attenuation factor,  $a$  is the same for each material and is the first fit parameter that is constrained using data. The denominator,  $v_F$  contains the  $z$  and  $v$  dependence and is given by,

$$v_F = \left[ \frac{v}{2.5} \right]^{v_p} (1 + (z - 0.55)) \tag{5.19}$$

in which  $v_p$  is taken as a fit parameter. The HERMES Collaboration produced fits to the ratio of fragmentation functions as a function of  $z$ . The dependence of  $v_F$  on  $z$  is based

on their fits Ref. [23]. The  $P_{h\perp}$  dependence is added into the attenuation by,

$$\begin{aligned}
A_T^{He}(Q^2, x_B, z, P_{h\perp}) &= 1 + A_T^{He}(Q^2, x, z) \left\{ \left[ \frac{P_{h\perp}}{p_T^{zshift}} \right]^{p_{Tp}} - 1 \right\} \\
A_T^C(Q^2, x_B, z, P_{h\perp}) &= 1 + A_T^C(Q^2, x, z) \left\{ \left[ \frac{P_{h\perp}}{p_T^{zshift}} \right]^{p_{Tp}} - 1 \right\} \\
A_T^N(Q^2, x_B, z, P_{h\perp}) &= 1 + A_T^N(Q^2, x, z) \left\{ \left[ \frac{P_{h\perp}}{p_T^{zshift}} \right]^{p_{Tp}} - 1 \right\} \\
A_T^{Al}(Q^2, x_B, z, P_{h\perp}) &= 1 + A_T^{Al}(Q^2, x, z) \left\{ \left[ \frac{P_{h\perp}}{p_T^{zshift}} \right]^{p_{Tp}} - 1 \right\}
\end{aligned} \tag{5.20}$$

where  $p_T^{zshift} = p_{Tz} + \frac{1}{2}(z - 0.4)$ . The function of the  $z$ ,  $P_{h\perp}$ , and  $v$  dependence here was based on the detailed hadron attenuation studies shown in Ref. [67]. The final two fit parameters used to constrain the model are  $p_{Tp}$  and  $p_{Tz}$ .

Combining the attenuation and individual cross section terms, we get

$$\begin{aligned}
\sigma_{He}^{\pi^+} &= \frac{\sigma_p^{\pi^+} + \sigma_n^{\pi^+}}{2} A_T^{He}(Q^2, x_B, z, P_{h\perp}) \\
\sigma_C^{\pi^+} &= \frac{\sigma_p^{\pi^+} + \sigma_n^{\pi^+}}{2} A_T^C(Q^2, x_B, z, P_{h\perp}) \\
\sigma_N^{\pi^+} &= \frac{\sigma_p^{\pi^+} + \sigma_n^{\pi^+}}{2} A_T^N(Q^2, x_B, z, P_{h\perp}) \\
\sigma_{Al}^{\pi^+} &= \frac{13\sigma_p^{\pi^+} + 14\sigma_n^{\pi^+}}{27} A_T^{Al}(Q^2, x_B, z, P_{h\perp})
\end{aligned} \tag{5.21}$$

Similar expressions can be written for the other pion flavors. There is no explicit  $\phi_h$  dependence in the model. Semi-inclusive rate ratios of ammonia to carbon

$$\frac{n_{NH_3}^{SIDIS}}{n_C^{SIDIS}} \tag{5.22}$$

are used to get fit parameters. The best fit parameters are then used to calculate the semi-inclusive DIS cross sections which in turn are substituted in Equation 5.4 to get the dilution factor.

### Testing the Model

To get an accurate determination of dilution, the data for carbon and ammonia were divided based on run period, beam energy and torus polarity. The run ranges used are (58799 - 59161) referred to as part A, and (59400 - 60200) referred to as part B, for in-bending torus polarity. Figure 5.6 shows the regions of the run used for this analysis. Sector 5 was removed for this study due to the leaking CC system as was the data with lower beam energy and negative torus polarity. Strict fiducial cuts on the IC were implemented for particles detected in CLAS. The stability of both carbon and ammonia is critical and is shown in Figure 5.6.

The ratio of semi-inclusive rates for each pion are calculated and the model is used to fit these ratios. The results of these are seen in Figure 5.7, Figure 5.8 and Figure 5.9 for the positive, negative and neutral pion respectively. The plots are constructed for the finest binning in  $(Q^2, x_B, z, P_{h\perp})$  seen on the horizontal axis. Each data point on this axis corresponds to a different kinematic bin. The black line shows the model fit with the lowest  $\chi^2$ . The second plot on each figure shows the resultant dilution factor. In order to display all points in 4 variables on the same graph; we loop over each bin in  $x_B$ ,  $Q^2$ ,  $z$  and  $P_{h\perp}$  in turn. The outer loop to display the data points in  $x_B$  which then includes variation for  $(Q^2, z, P_{h\perp})$  bins. The jump for each plot denotes a change in the range of  $x_B$ . For example, for the case of the positive pion the  $x_B$  bin change is seen at points 135 and 200. This is followed by divisions in  $Q^2$  which includes variation for  $(z, P_{h\perp})$ . Finally, the three

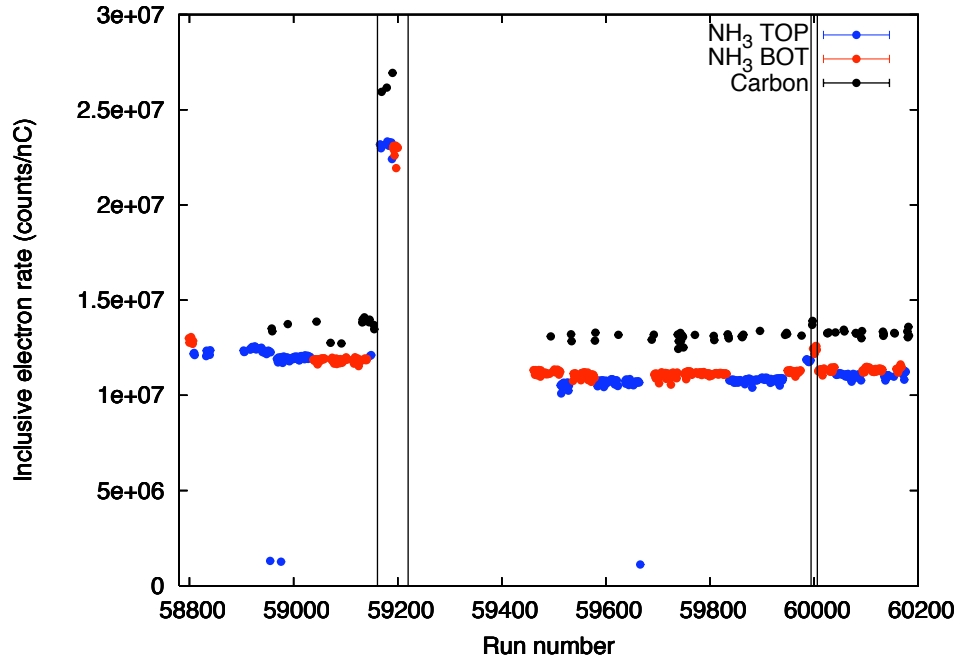


FIG. 5.6: Inclusive event rate as a function of run number for the NH<sub>3</sub> TOP (blue), NH<sub>3</sub> TOP (red) and carbon target (black). The horizontal lines indicate a change in run configuration. Around Run 59160 is a change in beam energy and around Run 59995 is a change in torus polarity.

divisions in  $z$  have variations in the value of  $P_{h\perp}$ .

Overall, the trend is for the dilution to rise with momentum fraction and fall with momentum transfer.

The  $\chi^2/dof$  values for each pion flavor are listed in Table ???. The  $P_{h\perp}$ ,  $z$  and  $Q^2$  dependence of the resultant dilution factor integrated over all other kinematics are shown in Figure 5.10, Figure 5.11 and Figure 5.12 respectively. More details of this study are found in Ref. [68]. We concluded that the results of the model are stable for the kinematic range that we explored.

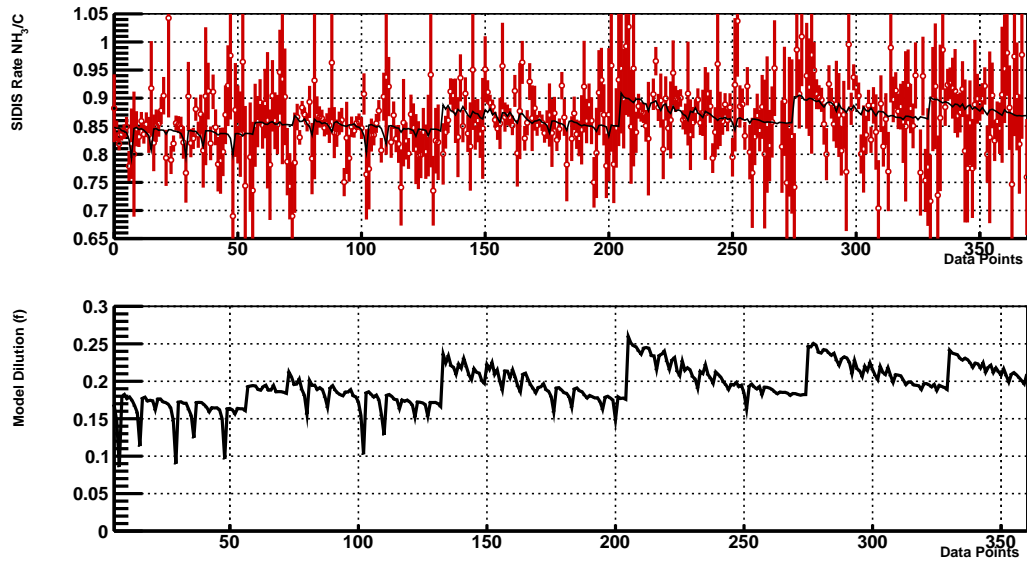


FIG. 5.7: SIDIS rate ratio of ammonia to carbon for the positive pion (top) and the corresponding model prediction for dilution (bottom). The run range in this case is 59400 - 60200 and each data point on the horizontal axis corresponds to one kinematic bin in  $(Q^2, x_B, z, P_{h\perp})$ .

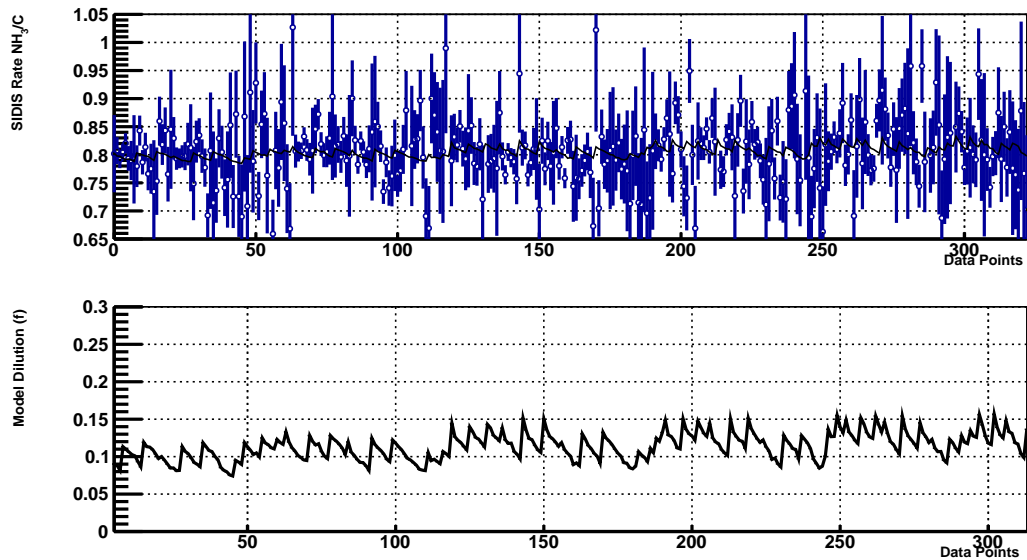


FIG. 5.8: Same as Figure 5.7 for the negative pion.

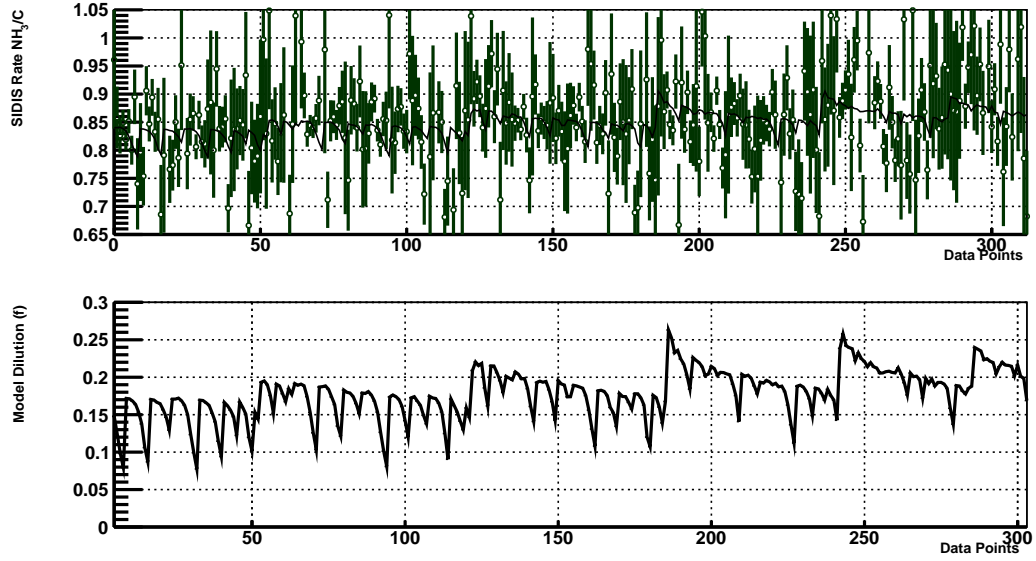


FIG. 5.9: Same as Figure 5.7 for the neutral pion.

Run Period	Pion Flavor	$\chi^2/dof$
A	$\pi^+$	1.12
A	$\pi^-$	1.80
A	$\pi^0$	1.35
B	$\pi^+$	1.07
B	$\pi^-$	1.02
B	$\pi^0$	1.19

TABLE 5.4: The  $\chi^2/dof$  values for fitting the semi-inclusive rate ratio of ammonia to carbon using the ad-hoc SIDIS model. The data were divided by eg1dvcs run periods A (58800 - 59161) and B (59400 - 60200).

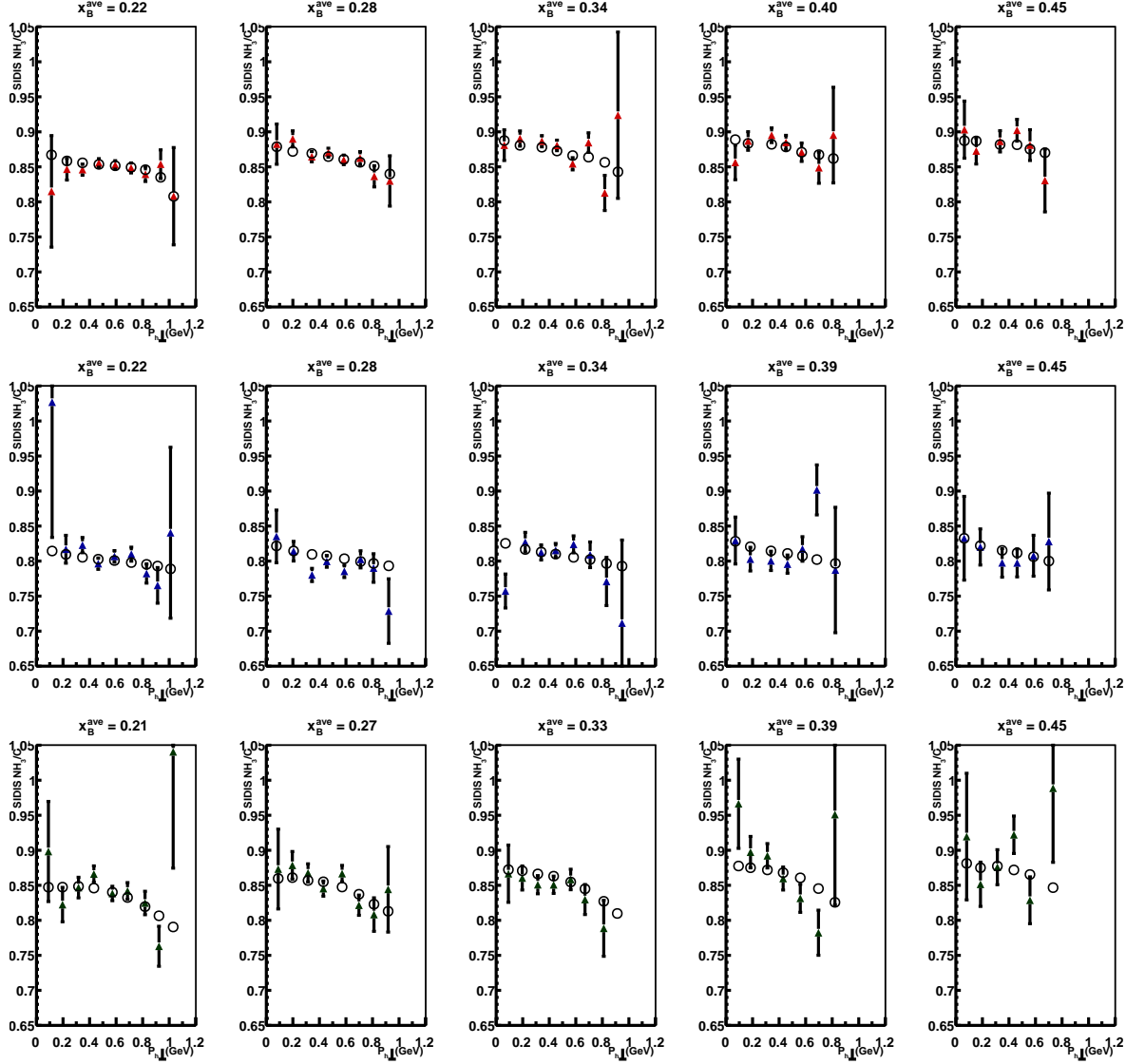


FIG. 5.10: The dependence of ratio of  $(\text{NH}_3/\text{C})$  on  $P_{h\perp}$  in different  $x_B$  bins for positive (top row), negative (middle row) and neutral (bottom row) pions. The data are integrated over all other kinematics and are shown here for Runs 59400 - 60250. The open circles show the SIDIS model result.

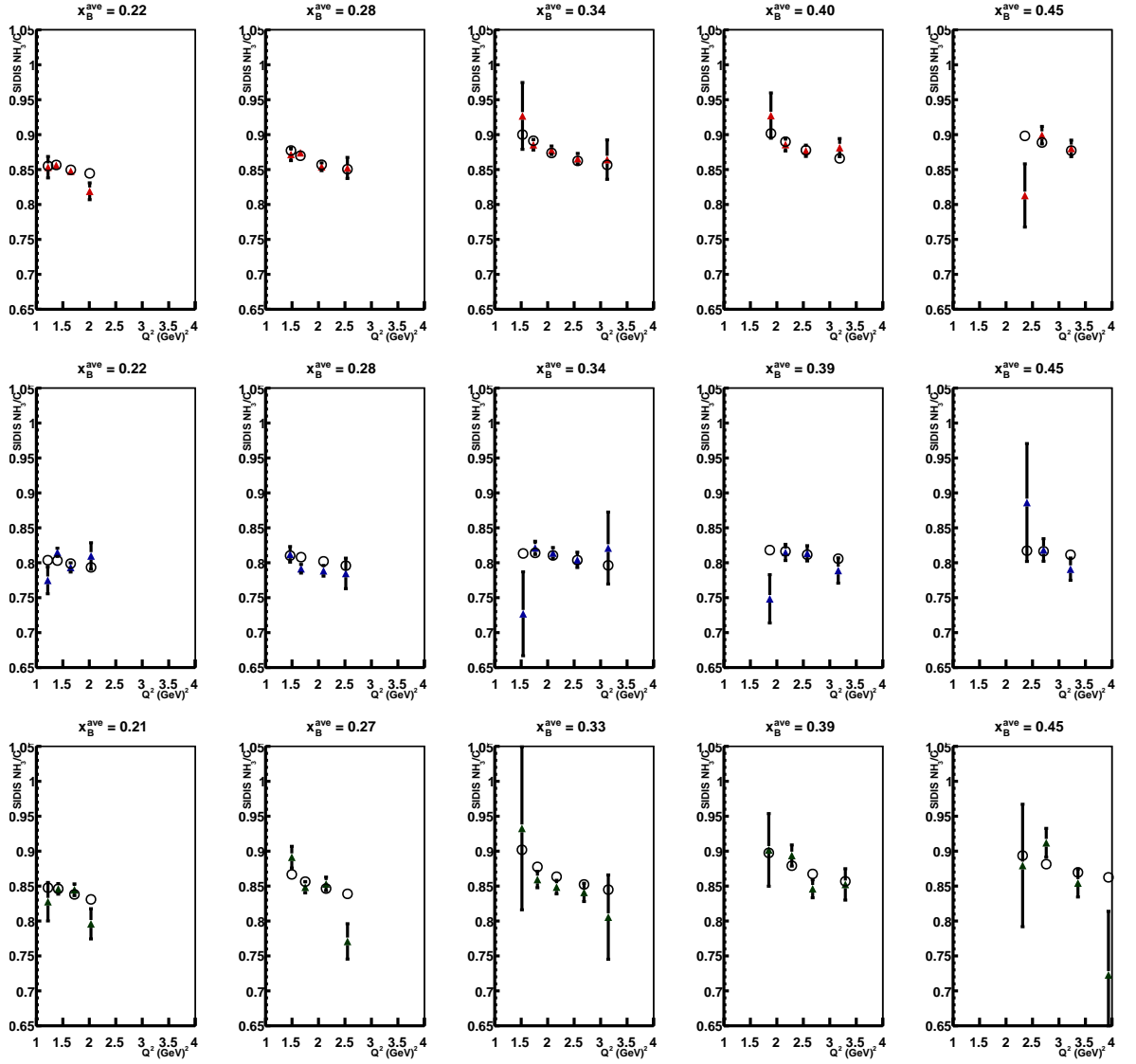
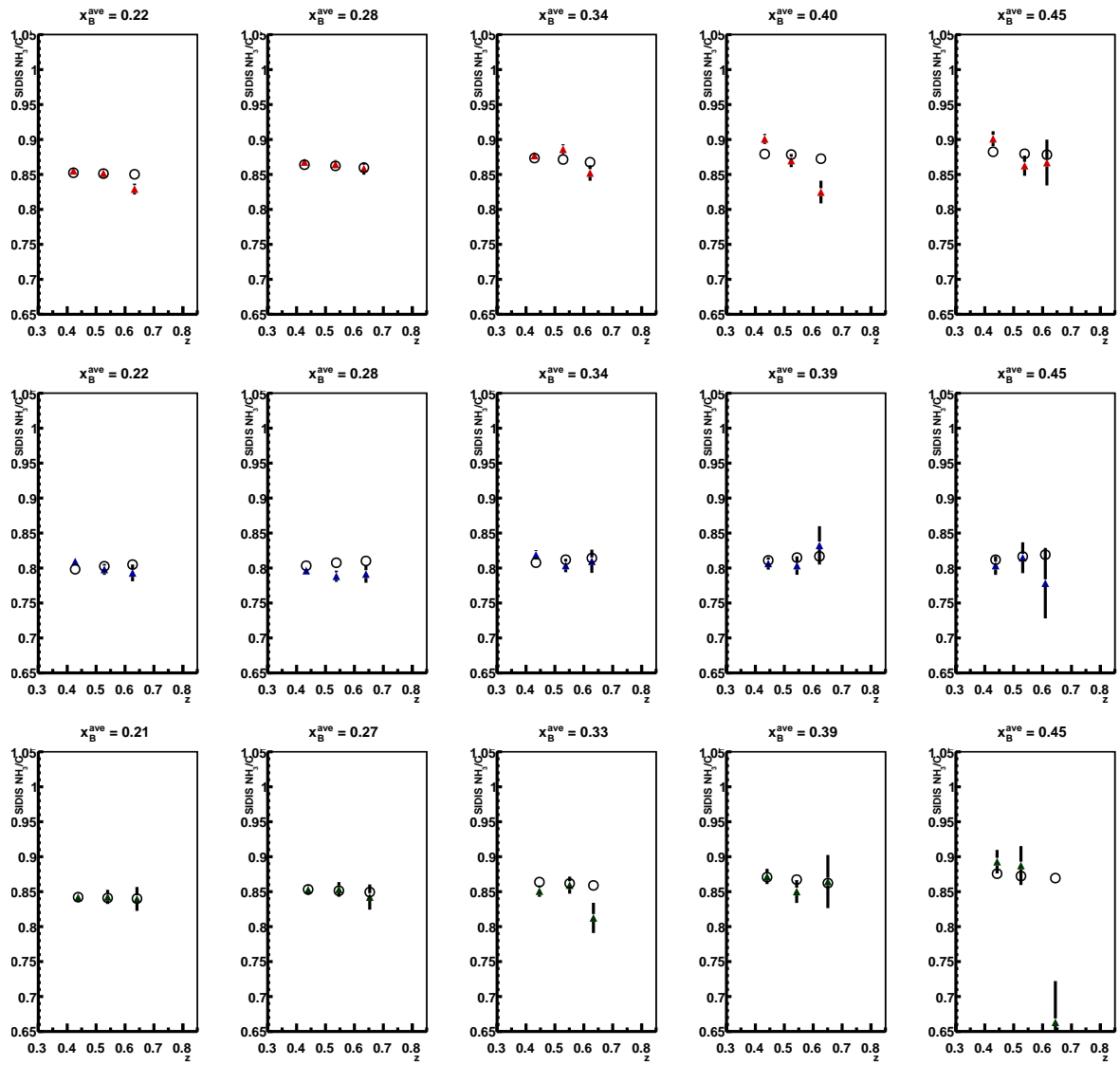


FIG. 5.11: Same as Figure 5.10 except as a function of  $Q^2$ .

FIG. 5.12: Same as Figure 5.10 except as a function of  $z$ .

## 5.2 Systematic Errors

The raw experimental asymmetries have several corrections applied to them, each with an associated uncertainty which is not included in the statistical error bar of the measurement. We account for these systematic errors by calculating the asymmetry by changing each correction in turn by its uncertainty, keeping all others corrections at their standard value. Since the corrections and their errors are uncorrelated, we add individual changes in the asymmetry in quadrature to give the final systematic error. The main sources of these errors are listed below.

1. Beam Polarization ( $P_b$ ): The beam polarization is measured by the Möller polarimeter as described in Section 4.3. The average statistical uncertainty for the measurements is 2.08%. The systematic relative uncertainty from the polarimeter has a maximum value of 3% Ref. [1]. This is converted to absolute uncertainty based on each beam energy option and added in quadrature with the statistical uncertainty. The total absolute error for each beam energy is shown in Table 5.5.
2. Beam and Target Polarization ( $P_b P_t$ ): As described in Section 4.3, the product of beam and target polarization is extracted using data from elastic scattering. The statistical error on  $P_b P_t$  for each beam energy is considered a systematic effect because it affects all asymmetries systematically. The error for each beam energy is shown in Table 5.5.
3. Dilution Factor ( $f$ ): The major source of systematic error in determining the dilution factor is the SIDIS model. The target model parameters are varied by one standard deviation and the effects on the dilution are calculated. The error on the dilution factor

varies with kinematics ( $Q^2, x_B, z, P_{h\perp}$ ) and for each pion case is calculated using

$$f_{\text{syserror}} = \begin{pmatrix} \frac{\partial f}{\partial p_1} & \frac{\partial f}{\partial p_2} & \frac{\partial f}{\partial p_3} & \frac{\partial f}{\partial p_4} \end{pmatrix} \begin{pmatrix} \sigma_{11}^2 & \sigma_{12}^2 & \sigma_{13}^2 & \sigma_{14}^2 \\ \sigma_{21}^2 & \sigma_{22}^2 & \sigma_{23}^2 & \sigma_{24}^2 \\ \sigma_{31}^2 & \sigma_{32}^2 & \sigma_{33}^2 & \sigma_{34}^2 \\ \sigma_{41}^2 & \sigma_{42}^2 & \sigma_{43}^2 & \sigma_{44}^2 \end{pmatrix} \begin{pmatrix} \frac{\partial f}{\partial p_1} \\ \frac{\partial f}{\partial p_2} \\ \frac{\partial f}{\partial p_3} \\ \frac{\partial f}{\partial p_4} \end{pmatrix}. \quad (5.23)$$

The partial derivatives are with respect to each of the four fit parameters ( $p_1, \dots, p_4$ ). The error matrix contains the error squared for each parameter along the diagonal and the correlation between parameters in the the off-diagonal elements. The relative error on the dilution varied between 2% and 10% depending on the pion type and and kinematics. The errors for each pion case are listed in tables in Ref. [69].

4. Pair Symmetric background ( $e^+/e^-$ ): The systematic error for the  $e^+/e^-$  background correction is negligible as the correction itself is on the order of a 1%.
5. Radiative Correction: We have no radiative tail from elastic scattering so the radiative corrections are already quite small. The largest effect comes from the miscalculation of  $\vec{q}$  because of the initial or final electron radiating a photon. We estimate this assuming the photons are emitted along the direction of motion of the electron which implies that  $v$  is overestimated and  $\theta_q$  is underestimated. Radiative effects from exclusive processes appear to be important, but a quantitative estimate of this does not exist as yet. No rigorous radiative corrections exist at this point. We assumed a 5% systematic error for internal and external radiative effects.
6.  $R = \sigma_L/\sigma_T$ : The double spin asymmetry ( $A_{LL}$ ) is converted to the ratio of polarized to unpolarized structure functions via a depolarization factor. The depolarization factor,

has in it the structure function  $R$ , which represents the ratio of longitudinal to transverse photon absorption cross-sections. The latest values for  $R$  for SIDIS, shown in Figure 5.13, have sizable error bars associated with them for the SIDIS range in  $z$ . The estimates for the error on  $R$  are shown in Table 5.5.

Item	Correction	Applicable for	Uncertainty A	Uncertainty B
1	$P_b$	$A_{UL}, A_{LU}$	3.33 (abs)	3.26 (abs)
2	$P_b P_t$	$A_{UL}, A_{LL}$	0.026 (abs)	0.020 (abs)
3	Dilution Model Parameters	$A_{UL}, A_{LL}$	2 - 10 % (rel)	2 - 10 % (rel)
4	$\pi^-, e^+/e^-$	$A_{UL}, A_{LU}, A_{LL}$	>1 %(rel)	>1 %(rel)
5	Radiative Effects	$A_{UL}, A_{LU}, A_{LL}$	5 %(rel)	5 %(rel)
6	$R = \sigma_L/\sigma_T$	$g_1/F_1$	0.1 (abs)	0.1 (abs)

TABLE 5.5: Sources of systematic uncertainties and their estimated values for eg1dvcs run periods A (58800 - 59161) and B (59400 - 60200).

Table 5.5 lists the sources of systematic error that are studied.

The systematic errors associated with each item in Table 5.5 is assumed to be uncorrelated with the others. The total systematic error for the physics asymmetry is calculated in multiple bins of  $(x_B, P_{h\perp})$  for  $A_{LL}$ ; and  $(x_B, P_{h\perp}, \phi_h)$  for  $A_{UL}$  and  $A_{LU}$ .

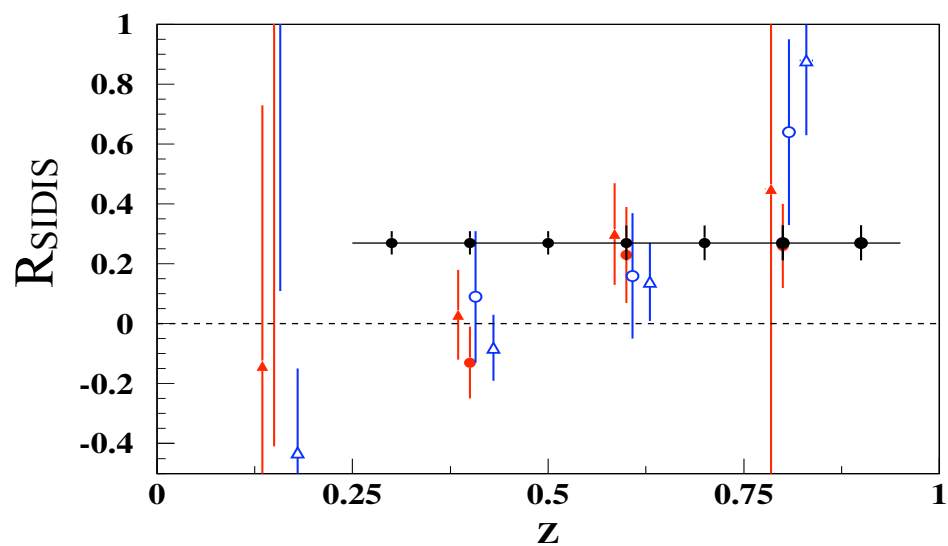


FIG. 5.13: The ratio ( $R = \sigma_L/\sigma_T$ ) in SIDIS as a function of  $z$  as measured at Cornell Ref. [22]. The red symbols reflect the data on a hydrogen target for  $\pi^+$  (filled circle), and  $\pi^-$  (filled triangle). The blue symbols reflect the data on a deuterium target for  $\pi^+$  (open circle), and  $\pi^-$  (open triangle). The solid curves reflect the parameterization of  $R$  for DIS. Projected data for the E12-06-104 experiment have been added as black solid circles Ref. [23].

# CHAPTER 6

## Asymmetry Results and Discussion

The primary goal of this work is to measure the single and double spin asymmetries that correspond to the helicity structure functions  $F_{UL}$ ,  $F_{LL}$  and  $F_{LU}$ . Extracting azimuthal moments of these asymmetries allows us to separate specific terms contributing to the SIDIS cross section in Equation 2.5. The final experimental results are detailed in each section below.

### 6.1 Asymmetry and Error Formulae

#### 6.1.1 $A_{LU}$

We write the experimental expression for the Beam Spin Asymmetry (BSA) in terms of the four different spin combinations as

$$A_{LU} = \frac{1}{|P_b|} \frac{n^{++} - n^{-+} - n^{--} + n^{+-}}{n^{++} + n^{-+} + n^{--} + n^{+-}} \quad (6.1)$$

in which  $n$  denotes the semi-inclusive event rate and  $P_b$  corrects for the fact that the beam is not 100% polarized. The notation for event rate for the positively polarized beam and positively polarized target is,

$$n^{++} = N^{++}/F^{++}. \quad (6.2)$$

Here  $N^{++}$  is the number of semi-inclusive counts for a positively polarized beam and target. To get the rate, it is scaled by the signal in the Faraday cup ( $F^{++}$ ) that indicates the charge collected for that combination of beam and target spins. The error on the beam spin asymmetry is calculated to be,

$$\Delta A_{LU} = \sqrt{\left(\frac{dA_{LU}}{dN^{++}}\right)^2 \Delta N^{++2} + \left(\frac{dA_{LU}}{dN^{+-}}\right)^2 \Delta N^{+-2} + \left(\frac{dA_{LU}}{dN^{-+}}\right)^2 \Delta N^{-+2} + \left(\frac{dA_{LU}}{dN^{--}}\right)^2 \Delta N^{--2}}. \quad (6.3)$$

The error on the Faraday cup values is miniscule in comparison with the statistical error on the number of events, so we ignore it. The derivatives for each term in the error calculation are

$$\frac{dA_{LU}}{dN^{++(+-)}} = \frac{1}{|P_b|} \frac{(n^{-+} + n^{--}) \cdot \frac{2}{F^{++(+-)}}}{(n^{++} + n^{+-} + n^{-+} + n^{--})^2} \quad (6.4)$$

and

$$\frac{dA_{LU}}{dN^{-+(-)}} = \frac{1}{|P_b|} \frac{(n^{++} + n^{+-}) \cdot \frac{2}{F^{-+(-)}}}{(n^{++} + n^{+-} + n^{-+} + n^{--})^2} \quad (6.5)$$

where,

$$\Delta N = \sqrt{N} \quad (6.6)$$

for each helicity combination.

### 6.1.2 $A_{LL}$

We write a similar expression for the Double Spin Asymmetry (DSA),

$$A_{LL} = -\frac{1}{f} \frac{n^{++} - n^{-+} + n^{--} - n^{+-}}{|P_b P_t^-|(n^{++} + n^{-+}) + |P_b P_t^+|(n^{--} + n^{+-})} \quad (6.7)$$

The asymmetry in this case is scaled by a product of the beam and target polarization, and the dilution factor. The superscript on  $P_t$  indicates the sign of the target polarization with respect to the beam direction.

The error on the double spin asymmetry is,

$$\Delta A_{LL} = \sqrt{\left(\frac{dA_{LL}}{dN^{++}}\right)^2 \Delta N^{++2} + \left(\frac{dA_{LL}}{dN^{+-}}\right)^2 \Delta N^{+-2} + \left(\frac{dA_{LL}}{dN^{-+}}\right)^2 \Delta N^{-+2} + \left(\frac{dA_{LL}}{dN^{--}}\right)^2 \Delta N^{--2}} \quad (6.8)$$

The derivatives for each term in the error calculation are

$$\frac{dA_{LL}}{dN^{++(--)}} = \frac{1}{f} \frac{(n^{-+} + n^{+-}) \cdot \frac{P_b P_t^+ + 1}{F^{++(--)}} + (n^{++} + n^{--}) \cdot \frac{P_b P_t^+ - 1}{F^{++(--)}}}{(|P_b P_t^-|(n^{++} + n^{-+}) + |P_b P_t^+|(n^{--} + n^{+-}))^2} \quad (6.9)$$

and

$$\frac{dA_{LL}}{dN^{-+(+-)}} = \frac{1}{f} \frac{(n^{++} + n^{--}) \cdot \frac{P_b P_t^+ + 1}{F^{-+(+-)}} + (n^{+-} + n^{-+}) \cdot \frac{P_b P_t^+ - 1}{F^{-+(+-)}}}{(|P_b P_t^-|(n^{++} + n^{-+}) + |P_b P_t^+|(n^{--} + n^{+-}))^2} \quad (6.10)$$

The physics quantity of interest is the double spin asymmetry scaled by the depolarization factor  $D'$ . The ratio of polarized to unpolarized structure functions can be written as

$$\frac{g_1}{F_1} = \frac{[A_{LL} + A_{\perp} \tan(\theta/2)]}{D'} \quad (6.11)$$

where  $\theta$  is the scattering angle and  $A_{\perp}$  is the double spin asymmetry for a transversely polarized target. We assume  $A_{\perp} \approx 0$ . The uncertainty on the ratio of structure functions

is written as

$$\Delta \left( \frac{g_1}{F_1} \right) = \frac{\Delta A_{LL}}{D'}. \quad (6.12)$$

The depolarization factor is given by Ref. [64],

$$D'(y) = \frac{y(2-y)(1+\gamma^2)}{y^2 + 2 \left(1-y - \frac{1}{4}y^2\gamma^2\right) (1+R)} \quad (6.13)$$

where  $\gamma^2 = 2M_{xB}/Q^2$  and  $R$  is the ratio of longitudinal to transverse cross sections given in terms of the unpolarized structure functions as

$$R+1 = \frac{(1+\gamma^2)F_2}{2x_B F_1} \quad (6.14)$$

The uncertainty in  $D'$  comes primarily from  $R$  and is treated in the systematic error section. The DSA results are shown in the form of  $g_1/F_1$ .

### 6.1.3 $A_{UL}$

The Target Spin Asymmetry (TSA) is written as

$$A_{UL} = \frac{1}{f} \frac{n^{++} + n^{-+} - n^{--} - n^{+-}}{|P_t^-|(n^{++} + n^{-+}) + |P_t^+|(n^{--} + n^{+-})} \quad (6.15)$$

which is scaled by target polarization and dilution for the target. The target polarization here is obtained by dividing the polarization product  $P_b P_t$  from the elastic scattering study by the average the  $P_b$  from the Möller measurements. The error on the target spin

asymmetry is,

$$\Delta A_{UL} = \sqrt{\left(\frac{dA_{UL}}{dN^{++}}\right)^2 \Delta N^{++2} + \left(\frac{dA_{UL}}{dN^{+-}}\right)^2 \Delta N^{+-2} + \left(\frac{dA_{UL}}{dN^{-+}}\right)^2 \Delta N^{-+2} + \left(\frac{dA_{UL}}{dN^{--}}\right)^2 \Delta N^{--2}} \quad (6.16)$$

The derivatives for each term in the error calculation are

$$\frac{dA_{UL}}{dN^{++(-+)}} = \frac{1}{f} \frac{(n^{+-} + n^{--}) \frac{P_t^{+1}}{F^{++(-+)}} + (n^{-+} + n^{++}) \frac{P_t^{-1}}{F^{++(-+)}}}{(|P_t^-|(n^{++} + n^{-+}) + |P_t^+|(n^{--} + n^{+-}))^2} \quad (6.17)$$

and

$$\frac{dA_{UL}}{dN^{+-(--)}} = \frac{1}{f} \frac{(n^{++} + n^{-+}) \frac{P_t^{+1}}{F^{+-(--)}} + (n^{+-} + n^{--}) \frac{P_t^{-1}}{F^{+-(--)}}}{(|P_t^-|(n^{++} + n^{-+}) + |P_t^+|(n^{--} + n^{+-}))^2} \quad (6.18)$$

We separate semi-inclusive rates in bins of helicity to calculate each asymmetry.

## 6.2 Kinematic Coverage

The sheer statistics available from the eg1-dvcs experiment sets this work apart from all previous measurements from HERMES, COMPASS and prior CLAS data on a longitudinally polarized target. The high statistics allow us to measure asymmetries and extract moments differential in  $Q^2$ ,  $x_B$ ,  $z$ ,  $P_{h\perp}$  and  $\phi_h$ . The size of the kinematic bins are listed in Table 6.1.

The kinematic coverage of the semi-inclusive data for  $\pi^{\pm,0}$  is shown in terms of the relevant kinematics in Figures 6.1 - 6.3. We probe a momentum fraction range of 0.1 - 0.48. The highest momentum for each pion are  $\approx 4.6$  GeV. The independent variables  $x_B$  and  $Q^2$  are kinematically correlated here because of CLAS acceptance. Figure 6.2 shows that the majority of  $\pi^{\pm}$ s are dominated at transverse pion momenta,  $P_{h\perp}$  around 0.45 GeV. The  $\pi^0$  events are concentrated at slightly lower  $P_{h\perp}$  values. There is significant improve-

Bin number	$Q^2$ (GeV) <sup>2</sup>	$\phi_h$ (degrees)	$z$	$P_{h\perp}$ (GeV)	$x_B$
1	0.800	0	0.2	0.000	0.06
2	1.000	30	0.3	0.125	0.12
3	1.250	60	0.4	0.250	0.18
4	1.562	90	0.5	0.375	0.24
5	1.952	120	0.6	0.500	0.30
6	2.440	150	0.7	0.625	0.36
7	3.049	180	0.8	0.750	0.42
8	3.811	210	0.9	0.875	0.48
9	4.763	240	1.0	1.000	0.54
10	5.953	270	1.1	1.125	0.60
11	7.440	300			
12		330			

TABLE 6.1: Lower bin edges for this experiment. The bin size was constant for all variables except  $Q^2$  for which we used logarithmic bin sizes.

ment in the coverage for the neutral pion due to the presence of the IC compared to earlier measurements in CLAS. Unfortunately, the IC reduces the  $\pi^\pm$  rates in its shadow, and Figure 6.3 shows a much lower  $\pi^-$  rate at small angles than for  $\pi^0$ .

The event selection is further restricted after particle identification to ensure a clean semi-inclusive sample. The additional restrictions are listed below.

- $0.0 < p_{electron} < \text{Beam Energy}$ : This ensures a realistic electron momentum.
- Momentum transfer  $Q^2 > 1 \text{ GeV}^2$  and  $W > 2 \text{ GeV}$ : This ensures that event are in the traditional DIS region.
- Fractional Energy  $0.4 > z > 0.7$ : This effectively eliminates events coming from target fragmentation at low  $z$  and coherent events such as  $\rho^0$  production at high  $z$ .
- Missing Mass  $M_x > 1.4 \text{ GeV}$ : Ensures that several particles are produced in the hadronization process.

- $y < 0.85$ : Removes data dominated by radiative corrections.
- Transverse momentum of pion  $P_{h\perp} > 0.05$  GeV: Removes low momentum noise.
- Momentum fraction  $0.12 < x_B < 0.48$ : Bins outside of this range have few events.
- Tight IC Fiducial Cuts : Ensure that the recoil particles are coming from the target and not the support structure of the IC. This is consistent with the IC fiducial cuts used for the dilution factor study.

An asymmetry value was calculated in each kinematic bin that had more than 10 events for each helicity. Hypothetically, if there were data available in every single prescribed bin we could calculate asymmetries in 132000 bins. However, the additional cuts placed on the data sample along with the acceptance of CLAS and the IC results in limited population of this space. Realistically, there are approximately 9000 bins populated for each pion.

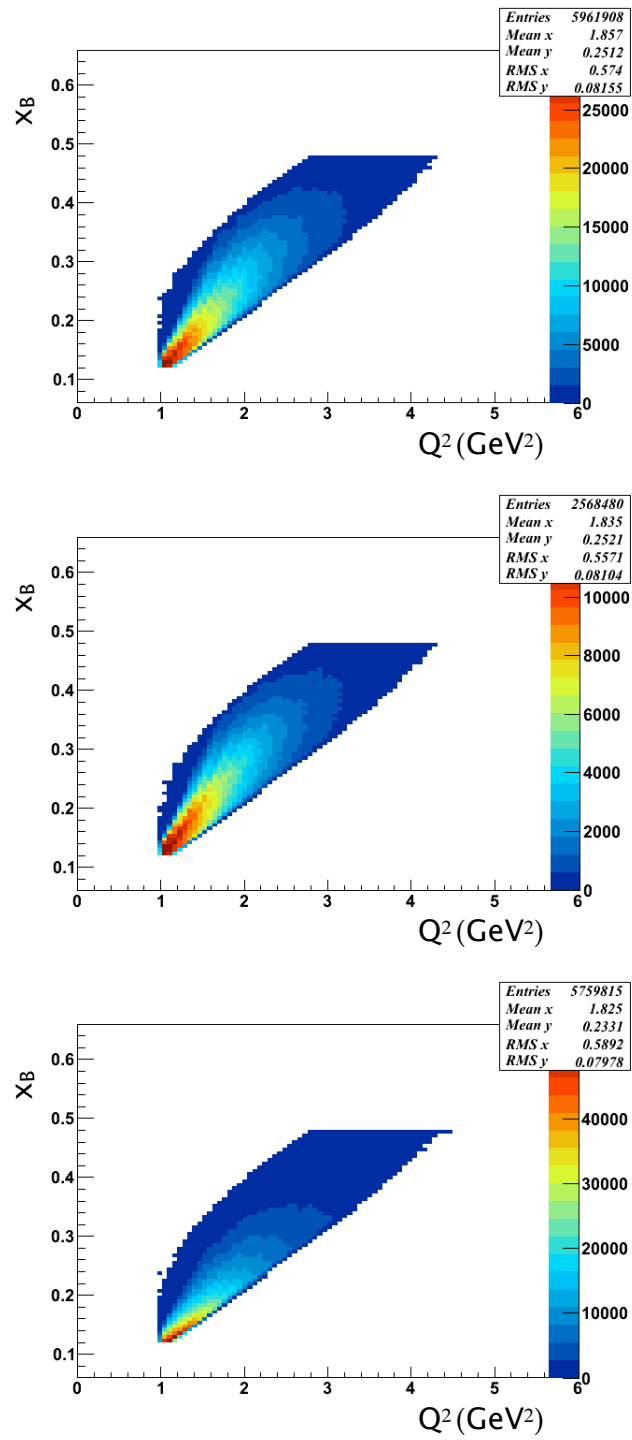


FIG. 6.1: The kinematic coverage in  $x_B$  and  $Q^2$  (GeV $^2$ ) in CLAS for semi-inclusive  $\pi^+$  (top),  $\pi^-$  (middle) and  $\pi^0$  (bottom) events. The independent variables  $x_B$  and  $Q^2$  are correlated here because of CLAS acceptance.

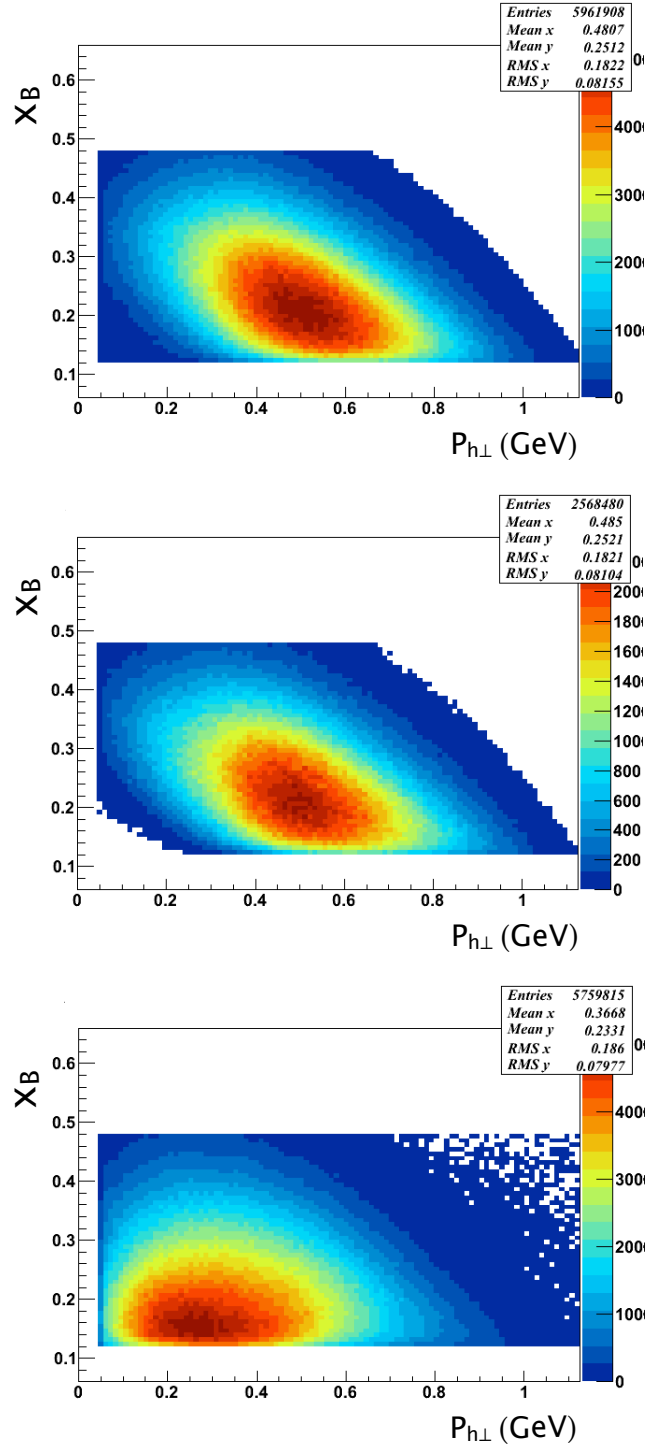


FIG. 6.2: The kinematic coverage in  $x_B$  and  $P_{h\perp}$  (GeV) in CLAS for semi-inclusive  $\pi^+$  (top),  $\pi^-$  (middle) and  $\pi^0$  (bottom) events. The majority of  $\pi^\pm$  are dominated by  $P_{h\perp}$  values around 0.45 GeV. The  $\pi^0$  events are concentrated at slightly lower  $P_{h\perp}$  values.

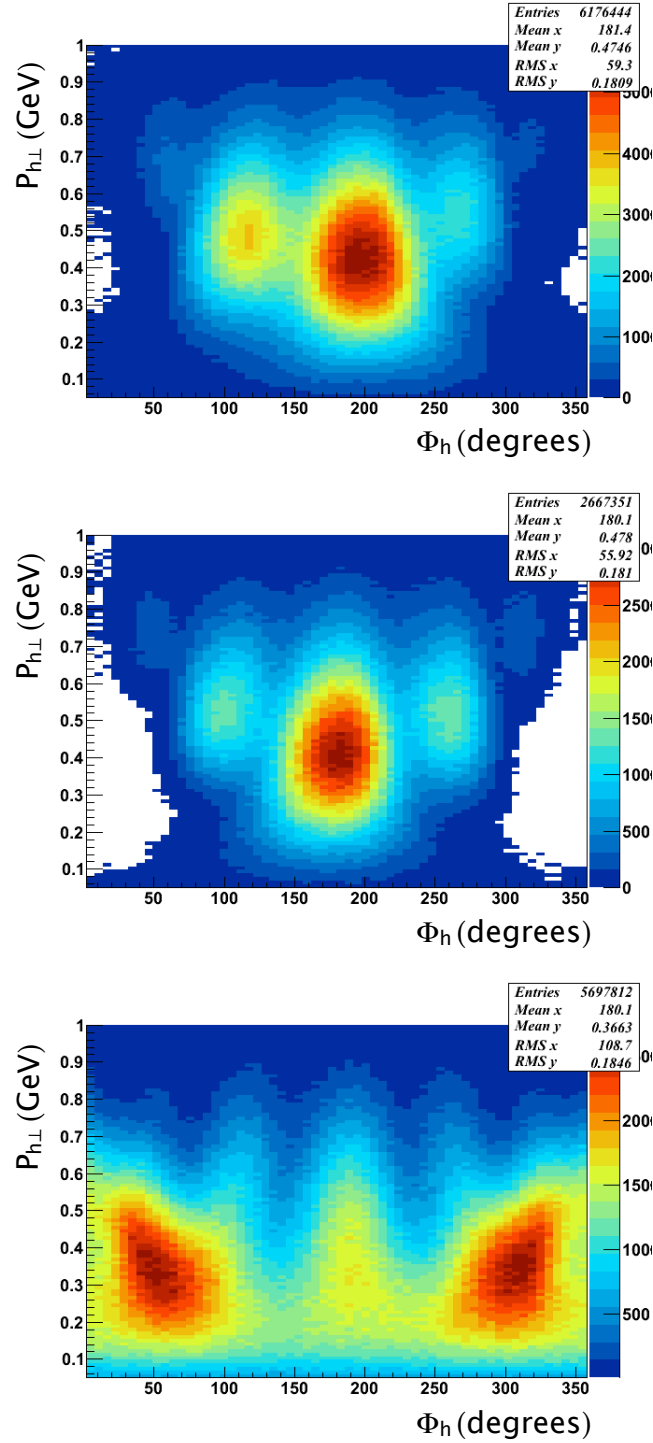


FIG. 6.3: The kinematic coverage in  $P_{h\perp}$  (GeV) and  $\phi_h$  (degrees) in CLAS for semi-inclusive  $\pi^+$  (top),  $\pi^-$  (middle) and  $\pi^0$  (bottom) events. About two thirds of the neutral pions are detected fully or partially in the IC. This is reflected in the higher event rate on the edges of the bottom plot as compared to the charged pions which are detected only in CLAS.

## 6.3 Results

Each asymmetry, along with its corresponding dilutions, were calculated for the bins specified in Table 6.1.

### 6.3.1 $A_{LU}$

The beam spin asymmetry integrated over all kinematics except for  $\phi_h$  is shown in Figure 6.4. These data were fit using

$$f(\phi_h) = A_{LU}^C + A_{LU}^{\sin\phi_h} \sin\phi_h + A_{LU}^{\sin 2\phi_h} \sin 2\phi_h. \quad (6.19)$$

A clear  $\sin\phi_h$  dependence is seen. The  $\sin 2\phi_h$  dependence is consistent with zero in all three cases. A similar trend is seen when we break this out into a larger number of bins. If we integrate only over  $Q^2$  and  $z$  we can plot the  $\phi_h$  distributions for a two dimensional array of  $x_B$  and  $P_{h\perp}$  bins as shown in Figures 6.5, 6.6, 6.7. The projections have one kinematic quantity relating to the quark distribution ( $x_B$ ) and the other to fragmentation function ( $P_{h\perp}$ ). We justify the  $z$  integration because little variation is seen with respect to  $z$  in the quantities involved. We integrate over  $Q^2$  because the data are predominantly in the range 1-2 GeV<sup>2</sup> and the logarithmic  $Q^2$  evolution is slight over this range of the data.

The three fit coefficients  $A_{LU}^C$ ,  $A_{LU}^{\sin\phi_h}$  and  $A_{LU}^{\sin 2\phi_h}$  for each pion case were extracted in  $(x_B, P_{h\perp})$  space. The dependence of the sine moments as a function of  $P_{h\perp}$  is shown in Figures 6.8 and 6.9. The constant term in the fit is consistent with zero and is not shown. The  $\sin\phi_h$  moment has a smooth dependence for  $\pi^0$ . Generally,  $\pi^+$  is largest,  $\pi^0$  a bit smaller, and  $\pi^-$  is close to zero or even negative.

The  $\sin 2\phi_h$  moment is consistent with zero for almost all of the bins except for  $\pi^-$

especially in the higher  $P_{h\perp}$  bins.

### 6.3.2 $g_1/F_1$

The double spin asymmetry integrated over  $(Q^2, x_B, z, P_{h\perp})$  in form of the ratio of the polarized to unpolarized structure functions, is shown in Figure 6.10. These plots are integrated over all kinematics except for  $\phi_h$ . The data are fit using

$$f(\phi_h) = A_{LL}^C + A_{LL}^{\cos \phi_h} \cos \phi_h. \quad (6.20)$$

A clear  $\cos(\phi_h)$  dependence is seen along with a non-zero constant term. The dependence of  $g_1/F_1$  on  $P_{h\perp}$  is shown in Figure 6.11 for  $\pi^{\pm,0}$ . There is a slight tendency for  $\pi^+$  and  $\pi^0$  to decrease with  $P_{h\perp}$ , and a more noticeable one for  $\pi^-$  to increase with  $P_{h\perp}$ . We also extracted the  $\cos \phi_h$  momentum of the double spin asymmetry for  $\pi^{\pm,0}$  as shown in Figures 6.12 - 6.15.

### 6.3.3 $A_{UL}$

The target single spin asymmetry integrated over all kinematics except for  $\phi_h$  is shown in Figure 6.16. The data are fit using

$$f(\phi_h) = A_{UL}^C + A_{UL}^{\sin \phi_h} \sin \phi_h + A_{UL}^{\sin 2\phi_h} \sin 2\phi_h. \quad (6.21)$$

A clear  $\sin \phi_h$  dependence is seen. The  $\sin 2\phi_h$  dependence is consistent with zero in all three cases. A similar trend is seen in when we break out into a larger number of bins. If we integrate only over the  $Q^2$  and  $z$ , what we see in terms of  $x_B$ ,  $P_{h\perp}$  and  $\phi_h$  is shown in Figures 6.17 - 6.20. Again, these projections, have one kinematic quantity from the quark

distribution ( $x_B$ ) and the other from fragmentation ( $P_{h\perp}$ ).

The three fit coefficients for each pion case were extracted in ( $x_B, P_{h\perp}$ ) space. The dependence of these coefficients as a function of  $P_{h\perp}$  is shown in Figures 6.8 and 6.9. The constant term in the fit is not shown. The  $\sin \phi_h$  moment has a smooth dependence for  $\pi^0$ . Generally,  $\pi^+$  and  $\pi^0$  are both positive and  $\pi^-$  is close to zero or negative.

The data tables for all three asymmetries are listed in Ref. [70].

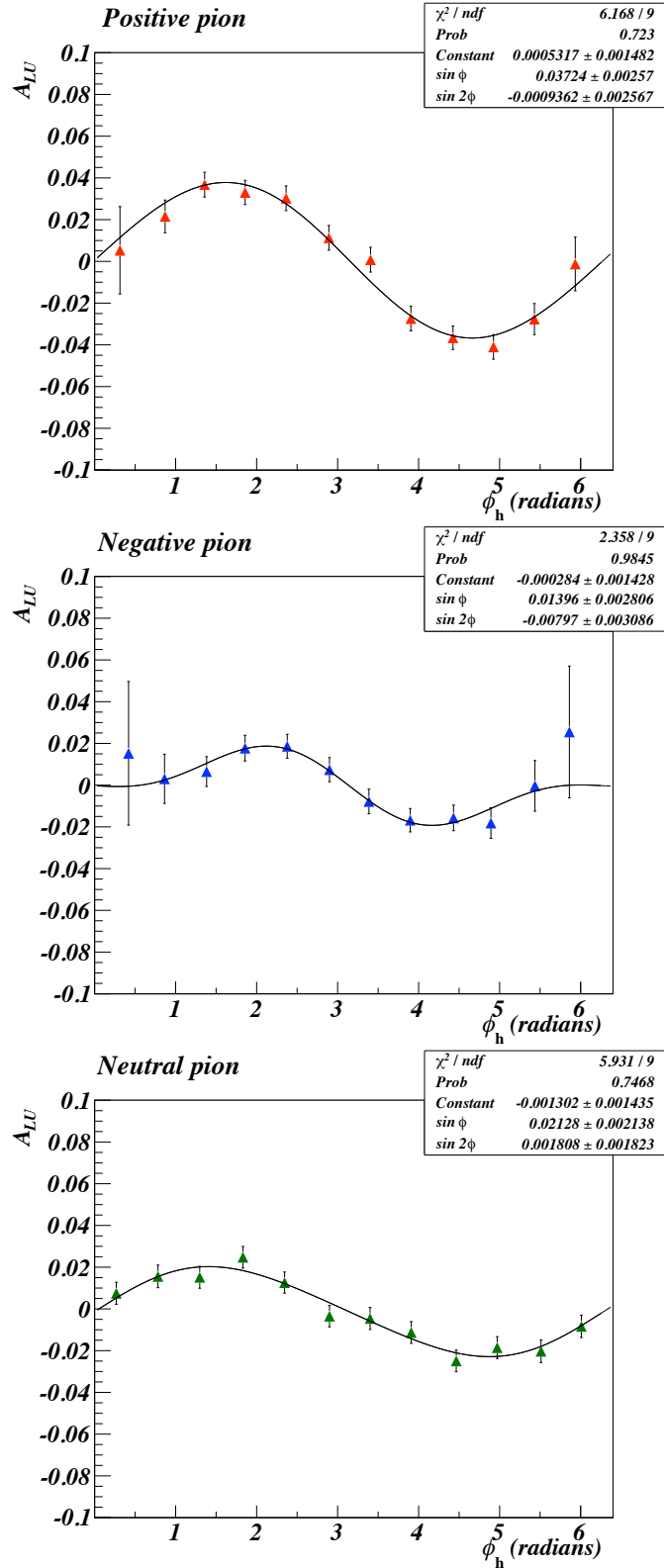


FIG. 6.4: The integrated beam spin asymmetry for  $\pi^+$  (top, red points),  $\pi^-$  (middle, blue points), and  $\pi^0$  (bottom, green points). The data were fit to  $f(\phi_h) = A_{LU}^C + A_{LU}^{\sin \phi_h} \sin \phi_h + A_{LU}^{\sin 2\phi_h} \sin 2\phi_h$  and were integrated over all bins of  $(Q^2, x_B, z, P_{h\perp})$ .

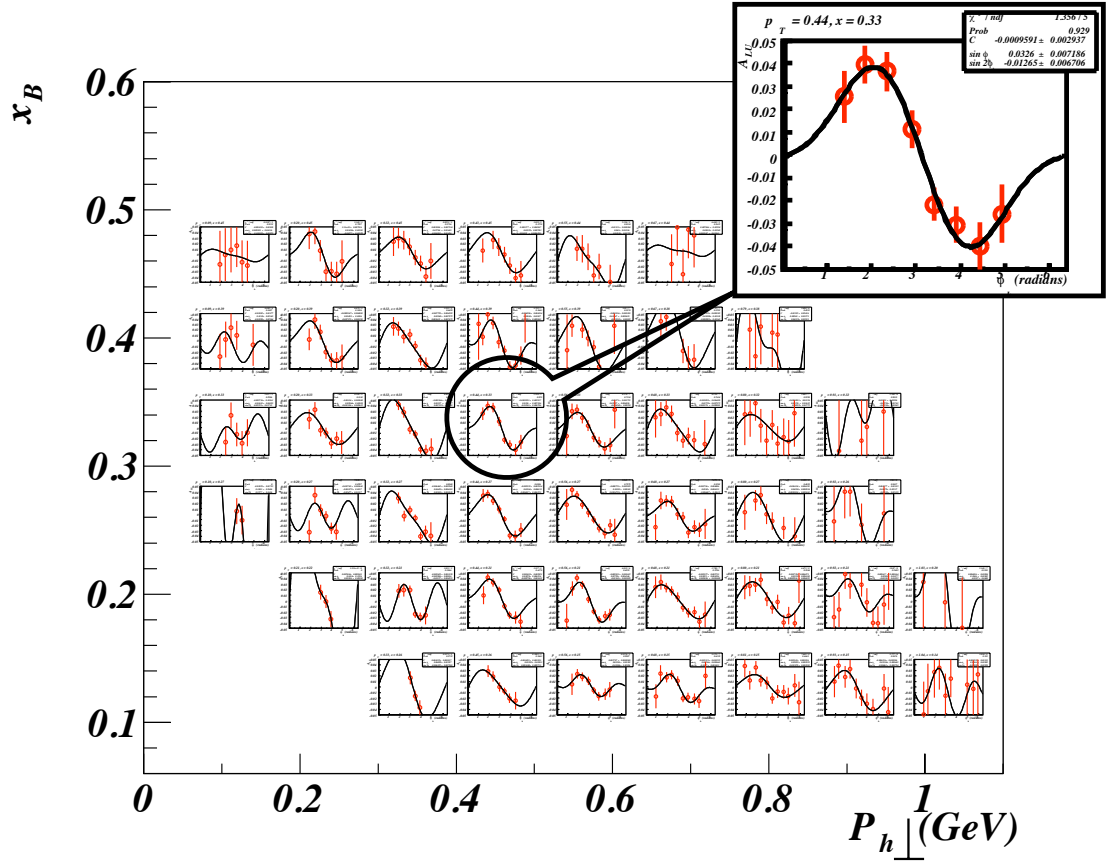


FIG. 6.5: The beam spin asymmetry vs  $\phi_h$  for  $\pi^+$  in bins of  $x_B$  and  $P_{h\perp}$ . Each  $x_B$  and  $P_{h\perp}$  bin is fit to  $f(\phi_h) = A_{LU}^C + A_{LU}^{\sin \phi_h} \sin \phi_h + A_{LU}^{\sin 2\phi_h} \sin 2\phi_h$ . The  $A_{LU}$  distribution for the  $\langle x_B \rangle = 0.33$  and  $\langle P_{h\perp} \rangle = 0.44$  is highlighted.

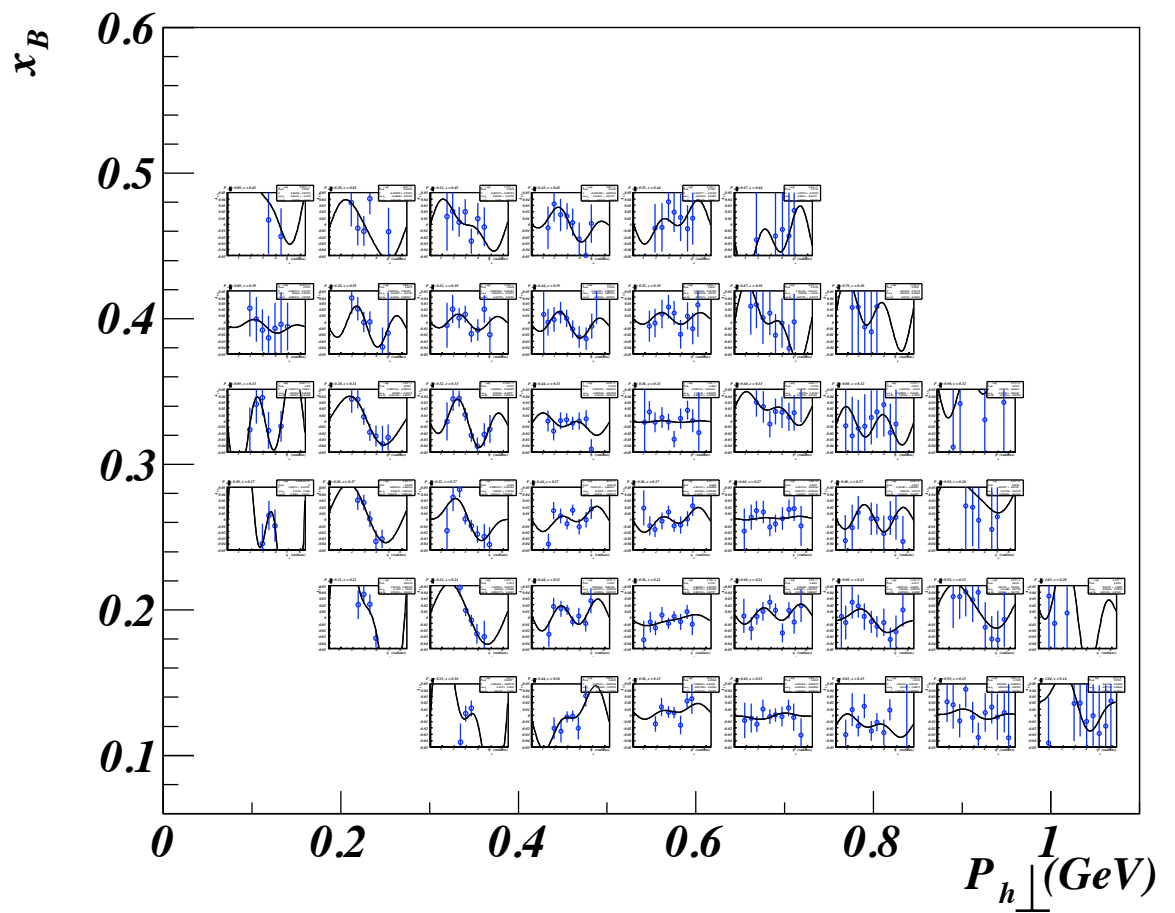


FIG. 6.6: Same as Figure 6.5 except for  $\pi^-$ .

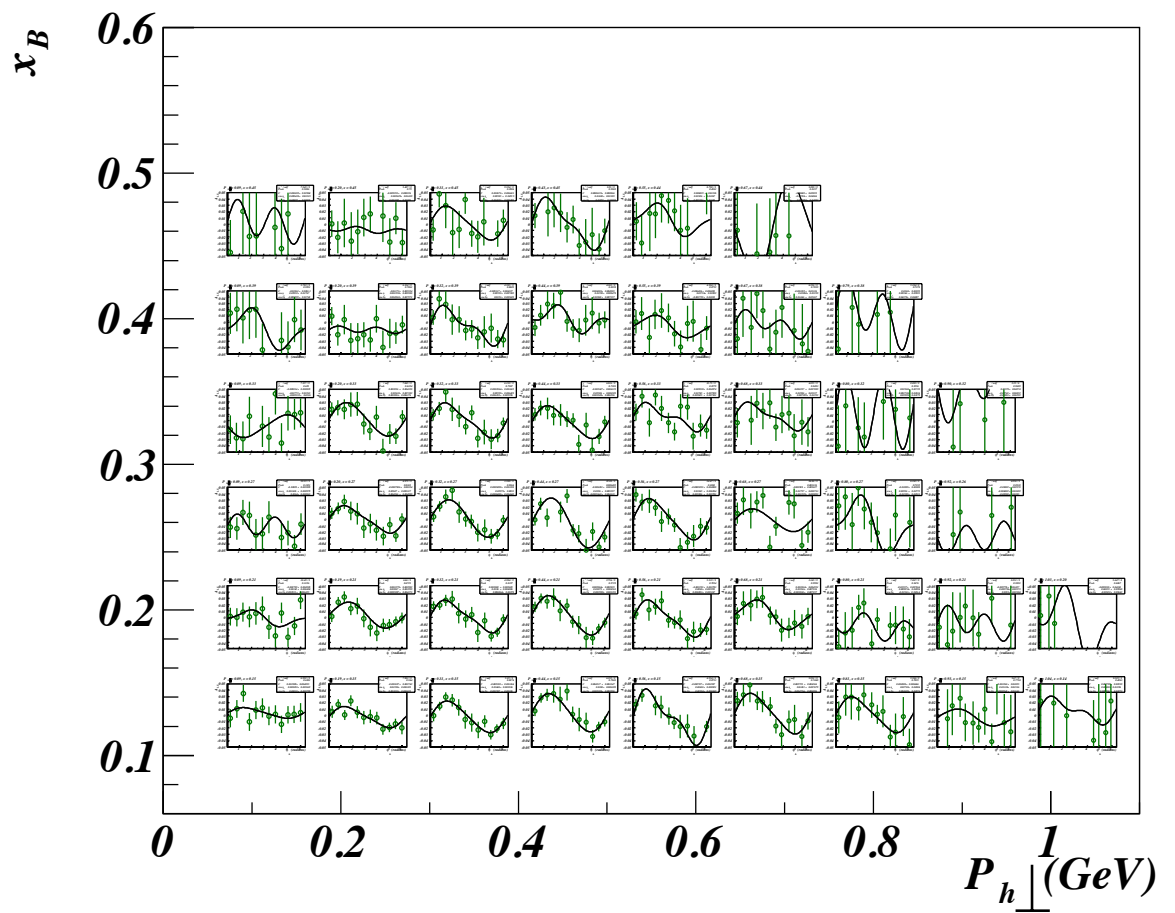


FIG. 6.7: Same as Figure 6.5 except for  $\pi^0$ .

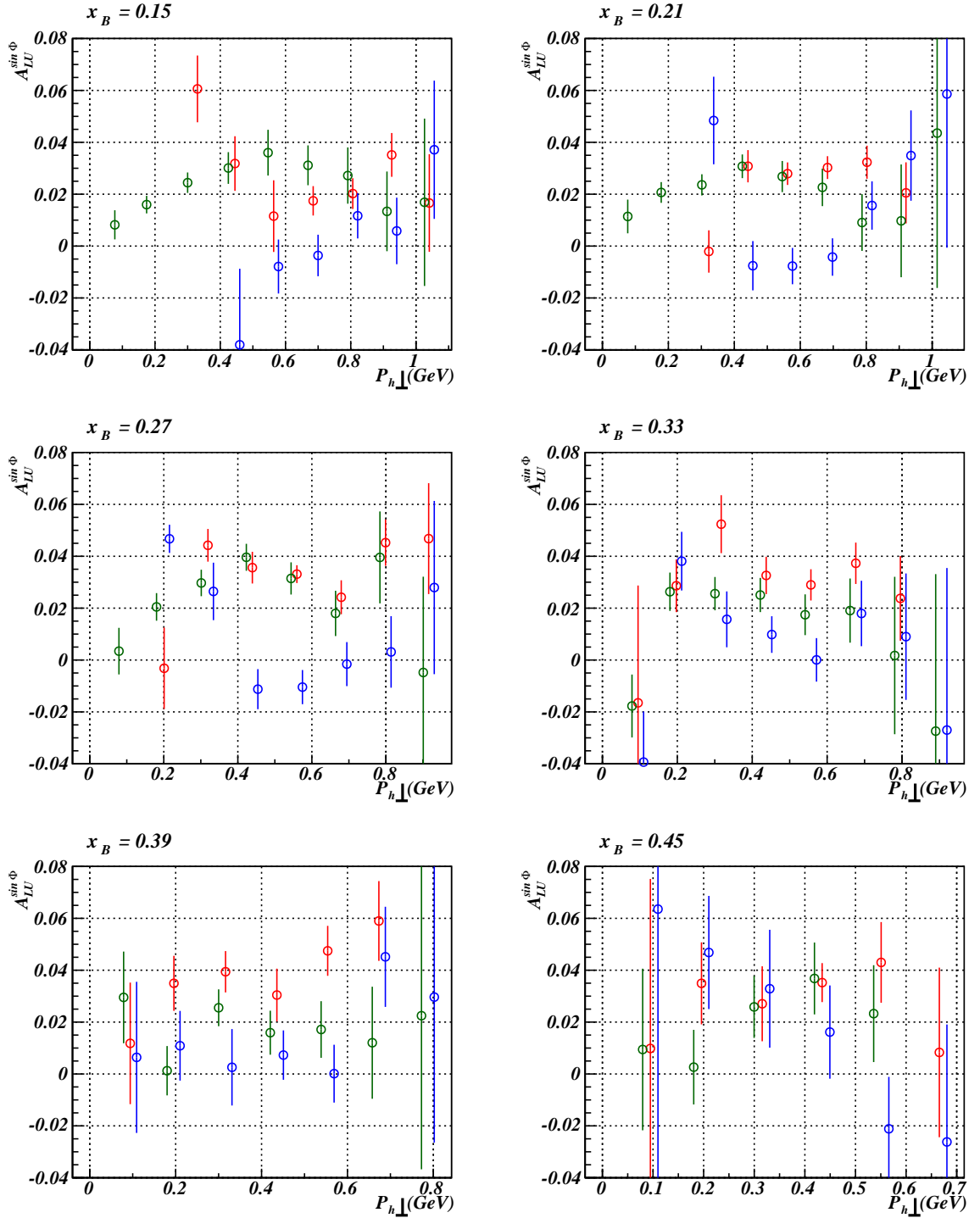


FIG. 6.8: The  $\sin \phi_h$  moments of  $A_{LL}$  as a function of  $P_{h\perp}$  for different bins in  $x_B$ . The average value of  $x_B$  is displayed in the title of each plot for  $\pi^+$  (red),  $\pi^-$  (blue), and  $\pi^0$  (green).

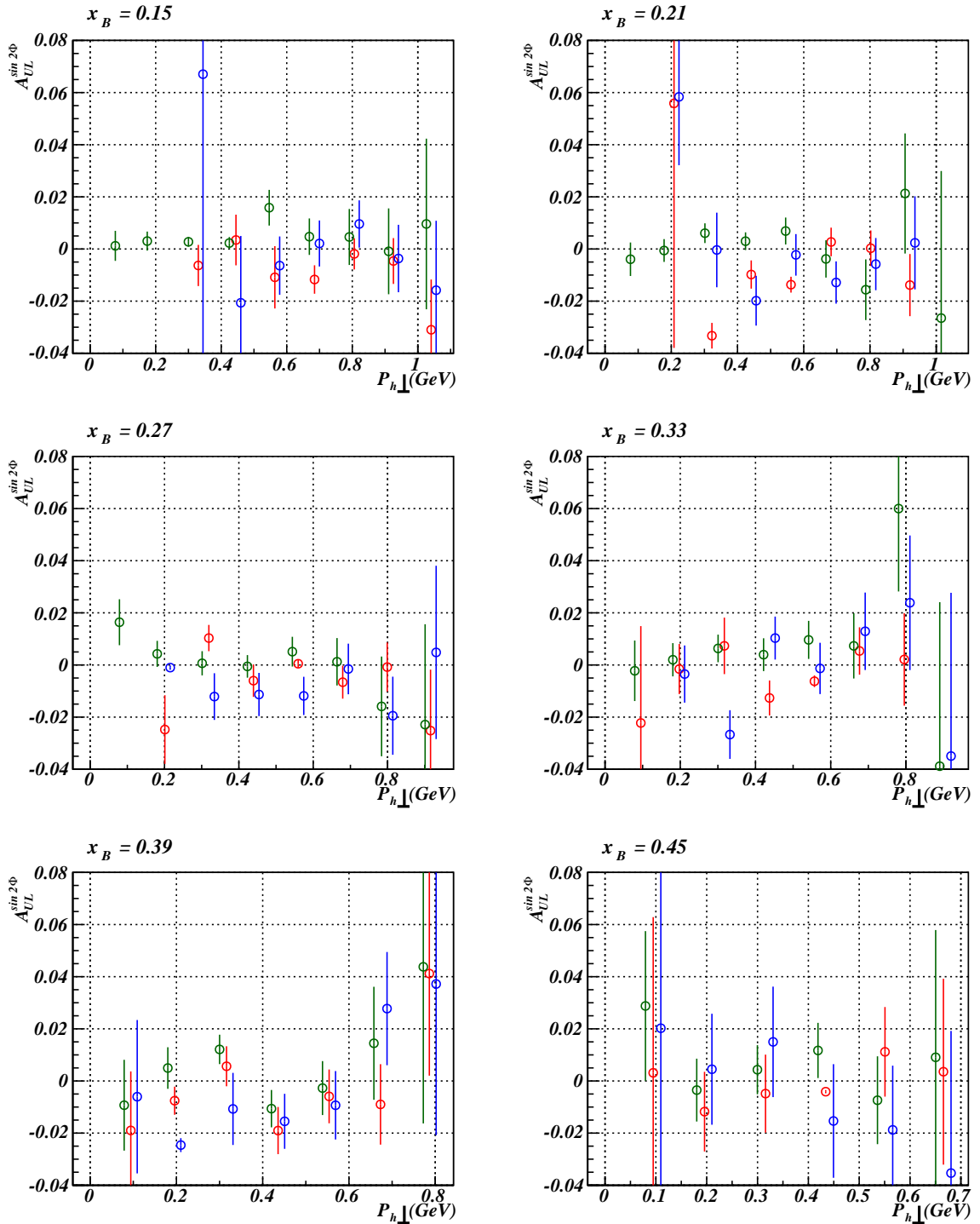


FIG. 6.9: The  $\sin 2\phi_h$  moments of  $A_{LU}$  as a function of  $P_{h\perp}$  for different bins in  $x_B$ . The average value of  $x_B$  is displayed in the title of each plot for  $\pi^+$  (red),  $\pi^-$  (blue), and  $\pi^0$  (green).

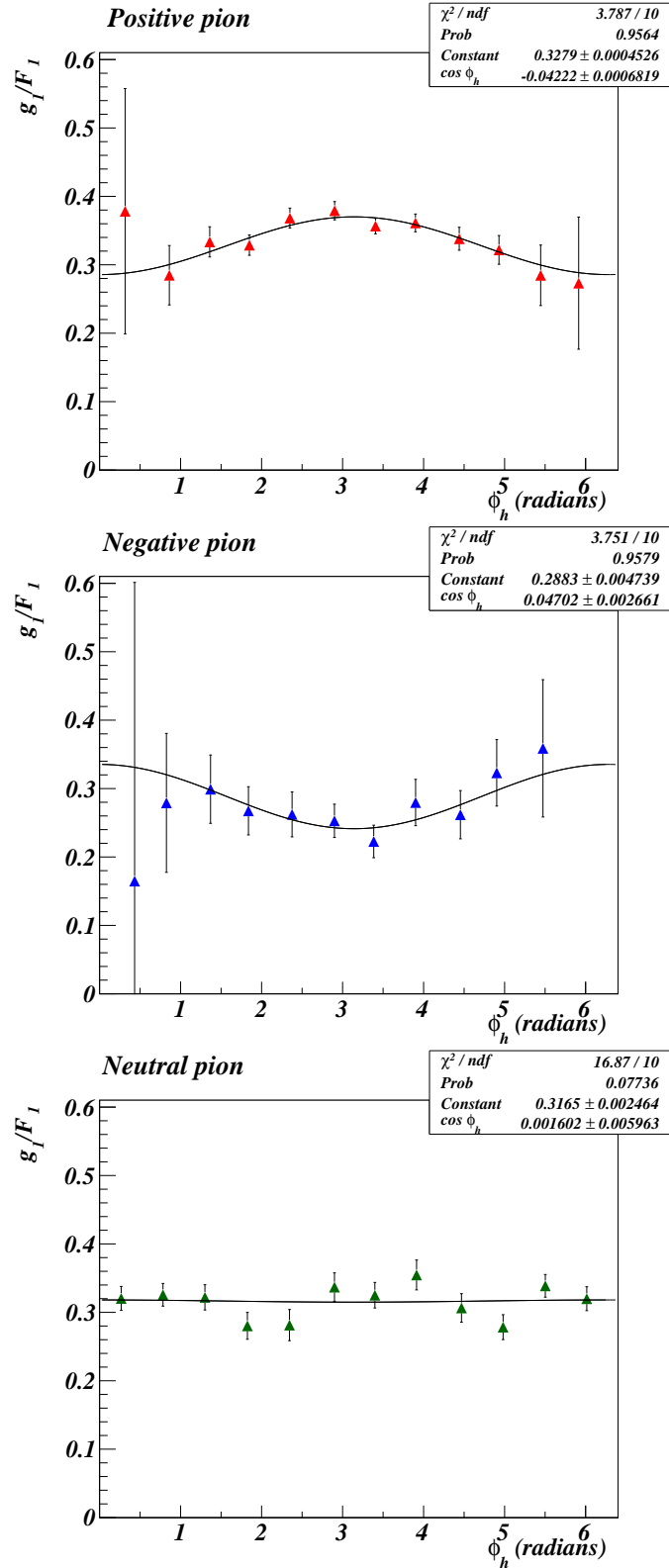


FIG. 6.10: The ratio of polarized to unpolarized structure functions integrated over  $(Q^2, x_B, z, P_{h\perp})$  for  $\pi^+$  (red, top),  $\pi^-$  (blue, middle) and  $\pi^0$  (green, bottom). The data are fit to  $f(\phi_h) = A_{LL}^C + A_{LL}^{\cos \phi_h} \cos \phi_h$ .

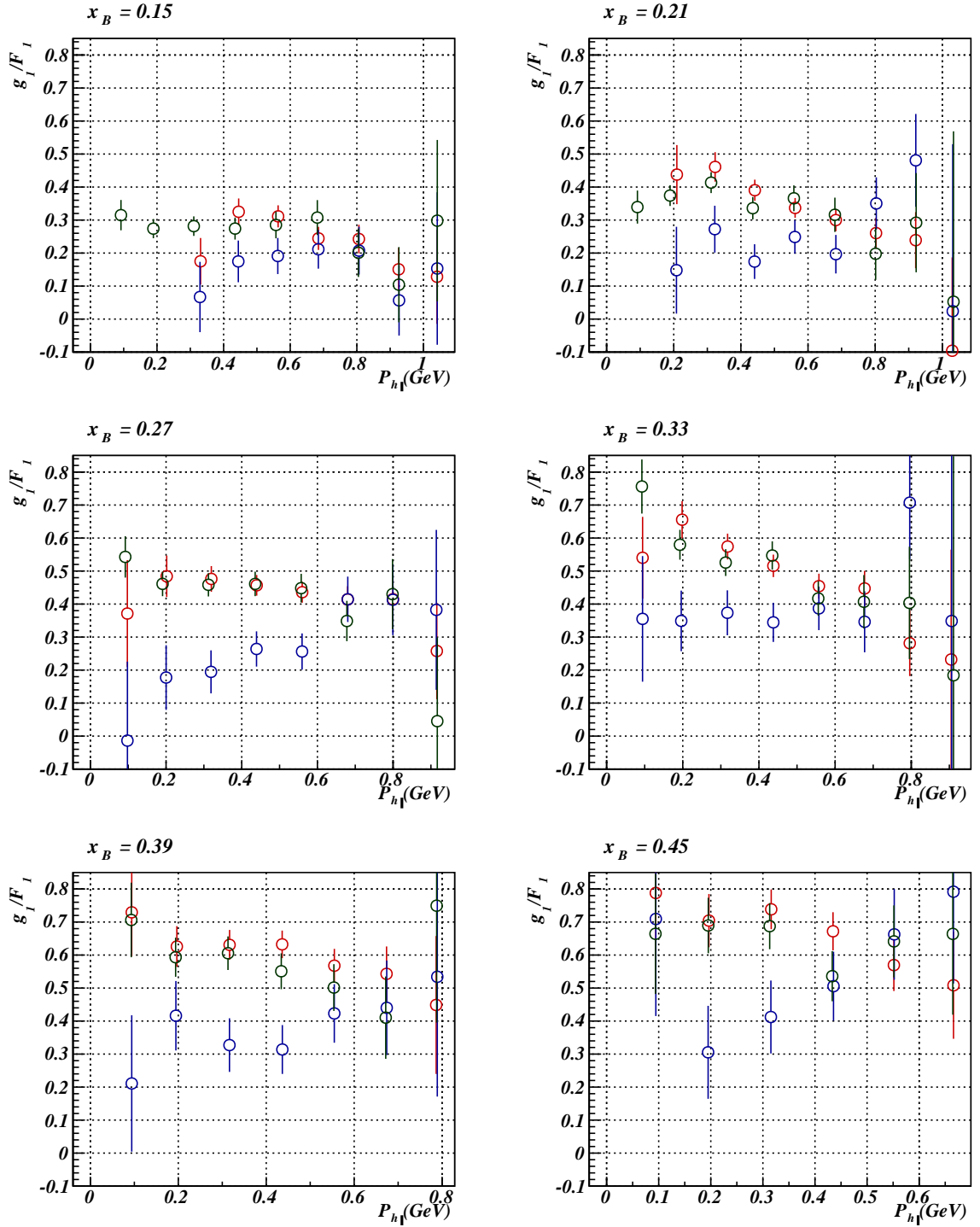


FIG. 6.11: The ratio of polarized to unpolarized structure functions,  $g_1/F_1$  versus  $P_{h_1}$  for different bins in  $x_B$ . The average value of  $x_B$  is displayed in the title of each plot for  $\pi^+$  (red),  $\pi^-$  (blue), and  $\pi^0$  (green).

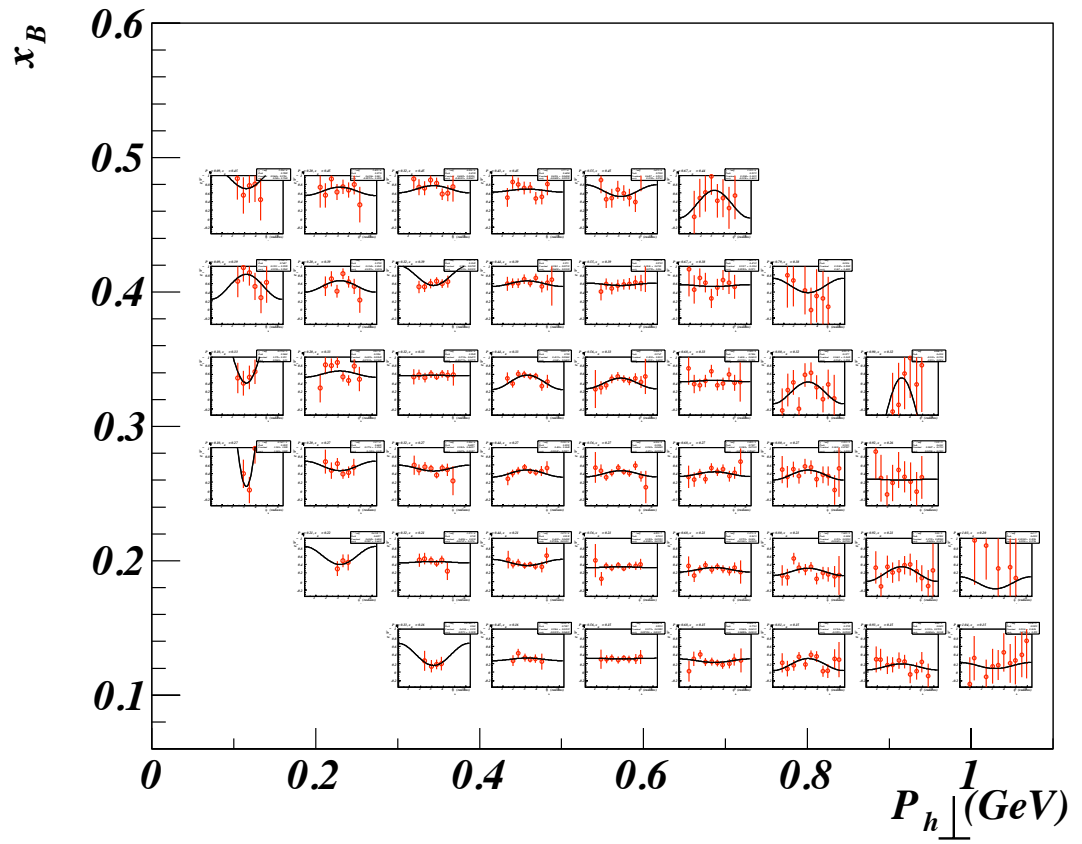


FIG. 6.12: The ratio of polarized to unpolarized structure functions integrated over  $(Q^2, z)$  for  $\pi^+$ . The data are fit to  $f(\phi_h) = A_{LL}^C + A_{LL}^{\cos \phi_h} \cos \phi_h$ .

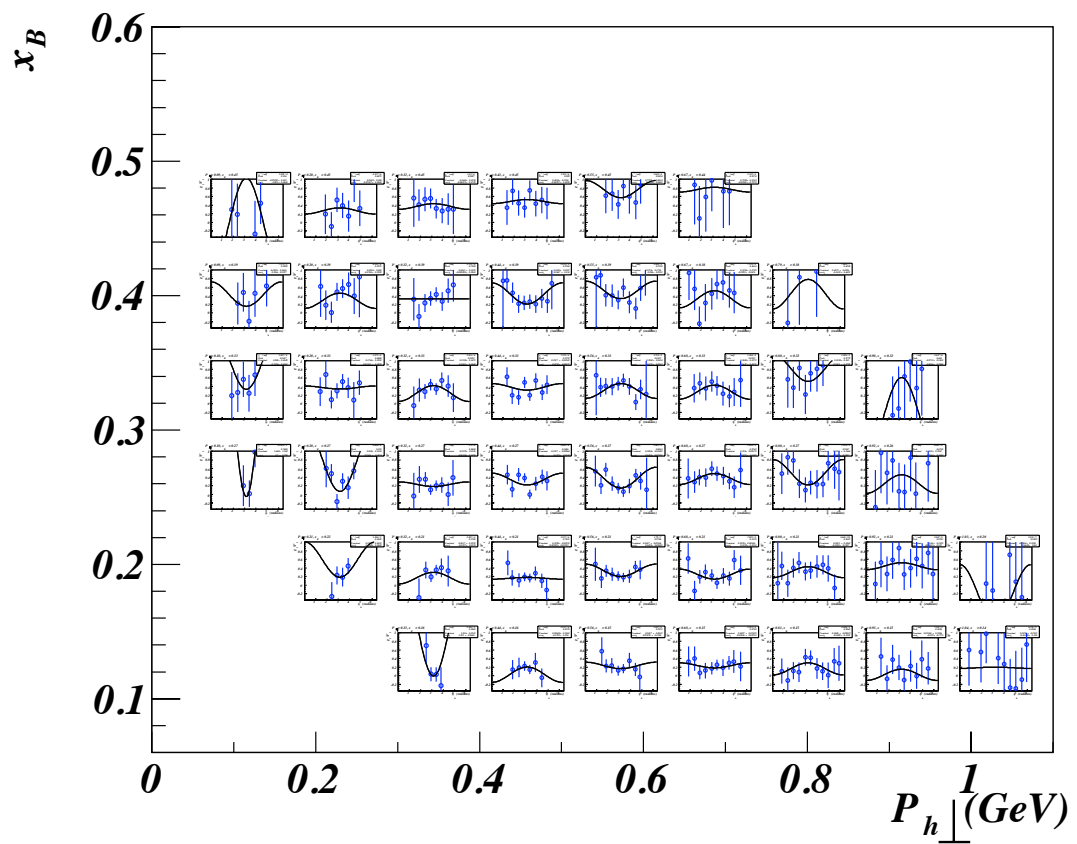
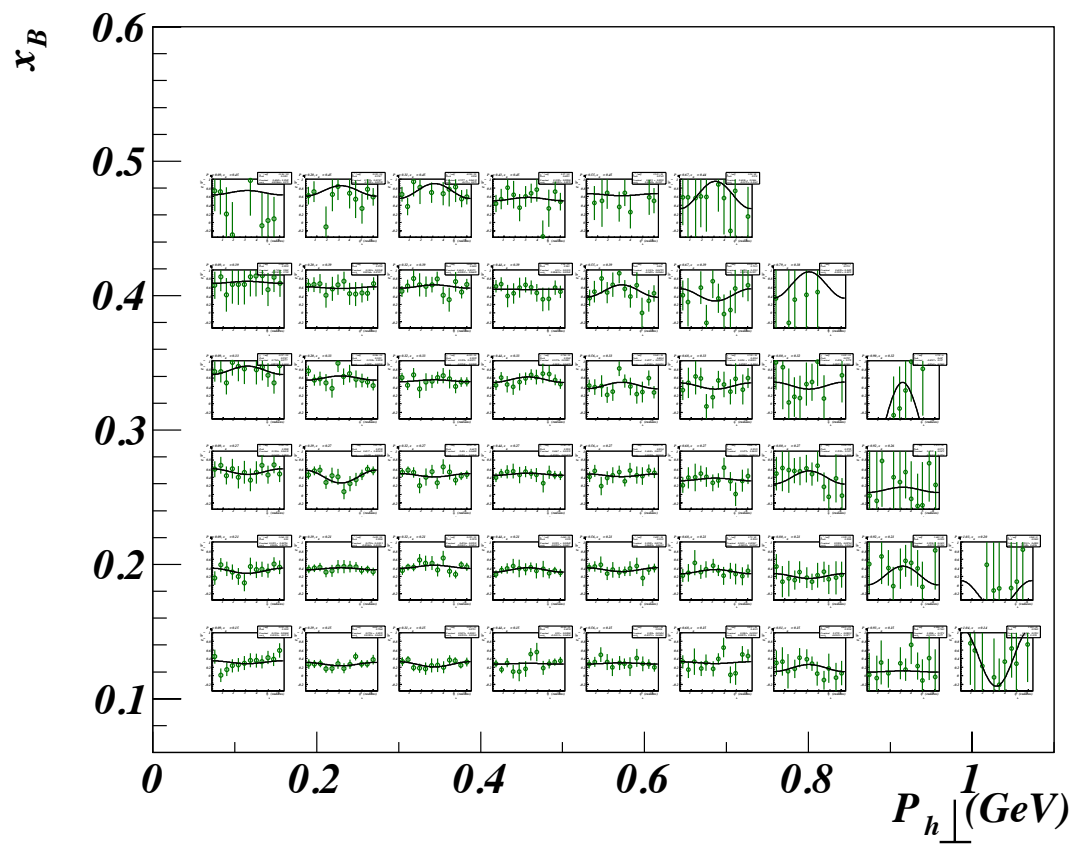


FIG. 6.13: Same as Figure 6.12 except for  $\pi^-$ .

FIG. 6.14: Same as Figure 6.12 except for  $\pi^0$

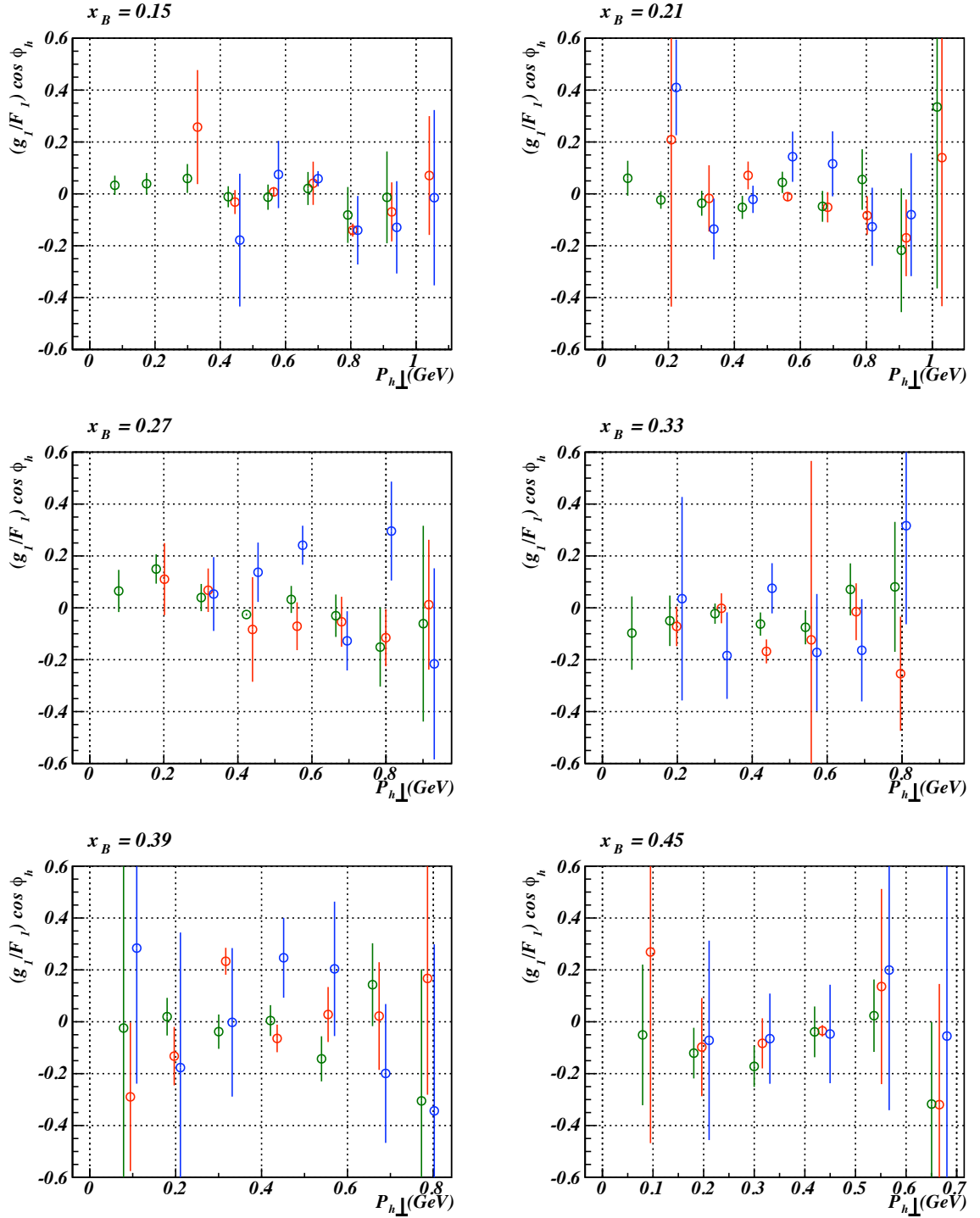


FIG. 6.15: The cosine  $\phi_h$  moment of the ratio of polarized to unpolarized structure functions,  $g_1/F_1$  versus  $P_{h\perp}$  for different bins in  $x_B$ . The average value of  $x_B$  is displayed in the title of each plot for  $\pi^+$  (red),  $\pi^-$  (blue), and  $\pi^0$  (green).

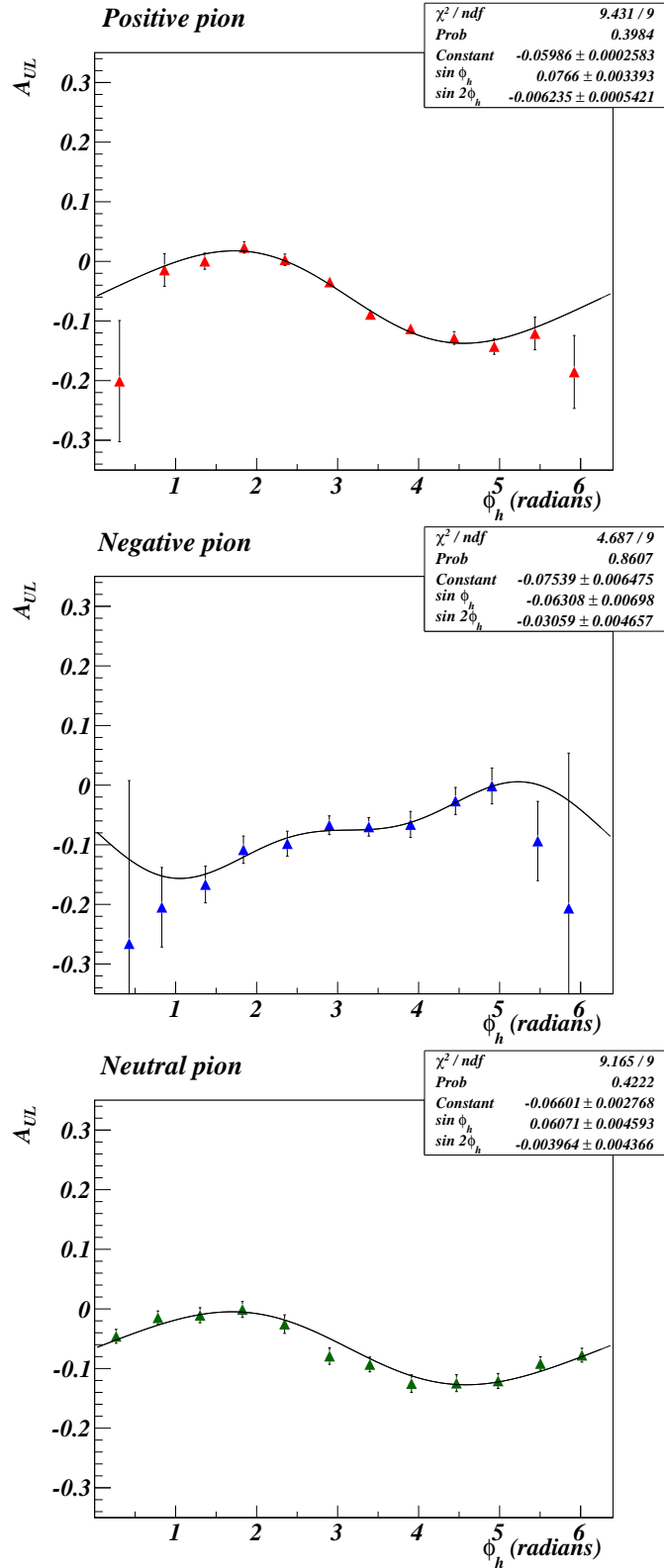


FIG. 6.16: The integrated target spin asymmetry for  $\pi^+$  (top, red points),  $\pi^-$  (middle, blue points), and  $\pi^0$  (bottom, green points). The data were fit to  $f(\phi_h) = A_{UL}^C + A_{UL}^{\sin \phi_h} \sin \phi_h + A_{UL}^{\sin 2\phi_h} \sin 2\phi_h$  and were integrated over all bins of  $(Q^2, x_B, z, P_{h\perp})$ .

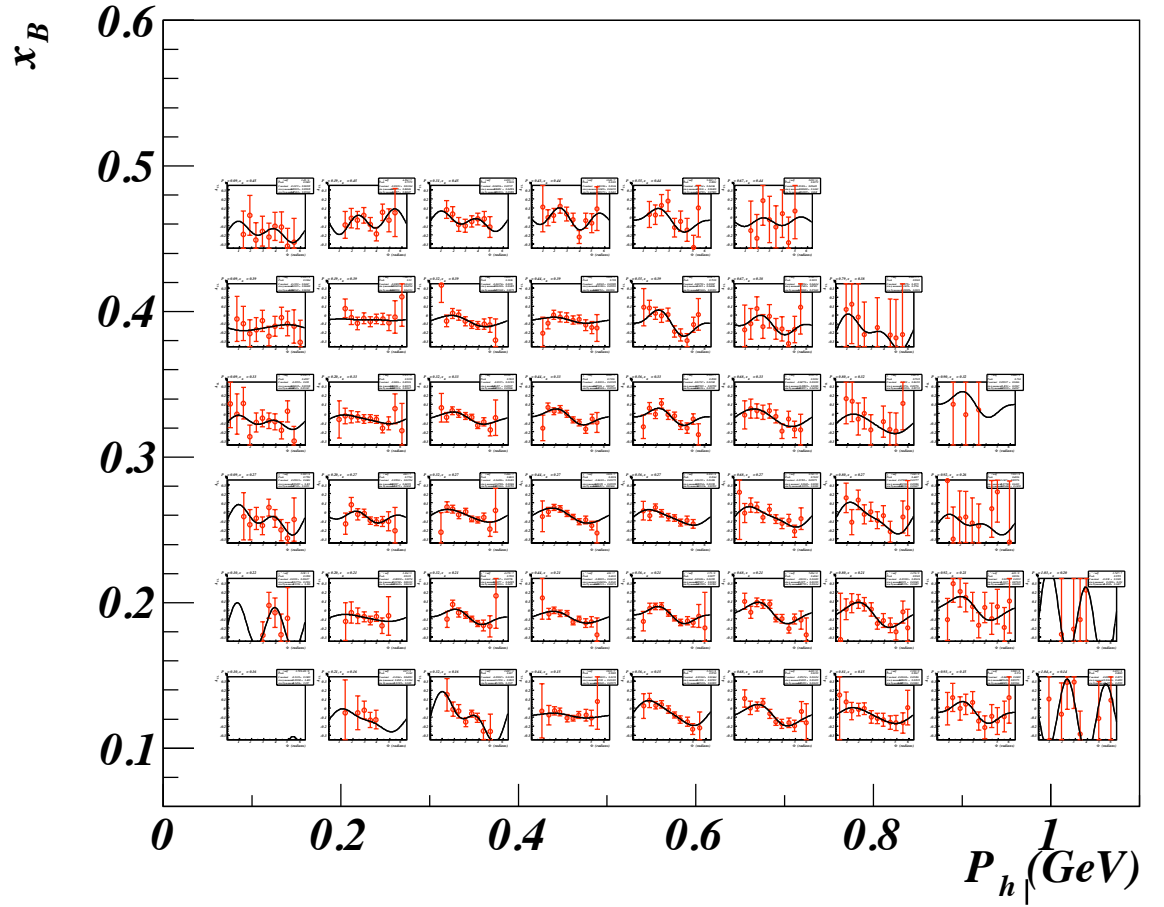


FIG. 6.17: The target spin asymmetry vs  $\phi_h$  for  $\pi^+$  in bins of  $x_B$  and  $P_{h\perp}$ . Each  $x_B$  and  $P_{h\perp}$  bin is fit to  $f(\phi_h) = A_{UL}^C + A_{UL}^{\sin\phi_h} \sin\phi_h + A_{UL}^{\sin 2\phi_h} \sin 2\phi_h$ .

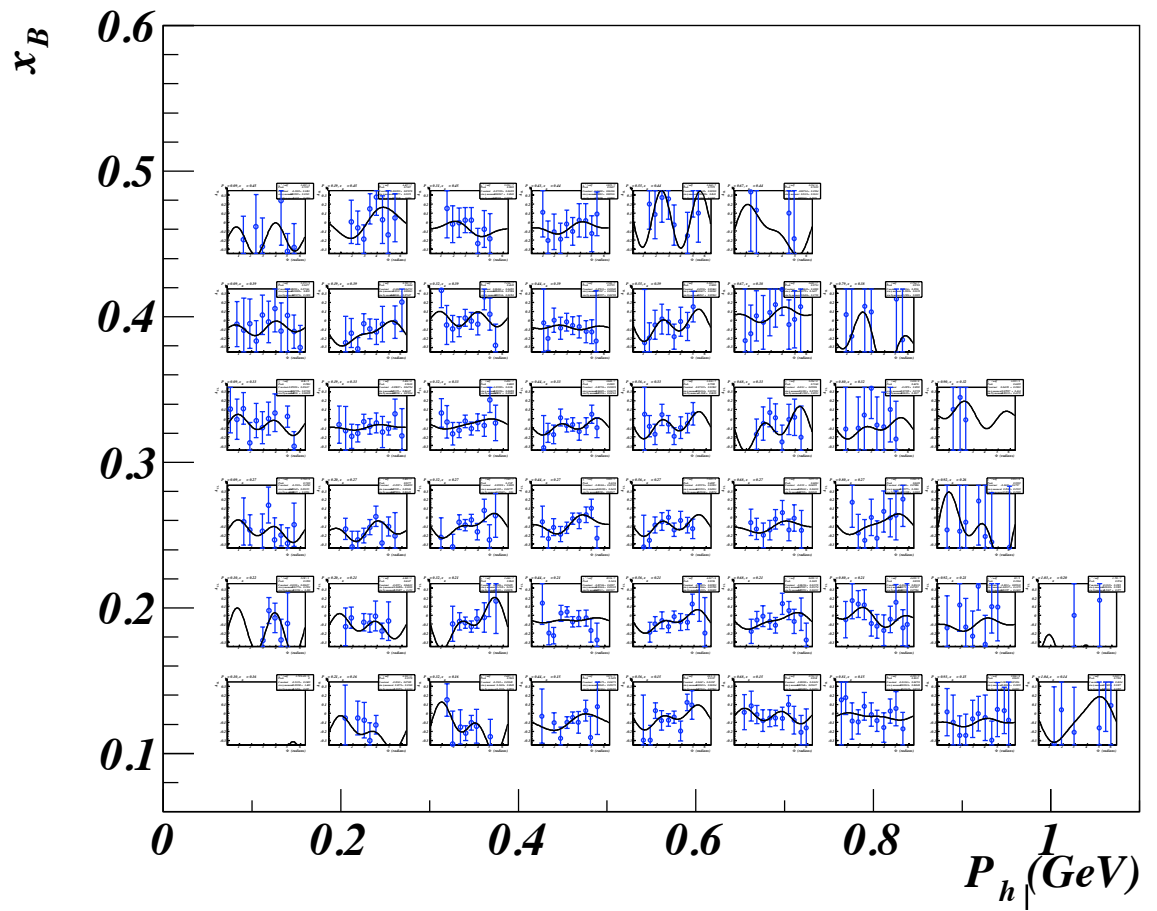


FIG. 6.18: Same as Figure 6.17 except for  $\pi^-$ .

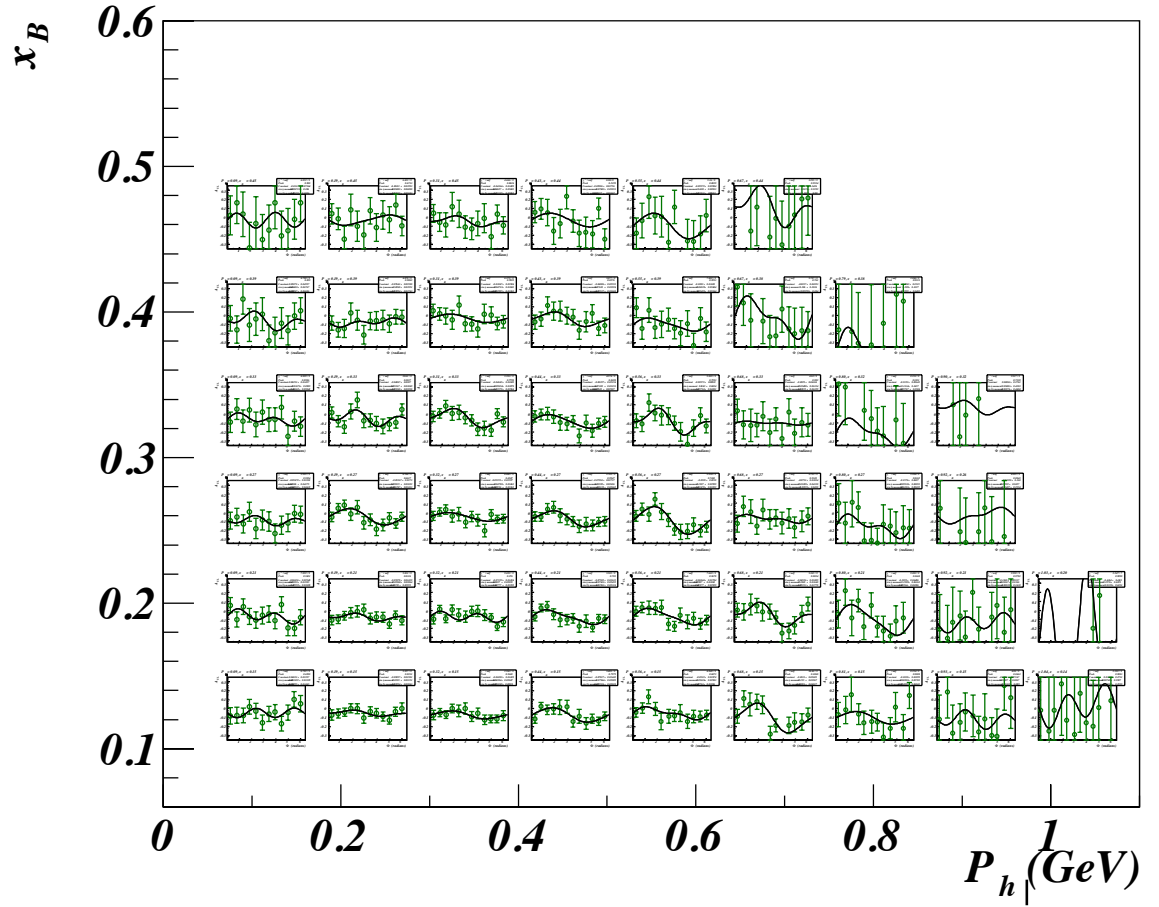


FIG. 6.19: Same as Figure 6.17 except for  $\pi^0$ .

FIG. 6.20: The target spin asymmetry vs  $\phi_h$  for  $\pi^0$  in bins of  $x_B$  and  $P_{h\perp}$ . Each  $x_B$  and  $P_{h\perp}$  bin is fit to  $f(\phi_h) = A_{UL}^C + A_{UL}^{\sin\phi_h} \sin\phi_h + A_{UL}^{\sin 2\phi_h} \sin 2\phi_h$ .

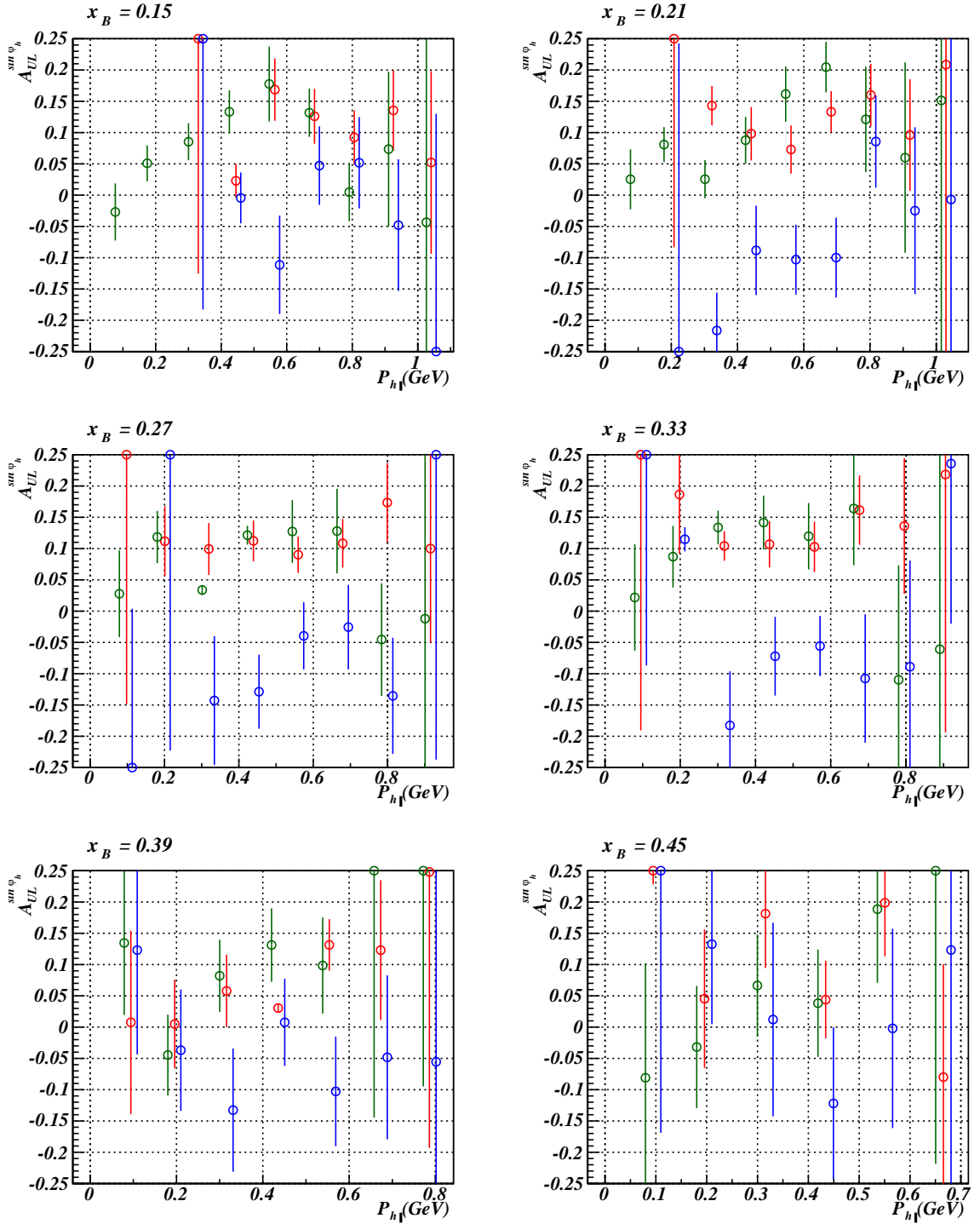


FIG. 6.21: The  $\sin \phi_h$  moments of  $A_{UL}$  as a function of  $P_{h\perp}$  for different bins in  $x_B$ . The average value of  $x_B$  is displayed in the title of each plot for  $\pi^+$  (red),  $\pi^-$  (blue), and  $\pi^0$  (green).

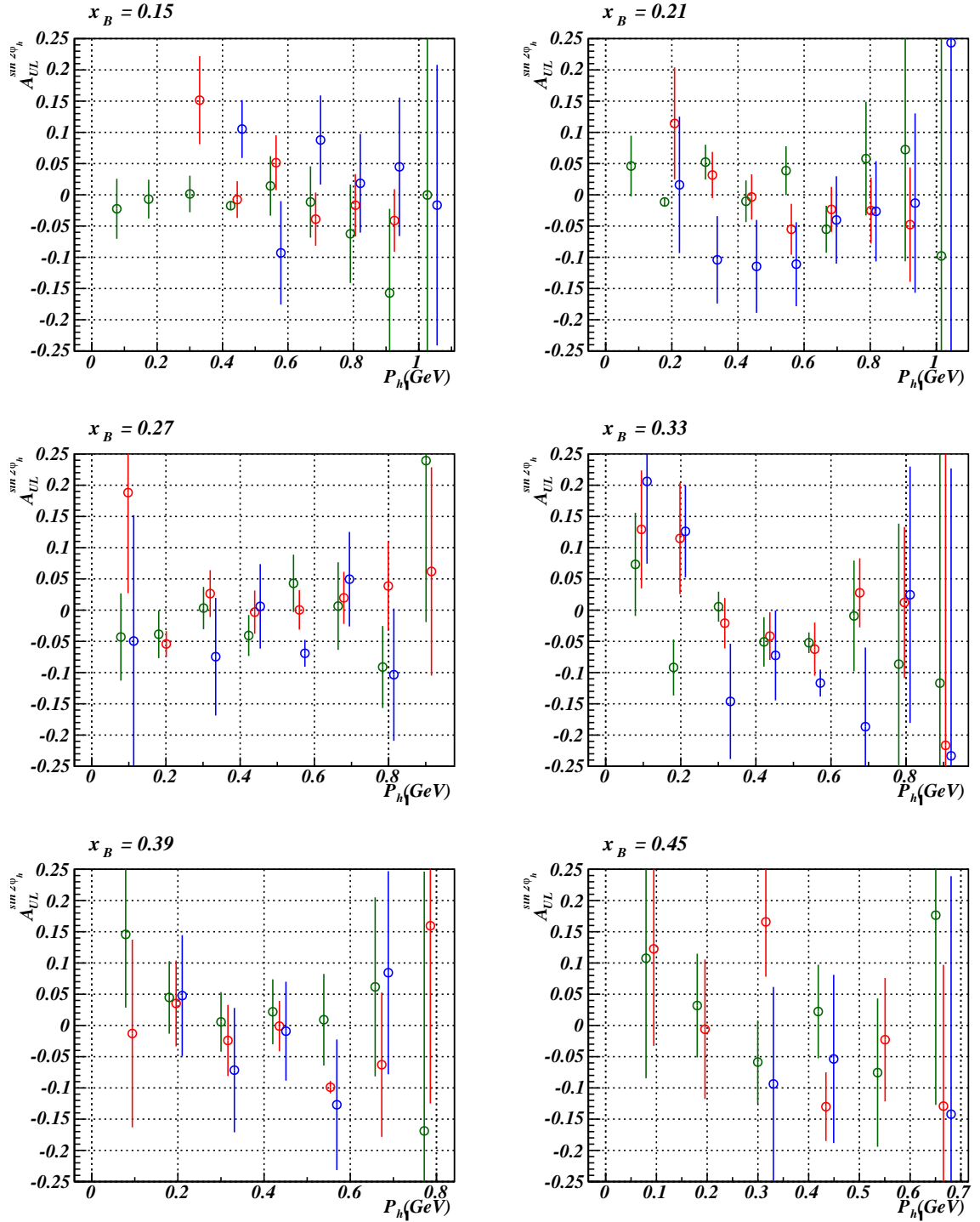


FIG. 6.22: The  $\sin 2\phi_h$  moments of  $A_{UL}$  as a function of  $P_{h\perp}$  for different bins in  $x_B$ . The average value of  $x_B$  is displayed in the title of each plot for  $\pi^+$  (red),  $\pi^-$  (blue), and  $\pi^0$  (green).

## 6.4 Comparison to Model and Existing Data

We interpret  $g_1/F_1$  by assuming the simple factorized model for TMDs and FFs of Anselmino [24] which assumes Gaussian distributions of transverse momenta. Under this assumption, the unpolarized TMD  $f_1$  summed over all quarks  $q$  for a hadron  $h$  in the final state has transverse momenta described as a Gaussian with width  $\mu_0$ ,

$$f_1^q(x_B, k_\perp) = f_1^q(x_B) \frac{1}{\pi\mu_0^2} \exp\left(-\frac{k_\perp^2}{\mu_0^2}\right) \quad (6.22)$$

and the unpolarized fragmentation function has transverse momenta described as a Gaussian with width  $\mu_D$  written as

$$D_q^h(z, p_\perp) = D_q^h(z) \frac{1}{\pi\mu_D^2} \exp\left(-\frac{p_\perp^2}{\mu_D^2}\right). \quad (6.23)$$

The momenta  $k_\perp$  and  $p_\perp$  refer to the quark before scattering and the fragmenting quark respectively<sup>1</sup>. These are written in terms of the transverse momentum of the hadron in the final state as

$$P_{h\perp} = p_\perp + zk_\perp. \quad (6.24)$$

A similar expression for the polarized structure function is written as

$$g_1^q(x_B, k_\perp) = g_1^q(x_B) \frac{1}{\pi\mu_2^2} \exp\left(-\frac{k_\perp^2}{\mu_2^2}\right) \quad (6.25)$$

where  $\mu_2$  is the width of the Gaussian associated with it.

Using Equations 6.22 - 6.25, we write the ratio of polarized to unpolarized structure functions for the example of the up quark hadronizing into  $\pi^+$  as,

---

<sup>1</sup>This definition of  $k_{perp}$  and  $p_{perp}$  is opposite that used by Bacchetta et. al. [71]. This document uses the Bacchetta convention except for this particular subsection.

$$\frac{g_1}{F_1}(x_B, z, P_{h\perp}) = \frac{g_1}{F_1}(x_B, z) \left( \frac{\mu_D^2 + z^2 \mu_0^2}{\mu_D^2 + z^2 \mu_2^2} \right) \exp [z^2 P_{h\perp}^2 (\mu_2^2 - \mu_0^2)] \quad (6.26)$$

The model introduces a  $P_{h\perp}$  dependence for the ratio of structure functions. The value for the width associated with  $f_1$  used here is  $\mu_0^2 = 0.25 \text{ GeV}^2$ . The values for  $\mu_D^2$  and,  $\mu_2^2$  are allowed to vary as long as they remain positive. The model predictions for  $\pi^{\pm,0}$  are shown using dashed lines in Figures 6.23 - 6.25.

We compared the beam spin asymmetry for  $\pi^0$  with the recently published results with an unpolarized hydrogen target Ref. [25]. The comparison seen in Figure 6.26 is for two bins in  $x_B$ . The data look consistent with each other. The ‘eg1-dvcs’ results are largely for proton plus neutron in a nucleus, whereas the results from Ref. [25] are for the proton only. This indicates that there is probably not much difference in this quantity for proton and neutron.

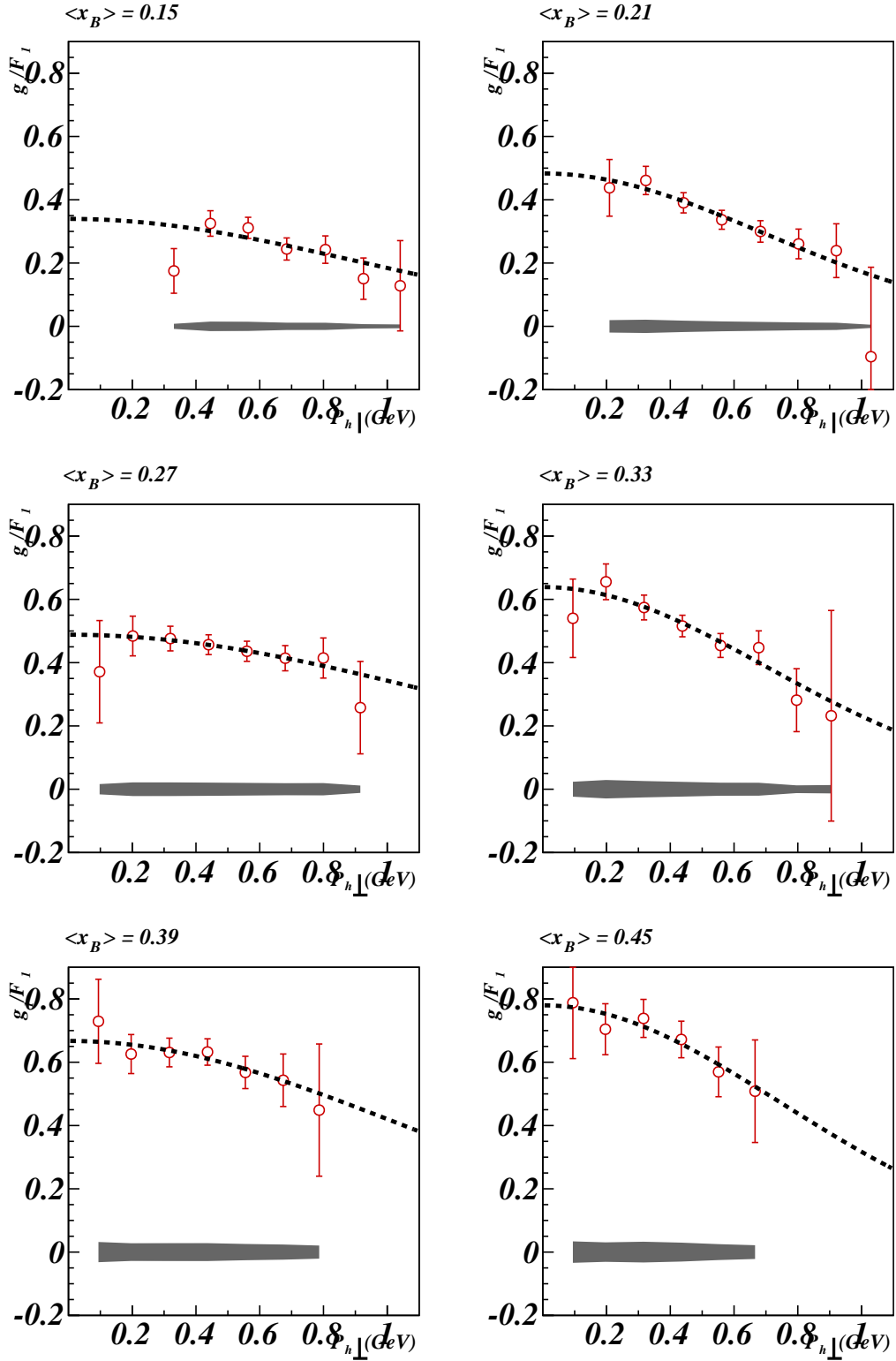


FIG. 6.23: The ratio of polarized to unpolarized structure functions integrated over  $(Q^2, x_B, z, P_{h\perp})$  for  $\pi^+$  (red). The gray bar at the bottom denotes systematic errors from Table 5.5. The dashed line represents the Anselmino model prediction Ref. [24].

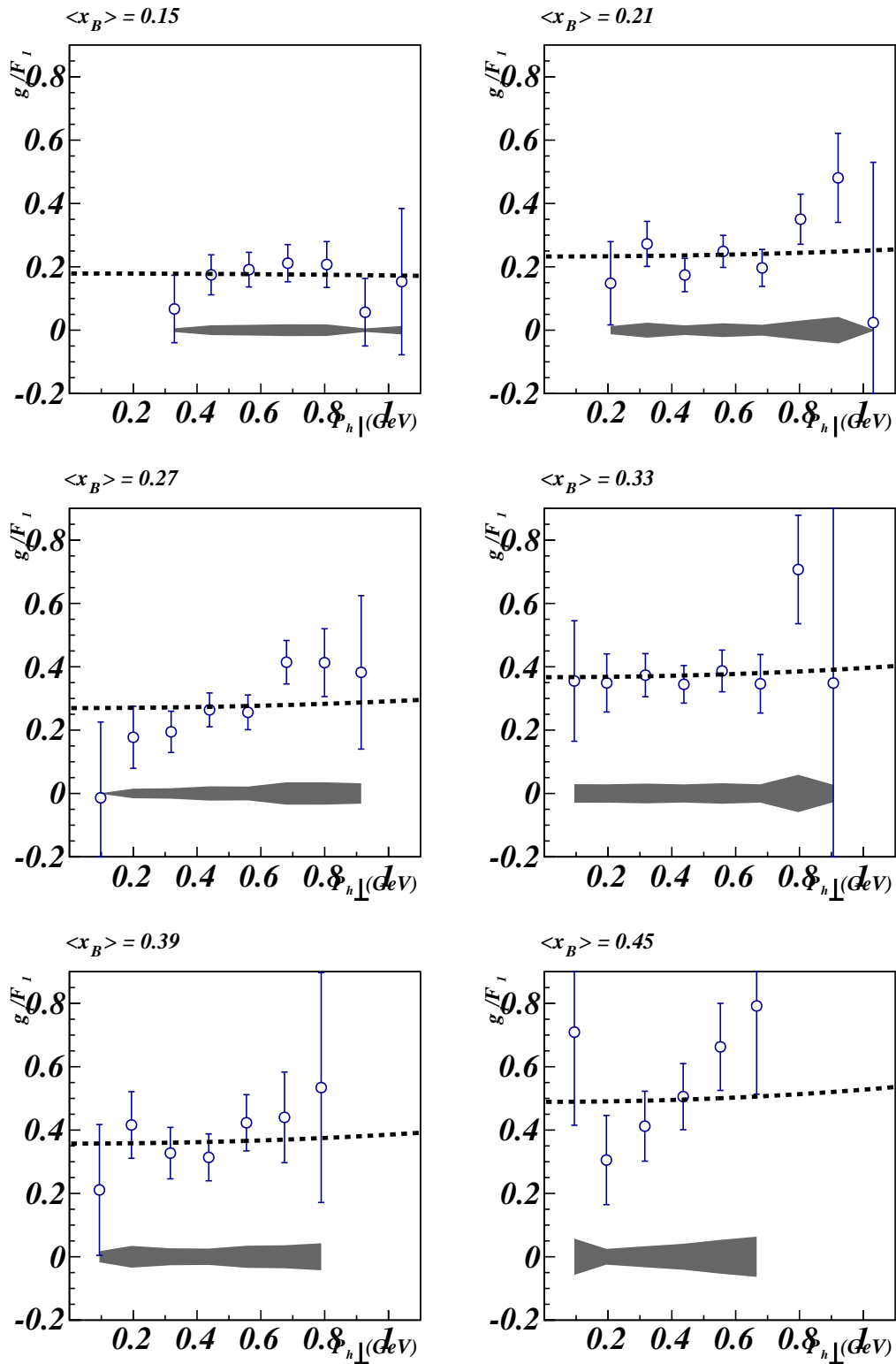
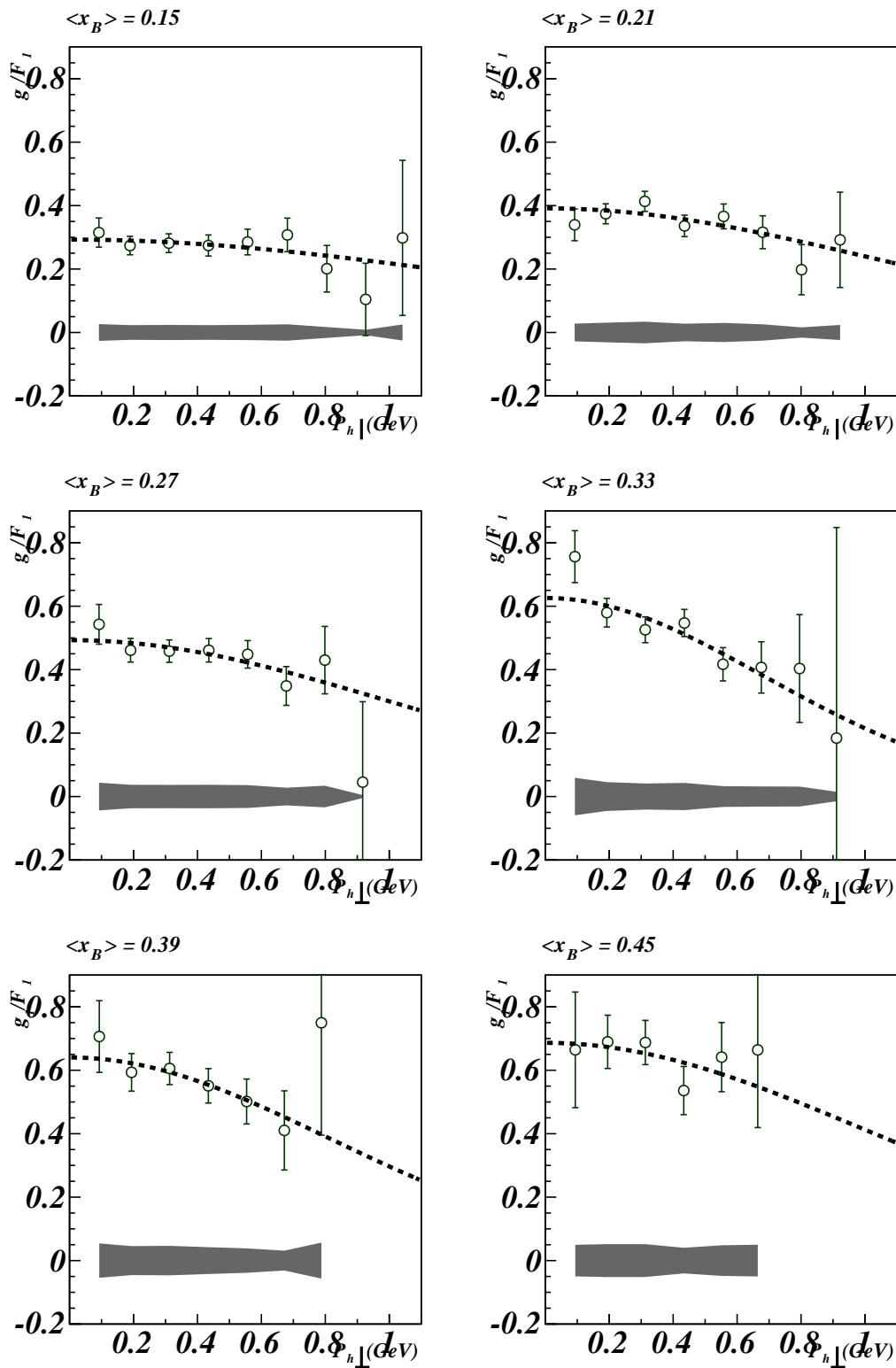


FIG. 6.24: Same as Figure 6.23 except for  $\pi^-$ .

FIG. 6.25: Same as Figure 6.23 except for  $\pi^0$ .

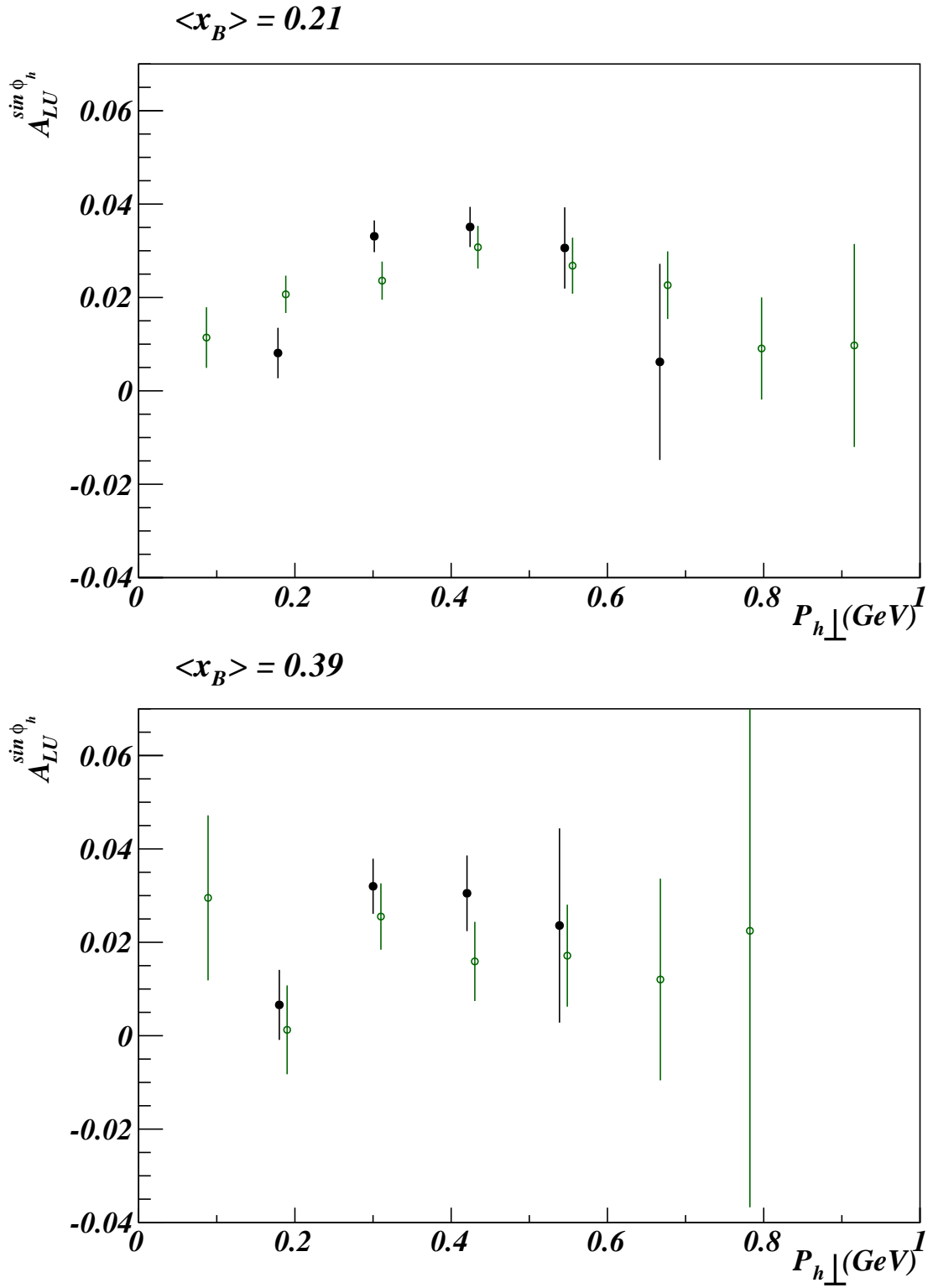


FIG. 6.26: The  $\sin \phi_h$  moments of  $A_{LU}$  as a function of  $P_{h\perp}$  for different bins in  $x_B$ . The average value of  $x_B$  is displayed in the title of each plot for  $\pi^0$  from eg1-dvcs data (green) and  $\pi^0$  from Ref. [25].

## 6.5 Future Studies

Others in the eg1-dvcs analysis group are developing a Monte Carlo (MC) simulation of this experiment that includes the precise target geometry and a realistic SIDIS event generator. Using this MC, will eventually lead to greater accuracy in the dilution factor, radiative corrections, and background corrections.

# CHAPTER 7

## Conclusion

The semi-inclusive DIS results of this work are divided into three categories, namely the beam spin asymmetry, double spin asymmetry and target spin asymmetry. The kinematic coverage of the eg1-dvcs experiment is:

- $Q^2 = 1.0 - 4.5 \text{ GeV}^2$
- $x_B = 0.15 - 0.48$
- $z = 0.4 - 0.7$
- $P_{h\perp} = 0.05 - 1.0 \text{ GeV}$
- $\phi_h = 0^\circ - 360^\circ$ .

### Beam Spin Asymmetry

We show a significant  $\sin\phi_h$  moment of the beam spin asymmetry for  $\pi^{\pm,0}$ . This is shown to be consistent with the latest CLAS measurement for  $\pi^0$ . It is also consistent

with the latest measurement by the HERMES Collaboration in Ref. [72] with significantly better precision. Both the HERMES and previous CLAS measurements were made with hydrogen targets. The eg1-dvcs measurement was made with polarized  $\text{NH}_3$ . The region of  $x_B$  and  $P_{h\perp}$  that we study does not show any significant deviation compared to the pure hydrogen results. The  $\sin 2\phi_h$  moment for the beam spin asymmetry is consistent with zero.

## Double Spin Asymmetry

The double spin asymmetry is studied in the form of the ratio of polarized to unpolarized structure functions which is a measure of the difference in behavior of quark transverse momenta in the polarized and unpolarized proton. The transverse momentum dependence of  $g_1/F_1$  shows some indication that longitudinally polarized quarks have a different distribution than unpolarized quarks. The preliminary ratios are in reasonable agreement for the neutral pion compared to predictions by Anselmino and others in Ref. [24]. The charged pions however, show possible deviations from predictions. The data indicate that the double spin asymmetry tends to increase for  $\pi^-$ , and decrease for  $\pi^+$ , and stays flat for  $\pi^0$ .

## Target Spin Asymmetry

We show a significant  $\sin \phi_h$  moment of the target single spin asymmetry for  $\pi^{\pm,0}$ . The  $P_{h\perp}$  dependence of the  $\sin \phi_h$  moment increases with  $P_{h\perp}$  and the moment for  $\pi^-$  has the opposite sign as that for  $\pi^+$ . The first measurement of the  $\sin 2\phi_h$  moment was reported by Ref. [6]. This is confirmed for two bins of  $\langle x_B \rangle = 0.21$  and  $\langle x_B \rangle = 0.33$ .

## Summary

These data significantly improve our knowledge of the spin structure of the proton and together with world data, one can extract individual transverse momentum distributions  $e$ ,  $h_{1L}^\perp$  and  $g_1$ ; and the Collins fragmentation function. A summary of the moments and their corresponding TMDs is listed in Table 7.1.

Asymmetry	Moment	Twist	FF	TMD
$A_{LU}$	$\sin \phi_h$	3	$H_1^\perp$	$e$
$A_{LL}$	-	2	$D_1$	$g_{1L}$
$A_{UL}$	$\sin \phi_h$	3	$H_1^\perp$	$h_L$
$A_{UL}$	$\sin 2\phi_h$	2	$H_1^\perp$	$h_{1L}$

TABLE 7.1: Transverse Momentum Distributions and Fragmentation Functions accessed by observables from the eg1-dvcs measurement.

Compared to the traditional structure functions that depend only on  $x_B$  and  $Q^2$ , the observables in SIDIS typically depend on five variables,  $(x_B, Q^2, z, P_{h\perp}$  and  $\phi_h)$ . This requires statistics in the data to study each dimension in terms of the others as opposed to projections for a single variable. This work takes a step in that direction by showing three semi-inclusive dimensions -  $x_B, P_{h\perp}$  and  $\phi_h$ . This is a departure from previous data which are shown in a one dimensional format with integration over the other four variables.

World data thus far in combination with the eg1-dvcs measurement play an important role in exploring TMDs on the longitudinally polarized nucleon. They have established important features, especially relating to the polarized semi-inclusive structure TMD,  $g_{1L}$  and sine- $\phi_h$  moments of the single spin asymmetries. Theoretical models are constrained using existing data. Assumptions are made to limit the number of parameters in models, which is important considering the scarcity of the data. One example of a questionable

assumption is that the  $P_{h\perp}$  dependence of the difference in parton TMDs is Gaussian.

In order to improve our understanding of TMDs and resolve theoretical model issues, it is important to perform precision measurements of the single and double spin asymmetries. The Jefferson Lab upgrade to 12 GeV has the promise to produce these semi-inclusive DIS measurements. There are four approved experiments for the higher energy using a transversely and longitudinally polarized  $^3\text{He}$  target in Hall A (E 1209018, E 1211007), and a longitudinally polarized  $\text{NH}_3$  target in Hall B (E 1206109, E 1209008).

# APPENDIX A

## Angles in SIDIS

Using the convention in [26], the target spin vector  $\mathbf{S}$  is defined in two different coordinate systems -  $C$  and  $C'$ . In the coordinate system  $C$ , the virtual photon direction is along the  $z$  axis.

$$\mathbf{S} \stackrel{C}{=} \begin{pmatrix} S_T \cos \phi_S \\ S_T \sin \phi_S \\ -S_L \end{pmatrix} \quad (\text{A.1})$$

where  $S_L$  and  $S_T$  specify the longitudinal and transverse components relative to the virtual photon direction. In the coordinate system  $C'$ , the incoming lepton beam direction is along the  $z'$  axis. The transformation between the two coordinate systems is described by a angular rotation  $\theta$  about the  $y = y'$  axes as seen in Figure A.1.

$$\mathbf{S} \stackrel{C'}{=} \begin{pmatrix} P_T \cos \psi \\ P_T \sin \psi \\ -P_L \end{pmatrix} \quad (\text{A.2})$$

where  $P_L$  and  $P_T$  specify the longitudinal and transverse components relative to the lepton beam direction.

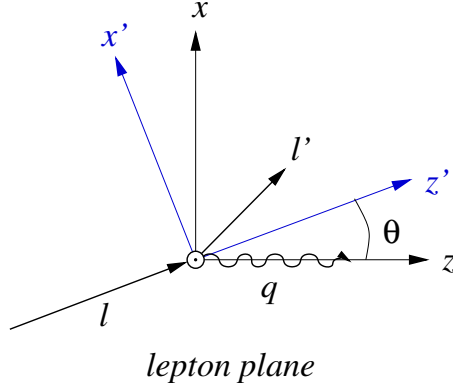


FIG. A.1: The lepton plane in the target rest frame. The  $y$  and  $y'$  axes coincide and point out of the plane of the paper [26].

The azimuthal angles  $\psi$  and  $\phi_S$  are defined as the angle formed by the target spin with respect to the lepton beam direction and virtual photon direction, respectively. The rotation transformation gives the relationship between the target spin vector in the two different reference frames.

$$S_T \cos \phi_S = \cos \theta P_T - \sin \theta P_L \quad (\text{A.3})$$

$$S_T \sin \phi_S = P_T \sin \psi$$

$$S_L = \sin \theta P_T \cos \psi + \cos \theta P_L$$

# APPENDIX B

## Light Cone Coordinates

A summary of light cone coordinates is described here as sketched in [3]. The light cone coordinate system is deemed particularly useful for calculating expressions for transverse momentum distributions and fragmentation functions. Consider an arbitrary four vector,

$$v = \begin{pmatrix} v^0 \\ v^1 \\ v^2 \\ v^3 \end{pmatrix} \quad (\text{B.1})$$

The light cone decomposition of a vector can be written in a Lorentz covariant fashion using two light-like vectors -  $n_+ = [0, 1, \mathbf{0}_T]$  and  $n_- = [1, 0, \mathbf{0}_T]$ .

$$v^\mu = v^+ n_+^\mu + v^- n_-^\mu + v_T^\mu \quad (\text{B.2})$$

where  $v^+ = v \cdot n_-$  and  $v^- = v \cdot n_+$ . Also,  $v_T \cdot n_- = v_T \cdot n_+ = 0$ . The transformation of  $v$  is

thus given by,

$$\begin{aligned}v^+ &= \frac{v^0 + v^3}{\sqrt{2}} \\v^- &= \frac{v^0 - v^3}{\sqrt{2}} \\v_T &= \begin{pmatrix} v^1 \\ v^2 \end{pmatrix}\end{aligned}\tag{B.3}$$

## BIBLIOGRAPHY

- [1] B. A. Mecking et al., Nucl. Ins. Meth. A **503**, 513 (2003).
- [2] J. P. Chen, A. Deur, S. Kuhn, and Z. E. Meziani, J. Phys. Conf. Ser. **299**, 01 (2011).
- [3] A. Bacchetta et al., JHEP **02**, 093 (2007).
- [4] A. Airapetian et al. (HERMES), Phys. Rev. Lett. **84**, 4047 (2000).
- [5] A. Airapetian et al. (HERMES), Phys. Lett. **B622**, 14 (2005).
- [6] H. Avakian et al. (CLAS Collaboration), Phys. Rev. Lett. **105**, 262002 (2010).
- [7] E. Zemlyanichkina (COMPASS Collaboration), PoS **DIS2010**, 254 (2010).
- [8] A. V. Efremov, K. Goeke, and P. Schweitzer, Phys. Rev. **D67**, 114014 (2003).
- [9] J. Zhu and B.-Q. Ma, Phys.Lett. **B696**, 246 (2011).
- [10] C. W. Leemann, D. R. Douglas, and G. A. Krafft, Ann. Rev. Nucl. Part. Sci. **51**, 413 (2001).
- [11] R. Fersch, Ph.D. thesis, College of William and Mary (2008).
- [12] J. Pierce, Ph.D. thesis, University of Virginia (2008).
- [13] C. D. Keith et al., Nucl. Ins. Meth. A **501**, 327 (2003).
- [14] H. Baghdasaryan, Private Communication (2011).
- [15] B. Zhao, *Drift chamber alignment* (2011), URL <http://www.jlab.org/Hall-B/secure/eg1-dvcs/technotes/DCAalign/DCAalign.pdf>.
- [16] P. Khetarpal, Private Communication (2011).
- [17] M. Ungaro, Private Communication (2011).
- [18] M. Amarian et al., Nucl. Ins. Meth. A **460**, 239 (2001).
- [19] P. E. Bosted, eg1-dvcs Technical Note 013 (2011), URL <http://www.jlab.org/Hall-B/secure/eg1-dvcs/technotes/fidcutic/fidic.pdf>.

- [20] P. E. Bosted and M. E. Christy, Phys. Rev. C **77**, 065206 (2008).
- [21] M. E. Christy and P. E. Bosted, Phys. Rev. C **81**, 055213 (2010).
- [22] C. J. Bebek et al., Phys. Rev. **D15**, 3085 (1977).
- [23] R. Ent et al., *Measurement of the Ratio  $R = \sigma_L/\sigma_T$  in Semi-Inclusive Deep-Inelastic Scattering* (2006), proposal to Jefferson Lab PAC 30 E-12-06-104.
- [24] M. Anselmino, A. Efremov, A. Kotzinian, and B. Parsamyan, Phys. Rev. **D74**, 074015 (2006).
- [25] M. Aghasyan, H. Avakian, P. Rossi, E. DeSanctis, D. Hasch, et al., Phys. Lett. **B704**, 397 (2011).
- [26] M. Diehl and S. Sapeta, Eur. Phys. J. **C41**, 515 (2005).
- [27] Halzen F. and Martin A. D., *Quarks and Leptons: An Introductory Course in Modern Particle Physics*, John Wiley & Sons, Inc. (1984).
- [28] J. Ashman et al. (European Muon), Phys. Lett. **B206**, 364 (1988).
- [29] R. Jaffe, H. Meyer, and G. Piller, *Spin, twist and hadron structure in deep inelastic processes*, Springer Berlin / Heidelberg (1997).
- [30] A. Airapetian et al. (HERMES), Phys. Rev. **D64**, 097101 (2001).
- [31] A. Airapetian et al. (HERMES), Phys. Lett. **B562**, 182 (2003).
- [32] A. Bacchetta, F. Conti, and M. Radici, Phys. Rev. D **78**, 074010 (2008).
- [33] H. Avakian, A. V. Efremov, P. Schweitzer, and F. Yuan, Phys. Rev. D **81**, 074035 (2010).
- [34] A. V. Efremov, K. Goeke, and P. Schweitzer, Phys. Lett. **B522**, 37 (2001).
- [35] F. Yuan, Phys.Lett. **B589**, 28 (2004).
- [36] A. V. Afanasev and C. E. Carlson, Phys.Rev. **D74**, 114027 (2006).
- [37] M. Wakamatsu, Phys. Rev. **D79**, 094028 (2009).
- [38] L. P. Gamberg, D. S. Hwang, and K. A. Oganessyan, Phys.Lett. **B584**, 276 (2004).
- [39] A. Metz and M. Schlegel, Eur.Phys.J. **A22**, 489 (2004).
- [40] R. P. Feynman, Phys. Rev. Lett. **23**, 1415 (1969).

- [41] S. Boffi, A. V. Efremov, B. Pasquini, and P. Schweitzer, Phys. Rev. D **79**, 094012 (2009).
- [42] A. Chodos, R. L. Jaffe, K. Johnson, and C. B. Thorn, Phys. Rev. D **10**, 2599 (1974).
- [43] B. Pasquini, S. Cazzaniga, and S. Boffi, Phys. Rev. D **78**, 034025 (2008).
- [44] M. L. Stutzman et al., Nucl. Ins. Meth. A **574**, 213 (2007).
- [45] D. Schultz et al. (1992), presented at 10th International Symposium on High Energy Spin Physics (SPIN 92 - 35th Yamada Conference), Nagoya, Japan, 9-14 Nov 1992.
- [46] H. Liu, Nucl. Ins. Meth. A **400** (1997).
- [47] A. Abragam and M. Goldman, Rep. Prog. in Phys **41**, 395 (1978).
- [48] Y. Prok, Ph.D. thesis, University of Virginia (1997).
- [49] N. Kvaltine, *Calibration of the polarized target for the deuteron runs of egl-dvcs part c* (2011), URL <http://twist.phys.virginia.edu/~ndk5g/TargPol/DeuteronTargetCalibration.pdf>.
- [50] I. Bedlinskiy et al., *An Inner Calorimeter for CLAS/DVCS experiments* (2010), to be published.
- [51] E. Smith and V. Dharmawardane, Tech. Rep., CLAS-NOTE 1999-011 (2001).
- [52] P. E. Bosted and A. Kim, eg1-dvcs Technical Note 003 (2010), URL <http://www.jlab.org/Hall-B/secure/eg1-dvcs/technotes/energy/energy.pdf>.
- [53] S. S. Jawalkar and P. E. Bosted, eg1-dvcs Technical Note 007 (2010), URL <http://www.jlab.org/Hall-B/secure/eg1-dvcs/technotes/nt22/nt22.pdf>.
- [54] P. E. Bosted, eg1-dvcs Technical Note 002 (2010), URL <http://www.jlab.org/Hall-B/secure/eg1-dvcs/technotes/raster/raster.pdf>.
- [55] P. E. Bosted, eg1-dvcs Technical Note 004 (2010), URL [http://wwwold.jlab.org/Hall-B/secure/eg1-dvcs/technotes/targetinfo/target\\_info.pdf](http://wwwold.jlab.org/Hall-B/secure/eg1-dvcs/technotes/targetinfo/target_info.pdf).
- [56] M. Osipenko and A. Vlassov (2004), cLAS-NOTE 2006-009, URL [http://wwwold.jlab.org/Hall-B/notes/clas\\_notes04/2004-020.pdf](http://wwwold.jlab.org/Hall-B/notes/clas_notes04/2004-020.pdf).
- [57] Y. Prok, eg1-dvcs Technical Note 007 (2010), URL <http://www.jlab.org/Hall-B/secure/eg1-dvcs/technotes/rastercheck/rasterTN.pdf>.
- [58] T. W. Donnelly and A. S. Raskin, Annals Phys. **169**, 247 (1986).

- [59] P. E. Bosted, Phys.Rev. **C51**, 409 (1995).
- [60] E. Seder, *Determination of polarization product using exclusive elastic scattering*. (2011).
- [61] K. Nakamura et al. (Particle Data Group), J. Phys. **G37**, 075021 (2010).
- [62] P. E. Bosted, eg1-dvcs Technical Note 005 (2010), URL <http://www.jlab.org/Hall-B/secure/eg1-dvcs/technotes/radcor/radcor.pdf>.
- [63] S. S. Jawalkar et al., eg1-dvcs Technical Note 008 (2010), URL <http://wwwold.jlab.org/Hall-B/secure/eg1-dvcs/technotes/LandLAv2/LandLA.pdf>.
- [64] H. Avakian et al., *Semi-Inclusive pion production with a Longitudinally Polarized target at 6 GeV*, pR05-113.
- [65] M. Gluck, E. Reya, M. Stratmann, and W. Vogelsang, Phys. Rev. **D53**, 4775 (1996), hep-ph/9508347.
- [66] H. Mkrtchyan, P. E. Bosted, et al., Physics Letters B **665**, 20 (2008).
- [67] W. K. Brooks and H. Hakobyan, Nucl. Phys. **A830**, 361c (2009).
- [68] P. Bosted and S. S. Jawalkar, eg1-dvcs Technical Note 020 (2011).
- [69] S. S. Jawalkar, *Systematic error for dilution lists (30, 31, 32)* (2011), URL <http://www.jlab.org/Hall-B/secure/eg1-dvcs/sucheta/>.
- [70] S. S. Jawalkar, *Unintegrated asymmetry lists* (2011), URL <http://www.jlab.org/Hall-B/secure/eg1-dvcs/sucheta/>.
- [71] A. Bacchetta, U. D'Alesio, M. Diehl, and C. A. Miller, Phys. Rev. **D70**, 117504 (2004).
- [72] A. Airapetian et al. (HERMES Collaboration), Phys.Lett. **B648**, 164 (2007).